AD-A029 135

USADAC TECHNICAL LIBRARY
5 0712 01016833 3
AI

ADA029735

AD

TECHNICAL
LIBRARY

PROCEEDINGS OF THE ARMY SYMPOSIUM ON SOLID MECHANICS, 1976 - COMPOSITE MATERIALS: THE INFLUENCE OF MECHANICS OF FAILURE ON DESIGN

September 1976

Approved for public release; distribution unlimited.

ARMY MATERIALS AND MECHANICS RESEARCH CENTER
Watertown, Massachusetts 02172

The findings in this report are not to be construed as an official Department of the Army position, unless so designated by other authorized documents.

Mention of any trade names or manufacturers in this report shall not be construed as advertising nor as an official indorsement or approval of such products or companies by the United States Government.

DISPOSITION INSTRUCTIONS

Destroy this report when it is no longer needed.
Do not return it to the originator.

UNCLASSIFIED

SECURITY CLASSIFICATION OF THIS PAGE (*When Data Entered*)

REPORT DOCUMENTATION PAGE		READ INSTRUCTIONS BEFORE COMPLETING FORM
1. REPORT NUMBER AMMRC MS 76-2	2. GOVT ACCESSION NO.	3. RECIPIENT'S CATALOG NUMBER
4. TITLE (*and Subtitle*) Proceedings of the Army Symposium on Solid Mechanics, 1976 - Composite Materials: The Influence of Mechanics of Failure on Design		5. TYPE OF REPORT & PERIOD COVERED Final Report 6. PERFORMING ORG. REPORT NUMBER
7. AUTHOR(*s*)		8. CONTRACT OR GRANT NUMBER(*s*)
9. PERFORMING ORGANIZATION NAME AND ADDRESS Army Materials and Mechanics Research Center Watertown, Massachusetts 02172 DRXMR-T		10. PROGRAM ELEMENT, PROJECT, TASK AREA & WORK UNIT NUMBERS
11. CONTROLLING OFFICE NAME AND ADDRESS U. S. Army Materiel Development and Readiness Alexandria, Virginia 22333		12. REPORT DATE September 1976 13. NUMBER OF PAGES 296
14. MONITORING AGENCY NAME & ADDRESS(*if different from Controlling Office*)		15. SECURITY CLASS. (*of this report*) Unclassified 15a. DECLASSIFICATION/DOWNGRADING SCHEDULE

16. DISTRIBUTION STATEMENT (*of this Report*)

Approved for public release; distribution unlimited.

17. DISTRIBUTION STATEMENT (*of the abstract entered in Block 20, if different from Report*)

18. SUPPLEMENTARY NOTES

19. KEY WORDS (*Continue on reverse side if necessary and identify by block number*)

(see Reverse Side)

20. ABSTRACT (*Continue on reverse side if necessary and identify by block number*)

Proceedings of the Army Symposium on Solid Mechanics, 1976 - Composite Materials: The Influence of Mechanics of Failure on Design, held at Bass River (Cape Cod), Massachusetts, 14-16 September 1976

DD FORM 1 JAN 73 1473 EDITION OF 1 NOV 65 IS OBSOLETE

UNCLASSIFIED

SECURITY CLASSIFICATION OF THIS PAGE (*When Data Entered*)

Block No. 19

KEY WORDS

Buckling
Composite materials
Composite structures
Computerized simulation
Cracking (fracturing)
Cracks
Damage
Damage tolerance
Defects
Failure
Fatigue
Fibers
Filaments
Fracture (mechanics)
Laminates
Mathematical analysis
Mathematical models
Mechanics
Reliability
Statistical analysis
Strain (mechanics)
Stress concentrations
Structural mechanics
Structural response

PREFACE

The Army Symposium on Solid Mechanics, 1976, was the fifth in a series of biennial meetings sponsored by the Technical Working Group (TWG) for Mechanics of Materials, one of nine TWG's of the U.S. Army Materiel Development and Readiness Command Materials Advisory Group. These meetings are coordinated by the Army Materials and Mechanics Research Center (AMMRC) in Watertown, Massachusetts. The first such conference was held in 1968 on the general theme of solid mechanics. Subsequent meetings were held on the themes: Lightweight Structures (in 1970), Ballistic Problems (in 1972) and Structural Joints (in 1974). This 1976 symposium was held on the theme, Composite Materials: The Influence of Mechanics of Failure on Design.

Participation in these symposia has broadened with time. Starting with the 1972 meeting, papers have been solicited from in-house and contract researchers and designers for the Navy, Air Force and other Government Agencies, in addition to those for the Army. Beginning with the 1974 meeting, the Symposium Committee was expanded to include representation from the Navy, Air Force, NASA and the U. S. Army Corps of Engineers. These expansions recognize that many mechanics research and/or design problems are not unique to a single service or government agency.

Essentially, these symposia are a vehicle for enhancing the responsiveness of the mechanics research efforts for the design of advanced military systems. They also facilitate communications and coordination between and among researchers and designers having common military theme interests whether they work for a government service or agency, industry, or at a university or research institute.

No endeavor of the magnitude of this 1976 symposium could have been successfully conducted without the enthusiastic cooperation and support of many individuals and groups. With fear of overlooking some whose contributions played a key role, it is nevertheless fitting to acknowledge:

Headquarters, U.S. Army Materiel Development and Readiness Command and the Materials Advisory Group for their support and cooperation in this undertaking.

The many authors and participants and Session Chairmen who made this conference a success.

The reviewers from universities, industry and government organizations, for their diligence in carrying out a thankless task.

Dr. Edward S. Wright, Acting Director of AMMRC. who welcomed the participants at the meeting.

LTC Edward E. Chick Commander/Deputy Director of AMMRC who delivered the Introductory Remarks at the Opening Session.

Dr. Wartan A. Jemian, Professor and Chairman, Materials Engineering, Auburn University who delivered the Keynote Address on "Composites Through the Ages."

And finally the clerical staff of the Mechanics Research Laboratory and the Technical Reports Office of the AMMRC for their unflagging efforts in the preparation and printing of numerous symposium materials.

PREVIOUS DOCUMENTS IN THIS SYMPOSIA SERIES*

Proceedings of the Army Symposium on Solid Mechanics, 1968,
AMMRC MS 68-09, September 1968, AD 675 463

Proceedings of the Army Symposium on Solid Mechanics, 1970 -
Lightweight Structures,
AMMRC MS 70-5, December 1970, AD 883 455L

Proceedings of the Army Symposium on Solid Mechanics, 1972 -
The Role of Mechanics in Design - Ballistic Problems,
AMMRC MS 73-2, September 1973, AD 772 827

Proceedings of the Army Symposium on Solid Mechanics, 1974:
The Role of Mechanics in Design - Structural Joints,
AMMRC MS 74-8, September 1974, AD 786 543

Work-In-Progress Presented at the Army Symposium on Solid Mechanics, 1974:
The Role of Mechanics in Design - Structural Joints,
AMMRC MS 74-9, September 1974, AD 786 524

Stress Analysis of Structural Joints and Interfaces -
A Selective Annotated Bibliography
by M. M. Murphey and E. M. Lenoe,
AMMRC MS 74-10, September 1974, AD 786 520

---

* These documents may be ordered from the National Technical Information Service, U. S. Department of Commerce, Springfield, VA 22161

SYMPOSIUM COMMITTEE

R. SHEA, Chairman, AMMRC
E. M. LENOE, Vice Chairman, AMMRC
R. J. MORRISSEY, Secretary, AMMRC

TECHNICAL PAPERS AND PROGRAM

E. M. LENOE, Chairman, AMMRC
J. I. BLUHM, AMMRC
E. N. CLARK, Army Armaments Command, Picatinny Arsenal
H. D. CURCHACK, Harry Diamond Laboratories
C. M. ELDRIDGE, Army Missile Command
J. FEROLI, Army Test & Evaluation Command, Aberdeen Proving Ground
G. L. FILBEY, Jr., Ballistic Research Laboratories, Aberdeen Proving Ground
G. W. FISCHER, Army Armaments Command, Rock Island Arsenal
W. E. FISHER (Representative of U.S. Army Corps of Engineers), Army Construction Engineering Research Laboratory
R. FOYE (Representative of NASA), Army Air Mobility Research and Development Laboratory, Langley Research Center
A. J. GUSTAFSON, Army Air Mobility Research & Development Laboratory, Eustis Directorate
G. E. MADDUX (Representative of U.S. Air Force), Air Force Flight Dynamics Laboratory, Wright-Patterson Air Force Base
D. R. MULVILLE (Representative of U.S. Navy), Office of Naval Research
R. P. PAPIRNO, AMMRC
E. W. ROSS, Jr., Army Natick R&D Command
E. SAIBEL, Army Research Office
M. SCHWARTZ, Army Armaments Command, Frankford Arsenal
T. SIMKINS, Army Armaments Command, Watervliet Arsenal

WORK IN PROGRESS SESSION

G. E. MADDUX, CO-Chairman, Air Force Flight Dynamics Laboratory, Wright-Patterson Air Force Base
R. P. PAPIRNO, Co-Chairman, AMMRC

ARRANGEMENTS

R. P. PAPIRNO, AMMRC

CONTENTS

OPENING SESSION

WELCOME 1

Dr. Edward S. Wright
Acting Director, Army Materials and Mechanics Research Center

INTRODUCTORY REMARKS 3

LTC Edward E. Chick
Commander/Deputy Director, Army Materials
and Mechanics Research Center

KEYNOTE ADDRESS: COMPOSITES THROUGH THE AGES (Abstract) 5

Dr. Wartan A. Jemian
Professor and Chairman, Materials Engineering
Auburn University

SESSION I: WORK-IN-PROGRESS

This session was comprised of a series of brief presentations and discussions of current (but not necessarily complete) research relating to the theme of the symposium. Abstracts of these presentations are published in a companion document to these proceedings: Army Materials and Mechanics Research Center Monograph Series Report, AMMRC MS 76-3, dated September 1976.

SESSION II: STRUCTURAL RESPONSE

FAILURE OF COMPOSITE PLATES SUBJECTED TO DYNAMIC LOADS 9

R. L. Sierakowski and L. E. Malvern, University of Florida,
and W. S. Strickland and C. A. Ross, Air Force Armament Laboratory

FAILURE BEHAVIOR OF FILAMENT WOUND CYLINDRICAL TUBES 26

B. M. Halpin, R. M. Lamothe and E. M. Lenoe,
Army Materials and Mechanics Research Center

SESSION III: BUCKLING

BUCKLING/CRIPPLING CHARACTERISTICS OF BORSIC-TITANIUM. 45

R. W. Gehring, Rockwell International, Columbus Aircraft
Division, and G. S. Doble, Materials Technology, TRW, Inc.

POST-BUCKLING BEHAVIOR OF GRAPHITE/EPOXY LAMINATED PLATES AND CHANNELS . .62

E. E. Spier, General Dynamics, Convair Division, and
F. L. Klouman, Norwegian Defence Research Establishment

SESSION IV: MICROMECHANICS OF CARBON-CARBON COMPOSITES

CRACKING IN 3-D CARBON-CARBON COMPOSITES DURING PROCESSING AND EFFECTS ON PERFORMANCE. 81

J. Jortner, McDonnell Douglas Astronautics Company

MICROSTRUCTURAL CHARACTERIZATION OF CRACK PROPAGATION AND ANALYTICAL MODELING OF CARBON-CARBON COMPOSITES 98

J. S. Evangelides, The Aerospace Corporation

SESSION V: COMPOSITE APPLICATIONS AND DESIGN CONSIDERATIONS

EFFECTS OF MANUFACTURING AND IN-SERVICE DEFECTS ON COMPOSITE MATERIALS 123

R. M. Verette, Northrop Corporation, and
E. Demuts, Air Force Flight Dynamics Laboratory

DAMAGE TOLERANT STRUCTURAL CONCEPTS FOR FIBER COMPOSITES. 138

J. G. Avery and T. R. Porter, Boeing Aerospace Company

FAIL-SAFE COMPOSITE ROTOR HUB 153

R. S. Mayerjak, Kaman Aerospace Corporation, and
G. T. Singley, III, Eustis Directorate, Army Air
Mobility R&D Laboratory

EFFECT OF VARIABILITY OF DESIGN PARAMETERS ON STRESS CONCENTRATION ESTIMATES 171

E. M. Lenoe and D. M. Neal, Army Materials
and Mechanics Research Center

SESSION VIa: FAILURE MODES

FAILURE MECHANICS OF FIBER COMPOSITE NOTCH CHARPY SPECIMENS 193

C. C. Chamis, NASA-Lewis Research Center

FATIGUE DAMAGE IN NOTCHED COMPOSITE LAMINATES 212

R. B. Pipes, University of Delaware, and
S. V. Kulkarni and P. V. McLaughlin,
Materials Sciences Corporation

FRACTURE BEHAVIOR OF CROSS-PLY COMPOSITE MATERIALS. 223

J. M. Slepetz, Army Materials and Mechanics Research Center

SESSION VIb: FAILURE MODES

FINITE ELEMENT ANALYSIS OF MECHANICAL AND THERMAL EDGE EFFECTS IN COMPOSITE LAMINATES. 237

C. T. Herakovich, G. D. Renieri and
H. F. Brinson, Virginia Polytechnic
Institute and State University

RELAXATION OF RESIDUAL STRESSES IN ANGLE-PLY COMPOSITE LAMINATES. 249

I. M. Daniel and T. Liber, IIT Research Institute

ON THE THREE-DIMENSIONALITY OF FAILURE MODES IN ANGLE-PLY STRIPS UNDER TENSION 263

D. W. Oplinger, B. S. Parker and A. F. Grenis,
Army Materials and Mechanics Research Center

AUTHOR INDEX. 287

WELCOME

Dr. Edward S. Wright
Acting Director, US Army Materials and Mechanics Research Center

It is a pleasure to welcome you all here today to open the Army Symposium on Solid Mechanics, 1976.

The Army Materials and Mechanics Research Center has the responsibility for operating the Materials Advisory Group (MAG) and its subordinate Technical Working Groups (TWG's). The MAG functions directly under the US Army Materiel Development and Readiness Command (DARCOM), and is concerned with matters of policy, management and administration of the Army's technology base programs in Materials and Mechanics. Operating under the MAG are Technical Working Groups in several materials and discipline-oriented areas. These groups are comprised of bench level technical people who are selected on the basis of their expertise in specific areas of materials and mechanics technologies. Perhaps the most important function carried out by these TWG's is the exchange of technical information.

One of these, the Mechanics of Materials TWG, was established in 1964, to assist in formulating the Army wide program in solid mechanics and in promoting scientific and technical interchange among DARCOM laboratories. It is led by AMMRC, and is made up of engineers and scientists from most of the DARCOM laboratories. This particular TWG has been the most active of the groups in furthering the exchange of information; the Army Symposium on Solid Mechanics being the principle vehicle.

This is the fifth in a series of biennial symposia. The first was held in 1968 at The Johns Hopkins University, Baltimore, Maryland under the general theme of solid mechanics. Subsequent meetings were held in 1970 (Lightweight Structures at AMMRC), 1972 (Ballistic Problems at Ocean City, Maryland) and in 1974 (Structural Joints at South Yarmouth, Massachusetts). This 1976 symposium, also being held at South Yarmouth, is, of course, being conducted under the theme, Composite Materials: The Influence of Mechanics of Failure on Design.

Participation in these symposia has broadened with time. Starting with the 1972 meeting, papers have been solicited from in-house and contract researchers and designers for the Navy, Air Force and other Government agencies, in addition to those for the Army. Beginning with the 1974 meeting, the Symposium Committee was expanded to include representation from the Navy, Air Force, NASA and The US Army Corp of Engineers. This expansion is based on the recognition that research and design problems in solid mechanics are not unique to a single service or Government agency, and that this broader communications band would provide much additional and extremely useful interchange.

A new feature was added in 1974. A work with-progress session was held. Based on the interest it received, it is being continued.

The specific objective of these symposia is to enhance the effectiveness of the coupling between research and design requirements. The anticipated results of this enhancement are two-fold. First, to insure that research resources are being directed towards pressing design needs. Second, to insure that design procedures reflect the best solid mechanics technology that research has provided.

It is most appropriate that this meeting is addressing the mechanics of failure on composite materials. It is clear that the use of these materials is increasing rapidly. It is also clear that design approaches based on those used for metallic structures are not adequate; a new branch of the solid mechanics technology is being developed - but there is a long way to go. This meeting testifies to the fact that we are moving in the direction to fill this gap in the technology.

Again, welcome to the symposium, and best wishes for a successful meeting.

INTRODUCTORY REMARKS

LTC Edward E. Chick
Commander/Deputy Director
US Army Materials and Mechanics Research Center

I would like to first add my welcome, and express my pleasure for being asked by the Symposium Committee to make a few introductory remarks.

As you are well aware, this, the Army Symposium on Solid Mechanics, 1976 is to address composite materials technology. As you are also aware, the Army has a vested interest in the exploitation of composite materials for application to advanced military systems. The extent and duration of the Army's interest may, however, not be evident to the majority of symposium participants. Therefore, a short digression on historical matters seems appropriate. In any case, in this bicentennial year there is a natural tendency to reflect on the past.

AMMRC professionals are rightfully proud of present progress but are also mindful of "ancestors" traceable to the Presidency of Andrew Jackson(1). For more than 135 years, AMMRC and its predecessor agencies at Watertown have made important contributions to the U.S. Army.

Materials research results in steel offer an excellent example of the invaluable results of AMMRC advances for our Army. AMMRC and steel literally grew up together. In the 1840's, AMMRC's predecessor agency at Watertown was helping the U.S. Army develop the superior cast iron that made its cannon the best in the world. Not so well known, however, are the contributions of Watertown Arsenal in wire wound composite guns. These were 10-inch, wire-wrapped, cast iron, breech loading guns weighing 29 tons. The 17 ton cast iron body was wrapped with 0.15 inch square wire with slightly rounded corners, applied (for the most part) with uniform tension at 41,000 psi. Longitudinal strength was provided by axial bars or staves. The work was suspended in June, 1886(2) after several relatively successful tests. In truth, these wire guns never passed the experimental stage. Nonetheless, they demonstrated a remarkable willingness to explore new concepts.

The continued study of mechanics of materials is demonstrated by the famed Emery Testing Machine (ETM) installed at Watertown after the Civil War.

Original motivation was to settle the raging controversy over the suitability of steel for making cannon. It proved of great significance in the study of metals, and was the prototype of a long line of hydraulic testing machines, many of which are still in operation.

The ETM had a capacity for precision testing of 800,000 pounds in tension and one million pounds in compression. Results of its tests were published annually for 36 years, from 1882 to 1918, and an incredible range of materials types were studied(3). Nowadays, emphasis has shifted to lighter weight, high strength materials with suitable environmental resistance. For many years, the Army has sought to introduce appropriate composite materials into aircraft, missiles, and armament. Recent AMMRC contributions include investigation of graphite reinforced aluminum graphite and Kevlar epoxies and the carbon-carbon materials. Fundamental contributions have been made at AMMRC towards the utilization of filament wound composites in lightweight antitank weapons, and the development of carbon-carbon ballistic missile nose tips.

All of this sounds as if we can simply make the commitment to use composites, and we automatically end up with a more mobile and effective Army, and can accomplish this while saving money. Well, there is promise, but there are many technological problems to be overcome. One of the most important is our inability to predict failure of composite materials in a reliable and consistent way. The reason for this symposium is to focus attention on that problem in the hope that we may solve it sooner and better.

Until we can develop valid and quantitative failure criteria, composites can not be exploited to their maximum advantage; we can not obtain our most attractive return on investment, and that is what the Army's technology base program is all about.

At AMMRC, we are carrying out a major technology base effort in composite materials which covers the spectrum from new materials development and characterization through process research, development and scale-up to reliability assessment, structural analysis and demonstration.

I do not want to take any more time from what promises to be a significant contribution to our quest for better and more economical ways to equip our Army.

REFERENCES

1. "Progress in AMMRC Materials Research for Army Needs," Army Research & Development News Magazine, May - June 1976

2. Gun Making in the United States, Col Rogers Birnie, Jr. Reprinted from Journal of the Military Service Institution, War Department Document No. 298, Copy Number 78, dated 1907

3. Index to the Reports of the Tests of Metals and other Materials made with the United States Testing Machine at Watertown Arsenal, Massachusetts from 1881 to 1912 Inclusive, Chief of Ordnance, Government Printing Office 1913.

KEYNOTE ADDRESS: COMPOSITES THROUGH THE AGES

Wartan A. Jemian
Professor and Chairman
Materials Engineering
Auburn University
Auburn, Alabama 36830

ABSTRACT

The application and existence of composites is based on the concept of synergism. Natural composites, such as wood and bone, are persistent reminders that materials are best used in combination.

Man-made composites of early history are macroscopic. Early man combined stone and wood to form useful tools and weapons. The ages of these artifacts are measured in megayears. The ancient Egyptians incorporated straw in mud to manufacture bricks. In this application, the straw promotes uniform drying and hence reduces the production of cracks. These aspects of composites technology are forerunners but do not, in any way, indicate the full benefits to be obtained.

The middle history involves attempts to duplicate texture through processing which results in neocomposites. Specific man-made composites in this category can be identified. Examples are the Merovingian Pattern-Welded Blade, of the 3rd century AD, the welded Damascus gun barrels of the 18th century, and more recently, plywood. Although these composite materials relate closely to modern composites, the similarities are more fortuitous than planned.

The modern history dates from the second World War. The objective is new, namely, to create new materials by special combinations of well known materials with the addition of new materials in special forms. The emphasis in modern composites is on structure at every level. Examples range from fiberglass, used in living structures and boats, to advanced composites, used in critical sections of high performance aircraft.

Composites have traditionally been speciality items, although plywood and other building materials are high volume commercial products. Concrete, the highest volume man-made material, is classed as a composite. The need for advanced composites is established but the technology is expensive and public interest has not been awakened. Recent statistics show that composites account for approximately ten percent of research funding and one-thousandth percent of the GNP. Another recent report predicts that the activity in composites will level off and possibly decline during this decade. The latter was based, apparently, on projections for military funding and does not include the spinoff applications in recreational equipment. There is every reason to believe that any decline in the market activity will only be short lived.

There is the problem of definition, primarily to outline the domain of technology necessary for effective progress. Structural composites technology is already drawing upon the talents of metallurgists, ceramicists, and plastics technologists. There are many subtle distinctions to be observed. Composites

technology is structure-intensive. The identity and significance of the "structural components" in materials phases as well as in the interfacial region in materials systems is recognized. The literature and conference presentations are devoted in ever increasing proportion to these features. The descriptive elements include such terms as crystalline, crowdion, molecular conformation, dislocation, and coherency. These are forced on us by circumstances and need.

This conference will further knowledge about structural elements in composites and their effects on performance. Failure is any undesirable change in shape or structure. Understanding the influence of these changes on design requires detailed knowledge of the system. There are advanced tools for use in analysis, testing and synthesis of mechanical characteristics. Looking for such changes at every structural level, and designing to control them, is the most promising approach to devloping future composites.

SESSION II: STRUCTURAL RESPONSE

Chairman: S. W. TSAI
Chief, Mechanics and Surface Interaction Branch
Non-Metallic Materials Division
Air Force Materials Laboratory

FAILURE OF COMPOSITE PLATES SUBJECTED TO DYNAMIC LOADS
R. L. Sierakowski and L. E. Malvern, University of Florida, and W. S. Strickland and C. A. Ross, Air Force Armament Laboratory 9

FAILURE BEHAVIOR OF FILAMENT WOUND CYLINDRICAL TUBES
B. M. Halpin, R. M. Lamothe and E. M. Lenoe, Army Materials and Mechanics Research Center 26

FAILURE OF COMPOSITE PLATES SUBJECTED TO DYNAMIC LOADS

R. L. SIERAKOWSKI
Professor

W. S. STRICKLAND
Project Engineer

L. E. MALVERN
Professor
Engineering Sciences Department
University of Florida
Gainesville, Florida

C. A. ROSS
Project Engineer
USAF Armament Laboratory
AFATL/DLYV
Eglin AFB, Florida

ABSTRACT

This paper presents the results of an experimental study to determine fracture/failure mechanisms of flat fiberglass epoxy plates when subjected to blast pressure and projectile impact. Fiberglass epoxy plates with fifteen plies of 0-90° orientation were fabricated using various ply and lamina arrangements. Plate failure begins by an interlamina delamination mechanism with delaminations moving away from the impact point for centrally impacted plates and delaminations moving away from plate boundaries for blast loading. A delamination mechanism appears to be the dominant failure mechanism for plates impacted below the critical penetration velocity and for fixed edge plates subject to blast loads below the edge failure load. Similar delamination patterns were observed in fiberglass cloth and polyester matrix plates.

INTRODUCTION

Failure modes of monolithic metal plates subjected to dynamic loads are influenced by many factors related to manner of loading and mechanical properties of the plate material. Failure modes in dynamically loaded composite plates are also dependent on material properties of the constituents and, in addition, are greatly influenced by geometrical fiber arrangement and spacing. Observed failure modes of composite materials are: fiber debonding, stretching, breaking and pullout, delamination, matrix deformation and fracture. Delamination induced by shear due to bending and sequential delamination initiated by a generator strip appears to be important energy absorption mechanisms for 0-90° layup fiberglass roving epoxy plates subjected to projectile impacts and blast loadings, respectively. This type of mechanism is especially apparent in the composite plates studied here at impact velocities below the perforation velocity and for blast loadings below that necessary for transverse shear failure.

Good penetration resistance for heavily delaminated glass epoxy plates has been reported by Wrzesian [1]. Askins and Schwartz [2] also observed extensive delamination in composite backup panels for armor applications. Ross and Sierakowski [3] examined the influence of various fiber layering sequences on the penetration resistance of fiberglass roving epoxy plates when subjected to central impact. Cristescu, Malvern, and Sierakowski [4] subsequently described the sequential delamination mechanism initiated by a generator strip for the same plates reported on in Reference [3]. Several papers [5, 6, 7] recently published by the authors describe this mechanism in some detail. Literature reviews have revealed no studies of blast loading of composite plates; however, flyer plate experiments conducted by deRosset [8], for example, show delamination to be a major failure mechanism of boron epoxy plates.

Fiberglass plates of the same type as those centrally impacted in earlier studies [5, 6, 7] were subjected to blast loading using a fuel air explosive (FAE) device. In addition, plates of woven roving (cloth) and polyester matrix were fabricated and tested using the same FAE device. An outline of the details of plate fabrication and a general description of the delamination process, along with results, discussion, and conclusions are given in the following sections.

SPECIMEN FABRICATION

Two types of fiberglass plates were fabricated for use in this study. For the first case, twelve ended E-glass fiber rovings and epoxy were used to fabricate crossplied layered plates containing fifteen layers and having varying numbers of laminae. These plates were fabricated by winding the roving on an aluminum mandrel mounted in a lathe. The lathe speed and cross-feed were adjusted to produce a uniform array along the edge of the plate and shims were used to give spacing in the thickness direction. The winding method used is shown schematically in Figure 1 and described in detail in References 5 and 6. Specifically, Owens/Corning precision controlled E-glass roving [No. 801AB-1167], Shell Epoxy 828 resin, and Magnolia Plastics Curing Agent 400 were used in this fabrication process. Fifteen different ply arrangements were fabricated using the layering sequences shown in Table 1.

Table I. Layering Arrangements in the Plates Test

Code	Layering Sequence	Number of Interlaminar Planes
b	1-1-1-1-1-1-1-1-1-1-1-1-1-1-1	14
c	1-2-3-4-5	4
d	2-1-2-1-2-1-2-1-2-1	9
e	2-2-2-2-2-2-2-1	7
g	3-1-3-1-3-1-3	6
h	3-2-3-2-3-2	5
i	3-3-3-3-3	4
j	3-4-3-4-1	4
k	3-5-3-4	3
l	4-1-4-1-4-1	5
m	4-4-4-3	3
n	5-1-5-1-3	4
r	5-4-3-2-1	4
o	5-5-5	2
p	8-7	1

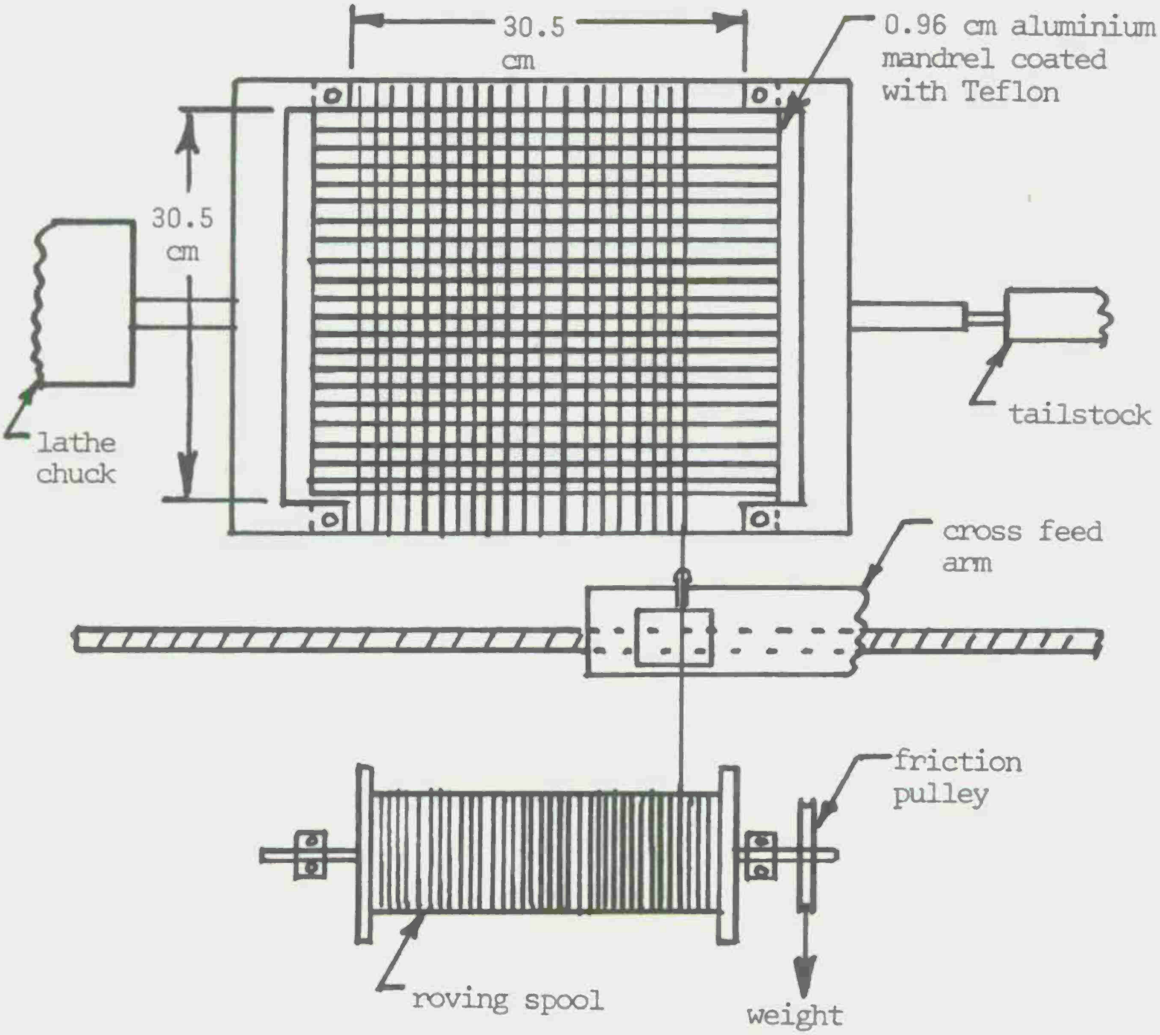
30.5 cm
0.96 cm aluminium mandrel coated with Teflon
30.5 cm
lathe chuck
tailstock
cross feed arm
friction pulley
roving spool
weight

Figure 1. Windinq appararus for crossplied plates.

The ply arrangement or layering sequence shown in Table 1 indicates the number of layers in each lamina, starting with the first lamina and progressing rearward. Each lamina is oriented 90° to each of its neighboring laminae. For example, a 1-2-3-4-5 plate has one layer in the first lamina, two layers in the second lamina whose fiber direction is 90° to the first lamina, three layers in the third layer whose fiber direction is 90° to the second lamina but parallel to fibers in the first lamina, etc. A schematic of a composite plate giving examples of plate components is given in Figure 2. Nominal thickness of all 0-90° plied plates was 0.64 cm.

The second plate types tested were fiberglass cloth plates fabricated using 4 oz.-Uniglass cloth, 24 oz.-Uniglass woven roving cloth and a polyester matrix. Seven layer plates, 0.32 cm thick, were fabricated by alternate layup of four layers of 4 oz.-cloth and three layers of woven roving. Thirteen layer plates 0.64 cm thick were also fabricated by alternate layup of seven layers of 4 oz.-cloth and six layers of woven roving. Both the cloth plates and wound roving crossplied plates contained approximately fifty percent fiberglass.

EXPERIMENTAL TESTS

The crossplied fiberglass epoxy plate fabrication technique produced plates approximately 30 cm square. For the blast loading these plates were used full size. For the central impact tests the plates were quartered to give plates approximately 15 cm square. The central impact experiments were conducted in the Engineering Sciences Composite Materials Laboratory at the University of Florida. The plates were held fixed on all edges and impacted centrally using blunt nose cylindrical projectiles of 0.96 cm diameter by 2.54 cm in length. The effective size of the plate in the holder was approximately 12.7 cm square. The projectile was propelled by an air gun at various velocities by varying the air pressure of the inner barrel chamber. The velocities were measured at the end of the barrel just prior to impact by an optical system using two light beams directed through the barrel onto photo electric cells. The time difference for the projectile to break consecutively both beams of light was displayed on a storage oscilloscope. A schematic of the gas gun assembly, plate holder, and velocity measuring device is shown in Figure 3. The overall system is further described, in some detail, in Reference 3.

The FAE gas bag technique used previously in blast loading of metal plates [9] was used at the Test Evaluation and Experimental Facility at Eglin AFB for blast loading of selected crossplied fiberglass plates 30 cm square. A plastic bag 1.22 x 1.22 x 6.11 m supported by a metal rod frame containing 0.89 kg of methyl acetylene propadiene (MAPP) gas was detonated by 100 grams of Data sheet explosive, and the resulting shock was directed onto the composite plate held fixed on all edges. The effective size of the plate in the holder was approximately 25.4 cm square. A schematic of the gas bag and plate holder is shown in Figure 4.

Pressure time histories of both side-on and reflected pressures were obtained in previous tests [9]. In all cases the given pressures are based

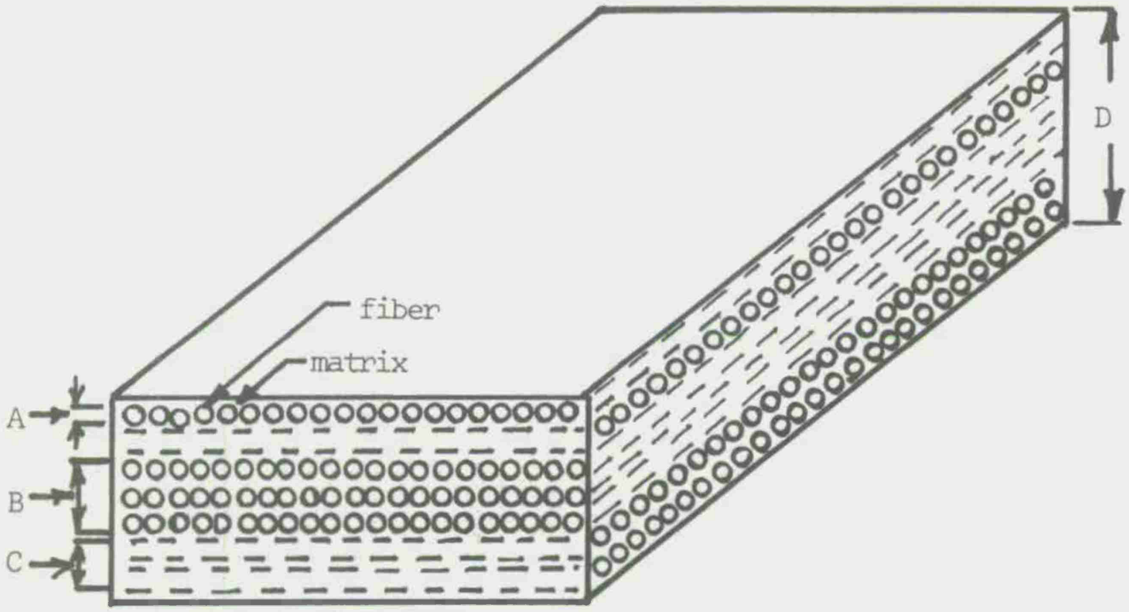
fiber
matrix
A
B
C
D

Figure 2. Composite plate nomenclature. A. One layer and also a one layer lamina. B. Three layer lamina. C. Two layer lamina. D. Plate thickness.

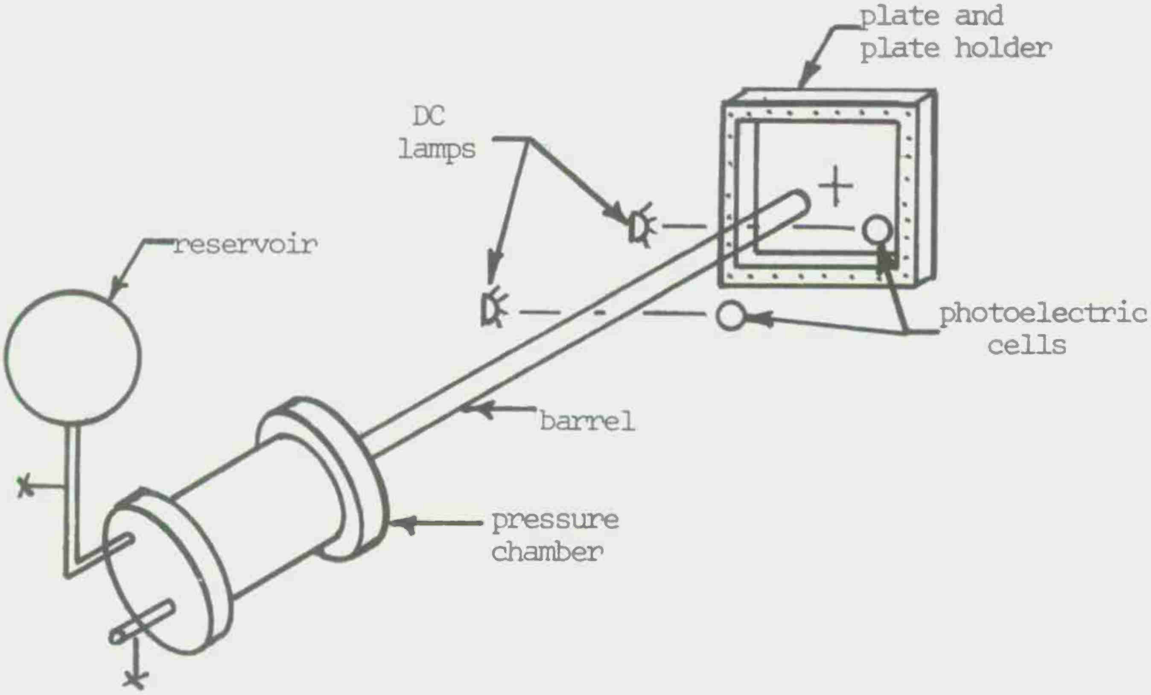
plate and plate holder
DC lamps
reservoir
photoelectric cells
barrel
pressure chamber

Figure 3. Gas gun assembly.

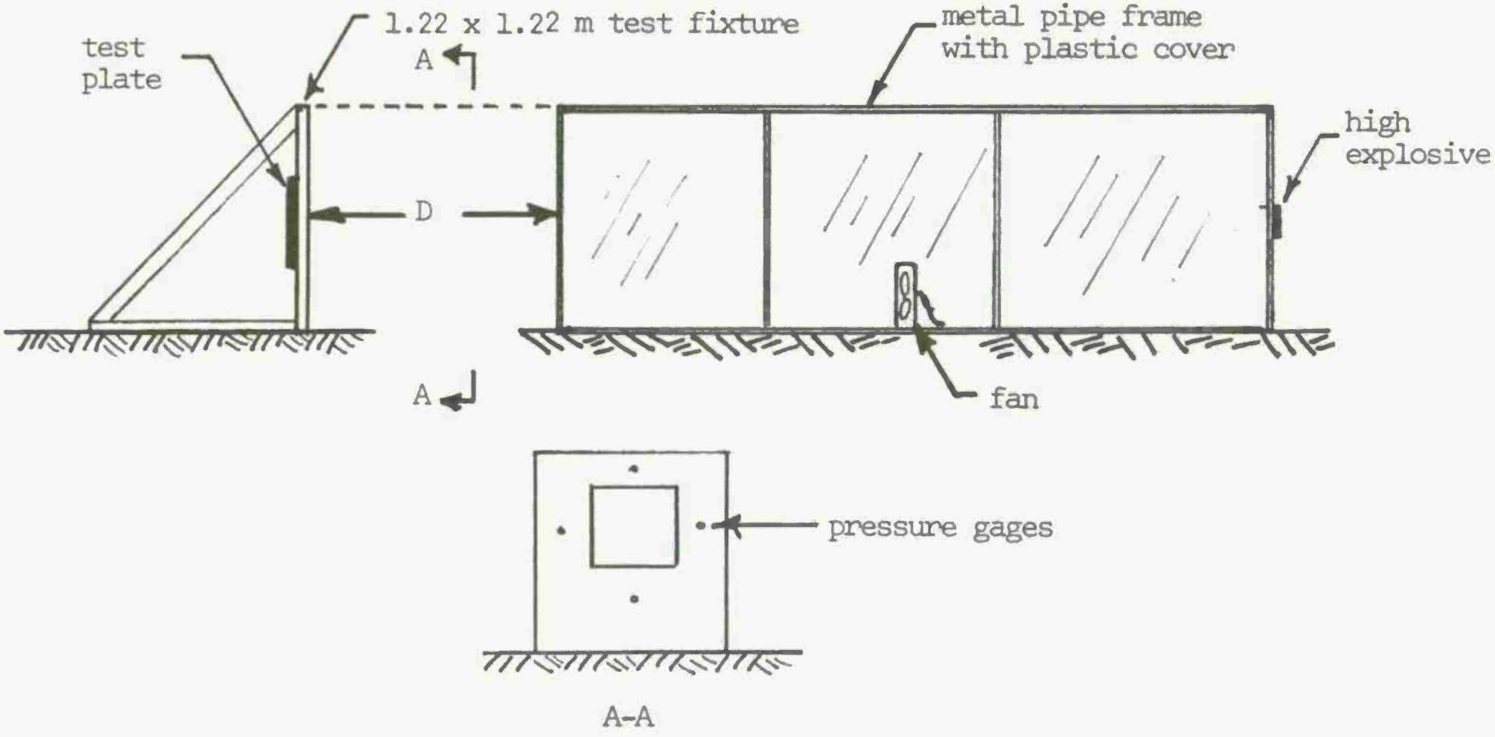
test plate
1.22 x 1.22 m test fixture
A
metal pipe frame with plastic cover
high explosive
D
A
fan
pressure gages
A-A

Figure 4. FAE gas bag for blast loading.

on reflected values obtained from a nondeforming thick plate placed at varying distances of D from the end of the FAE bag, as shown in Figure 4.

In order to check size effect, both 25 cm square and 46 cm square fiberglass cloth polyester plates were tested for FAE blast loading.

DISCUSSION OF EXPERIMENTAL RESULTS

Central impacts of crosspiled fiberglass plates at projectile velocities below the penetration velocity produced delaminated areas which grow progressively larger through the thickness of the plate. The delamination mechanism presented in a previous paper [4] for central impact starts as a strip one projectile diameter wide on the front lamina. This strip then loads transversely the second lamina generating a delamination between the first and second laminae. The second lamina then in turn loads the third lamina causing a delamination between the second and third lamina, etc. A schematic of this process is shown in Figure 5 in which the first generator strip, one projectile diameter wide and length L_1 generates a delamination of area A_1 between the first and second laminae. A second generator strip of length L_2 generates a delamination of area A_2 between the second and third laminae. Subsequent generator strips generate subsequent delamination areas. As an example, a plate containing five laminae would contain four generator strips corresponding to four delaminated areas associated with the four interlaminar planes of the plate. A photograph of a back lighted 3-3-3-3-3 plate, Figure 6a, shows four delaminated areas corresponding to the four interlaminar planes. For plates with more than four interlaminar planes it is difficult to distinguish one delaminated area from the other, especially in the case of the fifteen-lamina plate shown in the back lighted photograph of Figure 6b. This type of plate shows a highly localized delaminated area but distributed over many interlaminar planes, whereas plates with a smaller number of interlaminar planes such as the 3-3-3-3-3 plate show larger delaminated areas.

Using a back lighted 3-3-3-3-3 plate, the delamination areas were measured and plotted versus initial kinetic energy of the impactor in Figure 7. The straight line plot was fitted to the data and is expressed as

$$K = 3.5 + 0.315A \qquad K > 3.5 \qquad (1)$$

Where K is kinetic energy in joules and A is area in cm . For a kinetic energy above 3.5 joules and below the kinetic energy where delamination extends to the plate boundary, the delamination fracture surface energy γ appears to be constant at about 0.158 joules/cm^2 (15.8x10^5 ergs/cm^2). This value of γ is half the coefficient of A in Equation (1) because two surfaces are formed by the delamination. This value is an order of magnitude higher than that for pure epoxy (0.5 x 10^5 - 1.5 x10^5 ergs/cm^2) obtained in static tests by Bascom [10] and Sultan [11]; however, it is of the same order of magnitude for polymethyl-methacrylate (2x10^5 ergs/cm^2) and polystyrene (17 x 10^5 ergs/cm^2) obtained in static tests by Berry [12]. Comparable static figures for fiberglass-epoxy composite are not known.

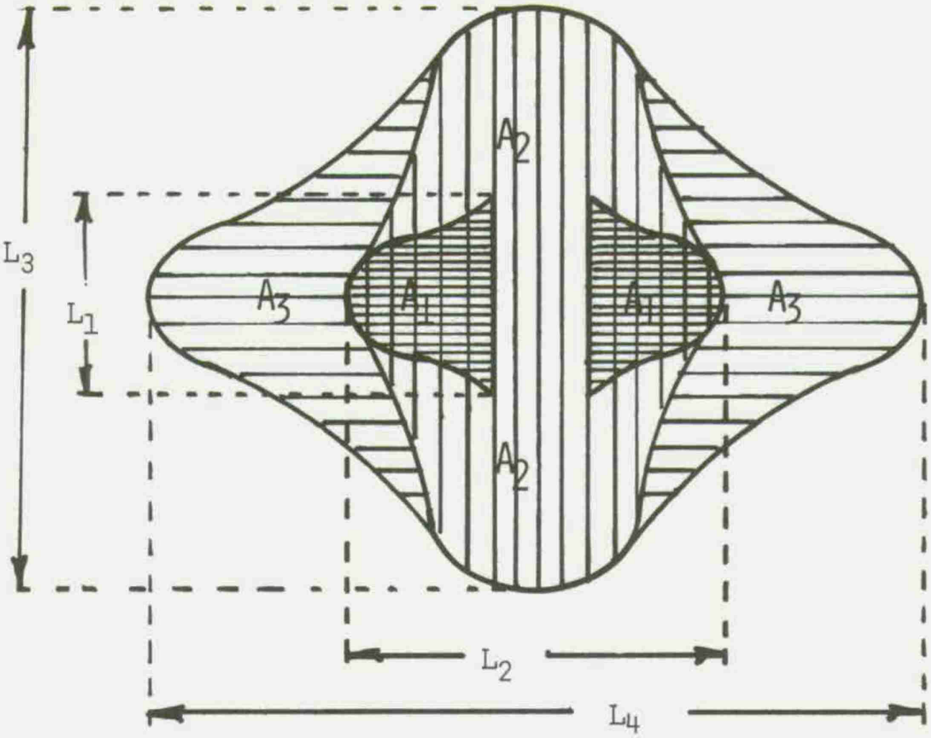
L3
L1
A2
A2
A3
A1
A1
A3
L2
L4

Figure 5. Schematic of delamination mechanism for centrally impacted plates.

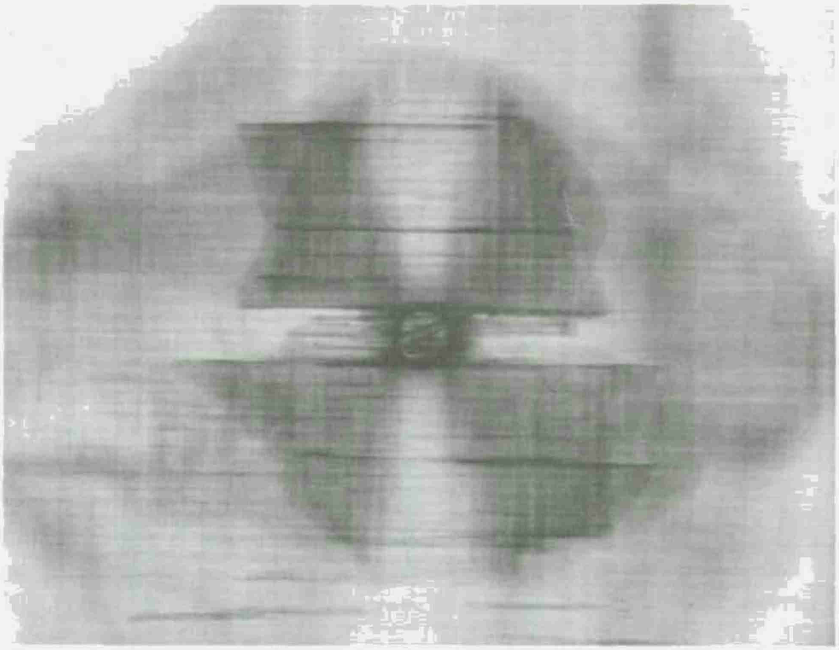

Figure 6a. 3-3-3-3-3 plate impacted at 140 m/sec.

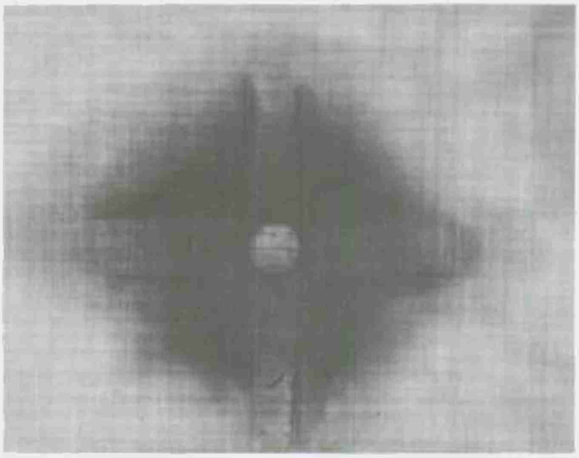

Figure 6b. 1-1-1-1-1-1-1-1-1-1-1-1-1-1-1-1 plate impacted at 107 m/sec.

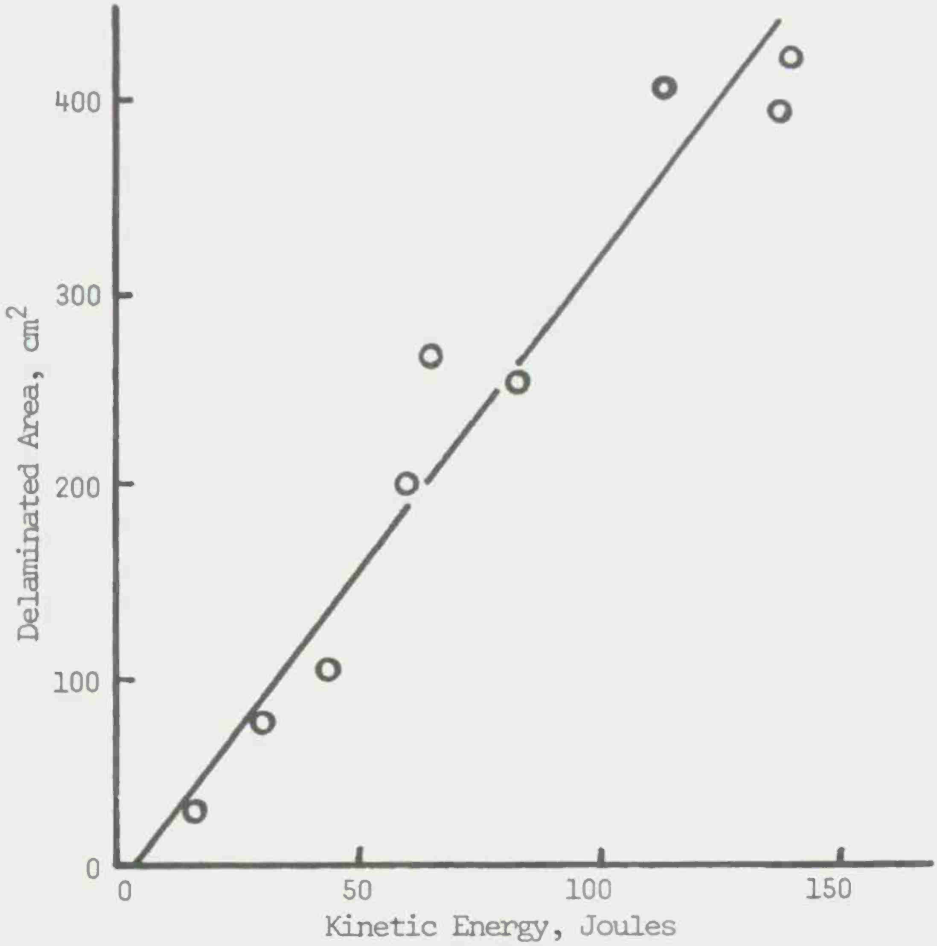

Figure 7. Delaminated area of 3-3-3-3-3 plates versus kinetic energy of impacting projectile.

Blast loading of 25.4 cm square crossplied plates at loadings below that necessary to cause edge failure results in delaminations that are generated at the edges of the plates. Visual examination of these plates using back lighting leads to the following general description of this type of delamination mechanism:

Delamination begins at the edges and progresses toward the center of the plate with the distance progressed appearing to be proportional to the amount of plate deflection and/or blast pressure. A traveling hinge movement is assumed to account for the deflection. Delamination on the first interlaminar plane occurs on the edges normal to the fiber direction of the first lamina. The next delamination then appears on the next interlaminar plane and extends out from the other two edges. This process then alternates through the thickness and through all the interlaminar planes with a rearward decreasing delaminated area. The time sequence of the delaminations is not necessarily in this order but the front to back positions of the delaminations are easily discernible. This delamination pattern is shown schematically in Figure 8 for a five lamina plate, and a back lighted photograph of the same type plate is shown in Figure 9. This type of delamination mechanism for blast loaded plates is readily discernible for plates with a low number of interlaminar planes, and, as with the centrally impacted plates, the higher the number of interlaminar planes the more difficult it is to differentiate between delaminated areas. The higher the peak blast pressure the further the delamination areas extend from the sides. This is quite evident in Figure 10 which shows a 3-3-3-3-3 type for three different blast pressures. A similar type increase in delamination area, shown in Figure 11, is observed for the same type of plate centrally impacted at three different projectile impact velocities.

The relation between the delaminated area and the peak blast pressure was found to be linear within measurable accuracy as is shown in Figure 12 for two types of crossplied plates.

High speed photography using a shadow Moire technique, described in Reference [9], showed that a blast loaded 3-3-3-3-3 plate deflected as much as 3.81 cm at the plate center but rebounded to a permanent deflection of .64 cm. Assuming the plate rebounds elastically, the major portion of the work done by the blast load during the plate deformation is recovered during the rebound. The unrecovered portion of the work may then be assumed to be transferred to the plate. A rough approximation of the unrecovered work can be obtained from an integration of the permanent deflection times the blast pressure over the plate area. The time required for plate deflection and rebound is of the same order of magnitude as the blast duration time; therefore, only half the peak blast pressure was used in this calculation. A plate of this unrecovered work versus delamination area is shown in Figure 13. The curve appears almost linear over the range shown and a straight line was arbitrarily drawn through these points. The slope of this line is 0.862 joules/cm^2 which would give a delamination fracture surface energy of 0.431 joules/cm^2 because two surfaces are formed during the delamination. This value of delamination fracture surface energy is of the same order of

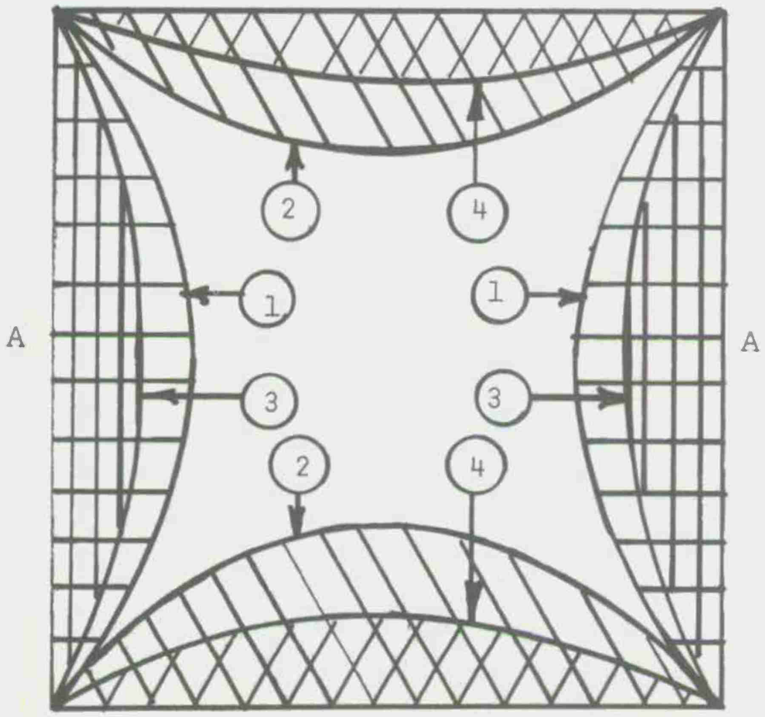

Figure 8. Schematic of delamination mechanism for blast loaded plates. Representive of a five lamina plate. Circled numbers refer to delamination sequence increasing from front to back. Edges marked A are perpendicular to fibers in first lamina.

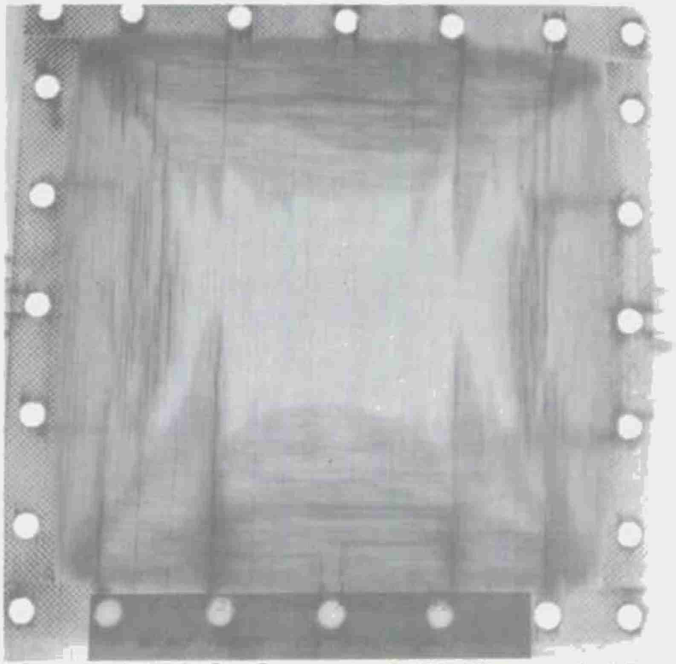

Figure 9. 5-4-3-2-1 plate at 2.59 MPa peak blast pressure and 0.78 MPa-sec impulse.

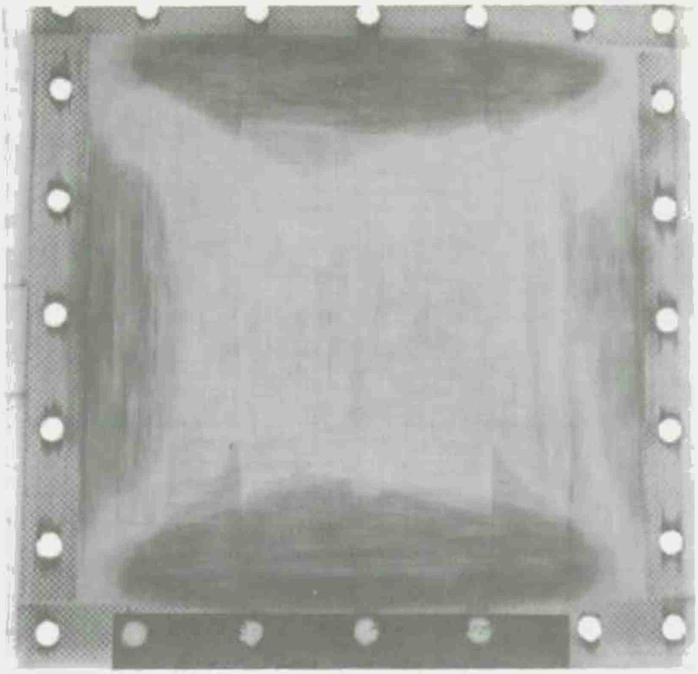

1.52 MPa (220 psi)
0.31 MPa-millisec (97 psi-millisec)

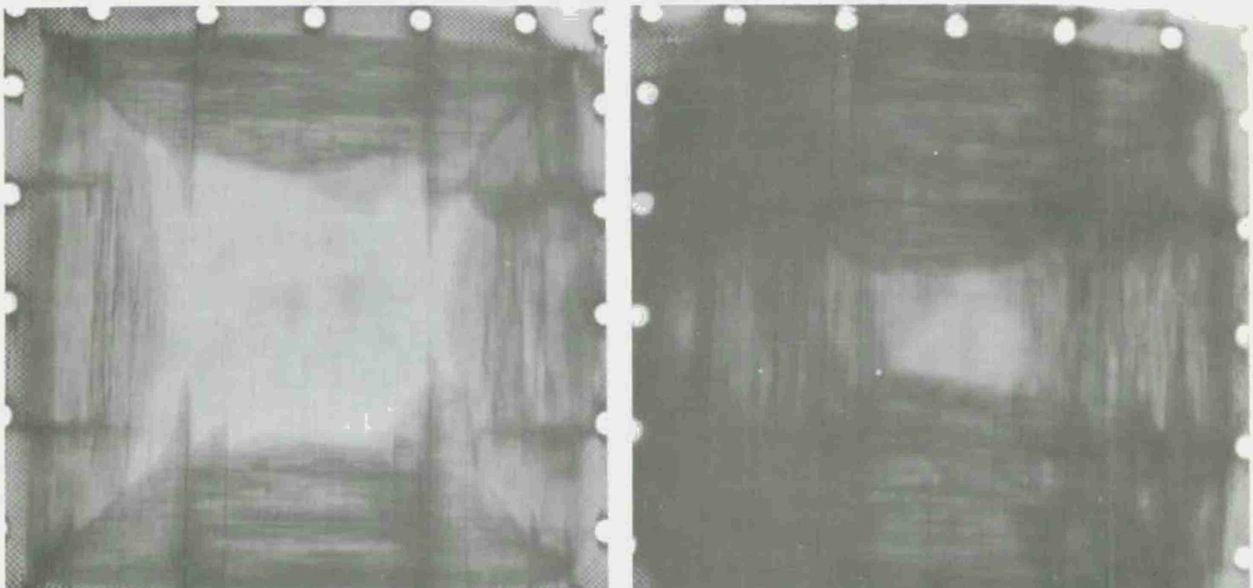

2.59 MPa (375 psi)
0.78 MPa-millisec (120 psi-millisec)

4.14 MPa (600 psi)
1.32 MPa-millisec (130 psi-millisec)

Figure 10. 3-3-3-3-3 plate for various peak blast pressures and impulse values.

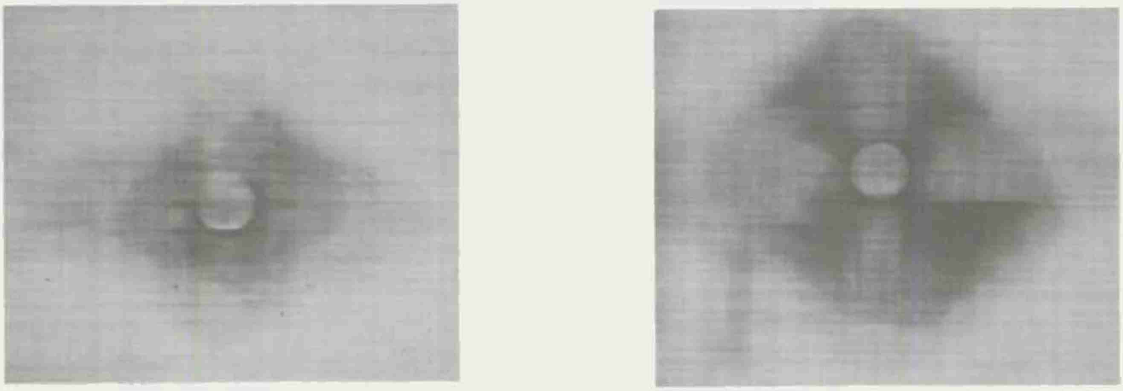

50 m/sec

66 m/sec

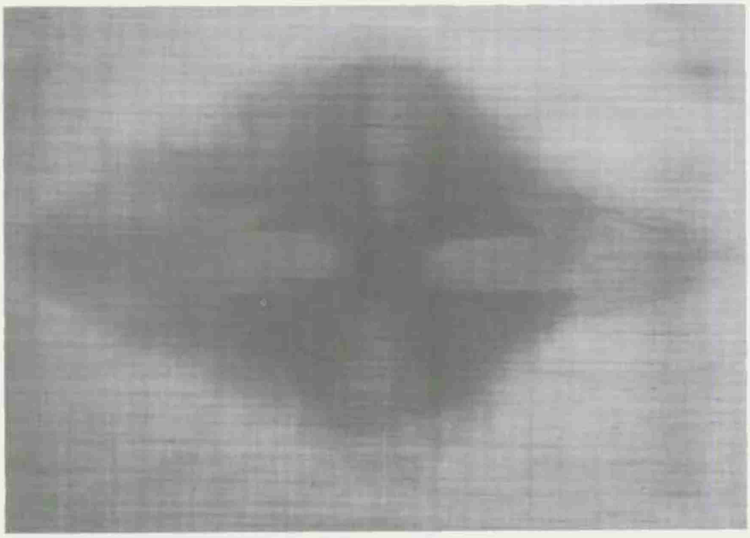

78 m/sec

Figure 11. 3-3-3-3-3 plate for various impact velocities.

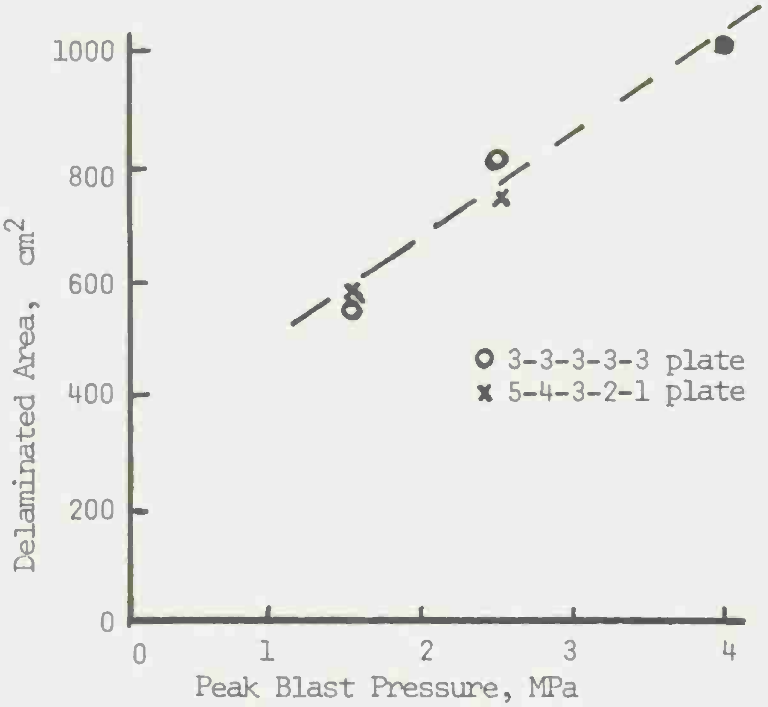

Figure 12. Delaminated area versus peak blast pressure.

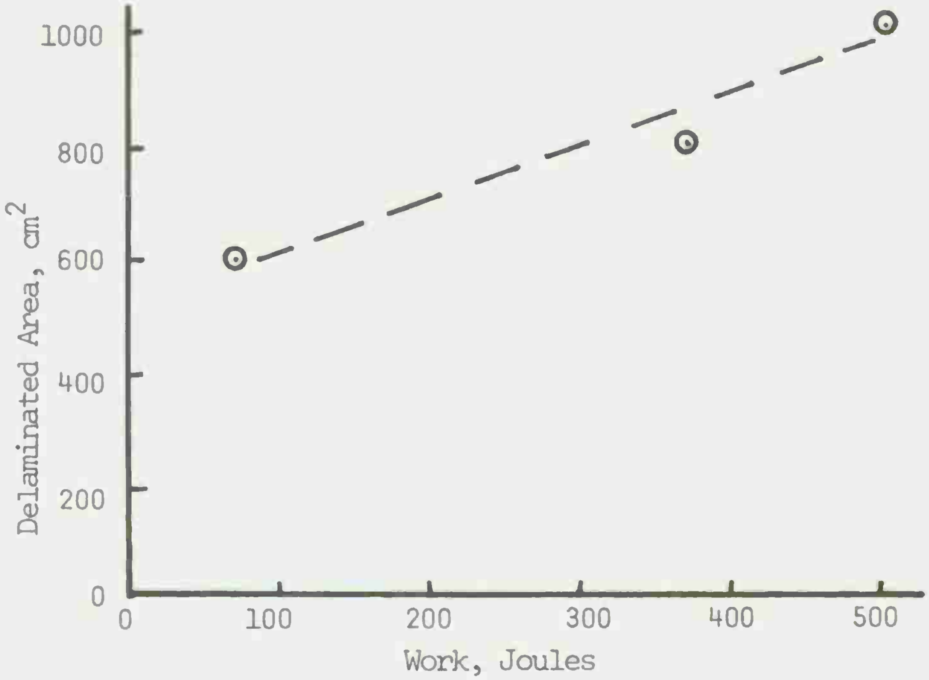

Figure 13. Delaminated area of 3-3-3-3-3 plate versus unrecovered work.

magnitude as that obtained for the impacted plates.

Tests were also performed on fiberglass cloth plates of various sizes and thicknesses. For centrally impacted plates, the delamination patterns appeared very similar to the localized delaminations of the fifteen-lamina crossplied plates [Figure 6b].

Blast loading of the 25 cm square fiberglass cloth plates also produced a delamination mechanism which extended from the plate edges toward the plate centers. Typical patterns at two different blast pressures are shown in Figure 14 for .64 cm thick plates. Several delamination areas are present but because of the high number of interlaminar planes for this thickness, the individual delaminations are difficult to distinguish from one another. Because of ease of fabrication of fiberglass cloth, plates of two widths (25 cm and 46 cm) and two thicknesses (.64 cm and .32 cm) were tested. The .32 cm thickness plates for both widths showed very little delamination but a rather uniform craze type pattern which might be expected for a highly stressed membrane type composite plate. The thicker .64 cm plates of 46 cm width show a delamination pattern very similar to that of the smaller width plate shown in Figure 14.

CONCLUSIONS

Sequential interlaminar delamination appears to be the dominant failure mechanism for centrally impacted plates at impact velocities below the penetration velocity and for blast loaded plates at blast pressures below that required for edge failure. However, for blast loading on thin cloth plates (.64 cm), interlaminar delamination is not as extensive as for the thicker plates, even for blast pressure large enough to cause edge failure.

For those plates where interlaminar delamination is prominent, the total delaminated area is a linear function of either peak blast pressure or the kinetic energy of the penetrator. Advantages of these types of composites are that the energy due to loading may be spread over larger areas with a possible increase in penetration resistance; however, this mechanism may not be desirable for multiple impact loadings. In the case of blast loading, the interlaminar delamination allows the central portion of the plate to remain reasonably flat with little permanent deformation after blast. In cases such as radar antennas where retention of surface contour is very important, this type material may be highly desirable.

ACKNOWLEDGEMENTS

This paper represents the combined results of a U. S. Army grant with the University of Florida, Gainesville FL and of an in-house test program at the U. S. Air Force Armament Laboratory, Eglin AFB FL.

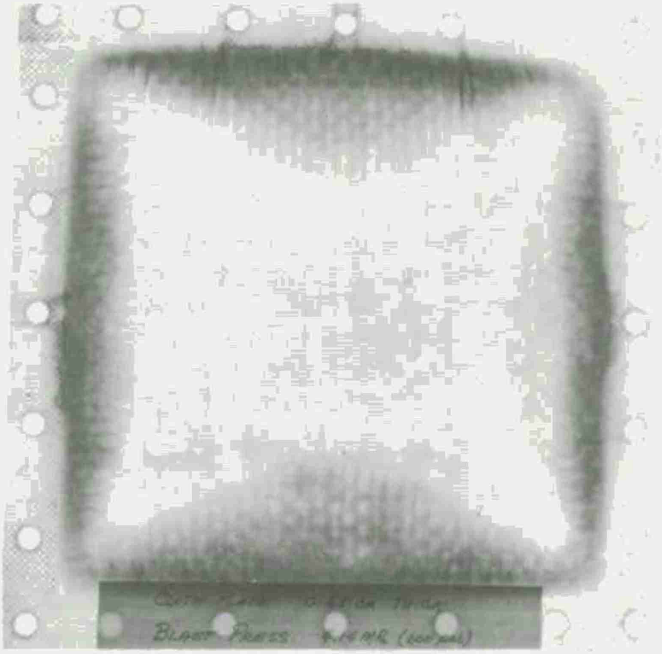

4.14 MPa (600 psi)

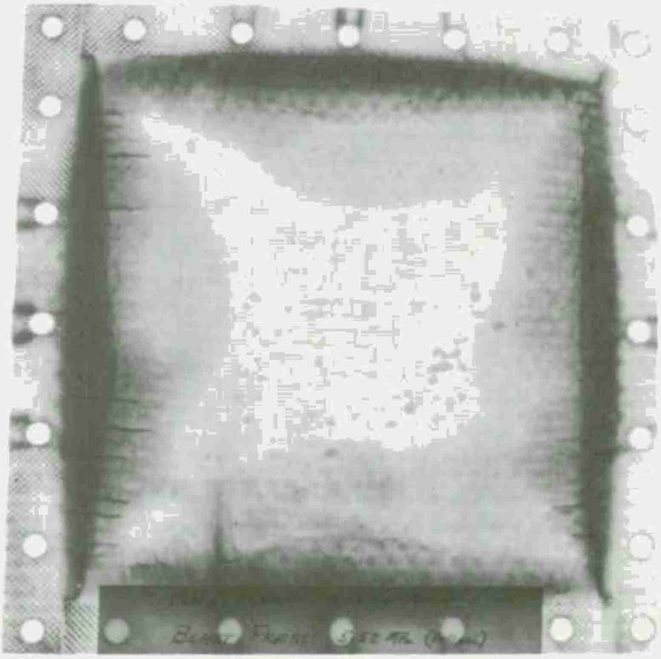

5.52 MPa (800 psi)

Figure 14. Delamination pattern in 0.64 cm thick cloth plates.

REFERENCES

1. Wrzesian, A. "Improving the Impact Resistance of Glass-Fibre Composites", *Composites*, Vol. 3, 1972, pp. 172-174.

2. Askins, D. R. and Schwartz, H. S., "Mechanical Behavior of Reinforced Backing Materials for Composite Armor", AFML-TR-71-283, Wright-Patterson AFB, Ohio, Feb. 1972.

3. Ross, C. A. and Sierakowski, R. L., "Studies on the Impact Resistance of Composite Plates", *Composites*, Vol. 4, 1973, pp. 156-161.

4. Cristescu, N., Malvern, L. E., and Sierakowski, R. L., "Failure Mechanisms in Composite Plates Impacted by Blunt-Ended Penetrators", in *Foreign Object Impact Damage to Composites*, ASTM STP 568, 1975, pp. 159-172.

5. Ross, C. A., Cristescu, N., and Sierakowski, R. L., "Experimental Studies of Failure Mechanisms of Impacted Composite Plates", *Fiber Science and Technology* (in press, 1976).

6. Ross, C. A. and Sierakowski, R. L., "Delamination Studies of Impacted Composite Plates", *Bulletin of the 46th Shock and Vibration Symposium*, 1975.

7. Sierakowski, R. L., Malvern, L. E., and Ross, C. A., "Dynamic Failure Modes in Impacted Composite Plates", 105th AIME Annual Meeting, Las Vegas, Nev., Feb. 22-26, 1976.

8. deRosset, W. S., "Fracture of Boron-Epoxy Composite Due to Impact Loading", *J. Composite Materials*, Vol. 9 (1975), pp. 114-117.

9. Ross, C. A. and Strickland, W. S., "Response of Flat Plates Subjected to Mild Impulsive Loadings", *Bulletin 45, Part 4, Shock and Vibration Information Center*, June 1975, pp. 105-116.

10. Bascom, W. D., Jones, R. L., and Timmons, C. O.,"Mixed Mode Fracture of Structural Adhesives", *Adhesion Science and Technology*, Vol. 9B.

11. Sultan, J. N., and McGarry, F. J., "Microstructural Characteristics of Thermoset Polymers", Mass. Inst of Tech.,MIT R-69-59, Oct. 1, 1969.

12. Berry, J. P., "Fracture of Polymeric Glasses" in *Fracture*, Vol. vii (ed. H. Liebowitz), New York and London: Academic Press, 1972, pp. 37-92.

FAILURE BEHAVIOR OF FILAMENT WOUND CYLINDRICAL TUBES

Bernard M. Halpin
Chemist

Roger M. Lamothe
Mechanical Engineer

Edward M. Lenoe
Supervisory Mechanical Engineer

Army Materials and Mechanics Research Center
Watertown, Massachusetts

ABSTRACT

In this particular application, filament-wound fiberglass epoxy tubes were required to contain a short-duration (10-millisecond) internal pressure pulse. Because of time and economic constraints, initial material evaluation was based on quasi-static hydroburst tests. Static hydroburst tests were conducted on conventional helically wound cylinders with wrap angles of 60°, investigating the influence of two types of glass surface finish (HTS 901, HTS 904) with four epoxy resins (GLY-CEL C-200, EPON 815, EPON 826 and ERL 2256) on the burst strength of the cylinders. Subsequently, explosive tests were completed on those glass-epoxy systems which performed favorably under static loading. Specimens were instrumented with strain gages and pressure transducers to monitor continuous strains and pressures up to and including failure. Attempts were made to obtain high-speed photographs during the explosive tests. Finally, as part of a long-range program to improve design and analysis procedures utilizing hot gas burst tests, thin-walled cylinders with four different fiber orientations and three different wall thicknesses were tested. The paper discusses the observed effects of fiber and matrix materials and the observed static and dynamic strength characteristics of these fiberglass shell components.

INTRODUCTION

In this application filament-wound cylinders were required to contain rapidly applied pressures having pulse durations of the order of milliseconds. However, materials selection had to be determined in a relatively short time frame and initial economics dictated the use of hydrostatic burst tests for screening candidate composites.

Cost and availability considerations were also decisive in choosing the manufacturing process. Components were produced using conventional wet winding procedures and relatively inexpensive epoxies and fiber reinforcements.

Test pieces described in this paper were fabricated on an EnTec model 830E, a horizontal filament winding machine equipped with a photo-servo control mechanism. Wet winding techniques were used throughout the study with the resin being applied to the reinforcement just prior to winding on the mandrel.

Mandrels were designed initially for use in a telescoping launch tube study and the test pieces represent the inner of the two tubes. Winding parameters were set to insure constant wall thickness. This accounts for observed variance in resin content between different resin systems and also for the consistency of resin content within the same resin system. The mandrels were machined from aluminum stock and to close tolerances so that the internal diameter of the finished tubes would be $3.250^{+0.003''}_{-0.000}$.

After winding to the desired wall thickness, the composite tubes were cured while rotating between centers with Cal Rod heaters. In most cases, the tubes were cured within an hour and then post-cured while still on the mandrels in a forced air oven according to schedules required by the different curing agents. Machining operations required to prepare test specimens were performed after post-curing. The ends of the tubes were released from the mandrel by means of a cut-off wheel, subsequently the tubes were removed by forcing them off the mandrel on a load frame press.

INITIAL MATERIALS SELECTION

STATIC TESTS

Static hydroburst tests were completed in our laboratory as well as elsewhere. Figure 1 is a schematic of our apparatus. Tubes with wrap angles of ± 60° and consisting of four helical wraps (see Figure 1) were prepared.

These cylinders were carefully ground to dimensions of $(0.040^{+0.003}_{-0.000})$ wall thickness. The specimens were instrumented with strain gages and the pressure, strain time response was recorded during the burst experiments. At first the tests were conducted on 36-inch-long tubes. In this instance, crazing of the resin occurred at relatively low pressures. It was observed that chance development of unsymmetrical local crazing and debonding stresses leads to severe bending stresses and consequent low burst pressures. Shortening the specimens alleviated this problem. Therefore all remaining tubes were shortened to 18 inches. In addition, for one resin system, 9-inch-long cylinders were burst, in order to establish lower bounds on the magnitude of this length effect.

Results of the static tests are presented in Figure 2 for the various fibers and resins. The materials are compared on the basis of nominal composite strength, computed from simple strength of materials formulae ($\sigma_c = PD/2t$, where P = burst pressure, D = mean tube diameter, and t = wall thickness). Note that there is a significant length effect, as shown in the EPON 815 and 826 resin systems, where the 9-inch tubes exhibit an observably higher burst strength. Shorter tubes also had substantially larger coefficients of variation, illustrating more pronounced dependency on edge effects.

Resin contents of the tubes were fairly uniform, although metallographic observations along the length of a few selected cylinders suggested substantial variation throughout each cylinder. Referring to Figure 2, the various fiber/resin combinations possessed similar magnitudes of nominal burst strength.

Highest individual strength was attained in the S901/GLY-CEL C-200 composites. However, the range in strength observations, as well as the limited number of test specimens is such that it would be difficult to justify choice of one composite over any other. Moreover, costs and relative ease of manufacture in the wet winding operation were all comparable. Thus choice of a particular resin/fiber combination was motivated by other factors.

The strength degradation of the EPON 826 system had been previously evaluated under field service conditions. Based on more than fifty burst pressure tests on these tubes, strength reduction was not detectable within scatter of the strength data.

Since the S901/GLY-CEL system had the highest mean strength and lowest coefficient of variation, it was decided to determine whether any serious environmental degradation occurred in this composite system.

ENVIRONMENTAL EFFECTS

The tubes were expected to be used in rather severe tropical environments and it was therefore necessary to establish maximum degradation due to extreme thermal and humidity influences. A controlled artificial environmental exposure program was conducted to determine the amount of strength deterioration. The conditioning cycle chosen was 160°F and 95% relative humidity [1]. Components wound from HTS901 glass and GLY-CEL C-200 resin were exposed for a period of 16 weeks to this environment and burst tests were conducted periodically throughout the exposure duration. It was found that approximately one third of the strength was lost in the first six weeks. At the end of the 16 weeks of exposure, strength appears to have leveled off to about one half the initial value. Some of the results obtained are listed in Table I.

Table I Summary of Environmental Effects on Burst Strengths

S901/GLY-CEL-C200 Cylinders

Base Line Burst Pressures, psi		Conditioned Cylinder Burst Pressures, psi
2015		934
2040		997
2040		1004
2050		1046
2092		1092
2134		1103
2063	Average	1029
39	Standard Deviation	58
1.9%	Coefficient of Variation	5.65%

The design pressures for these tubes were 725 psi and from a conventional safety factor view point the virgin burst pressures are certainly sufficient. However, the environmental deterioration is drastic. While it is true that the probability of occurrence of 160°F temperatures is rather low, nonetheless service temperatures approaching 140°F are definitely anticipated.

Therefore, on the basis of potential environmental degradation effects the GLY-CEL-C200 resin system was eliminated from further consideration.

HOT GAS BURST TESTS

Static strengths of the cylinders were substantially larger than the design pressure; but it was apparent that the component reliability levels were severely reduced due to the environmental exposures. Furthermore, in field service these tubes had to retain dynamic pressures with orders of magnitude shorter duration than in the hydroburst tests. Since high speed loadings were expected to result in higher strength levels, it was prudent to determine the extent of deterioration of dynamic strengths.

Selection of sensors, instrumentation and hot gas generator was based on review of pressure-time histories of actual field service in similiar types of components. From representative pressure-time histories, the pressure rate, magnitude and duration of the pressure pulse could be determined or at least approximated.

A variety of experimental measurements were recorded during the hot gas burst tests. Besides pressure-time pulses, strain (see Figure 3) and gross displacements were studied. A schematic of the experiment appears in Figure 4.

INSTRUMENTATION

STRAIN GAGES

Selection of the strain gages was based on strain capacity (3-5%) and power dissipation since fiberglass material is a very poor heat conductor. Two types of gages were selected, e.g., Micro-Measurement (M-M) EA-06-125TM-120 Option L which is a general purpose two-element 90° rosette and M-M-EA-06-062TW-120 Option L which is a so-called torque gage and can measure shear directly.

The strain gage site was carefully sanded and ground to remove resin without abrading the fibers and also in order to insure close contact to the reinforcing fibers. Previous studies concerning effect of varying resin thicknesses beneath strain gages on composite materials had shown that resin-rich areas can drastically attenuate strain. Furthermore, nonuniform resin deposits lead to increased scatter in the measurements and to spurious results.

In order to choose adequate adhesive bonding techniques, comparative data was obtained on Eastman 910 and BLH-EPY 150 epoxy-bonded gages. While specimen preparation is far less time consuming for the Eastman 910 adhesive, previous experiences led to reasonable doubts as to suitability of this material for dynamic tests. Thus a brief study was completed to determine suitability of these adhesives. The gages on two of the cylinders were bonded with a BLH-EPY-150 adhesive, while gages on two comparable cylinders were bonded with the Eastman 910 adhesive. Standard surface preparations, bonding and curing techniques were strictly followed. Results of three of these tests are shown in Table II. Due to similarity of response of the epoxy-bonded gages only one set of test data is shown. Examination of the strain-time curves for these tests reveals similar early-time response. However, the tabulated data suggests that the Eastman 910 bonded gages fail more often than the epoxy-bonded gages prior to peak pressure. Thus BLH-EPY-150 was chosen for gage preparation in the remaining test series.

Table II Comparison of Strain Gage Response for Different Adhesives

	BLH-EPY-150 Adhesive		Eastman 910 Adhesive			
Test:	A-1		A-2		B-2	
Burst Pressure:	2025 psi		2197 psi		2666 psi	
	Gage #	Strain μin./in.	Gage #	Strain μin./in.	Gage #	Strain μin./in.
	1 H	23,696	1 (BAD)	-	1 H*	-
	2 L	29,295	2 L*	16,548	2 L	-
	3 H	36,284	3 H*	10,875	3 H	28,528
	4 L	-	4 L*	2,625	4 L†	6,426
	5 H	-	5 H	38,625	5 H	28,875
	6 L	31,820	6 L	30,360	6 L	29,991
	7 H*	20,116	7 H*	15,180	7 H*	-
	8 L†	16,093	8 L	12,750	8 L†	7,140
	11 S	5,246	11 S (BAD)	-	11 S	13,912

*Gage broke before peak pressure
†Gage broke before peak pressure but peaked out

PRESSURE TRANSDUCERS

Pressure measurements were obtained simultaneously at both ends of the tube in the hot gas burst experiments. Verification of the accuracy of the sensors was determined under static loading and compared to a Heise gage. Subsequent calibration of the sensors was performed electronically utilizing a test signal designed into the Kistler charge amplifier.

DISPLACEMENT TRANSDUCERS AND HIGH SPEED PHOTOGRAPHY

Measurement of radial displacements was attempted with a Bournes Lini-Pot as the electronic sensor. The threaded end of the Lini-Pot shaft was coupled to a spring loaded rod. The displacement assembly was then attached to the hot gas burst fixture. Initially, some measurements obtained were somewhat erratic but the mortality rate of the sensors precluded any further attempts to monitor displacements.

Visual records of dynamic tests were obtained with a Hycam 41-0004 16-mm high speed camera. However, the expanding gas prevented any visual insight as to the final mode and locality of the failure.

HOT GAS PRESSURE PULSE GENERATOR

The prime factor considered in designing the methodology for producing the hot gas pressure pulse was simulation of the pressure rate to coincide with actual field firing tests. The method arrived at for generating a uniform pressure pulse consisted of electrically igniting a slow-burning propellant. The propellant charge consisted of a measured amount of Improved Military Rifle (IMR) Powder 8208 and an igniter encapsulated in a plastic bag (Figure 5).

Throughout the testing, the procedure for fabricating the igniter was not altered and utilized the following components:

One electric squib type USF-107

Six grams of ignition granules 2C

One 2" x 5" x 0.10" thick sheet of M-8 propellant formed into a cylinder and sealed at one end.

The overall dimensions of the finished product were 6" long x 2.16" in diameter. Whenever possible, the propellant charge was located along the axis of the test specimen and equidistant from its ends.

DYNAMIC STRENGTH OF GROUND TUBES

Composite tubes similar to those used in the static screening tests were fabricated with helix wrap angles of ±60° and nominally 40 mils thick. HTS 904 finished fibers and 826 epoxy resin were used. However, unlike the static specimens which were tested in this as-wrapped condition, the outside diameter of the dynamic test specimens was carefully ground to arrive at design dimensions.

Typical pressure-time records resulting from explosive tests on these tubes are shown in Figure 6. Note that these pressure pulses can be superposed by shifting the horizontal time axies, i.e., the major variation occurs in the early rise time portions of the pulse. The burst data obtained is fairly reproducible and this fact is borne out by the summary of burst pressures in Table III.

Note the variation of pressure readings with locations. With the exception of test #4, higher pressures were observed at the top position. It should be noted here that in each test the pressure transducer and associated readout equipment was alternated. The difference between pressures does appear to be systematic with the upper transducer usually recording the maximum observed pressure. However, when the maximum and minimum pressures are compared, the scatter is within the accuracy of the experiment. The burst pressures under dynamic loading are 43% higher on the average than the static results obtained on identical samples listed in Table IV.

Table III Summary Burst Pressures (psi)

	Transducer Position	
Test No.	Top	Bottom
1	3195	3168
2	3148	2977
3	3138	3031
4	2747	3090
5	3146	3296

Average 3115 psi

Table IV Comparison of Static and Dynamic Burst Strengths, Ground Tubes

Test Facility	Specimen Length, Inches	Type of Loading	Average Burst Pressure, psi
Lab "A"	18	Static	1858
Lab "A"	9	Static	2104
AMMRC	9	Static	2179
AMMRC	9	Dynamic	3115

PRELIMINARY EVALUATION OF DESIGN PROCEDURE

Thus far our observations lead to the conclusion that the current tubular configuration has a substantial safety factor and as a matter of fact, the design of the component is controlled by other criteria related to field handling and ruggedness. Furthermore, the helix wrap orientation had been selected predominantly on the basis of a netting analysis combined with static burst tests on cylinders and coupon tests performed on rectangular tension specimens of HTS 904 and 826 resin and illustrated in Figure 7. A comparison of the strength variation in a unidirectional laminate based on these coupon tests and a classical failure theory [2] for composites is shown in Figure 8. While the data closely matches the theoretical curve, this fit is more a check of the ability of a nonlinear equation to fit a few test results, rather than a positive validation of a particular failure theory. Ability to predict the behavior of the fiberglass components is the appropriate concern. The properties of a single lamina deduced from these coupon experiments are given in the Appendix.

EFFECTS OF WRAP ANGLE AND LAMINATE THICKNESS

Using hot gas burst procedures just described, experiments were conducted on cylindrical specimens with wrap angles of ± 11°, ± 30°, ± 60° and 90°. The number of helix wraps was also varied. Results available to date are shown in Figures 9 through 14. In Figure 9, the general trend of dynamic burst strength versus number of helix layers is shown for three configurations. Most of the data accumulated has been on the ± 60° orientation and the behavior of this type of composite is well explored. As expected, the ± 30° cylinders were significantly weaker than the other helix angles. Results for two thicknesses of the ± 30° material are shown and the two-layer shell has comparatively low strength. This type of shell is rather compliant and accordingly subjected to early crazing and easier penetration by hot gases. It is conjectured, therefore, that thermal influences become more significant in this case for the thinner shells. As a matter of fact, more frequent and extensive burn throughs occurred for the ± 30° laminates.

The ± 60° shell behavior is further illustrated in Figure 10, which is a typical pressure, strain versus time recording. It is worthwhile to note that only one of the gages indicated failure at peak pressure. (Hoop gage #1.) Supposedly these gages were capable of a least 3% strain. A number of the other gages failed at lower than 3% strain. There are several possible explanations; either local failures occurred under the gages and terminated their response, or the gages are otherwise blown off and incapable of continually following large deformations. In any case the maximum strains reported ought generally to be considered as lower bounds on total elongation.

Figure 11 compares strengths of the ± 60° shells for several conditions. The uppermost line of the illustration is dynamic strength for as-wrapped shells, i.e., wet wound and cured without subsequent machining. For the four-layer helix wraps these averaged 3700 psi. Other cylinders were prepared in a similar fashion, except they were carefully ground to remove the slight exterior resin-rich coating, in order to meet dimensional tolerances. This resulted in mean strengths of 3150 psi. Surface-ground specimens were also statically hydroburst and these shells attained average strengths of 2060 psi. Thus the as-wrapped process resulted in 80% strength increase when compared to the static strengths. Obviously it is worthwhile to seek alternate methods to grinding in order to control tolerances. A final matched die molding step might, for instance, be introduced in the curing operation.

The two lower curves are burst strength predictions based on moduli and strengths measured by means of the flat laminate coupon specimens discussed previously. The most elementary form of anisotropic shell theory was used. For the lowest curve, measured moduli and strengths were used in the predictions, resulting in very conservative strength estimates. The dashed curves are based on increased transverse tension (40 ksi) and shear strengths with obvious effect on the predictions.

The simplest shell theory and failure criterion is not adequate for predicting dynamic response but fortunately is usually conservative. In terms of further assessment of higher order theories, it is well to commment on the test procedure. One of the difficulties in comparing theoretical and experimental shell response relates to specifying boundary conditions; i.e., fixed or free ends, displacements and forces at the specimen end caps. The hot gas apparatus was generally a close approximation to zero inward radial shell end motion and virtually no axial friction loads. Figure 12, for example, is a comparison of typical strain distributions throughout a ± 60° cylinder, indicating fairly uniform strain conditions. This uniformity is somewhat surprising considering that these are strains at failure. (Refer to Figure 10 with apparently premature strain failures.)

However, the magnitude of frictional forces apparently varies for different wrap orientations. Consider Figure 13, illustrating typical hot gas burst failures. The 11° and 90° laminates fractured with relatively small deformation. The 60° shell has undergone gross distortion while the 30° wrap typically achieved extraordinary dimensional changes. Obviously, these characteristic failures have associated varying shell end conditions. Note especially the 90° shell where fractures invariably occurred at the specimen end caps, as well as in the shell midsection. The 90° failure modes are further illustrated in Figure 14, where fractures are shown for 2, 4 and 6 layers. The thinnest shells generally failed in many more distant locations and also gave evidence of more frequent burn throughs perhaps during bursting.

In order to attempt verification of higher order shell theories, it appears that slightly different types of specimen end fittings would be required to achieve consistent restraint conditions for the different helix configurations.

CONCLUSIONS

The series of static hydroburst and dynamic hot gas experiments discussed in this paper have revealed the following:

The static and dynamic burst strengths of the composite tube under consideration (i.e., ± 60° wrap and 40 mils thick) are more than sufficient to withstand the anticipated loading conditions. It should be noted here that other investigators [3] have conducted analytical and experimental studies of helically wound composite tubes. Their results indicate that the optimum winding angle should be in the range of ± 55 to ± 58 degrees.

Environmental effects must be considered in the selection of fibers and resins for a given application.

Surface grinding for dimension control results in a marked reduction in burst strengths.

Further refinements are required in specimen end fittings as well as alternate shell edge constraints to provide some meaningful comparison of theoretical and observed shell response.

Finally, in order to make reasonable predictions on dynamic response, the dynamic mechanical properties (moduli and failure strengths) must be obtained on representative configurations.

ACKNOWLEDGMENT

The authors acknowledge the assistance of Mr. Charles Polley of the Mechanics Research Laboratory in conducting both the static hydroburst and the dynamic hot gas experiments.

APPENDIX. Single Lamina Properties from Coupon Tests

Mechanical Property	Average Value
Longitudinal Modulus, E_1	7.58×10^6 psi
Transverse Modulus, E_2	1.77×10^6 psi
Major Poisson's Ratio, ν_{12}	0.267
Minor Poisson's Ratio, ν_{21}	0.065
Shear Modulus, G_{12}	0.50×10^6 psi
Longitudinal Tensile Strength, σ_1	233.3 ksi
Transverse Tensile Strength, σ_2	7.33 ksi
Shear Strength, τ_{12}	7.46 ksi

The shear modulus was estimated using uniaxial and off-axis test data and the relation

$$G_{12} = \frac{1}{(4/E_{45^\circ}) - (1/E\ ) - (1/E\ )\,(1-2\nu_{12})}$$

REFERENCES

1. Clodfelter, G. A. and Lovelace, D. E., "Effect of Environmental and Artificial Conditioning on Composite Tubes M 72 LAW Launcher," Report No. RL-TR-71-13, U. S. Army Missile Command, Huntsville, Alabama, October 1971.

2. Tsai, S. W., "Mechanics of Composite Materials Part I," Technical Report AFML-TR-66-149, June 1966.

3. Yamawaki, K. and Vemura, M., "Fracture Strengths of Helically Wound Composite Cylinders, Burst Strength Under Internal Pressure," Japan Society of Materials Science Journal, v. 21, April 1972.

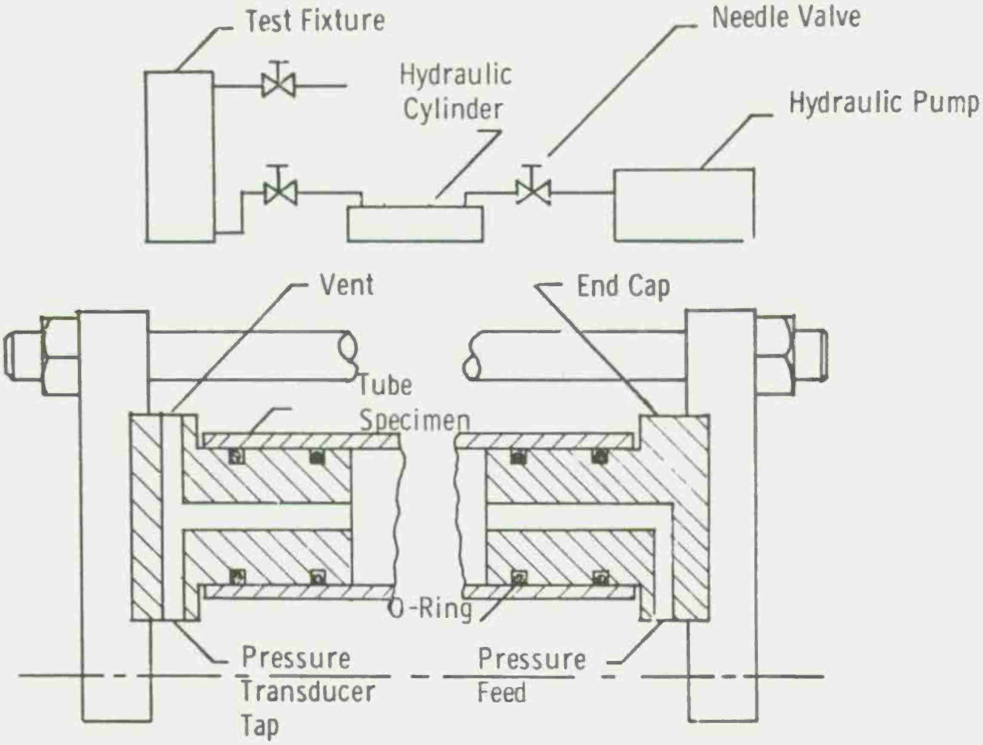
Test Fixture
Needle Valve
Hydraulic Cylinder
Hydraulic Pump
Vent
End Cap
Tube Specimen
O-Ring
Pressure Transducer Tap
Pressure Feed

Figure 1 Schematic of Static Hydroburst Apparatus

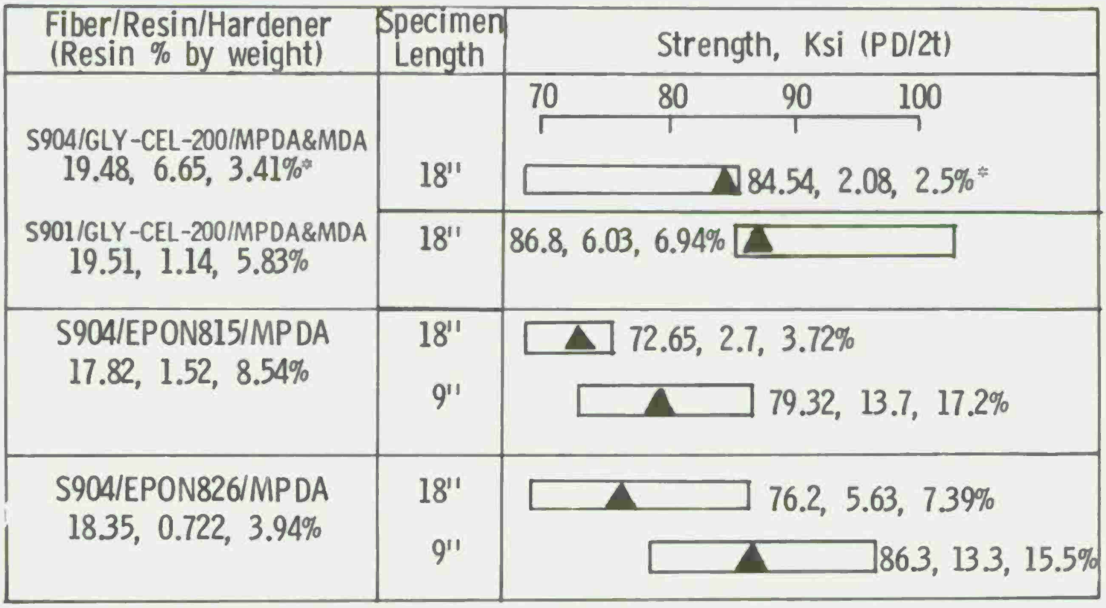

Fiber/Resin/Hardener (Resin % by weight)	Specimen Length	Strength, Ksi (PD/2t)
S904/GLY-CEL-200/MPDA&MDA 19.48, 6.65, 3.41%*	18"	84.54, 2.08, 2.5%*
S901/GLY-CEL-200/MPDA&MDA 19.51, 1.14, 5.83%	18"	86.8, 6.03, 6.94%
S904/EPON815/MPDA 17.82, 1.52, 8.54%	18"	72.65, 2.7, 3.72%
	9"	79.32, 13.7, 17.2%
S904/EPON826/MPDA 18.35, 0.722, 3.94%	18"	76.2, 5.63, 7.39%
	9"	86.3, 13.3, 15.5%

*Notation: Mean Value, Standard Deviation, Coefficient of Variation

Figure 2 Comparison of Static Burst Strengths, Initial Screening Tests

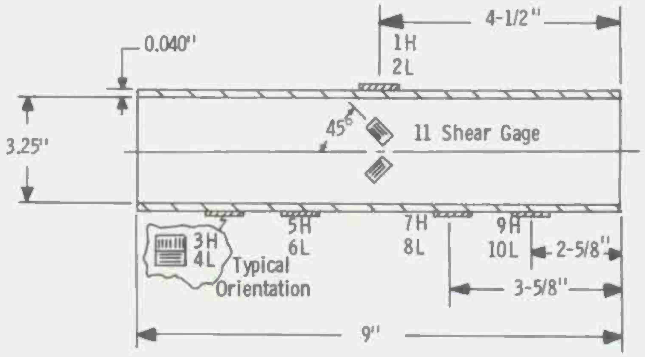
0.040"
4-1/2"
1H
2L
3.25"
45°
11 Shear Gage
3H
4L
Typical Orientation
5H
6L
7H
8L
9H
10L
2-5/8"
3-5/8"
9"

Figure 3 Cylindrical Tube Dimensions and Strain Gage Locations

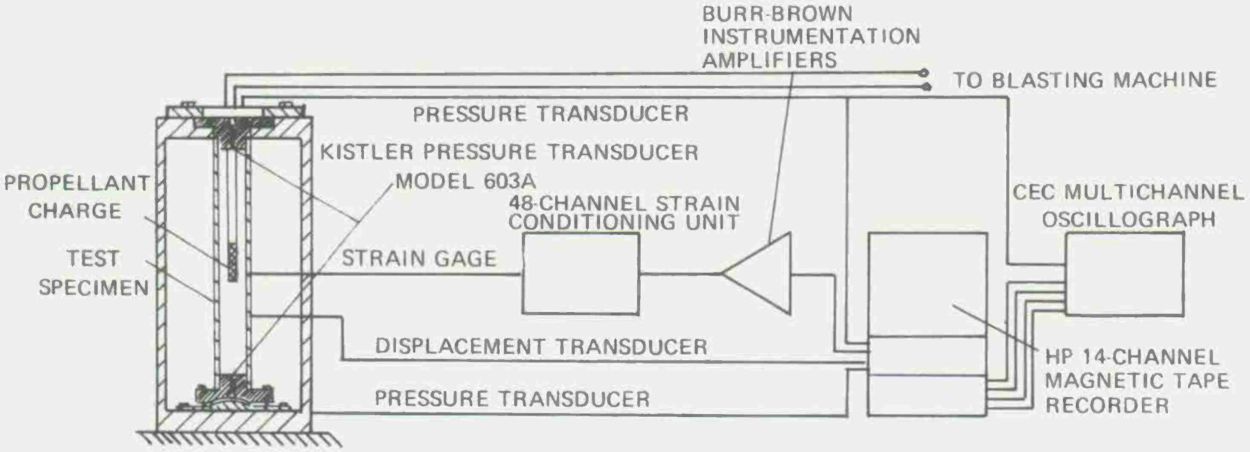
BURR-BROWN INSTRUMENTATION AMPLIFIERS
TO BLASTING MACHINE
PRESSURE TRANSDUCER
KISTLER PRESSURE TRANSDUCER
MODEL 603A
PROPELLANT CHARGE
TEST SPECIMEN
48-CHANNEL STRAIN CONDITIONING UNIT
CEC MULTICHANNEL OSCILLOGRAPH
STRAIN GAGE
DISPLACEMENT TRANSDUCER
PRESSURE TRANSDUCER
HP 14-CHANNEL MAGNETIC TAPE RECORDER

Figure 4 Schematic of Hot Gas Fixture and Instrumentation

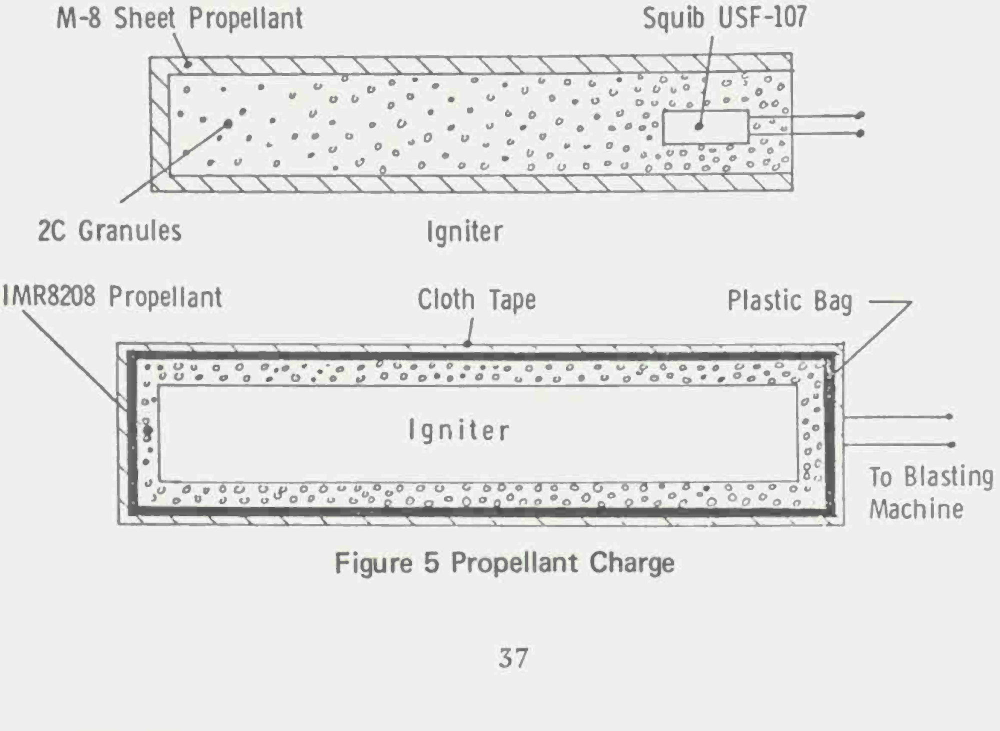
M-8 Sheet Propellant
Squib USF-107
2C Granules
Igniter
IMR8208 Propellant
Cloth Tape
Plastic Bag
Igniter
To Blasting Machine

Figure 5 Propellant Charge

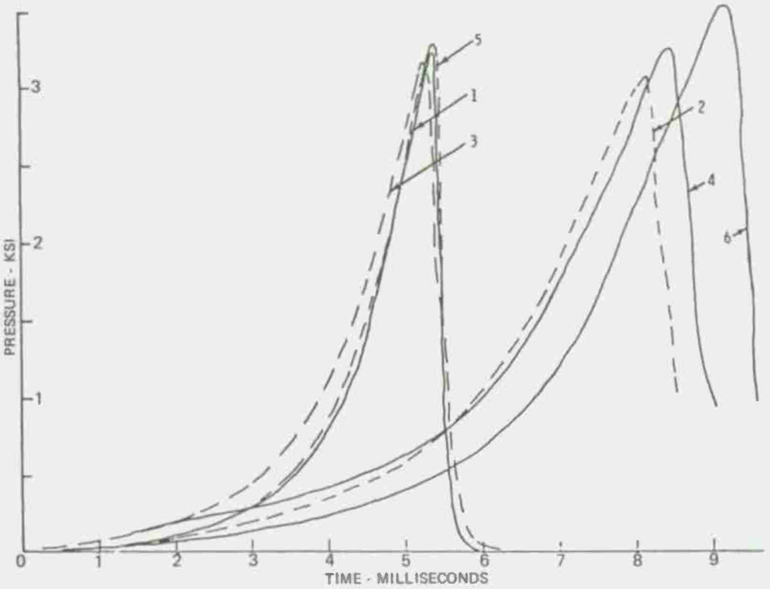

Figure 6 Pressure Versus Time, Barrel Tests 1 through 6

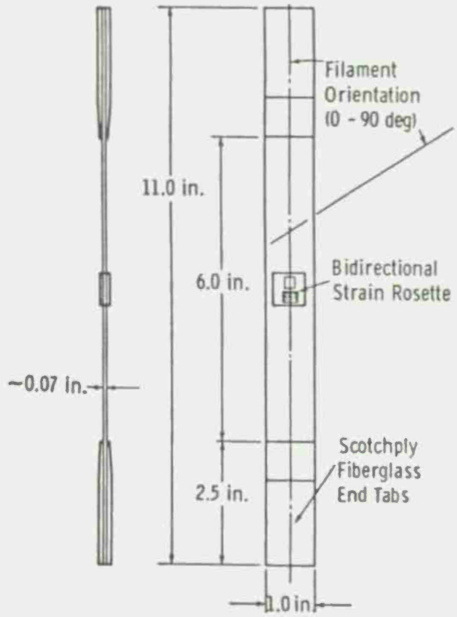

11.0 in.
6.0 in.
2.5 in.
~0.07 in.
1.0 in.
Filament Orientation (0 - 90 deg)
Bidirectional Strain Rosette
Scotchply Fiberglass End Tabs

Figure 7 Typical Coupon Test Specimen

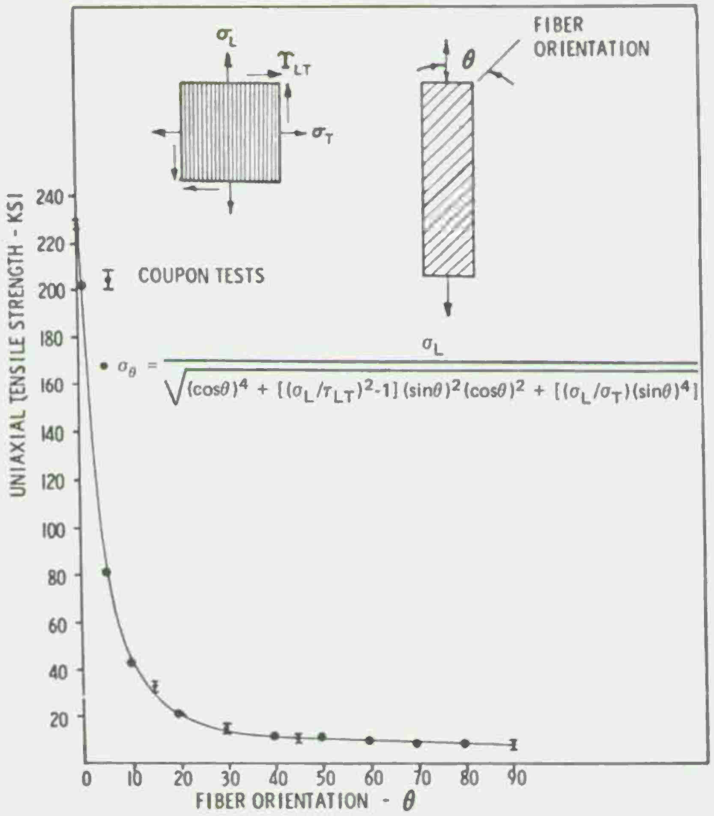

Figure 8 Unidirectional Strength Prediction

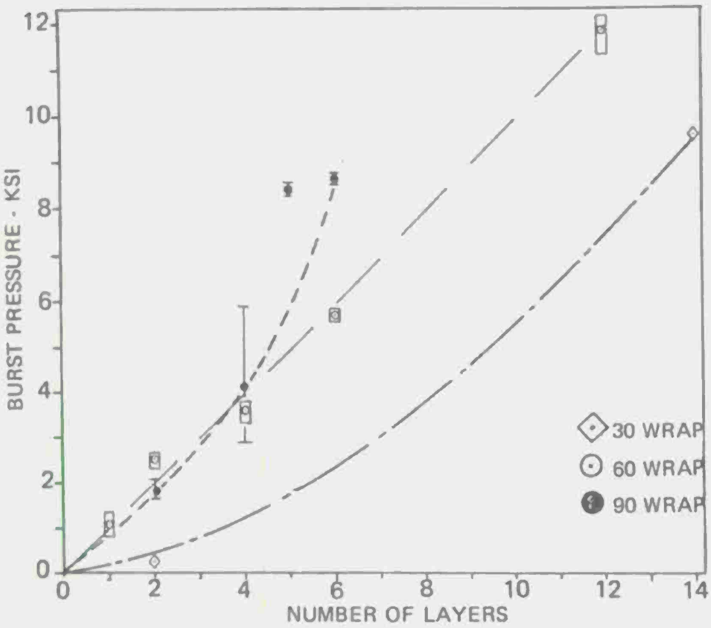

Figure 9 Dynamic Burst Strength of Fiberglass Cylinders

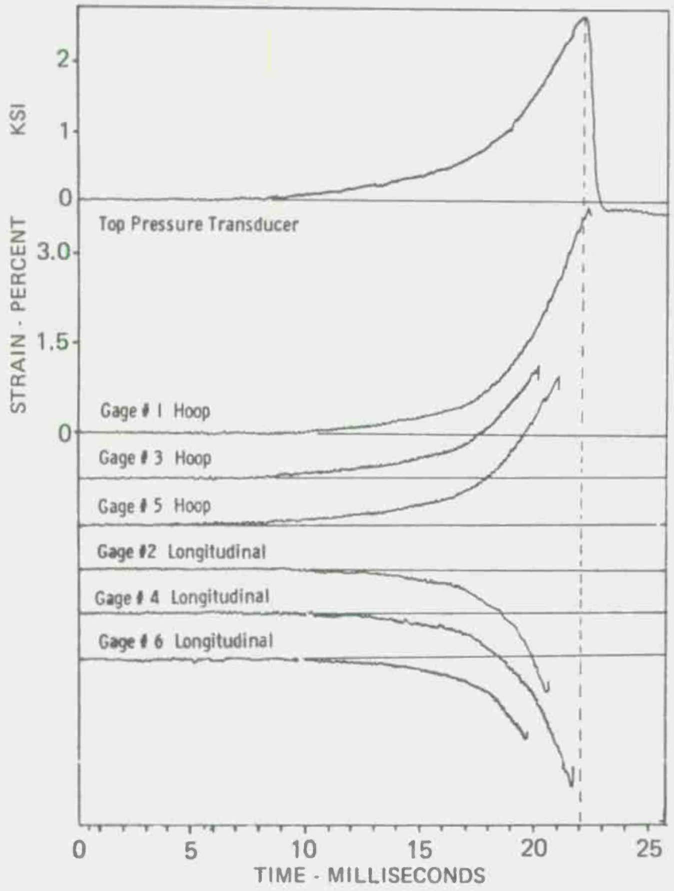

Figure 10 Typical Pressure, Strain Versus Time Record

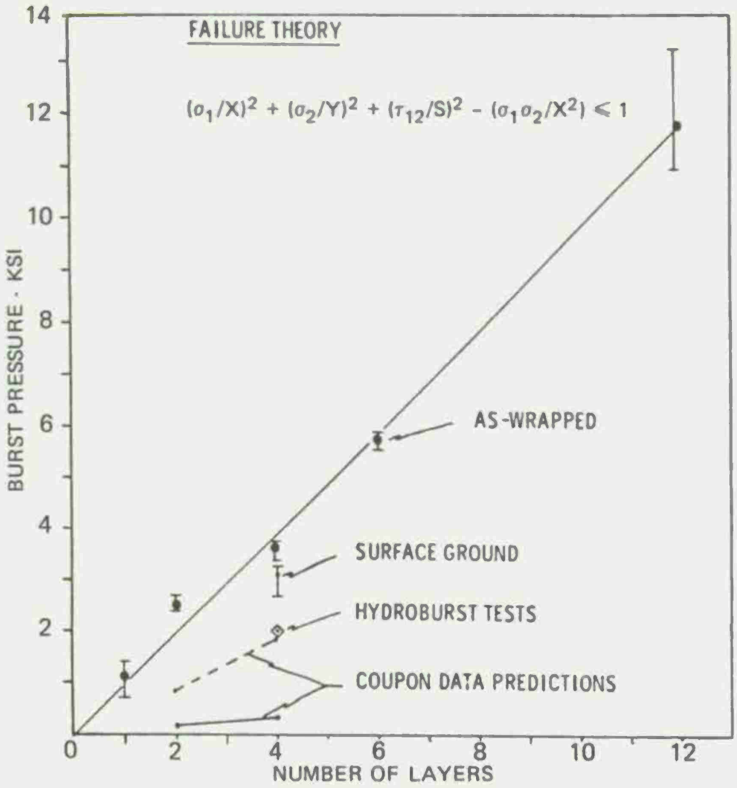

Figure 11 Hot Gas Burst Strengths of 60-Wrap Cylinders

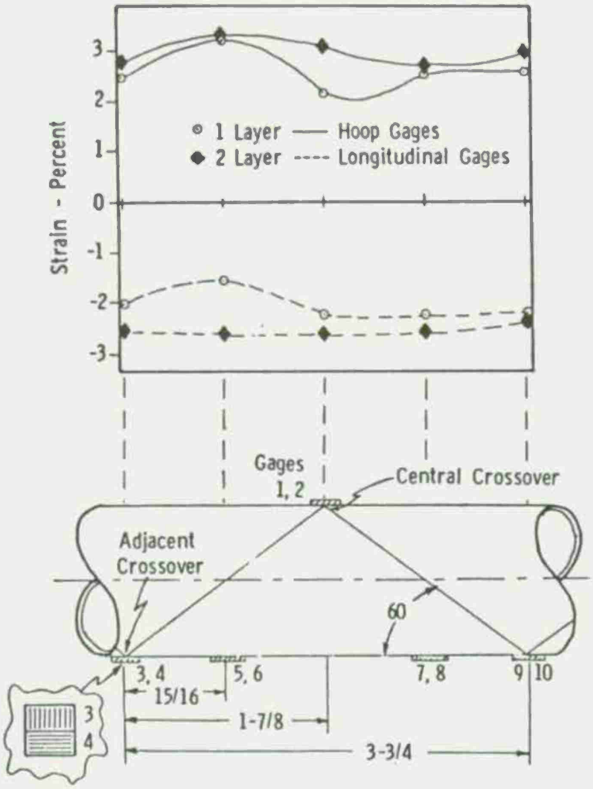

Figure 12 Strain Distribution Along 60-Wrap Cylinder

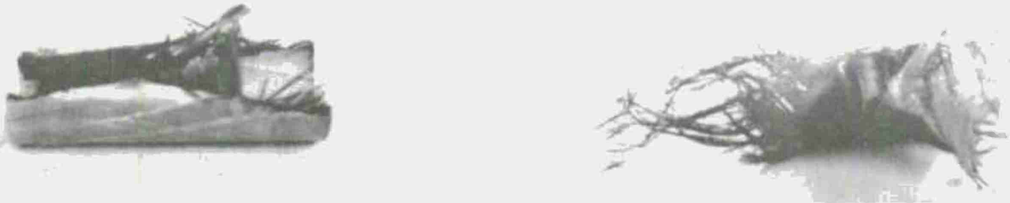

Test 50 Wrap Angle: 11
No. of layers - 4
Avg. burst pressure - 137 psi

Test 6 Wrap Angle: 60
No. of layers - 1
Avg. burst pressure - 868 psi

Test 44 Wrap Angle: 30
No. of layers - 2
Avg. burst pressure - 296 psi

Test 40 Wrap Angle: 90
No. of layers - 6
Avg. burst pressure - 7657 psi

Figure 13 Typical Failures - 11-, 30-, 90-Wrap Cylinders

2-LAYER 4-LAYER 6-LAYER

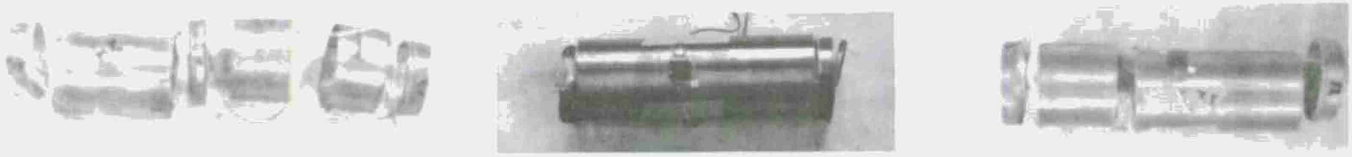

Test 24 B_p: Top = 3052 psi Test 20 B_p: Top = 6165 psi Test 32 B_p: Top = 8722 psi

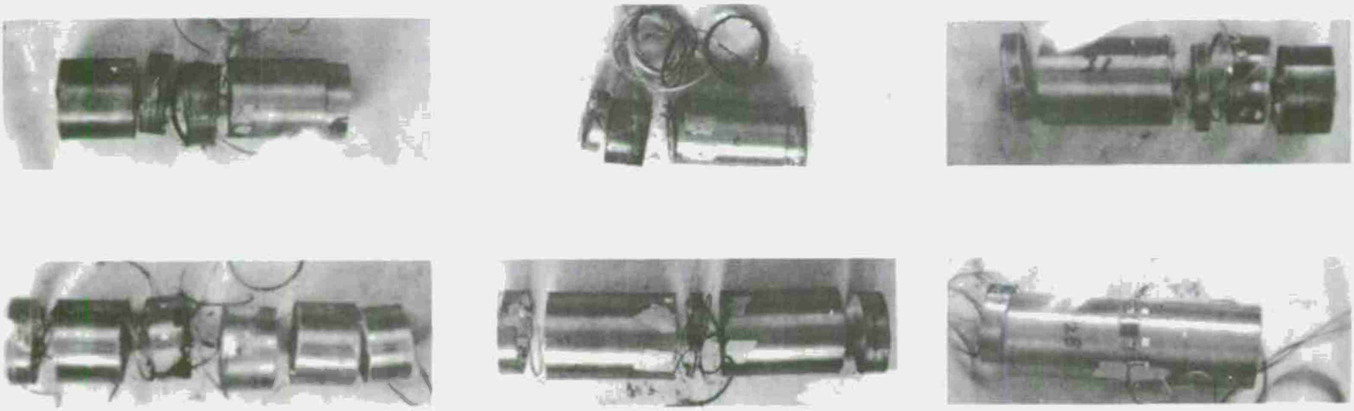

Test 34 B_p: Top = 1375 psi Test 23 B_p: Top = 3523 psi Test 28 B_p: Top = 8496 psi

Figure 14 Typical Failures - 90-Wrap Cylinders

19-066-1048/AMC-76

SESSION III: BUCKLING

Chairman: R. FOYE
Aerospace Technologist
Army Air Mobility Research Laboratory

BUCKLING/CRIPPLING CHARACTERISTICS OF BORSIC-TITANIUM
R. W. Gehring, Rockwell International Corporation, Columbus Aircraft Division, and G. S. Doble, Materials Technology, TRW, Inc. 45

POST BUCKLING BEHAVIOR OF GRAPHITE/EPOXY LAMINATED PLATES AND CHANNELS
E. E. Spier, General Dynamics, Convair Division, and F. L. Klouman, Norwegian Defence Research Establishment 62

BUCKLING/CRIPPLING CHARACTERISTICS OF BORSIC-TITANIUM

R. W. Gehring

Member of Technical Staff
Rockwell International Corporation–Columbus Aircraft Division
Columbus, Ohio

G. S. Doble

Principal Engineer
Materials Technology–TRW, Inc.
Cleveland, Ohio

ABSTRACT

An experimental-empirical study of 50 percent volume fraction Borsic-Ti (3Al-2.5V) equal leg angles at room temperature revealed high post-buckling strength throughout a wide practical range of b'/t. This strength is achieved without the necessity of cross-plying or the use of interleaving in the unidirectional laminate. Empirical equations for both buckling and crippling are presented in a form useful for extension to elevated temperatures and/or improvements in the basic material properties. Comparison with other materials is presented and recommendations are given for extending the present data to other shapes.

NOMENCLATURE

A = area, in.^{2}

a = effective width of outstanding leg, inches

b = effective width of outstanding leg, inches

E_{xx} = tension modulus of elasticity in longitudinal direction, lbs/in.^{2}

E_{yy} = tension modulus of elasticity in transverse direction, lbs/in.^{2}

$(E_c)_{xx}$ = compression modulus of elasticity in longitudinal direction, lbs/in.^{2}

$(E_c)_{yy}$ = compression modulus of elasticity in transverse direction, lbs/in.^{2}

e = strain, in./in.

$(F_{cc})_{xx}$ = crippling stress in longitudinal direction, lbs/in.^{2}

$(F_{cr})_{xx}$ = initial compression buckling stress in longitudinal direction, lbs/in.^{2}

$(F_{cu})_{xx}$ = ultimate compression stress in longitudinal direction, lbs/in.^{2}

$(F_{tu})_{xx}$ = ultimate tensile stress in longitudinal direction, lbs/in.^{2}

G_{xy} = shear modulus, lbs/in.^{2}

L, ℓ = length, inches

P = load, lbs

$(P_{cc})_{xx}$ = crippling load in longitudinal direction, lbs

$(P_{cr})_{xx}$ = initial compression buckling load in longitudinal direction, lbs

R = corner radius, inches

t = thickness of laminate, inches

w = total width of outstanding legs, inches

GREEK SYMBOLS

ν_{xy}, ν_{yx} = Poisson's Ratio, dimensionless

ρ = density, lbs/in.^{3}; radius of gyration, inches

INTRODUCTION

Unidirectional filamentary reinforced metal matrix composites are of interest in stiffened panels and stringers because of their very high specific stiffness. Typical cross sections are angles, T, Z, I, hats, etc. The majority of aerospace structures containing these shapes are designed for compressive loading. The anisotropic strength and modulus of metal matrix composites complicate the analytical treatment of these otherwise simple structural elements. Since theoretical buckling calculations of composite elements have been reported to be nonconservative [1], it is important to obtain experimental data on these systems. Therefore, a series of angle specimens covering a wide range of b/t was constructed of Borsic*-Ti (3Al-2.5V) and tested in compression to obtain buckling and crippling strength. The purpose of this program was primarily to assess the post-buckling strength of formed shapes in the longitudinal direction and to obtain data for comparison with other materials. Although the test program, consisting of fifteen specimens, was limited to room temperature, the use of empirical equations in terms of the appropriate geometry and material property factors allows extension to other temperatures. The titanium matrix was selected because the material is being considered for elevated temperature applications. The titanium alloy was also chosen because the high transverse strength was expected to resist induced transverse bending stress and increase the crippling strength.

---

*Borsic is a registered trademark of Composite Materials Corporation

The Borsic fiber used was 5.7 mils in diameter and consisted of a boron substrate with a 0.1-mil coating of silicon carbide to reduce interaction with the matrix. The Ti-3Al-2.5V alloy is a near alpha alloy having good formability, notch tensile strength, and corrosion resistance. Typical applications for this alloy are ducting, honeycomb, and sheet metal fabrications. Of particular interest is the alloy availability in foil form at low cost. At 50 volume percent reinforcement, the composite achieves rule of mixture modulus values. Typical longitudinal ultimate tensile strength values are approximately 170,000 to 180,000 psi and transverse ultimate tensile strength values are 60,000 to 70,000 psi [2]. In general, the compressive ultimate strength of the composite is three or four times higher than the tensile strength [3]. This is due to the brittle fiber which reacts to surface flaws in tension but not in compression. These higher compressive strength values are well known in metal matrix composites [4] but are realized only with great difficulty experimentally, by preventing buckling and forcing a compressive failure mode. The shear strength of a titanium matrix composite corresponds to the shear strength of the matrix [3] and may be taken as 60,000 to 70,000 psi for this composite system.

Titanium matrix composites are used in applications requiring elevated temperature capability, off-axis strength, matrix shear strength, erosion and impact resistance, and ease of diffusion bonding. Borsic-titanium is an attractive candidate for service temperatures above 450°F and maintains useful strength to 1000°F. The high off-axis strength of Borsic-titanium frequently eliminates the need for cross-ply construction. The high matrix shear strength of titanium and the ease of diffusion bonding allows the attachment of the composite without complex end or joint geometries. Borsic-titanium also has impact resistance superior to either resin matrix or boron-aluminum composites.

Applications for titanium matrix composites may include use of a completely reinforced or selectively reinforced component. Examples of complete reinforcement are applications such as compressor fan blades, struts, reinforcing members, and skin covering. Selective reinforcement may be used to increase stiffness, tensile strength, compressive strength, or shear strength in specific locations of existing components or structures and has been used for fan blades and aircraft structural sections. The maximum potential of composite materials is realized when the properties of the composite are considered in the initial design stage rather than in a subsequent modification of an existing design.

SPECIMEN DESIGN AND FABRICATION

Angle specimens were designed for a wide range of b'/t typical of outstanding leg dimensions of typical airframe components. To prevent, as nearly as possible, column action the slenderness ratio was established as $L'/\rho \approx 12$ to ensure local instability failures. Table I shows the specimen dimensions selected for test where three replicates of each b'/t ratio were fabricated.

Table I. Specimen Dimensions

b/t (Ref.) Nominal	w, in.	ℓ, in.	R (R = 6t) in.	t (Nominal), in.
10	0.40	1.00	0.24	0.040
15	0.60	1.50	↑	↑
20	0.80	2.00		
30	1.20	2.80	↓	↓
40	1.60	3.75	0.24	0.040

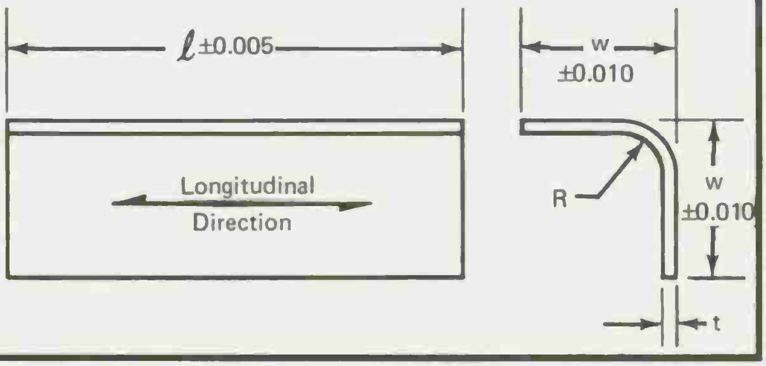

The crippling specimens were fabricated of 50 volume percent Borsic-Ti (3Al-2.5V) in a unidirectional laminate. The fabrication process employed vacuum press diffusion bonding which provides good properties and is applicable to the production of reinforced metal matrix composites. The basic fabrication procedure involved press bonding of monotapes, bending the monotapes into the required radii, and subsequently diffusion bonding the monotapes together into the five-ply laminate crippling specimen.

Monotape fabrication was performed in a vacuum after collimating the fibers by drum winding and placing the resulting mat in between two plies of rolled titanium alloy foil. Consolidation conditions were 1550°F/25 ksi for 15 minutes. The resulting monotape is completely dense with the filaments very uniformly spaced. Monotapes up to 15 feet in length have been produced in this manner by step press bonding.

Monotapes were formed to the required radius at elevated temperature and were nested in packs of five to obtain the differential radii required from the I.D. to the O.D. of the corner radius. A typical formed monotape is shown in Figure 1. No difficulty was encountered in forming to the 1/4-inch radius. The monotapes were then cleaned and etched to 50 volume percent reinforcement prior to bonding together.

The crippling specimens were then diffusion bonded in a vacuum using the nested individual monotapes. The final bonding operation was performed in an 1N-100 die which consisted of a radiused V-block female member and a radiused "V" punch. The individual monotapes bond together with bare metal strength. The basic advantage of the monotape approach is that the fibers are very uniformly spaced and do not move together during subsequent fabrication.

The angle crippling specimens produced are shown in Figure 2. All specimens were inspected by radiography, metallographic sections cut off from the ends, and optical microscopy of the as-machined specimen ends. Selected specimens were destructively evaluated by dissolving the matrix to ensure that no filament breakage had occurred. A typical microsection is shown in Figure 3. The filaments were well distributed, the initial monotape well consolidated, and the monotapes were completely bonded together.

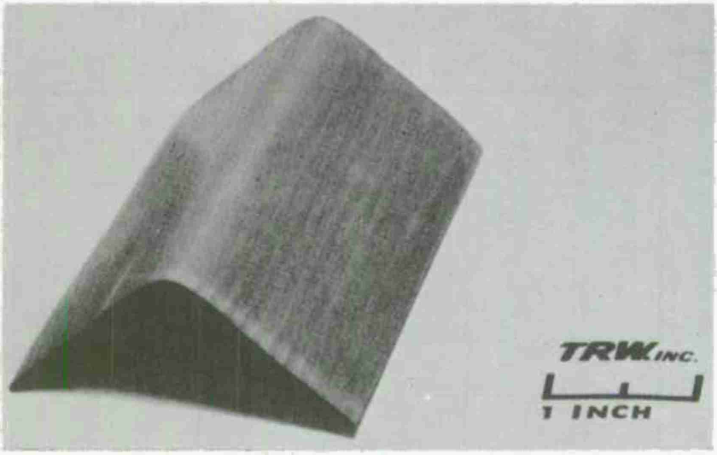

Figure 1. Borsic-Ti (3–2-1/2) Monotape Bent to 1/4-inch Transverse Radius

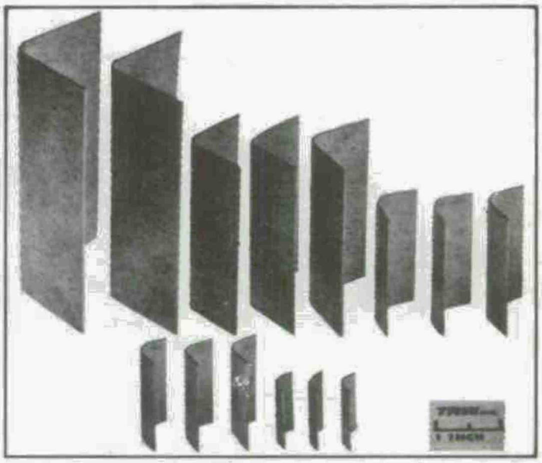

Figure 2. Borsic-Ti (3–2-1/2) Crippling Specimens

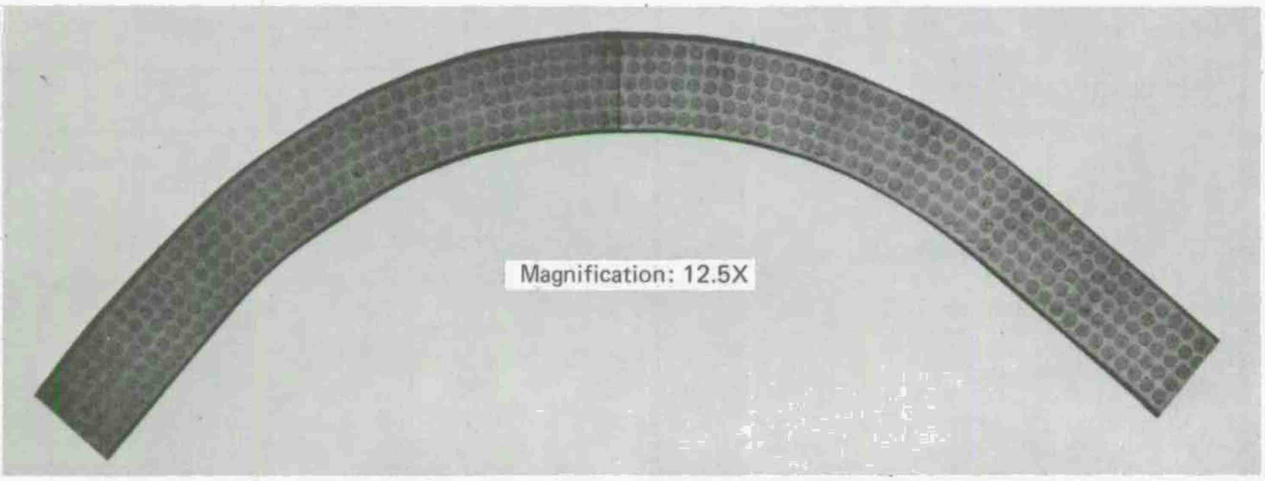

Figure 3. Macrosection of Typical Borsic-Ti (3–2-1/2) Crippling Specimen

MATERIAL PROPERTIES

Material properties were obtained from various sources as shown in Table II. Of particular importance are the unidirectional compression modulus and the unidirectional compression strength. References are shown for each of the material property values with $(F_{cu})_{xx}$ being obtained from IITRI [3] data and the compression modulus, $(E_c)_{xx}$, obtained from strain gage data during the investigation described herein. Reference [3] indicates the ultimate compression strength, $(F_{cu})_{xx}$, to be 690 ksi for a unidirectional Borsic-Ti laminate of 45 percent volume fraction. In these laminates the matrix was Ti-6Al-4V rather than the Ti-3Al-2.5V matrix used in the present investigation. However, both rule of mixtures and a strain analysis show the 50 percent volume fraction Ti-3Al-2.5V laminate to have nearly identical compression strength with the 45 percent volume fraction laminate using the Ti-6Al-4V matrix as reported in Reference [3]. Therefore, the value of $(F_{cu})_{xx} = 690$ ksi may be accepted as a typical compression strength of the laminates and specimens described in this paper. Average values for two strain gages are shown in Table III for the compression modulus, $(E_c)_{xx}$.

Table II. Borsic-Ti Material Properties

TENSILE MODULUS

$E_{xx} = 33 \times 10^6$ psi (TRW data)

$E_{yy} = 23 \times 10^6$ psi* (TRW data)

COMPRESSION MODULUS

$(E_c)_{xx} = 38.5 \times 10^6$ psi* (CAD data from angle test specimens)

SHEAR MODULUS

$G_{xy} = 11.25 \times 10^6$ psi

COMPRESSION STRENGTH

$(F_{cu})_{xx} = 690{,}000$ psi*, Reference [3]

TENSILE STRENGTH

$(F_{tu})_{xx} = 170{,}000$ psi (TRW data)

POISSON'S RATIO

$\nu_{xy} = 0.25$*, Reference [3]

$\nu_{yx} = 0.17$*, Reference [3]

DENSITY

$\rho = 0.125$ lbs/in.^{3} (TRW data)

*Values used to define empirical equations

Table III. Compression Modulus of Elasticity from Strain Gage Data, Borsic-Ti Angles

b'/t	Compression Modulus of Elasticity, $(E_{cc})_{xx}$, psi
9.4	36.8×10^6
9.2	40.5×10^6
13.8	38.8×10^6
13.7	39.7×10^6
14.1	36.5×10^6
19.5	38.0×10^6
19.1	39.2×10^6
Average $(E_c)_{xx} = 38.5 \times 10^6$ psi	

TEST PROCEDURE AND INSTRUMENTATION

All tests were performed at room temperature on a 10,000-pound Instron test machine. Although the specimens were found to be flat and parallel on the loaded ends, an aluminum plate was placed between the specimen ends and the loading head of the test machine to ensure a uniformly distributed load. The cross-head speed was 0.05 inch/minute for all tests and load-deformation curves were continuously plotted on the Instron chart recorder to ascertain the peak load for crippling definition.

Specimen instrumentation consisted of two back-to-back axial strain gages at the edge of one outstanding leg and located in the center of the specimen lengthwise. Each strain gage was read separately and continuously recorded on an X-YY recorder to determine the point of initial buckling and provide data in the elastic range for compression modulus of elasticity definition.

BUCKLING ANALYSIS

Buckling data from eleven specimens were utilized to determine the initial buckling characteristics of the outstanding legs of the angle specimens. These included three specimens at $b'/t = 9$, three at $b'/t = 14$, three at $b'/t = 19$, and two at $b'/t = 29$. See Figure 4 for the definition of b'/t which allows for equal or unequal leg angles according to Reference [5]. The definition of buckling stress was determined from the two back-to-back strain gages mounted longitudinally at the outer edge of one leg of the angle. Figure 5 shows typical curves obtained from the two strain gages with strain plotted versus applied load for a specimen with $b'/t = 19.1$. These curves illustrate the linear variation up to initial buckling and the strain reversal as the crippling load is approached. For a more precise definition of the initial buckling stress the bending strain (Δe), as shown in Figure 5, is plotted in Figure 6 versus the applied compression stress. Two typical curves are shown, one for $b'/t = 14.1$ and one for $b'/t = 19.1$, with the initial buckling stress defined by $(F_{cr})_{xx}$. This procedure was followed for each of the applicable specimens. In the higher b'/t ranges the strain gage data were somewhat erratic due to initial waviness or slight eccentricities and were not considered reliable. Using the above definition of buckling stress from the experimental data the buckling

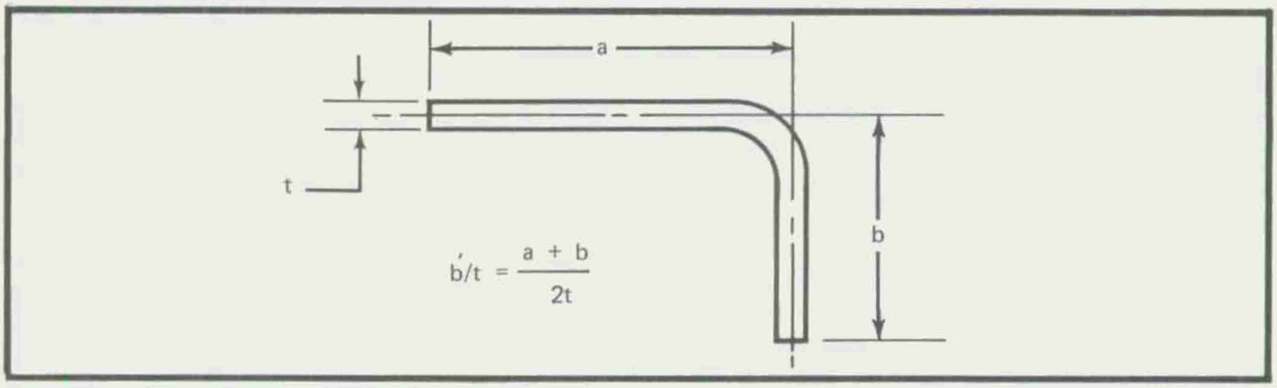

Figure 4. b'/t Definition for Angles

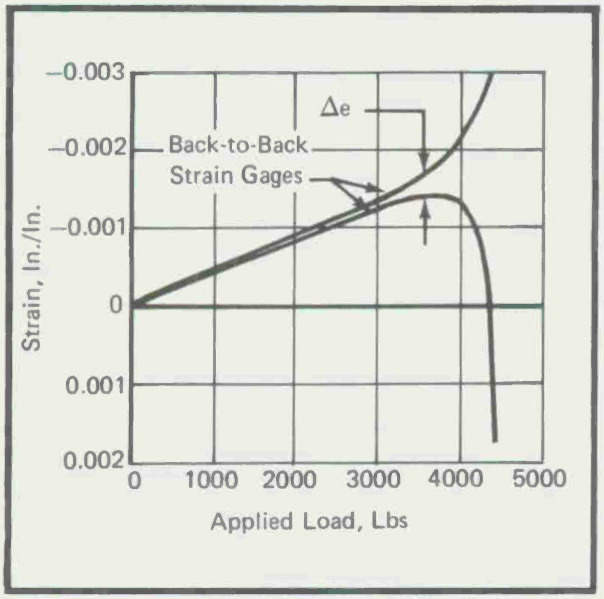

Figure 5. Critical Buckling Load Definition, $b'/t = 19.1$, Borsic-Ti Angles

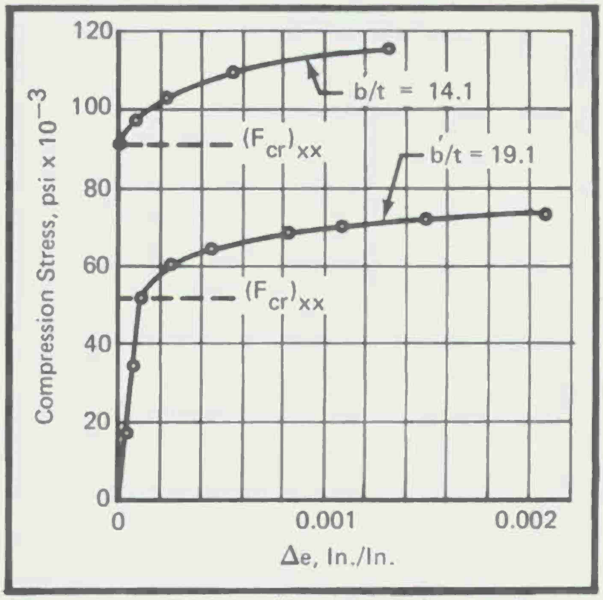

Figure 6. Initial Buckling Stress by Strain Difference Method, Borsic-Ti Angles

stresses were plotted versus b'/t on a log-log plot as shown in Figure 7. For buckling of isotropic materials this results, basically, in a linear plot. Therefore, it is interesting to note from Figure 7 that the data from the orthotropic Borsic-Ti angle legs indicated a linear relationship. With this assumption a least squares fit of the data produced the straight line in Figure 7 defined by the general equation

$$(F_{cr})_{xx} = (4.71 \times 10^6)\,(t/b')^{1.523} \tag{1}$$

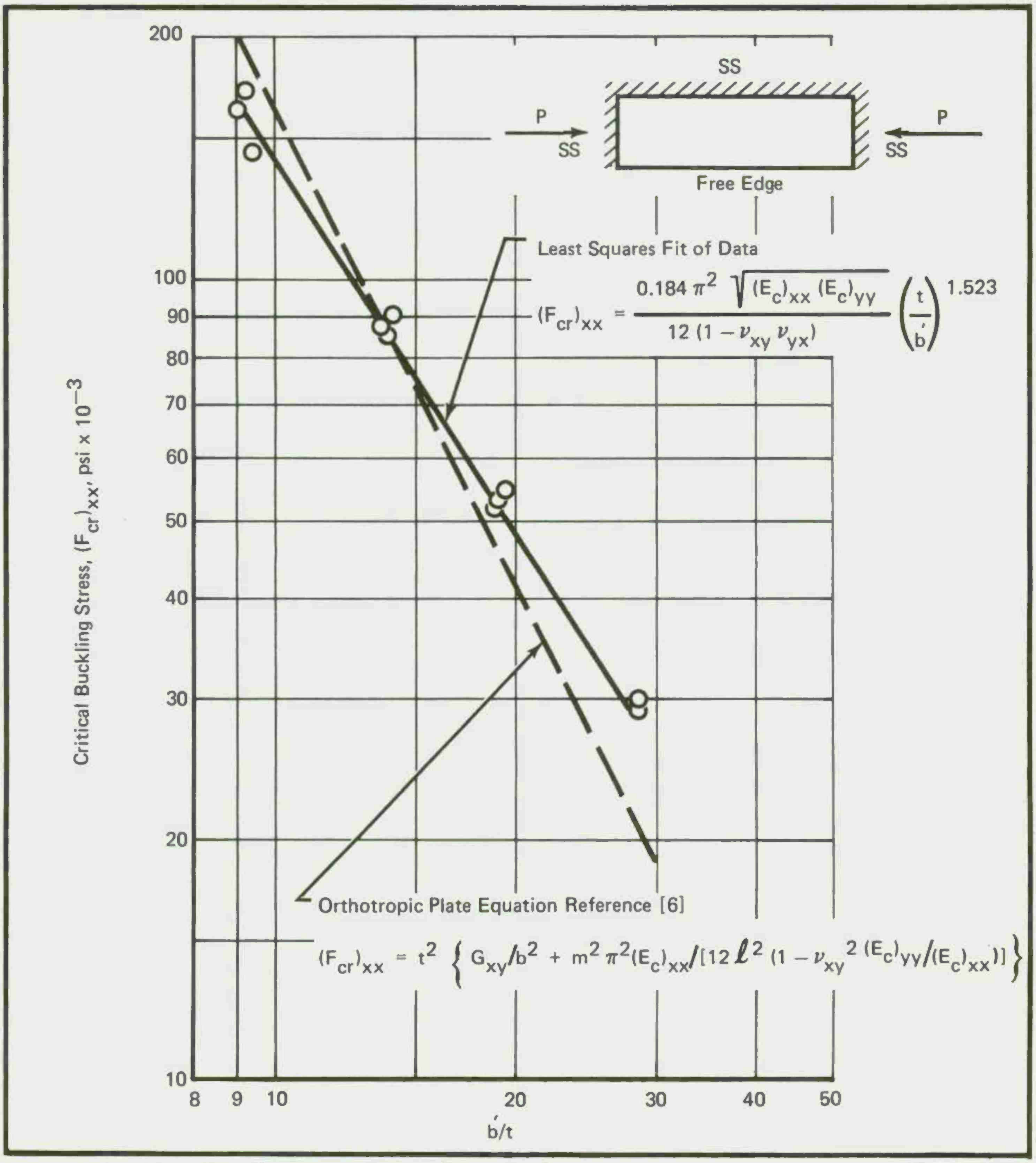

Figure 7. Buckling Data for Borsic-Ti Equal Leg Angles

However, to allow more general use of the buckling equation for elevated temperature or improvements in material properties, a form of the equation is defined which is equivalent to the isotropic plate buckling equation where

$$(F_{cr})_{xx} = \frac{k\,E\,\pi^2}{12\,(1-\nu^2)} \left(\frac{t}{b}\right)^n . \tag{2}$$

Substituting $E = \sqrt{(E_c)_{xx}\,(E_c)_{yy}}$ and $\nu^2 = \nu_{xy}\,\nu_{yx}$ with $n = 1.523$ the equation for Borsic-Ti plates with one edge free becomes

$$(F_{cr})_{xx} = \frac{0.184\,\pi^2 \sqrt{(E_c)_{xx}\,(E_c)_{yy}}}{12\,(1-\nu_{xy}\,\nu_{yx})} \left(\frac{t}{b}\right)^{1.523} \tag{3}$$

to fit the data of Figure 7. Note that the buckling coefficient, k, apparently has a value of 0.184. For isotropic materials this value is highly dependent on the aspect ratio of the plate. However, for the dimensions of the outstanding legs of the test angles there was very little difference in the aspect ratio. Therefore, no inference can be drawn on the variation of the buckling coefficient, k, with aspect ratio and the value of 0.184 is adequate for all test specimens.

For comparison in Figure 7 the orthotropic plate buckling equation from Reference [6] was selected for comparison. This equation is recommended by Reference [7]. From Reference [6] the buckling load per inch on a plate with one edge free and three sides simply supported is defined by

$$N_{xx} = t^3 \left\{ G_{xy}/b^2 + m^2\,\pi^2\,(E_c)_{xx}/[12\,\ell^2\,(1-\nu_{xy}^2\;(E_c)_{yy}/(E_c)_{xx})] \right\} \tag{4}$$

where m is the number of half-waves in the x-direction. Thus, the smallest buckling load in Equation (4) is defined with m = 1. From Equation (4) the initial buckling stress according to Reference [6] would be

$$(F_{cr})_{xx} = t^2 \left\{ G_{xy}/b^2 + \pi^2\,(E_c)_{xx}/[12\,\ell^2\,(1-\nu_{xy}^2\;(E_c)_{yy}/(E_c)_{xx})] \right\} . \tag{5}$$

This equation appears to be somewhat unconservative at $b/t \lesssim 14$ and conservative at $b/t > 14$ based on the present test data shown in Figure 7.

For a summary of the buckling loads and stresses, refer to Table IV which also defines the post-buckling strength of the specimens.

Table IV. Buckling/Crippling Test Summary, Borsic-Ti Equal Leg Angles

b'/t	Area, in.^{2}	Buckling Load, $(P_{cr})_{xx}$, lbs	Initial Buckling Stress, $(F_{cr})_{xx}$, psi	Failing Load, $(P_{cc})_{xx}$, lbs	Crippling Stress $(F_{cc})_{xx}$, psi	$(F_{cc})_{xx}/(F_{cr})_{xx}$
9.4	0.0280	3,985	142,305	5,420	193,600	1.360
9.2	0.0279	4,719	169,155	6,000	215,100	1.271
9.0	0.0257	4,117	160,205	5,320	207,000	1.292
13.8	0.0414	3,490	84,309	4,830	116,700	1.384
13.7	0.0417	3,590	86,099	4,890	117,300	1.362
14.1	0.0412	3,669	89,052	4,860	118,000	1.325
19.0	0.0573	2,948	51,462	4,450	77,700	1.509
19.5	0.0573	3,128	54,595	4,320	75,400	1.381
19.1	0.0583	3,047	52,268	4,440	76,200	1.457
28.7	0.0915	2,625	28,683	4,650	50,800	1.771
28.7	0.0906	2,685	29,635	4,900	54,100	1.825
28.7	0.0902	*	*	4,900	54,300	---
39.5	0.1180	*	*	4,620	39,200	---
39.7	0.1193	*	*	4,720	39,600	---
38.6	0.1228	*	*	4,800	39,200	---

*Erratic strain gage results produced by slight eccentricities or waviness of the outstanding legs.

CRIPPLING ANALYSIS

The test data obtained from the fifteen angle specimens are summarized in Table IV and plotted in Figure 8. This figure shows a log-log plot of crippling stress, $(F_{cc})_{xx}$, versus b'/t to determine linearity for equation definition. It is obvious from Figure 8 that a single linear equation would not represent the data satisfactorily, but it appears that a two-piece linear representation would be quite adequate. Therefore, it is necessary to define two different equations, one for each linear segment. From Reference [5] each linear segment is represented by a least squares fit equation of the form

$$(F_{cc})_{xx} = K/(b'/t)^m. \tag{6}$$

Two least squares solutions were performed. The low b'/t segment utilized nine data points for b'/t = 9, 14, and 19. The higher b'/t segment used nine data points for b'/t = 19, 29, and 39 where exact failing stresses and b'/t values were used in the least squares solution. The least squares solution equations in the form of Equation (6) are

$$\left.\begin{aligned} (F_{cc})_{xx} &= \frac{K}{(b'/t)^{1.34}} = \frac{4.01 \times 10^6}{(b'/t)^{1.34}} \qquad \text{(lower } b'/t \text{ range)} \\ \text{and} \\ (F_{cc})_{xx} &= \frac{K}{(b'/t)^{1.027}} = \frac{1.655 \times 10^6}{(b'/t)^{1.027}} \qquad \text{(higher } b'/t \text{ range).} \end{aligned}\right\} \tag{7}$$

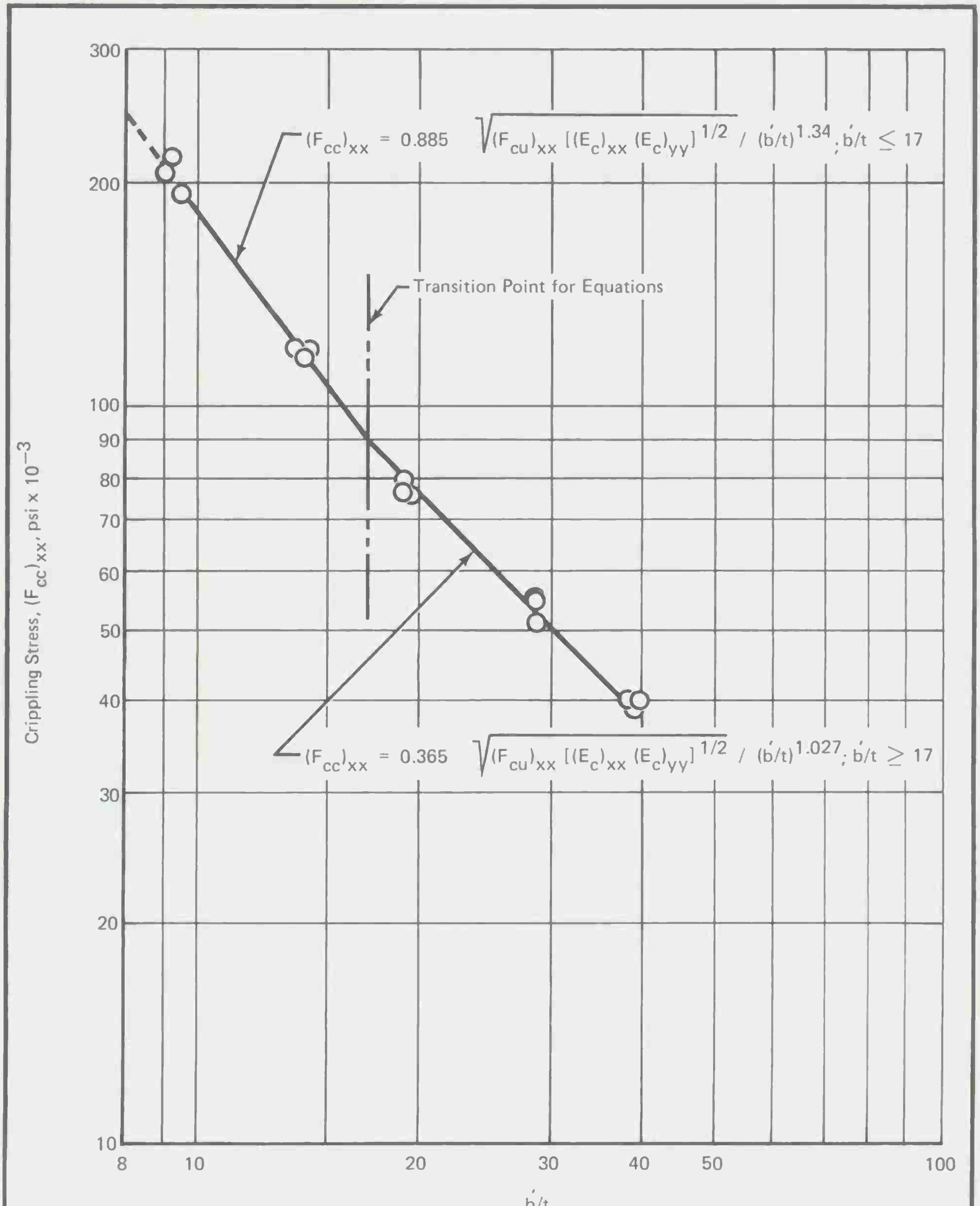

Figure 8. Crippling Data for Borsic-Ti Equal Leg Angles

Equating Equations (6) and (7) leads to the intersection point

$b'/t = 17$ and $(F_{cc})_{xx} = 90{,}500$ psi.

The basic empirical equations for crippling stress for the Borsic-Ti angles are

$$\left.\begin{aligned} (F_{cc})_{xx} &= \frac{4.01 \times 10^6}{(b'/t)^{1.34}}\,; \quad b'/t \leq 17 \\ &\text{and,} \\ F_{cc} &= \frac{1.655 \times 10^6}{(b'/t)^{1.027}}\,; \quad b'/t \geq 17. \end{aligned}\right\} \tag{8}$$

Although Equation (8) is sufficient to determine the crippling stress for any b'/t value at room temperature, the equations are not sufficiently general to allow for elevated temperature properties or improvements in material properties for the Borsic-Ti. Therefore, the procedures of Needham [5] are utilized to provide a more general equation which includes material property parameters.

In Equation (6) the form of K is based on the effective width equations of von Kármán [8] and Marguerre [9] where the proposed form for K is

$$K = C \sqrt[m]{f_{se}^{\,m-1}\, E}. \tag{9}$$

Since m was selected as 2 for isotropic materials it will also be assumed to be effective for the metal matrix materials. From References [8] and [9] f_{se} is the stress at the junction of flat plate elements and ordinarily would be selected as the compression yield stress, F_{cy}, for isotropic materials. However, metal matrix materials do not possess an offset yield stress and some other reasonable value must be selected. Spier [10] essentially uses $(F_{tu})_{xx}$ as a value of f_{se} for boron-Al but there is no justification for this value other than the fact that no compression data were available. Also, since a stress-strain curve for metal matrix materials is essentially straight a yield point would be very difficult to define. This leads to the conclusion that a compression ultimate stress, $(F_{cu})_{xx}$, would be a logical choice in place of the F_{cy} used for isotropic materials. Furthermore, the general equations are intended for extension to elevated temperature use and for improvements in material properties. This dictates that a representative compression strength value such as $(F_{cu})_{xx}$ be used since the variation of $(F_{cu})_{xx}$ with temperature may well be different than the variation of $(F_{tu})_{xx}$ with temperature. Therefore, the value of f_{se} in Equation (9) is replaced with a value for $(F_{cu})_{xx}$. From Reference [10] the value of E in Equation (9) can be replaced by

$$E = \sqrt{(E_c)_{xx}\,(E_c)_{yy}}. \tag{10}$$

Substituting $(F_{cu})_{xx}$, $m = 2$, and Equation (10) into Equation (9) yields

$$K = C \sqrt{(F_{cu})_{xx} \left[(E_c)_{xx} (E_c)_{yy}\right]^{1/2}} . \tag{11}$$

The values of the coefficient, C, are defined by Equation (11) for the two linear portions of the curve ($b'/t \leq 17$ and $b'/t \geq 17$). The material properties used are $(F_{cu})_{xx} = 690{,}000$ psi, $(E_c)_{xx} = 38.5 \times 10^6$ psi, and $(E_c)_{yy} = E_{yy} = 23 \times 10^6$ from Table II. With $K = 4.01 \times 10^6$ for $b'/t \leq 17$ and $K = 1.655 \times 10^6$ for $b'/t \geq 17$ the values of the coefficients are

$$\left.\begin{aligned} C &= 0.885, \; b'/t \leq 17 \\ C &= 0.365, \; b/t \geq 17. \end{aligned}\right\} \tag{12}$$

Substituting the values of C from Equation (12) into Equation (11) and hence into Equation (7) yields the general equations

$$\left.\begin{aligned} (F_{cc})_{xx} &= 0.885 \sqrt{(F_{cu})_{xx} \left[(E_c)_{xx}(E_c)_{yy}\right]^{1/2}} \; / \; (b'/t)^{1.34}; \; b'/t \leq 17 \\ (F_{cc})_{xx} &= 0.365 \sqrt{(F_{cu})_{xx} \left[(E_c)_{xx}(E_c)_{yy}\right]^{1/2}} \; / \; (b'/t)^{1.027}; \; b'/t \geq 17. \end{aligned}\right\} \tag{13}$$

A test data summary is presented in Table IV where an indication of the high post-buckling strength of Borsic-Ti is shown in the last column. Photographs of the failed specimens are shown in Figure 9. All failures were indicated by the Instron chart recorder as the peak load was reached. All specimens except those at $b'/t = 10$ exhibited excellent resiliency and no transverse cracks or delaminations were observed after unloading from the peak load. Some local failures and lateral

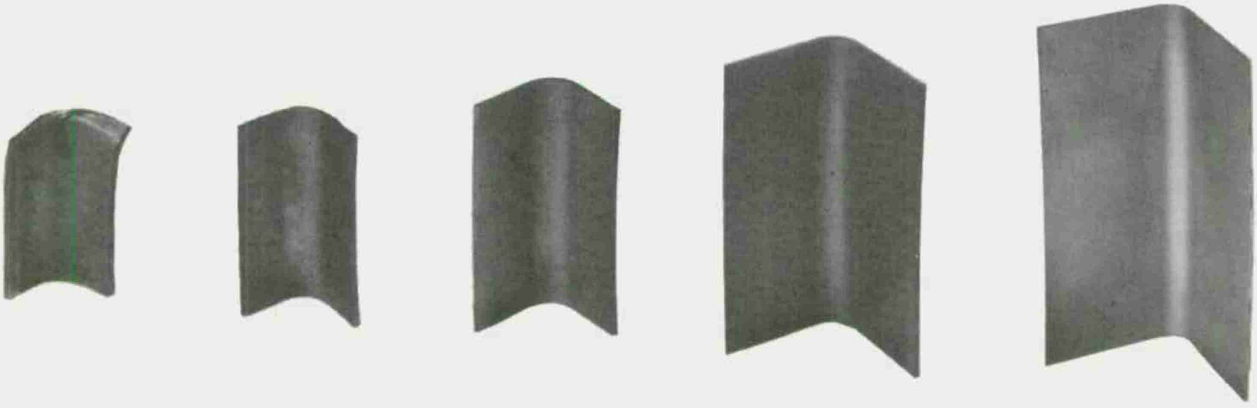

$b'/t = 10$ $b'/t = 15$ $b'/t = 20$ $b'/t = 30$ $b'/t = 40$

Figure 9. Typical Failed Borsic-Ti Angle Test Specimens

instability were observed, however, in those specimens with $b'/t = 10$. Some permanent buckles were observed in the larger b'/t specimens but no sharp wrinkling or catastrophic failures were in evidence. Post-buckling strength and failures were similar to isotropic materials except for the sudden catastrophic failures common to isotropic metal crippling failures. This difference is believed to be due to the high stiffness, high strength, and lack of a definite yield point for the Borsic filaments.

A comparison with the boron-Al data of Spier [10], and Otto and Bohlmann [11] is shown in Figure 10. These metal matrix materials exhibit greater efficiency than the best of the isotropic metals in present use as shown in Figure 11. In this figure the clear superiority of Borsic-Ti is shown when used in a unidirectional compression load application throughout a wide range of b'/t.

Recognizing the quasi-isotropic behavior of the Borsic-Ti angle test specimens leads to the conclusion that the data presented herein could be readily extended to tubes, V-groove plates, multicorner sections, and stiffened panels using the "g-correlation" scheme of Gerard [12]. This would only require fitting Gerard's basic crippling equation to the two linear portions of the curve presented in Figure 8.

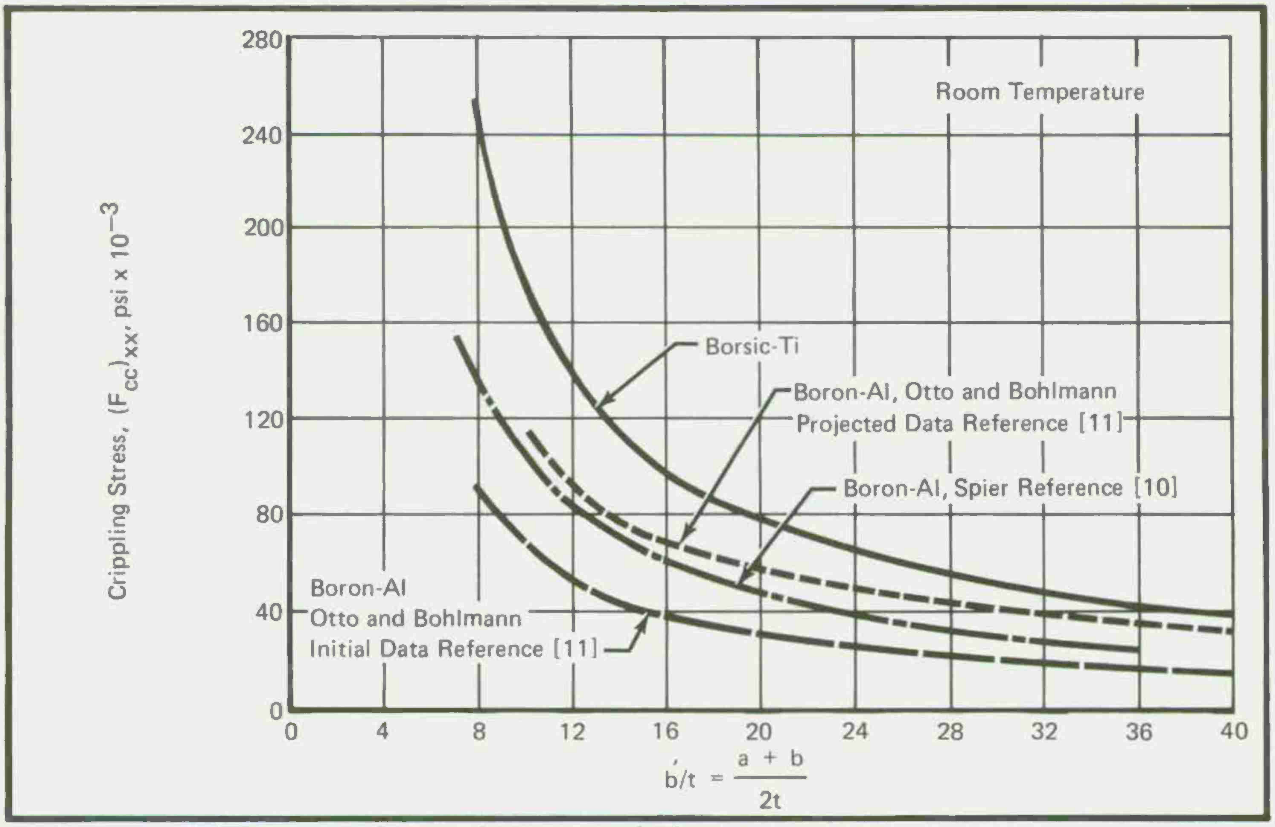

Figure 10. Crippling Stresses for Metal Matrix Angle Sections

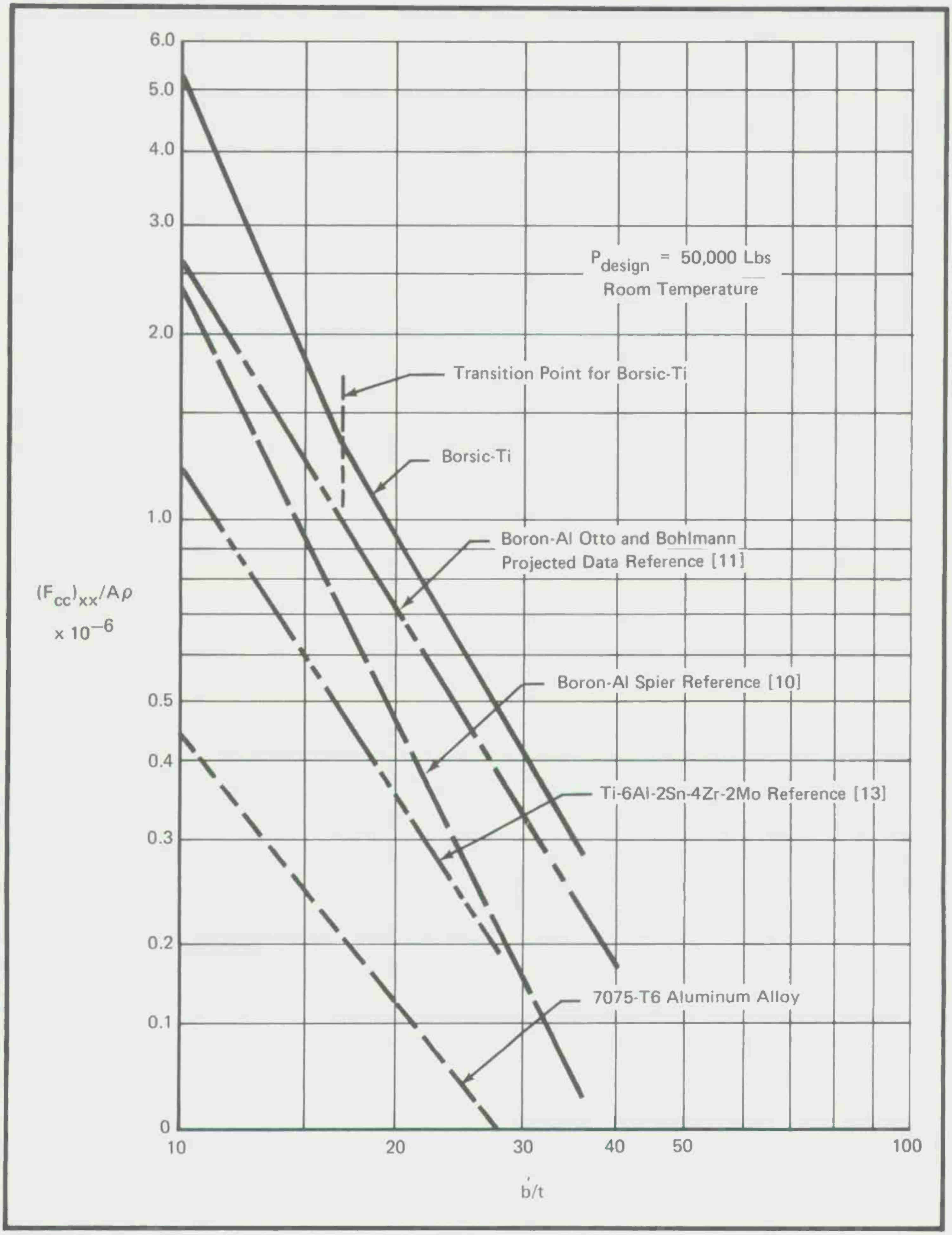

Figure 11. Material Comparison for Crippling of Equal Leg Angles

CONCLUSIONS

In summary, a high degree of post-buckling strength is present in unidirectional Borsic-Ti without requiring cross-plying or interleaving titanium foil. This capability is attributed to the high interlaminar shear strength and high transverse strength of the titanium matrix. The empirical equations presented for buckling and crippling utilized appropriate available mechanical property data at room temperature and are considered adequate for extension to elevated temperature application and improvements in the basic material properties. For the most accurate use at elevated temperature the best procedure is to use a curve of percent room temperature $(F_{cu})_{xx}$ versus temperature with the value at room temperature taken as $(F_{cu})_{xx} = 690$ ksi since this value was used in the equation for crippling. Using this procedure, neither the equation constant nor exponent would be affected which allows direct use of the equation presented herein. Tentatively, it may be recommended that the data presented may be used with the "g-correlation" scheme of Gerard [12] for extension to other formed shapes.

It is, therefore, recommended that some further effort investigate the extension to high temperature application and to more practical formed shapes as well as V-grooved plates.

ACKNOWLEDGEMENT

The authors gratefully acknowledge the support of the Rockwell International Corporation—Columbus Aircraft Division and the Materials Technology Division of TRW, Inc.

REFERENCES

1. Spier, E. E. and G. Wang, "On Buckling of Unidirectional Boron/Aluminum Stiffeners," J. Composite Materials, Vol. 9, October 1975, p 347.

2. Doble, G. S., P. Melnyk, and I. J. Toth, "Manufacturing Methods for Filamentary Reinforced Titanium Monotape," AFML-TR-74-14, January 1974.

3. Hofer, K. E., N. Rao, and D. Larsen, Development of Engineering Data on the Mechanical and Physical Properties of Advanced Composites Materials, AFML-TR-72-205, Part II, February 1974.

4. Kreider, K. C., "Mechanical Testing of Metal-Matrix Composites," ASTM STP 460, p 203, 1969.

5. Needham, R. A., The Ultimate Strength of Aluminum-Alloy Formed Structural Shapes in Compression, Journal of the Aeronautical Sciences, Vol. 21, No. 4, April 1954.

6. Halston Jr., A., Buckling of Orthotropic Plates with One Edge Free, AIAA Journal, Vol. 8, No. 7, July 1970.

7. Advanced Composites Design Guide; Volume II, Analysis, Third Edition, January 1973.

8. von Kármán, Th., E. E. Sechler, and L. H. Donnell, The Strength of Thin Plates in Compression, ASME Trans., APM-54-5, Vol. 54, No. 2, June 30, 1932.

9. Marguerre, K., The Apparent Width of the Plate in Compression, NACA TM No. 833, July, 1937.

10. Spier, E. E., Crippling Analysis of Unidirectional Boron/Aluminum Composites in Compression Structures, Proceedings of the First Air Force Conference on Fibrous Composites in Flight Vehicle Design, AFFDL-TR-72-130, Dayton, Ohio, September 1972.

11. Otto, O. R., and R. E. Bohlmann, Boron Aluminum Crippling Strength Shows Improvement, AIAA Paper No. 74-378, AIAA/ASME/SAE 15th Structures, Structural Dynamics and Materials Conference, Las Vegas, Nevada, April 17–19, 1974.

12. Gerard, G., The Crippling Strength of Compression Elements, Journal of the Aeronautical Sciences, Vol. 25, No. 1, January 1958.

13. Gehring, R. W., Crippling Allowables for Elevated Temperature and Creep Environments, AIAA Paper No. 73-388, AIAA/ASME/SAE 14th Structures, Structural Dynamics, and Materials Conference, Williamsburg, Virginia, March 20–22, 1973.

POST BUCKLING BEHAVIOR OF GRAPHITE/EPOXY LAMINATED PLATES AND CHANNELS

EDWARD E. SPIER
Design Specialist
General Dynamics Convair Division
San Diego, California

FREDRIK L. KLOUMAN
Research Engineer
Norwegian Defence Research Establishment
Kjeller, Norway

ABSTRACT

During a series of compression tests, post buckling behavior was observed of A-S/3501 graphite/epoxy laminated plates and channels; layups were $[\pm 45_A/0_B/\mp 45_A]_T$ for B/A ratios of two, four, and six. These laminates spanned practical configurations for plate elements of stiffeners. Plates and channels were designed for a crippling test program in which the loaded ends of the test specimens were clamped, and the unloaded edges of the plates were simply-supported. Post buckling behavior of the laminated plates was surprisingly analogous to that of isotropic metal plates.

NOMENCLATURE

b = Width of plate
b_f = Width of channel flange measured to mid-surface of channel web
b_w = Width of channel web measured to mid-surfaces of channel flanges
B = Number of 0-degree plies in laminate
L = Free length of laminated specimen before mounting in end blocks
L' = Effective column length
P^{cc} = Ultimate or crippling load
P^{cr} = Classical theoretical linearly elastic buckling load
P_i^{cr} = Incipient buckling load
t = Mean thickness of laminated plate or channel
ρ_{min} = Minimum radius of gyration of channel cross-section

INTRODUCTION

Compression testing of graphite/epoxy laminated plates and channels was performed to obtain post buckling characteristics and determine ultimate or crippling strength [1] of these structures. In this research, the behavior of the plates and channels is observed at and beyond the point of incipient buckling; further, the incipient buckling value is compared with that predicted by the elastic buckling theory, used widely for estimating the buckling strengths of graphite/epoxy plates and channels.

EXPERIMENTAL PROCEDURE

Dimensions of flat plate test specimens are given in Figure 1. Figure 2 shows one of the longer specimens in the test fixture with the loaded ends potted in aluminum blocks and unloaded edges supported in the V-grooves of steel plates (Figure 3). Unloaded edges are considered to be simply-supported if the test specimen is free to move in the loaded direction without friction in the blocks; the blocks, then, prevent lateral movement of unloaded edges to the point of incipient buckling. Beyond this point, warping of the specimen could occur, resulting in some lateral movement of the unloaded edges. After the V-groove plates are adjusted to the edges of the specimen, clamp-down bolts secure them in place. Plate length is approximately four times the width. Two sizes of plate test specimens are shown in Figure 4.

Figure 5 gives the dimensions of channel test specimens whose ends are potted in aluminum blocks. The slenderness ratios (L'/ρ_{min}) of channel test specimens are approximately equal to 12, which is the ratio required for a crippling test. Moreover, the value ρ_{min}/b_f (maintained at about one-third) is the approximate value when $b_f/b_w > 0.3$. The two common channel sizes are shown in Figure 6. A-S/3501 graphite/epoxy was used exclusively in the test program with the following three laminates.

$$[\pm 45_2/0_4/\mp 45_2]_T$$

$$[\pm 45_2/0_8/\mp 45_2]_T$$

$$[\pm 45_2/0_{12}/\mp 45_2]_T$$

These three laminates are most appropriate for the plate elements of stiffeners. End blocks are loaded directly by the testing machine platens, thus simulating clampled-end conditions for both plates and channels.

TEST RESULTS FOR THE PLATES

Compression test results for graphite/epoxy laminated plates with simply-supported, unloaded edges are presented in Table 1. Values for P^{cr} were computed using equations presented by the authors[1]. Values for P_i^{cr} indicate that in all cases, the theoretical buckling load was unconservative; values for P^{cc}/P^{cr} show that in certain tests, the ultimate loads were less than the corresponding theoretical elastic buckling loads, exposing the futility of using classical buckling theory for laminated plates.

In Figures 7, 8, and 9, specimen displacement is plotted against machine load. In each figure, the slope of the load displacement curve suddenly drops to about one half at the point of incipient buckling. This same behavior was observed in orthotropic laminated plates by Harris[2] and in metal plates by Stein [3]. Stein's experiments agree quite well with his plate buckling analyses in which a set of linear equations yield accurate results in simple form. In the authors' analysis[1] equations were derived from classical, closed-form orthotropic elastic buckling theory of plates.

Figure 10 shows one of the longer plates loaded in compression; the post buckling pattern (four half waves with amplitudes of several times the thickness) is typical of the longer specimens. The C-clamp applies light pressure against the V-blocks, preventing deflection caused by warping of the test specimen. For shorter specimens, V-blocks require no additional support, and buckling patterns are less pronounced.

Figure 11 shows the same test specimen after failure. The failure appears to start at the point of contact with the V-block, and then the crack in the outer 45-degree ply propagates toward the center of the specimen. For many specimens, this failure is typical, but some specimens failed by transfer shear cracks through the thickness along a line of contact with the V-blocks. In all cases, some delamination occurred somewhere along at least one of the edges in contact with the V-block. None of the failures, however, are considered catastrophic. Ultimate compressive strengths of the laminates, reported in Reference 1, were determined by the authors[4] by testing small specimens in the compression fixture and by testing Celanese specimens. All tests resulted in catastrophic failures.

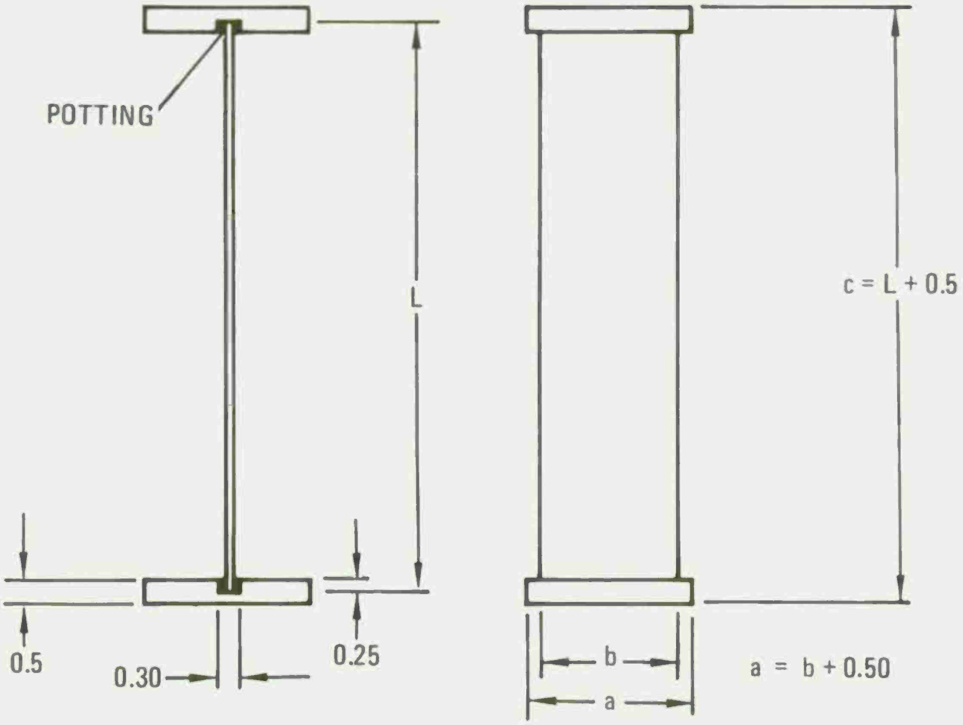

DIMENSION (IN.)		SPECIMENS
b	2.00	2, 4, 6
L	8.00	
b	3.00	1, 3, 5
L	12.00	

Figure 1. Plate test specimens.

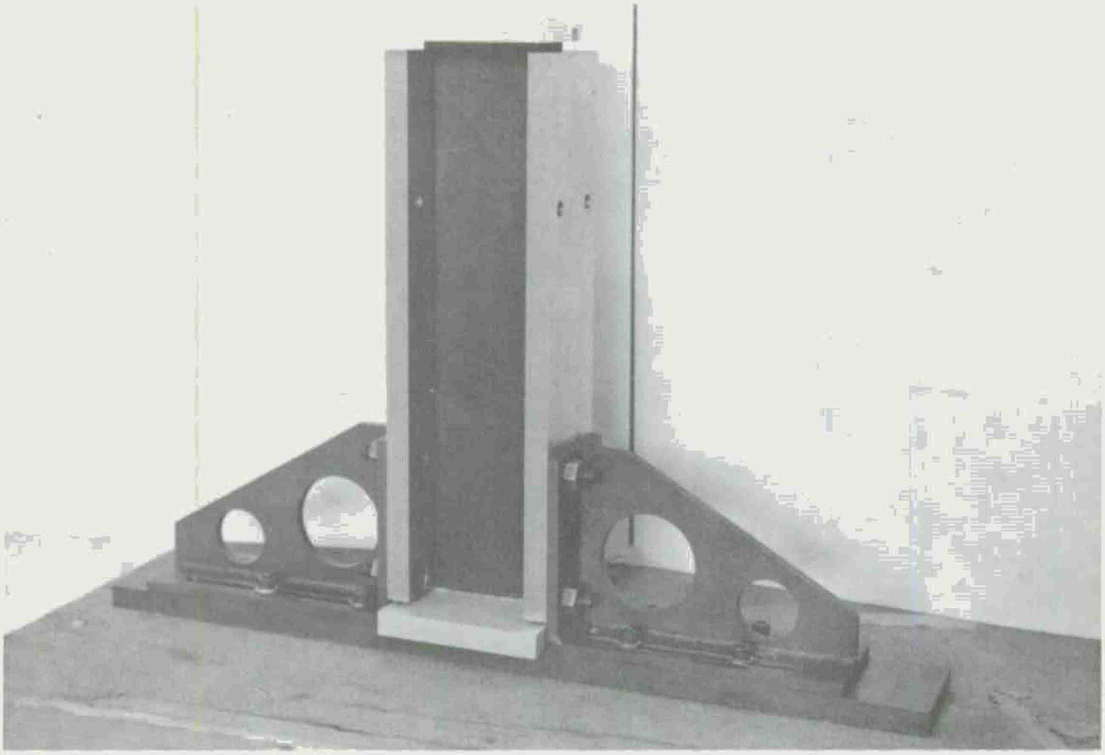

Figure 2. Flat plate specimen in compression fixture.

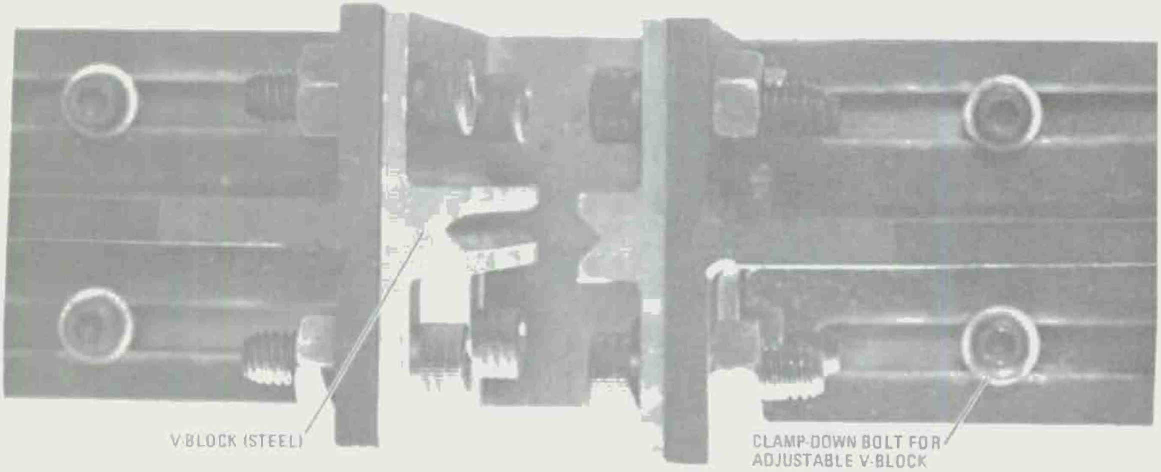

V-BLOCK (STEEL)
CLAMP-DOWN BOLT FOR ADJUSTABLE V-BLOCK

Figure 3. View of V-blocks in plate compression fixture.

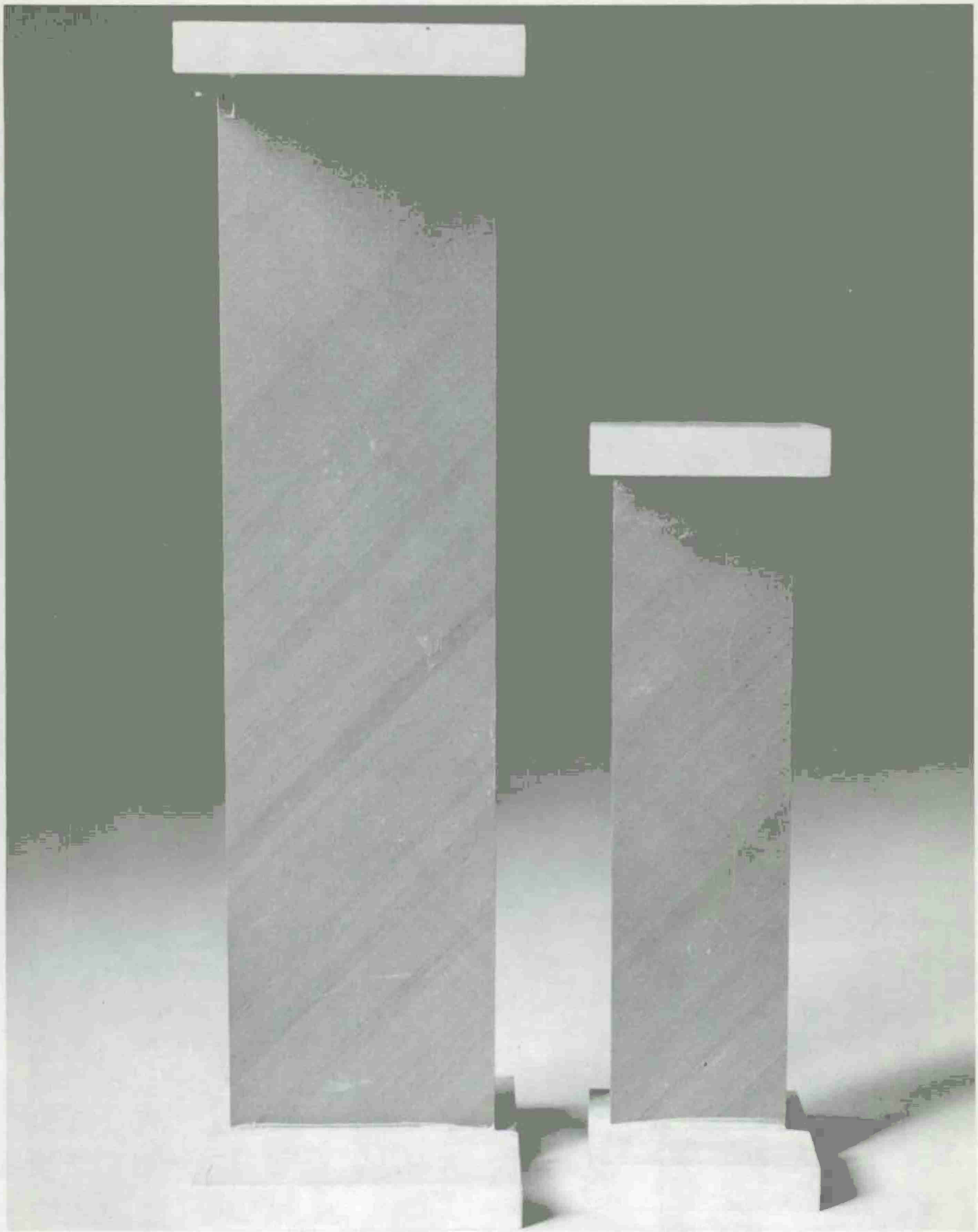

Figure 4. Two sizes of flat plate compression test specimens.

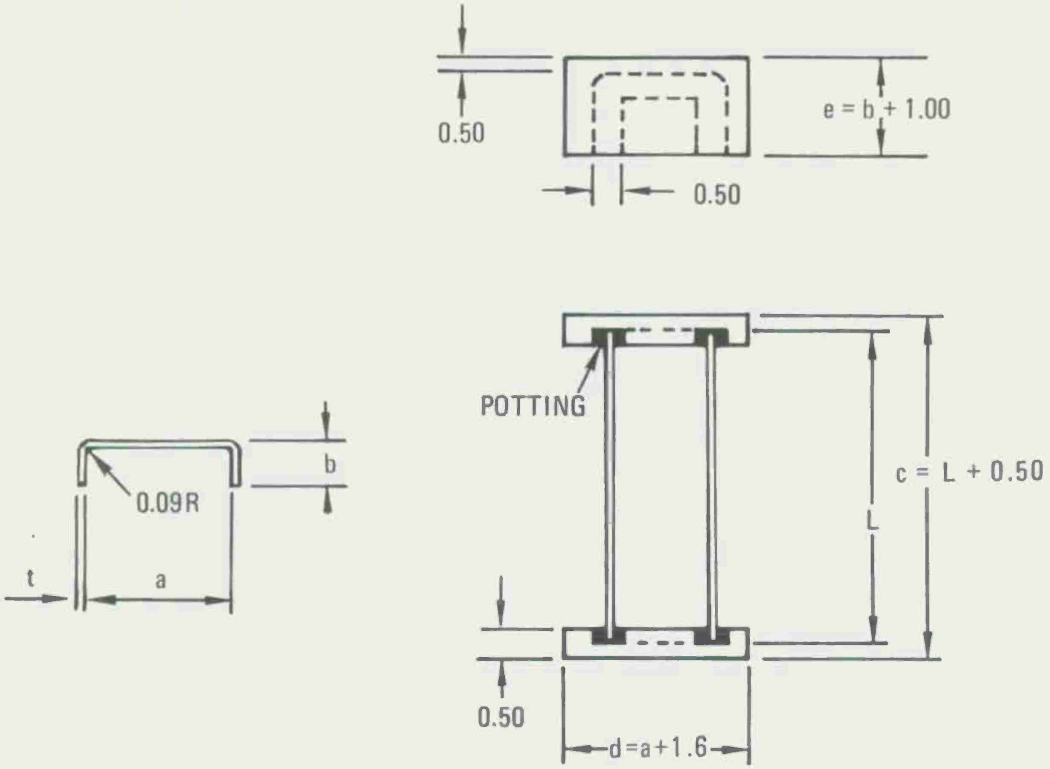
0.50
e = b + 1.00
0.50
POTTING
b
0.09R
t
a
c = L + 0.50
L
0.50
d=a+1.6

DIMENSION (IN.)		SPECIMENS
a	2.55	14, 18, 22
$(b - \frac{t}{2})$	0.75	
L	5.25	
a	5.17	16, 20, 24
$(b - \frac{t}{2})$	1.50	
L	10.50	

Figure 5. Channel specimens.

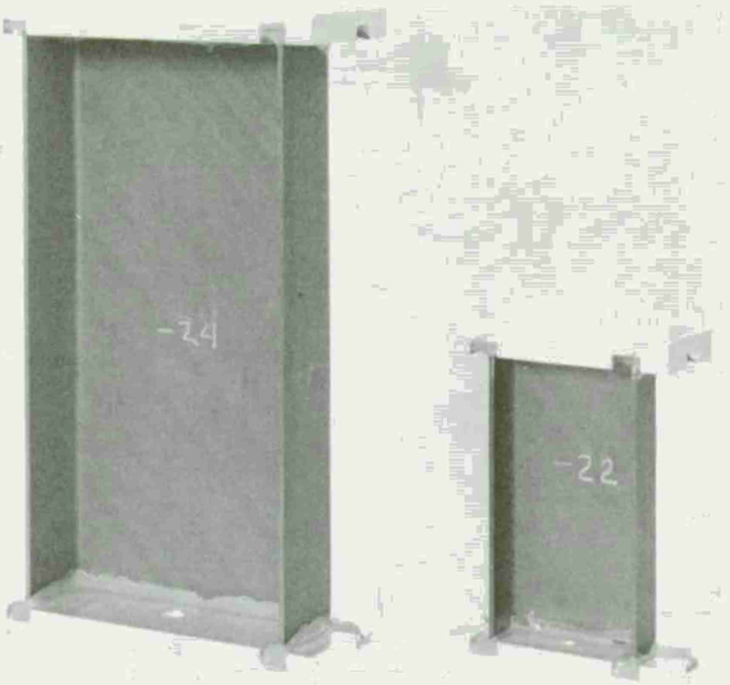

Figure 6. Typical channel compression test specimens.

Table 1. Compression test results of $[\pm 45_2/0_B/\mp 45_2]_T$ *laminated plates.*

Geometry							Theoretical Buckling	Test Results			
Specimen No.	v/o %	B	L (in.)	b (in.)	t (in.)	$\frac{b}{t}$	P^{cr} (lb)	P_i^{cr} (lb)	P_i^{cr}/P^{cr}	P^{cc} (lb)	P^{cc}/P^{cr}
2A	60	4	8	2.002	0.0630	31.75	3,990	3,000	0.75	3,570	0.89
2B	60	4	8	2.001	0.0642	31.17	4,220	3,250	0.77	4,260	1.01
2C	60	4	8	2.002	0.0617	32.45	3,745	3,250	0.87	4,115	1.10
4A	65	8	8	2.001	0.0838	23.88	9,010	6,300	0.70	7,680	0.85
4B	65	8	8	2.001	0.0821	24.38	8,470	6,400	0.76	7,500	0.88
4C	65	8	8	2.007	0.0849	23.64	9,340	6,350	0.68	7,175	0.77
6A	65	12	8	2.001	0.1030	19.43	15,940	10,200	0.64	11,360	0.71
6B	65	12	8	2.001	0.1052	19.02	16,985	10,300	0.61	12,300	0.72
6C	65	12	8	2.004	0.1031	19.44	15,960	12,400	0.78	13,125	0.82
1A	60	4	12	3.000	0.0644	46.58	2,840	2,300	0.81	3,900	1.37
1B	60	4	12	3.010	0.0644	46.74	2,830	1,900	0.67	4,070	1.44
1C	60	4	12	3.000	0.0642	46.73	2,815	2,250	0.80	4,375	1.55
3A	65	8	12	3.000	0.0836	35.89	5,965	5,100	0.85	7,800	1.31
3B	65	8	12	3.000	0.0867	34.60	6,655	5,200	0.78	7,400	1.11
3C	65	8	12	3.000	0.0860	34.88	6,495	5,700	0.88	7,100	1.09
5A	65	12	12	3.000	0.1057	28.38	11,495	9,250	0.80	11,550	1.00
5B	65	12	12	3.000	0.1066	28.14	11,790	10,400	0.85	12,250	1.04
5C	60	12	12	3.000	0.0980	30.60	9,170	8,000	0.87	11,825	1.29

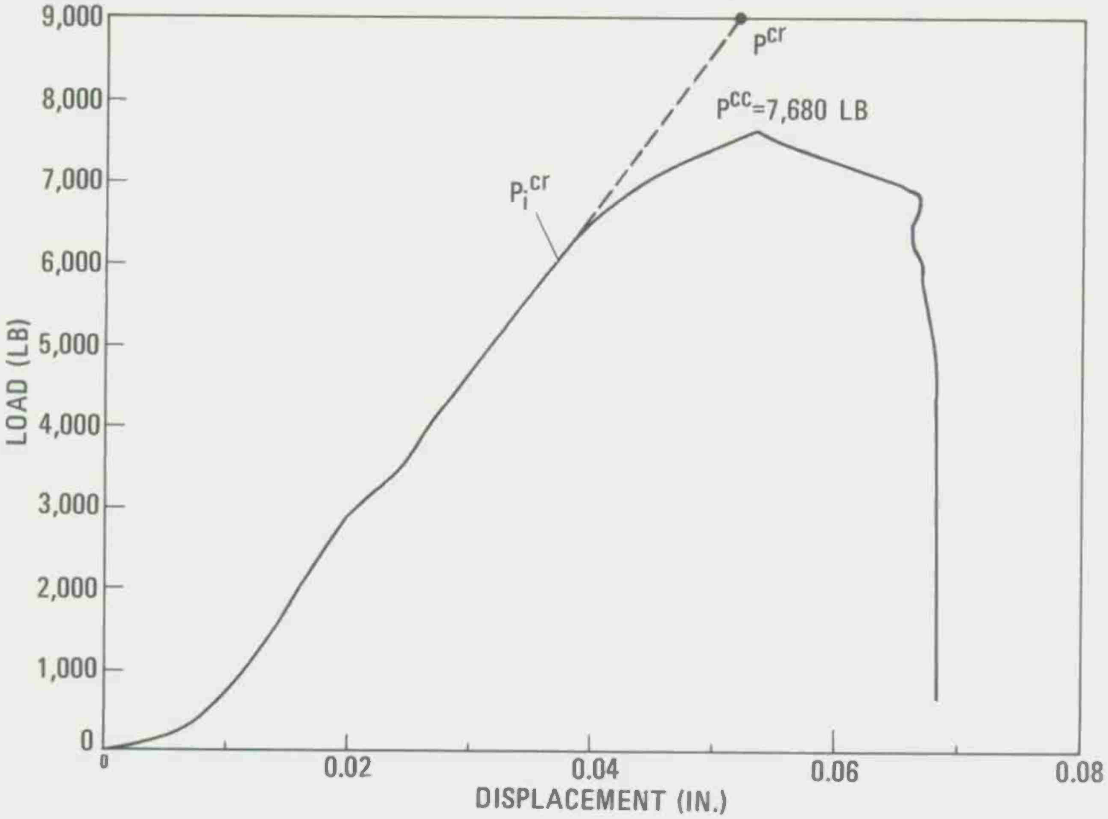

Figure 7. Testing machine load versus head travel for flat plate specimen 4A.

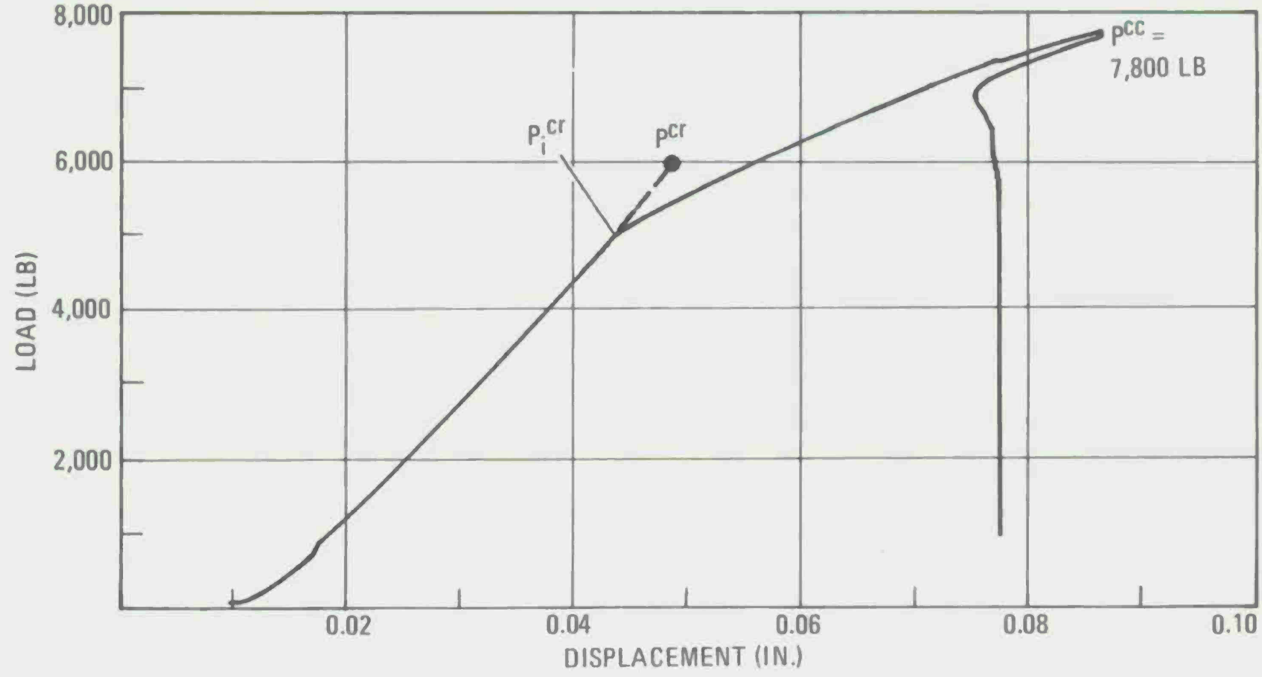

Figure 8. Testing machine load versus head travel for flat plate specimen 3A.

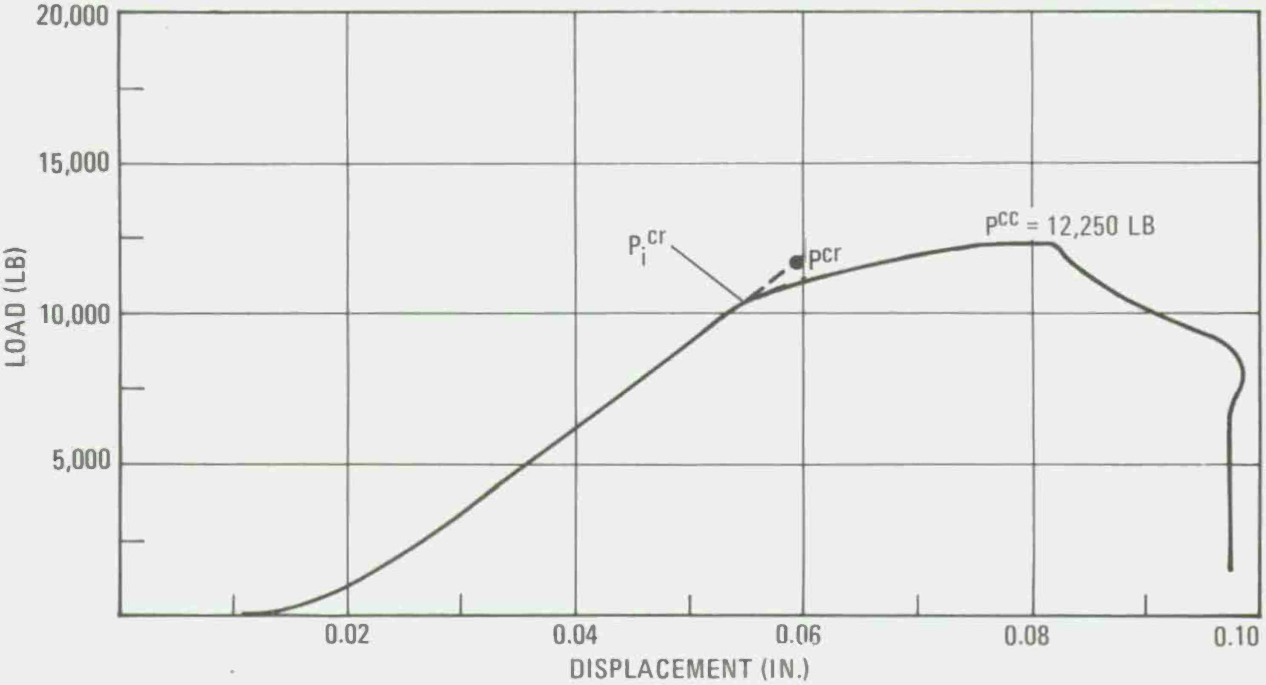

Figure 9. Testing machine load versus head travel for flat plate specimen 5B.

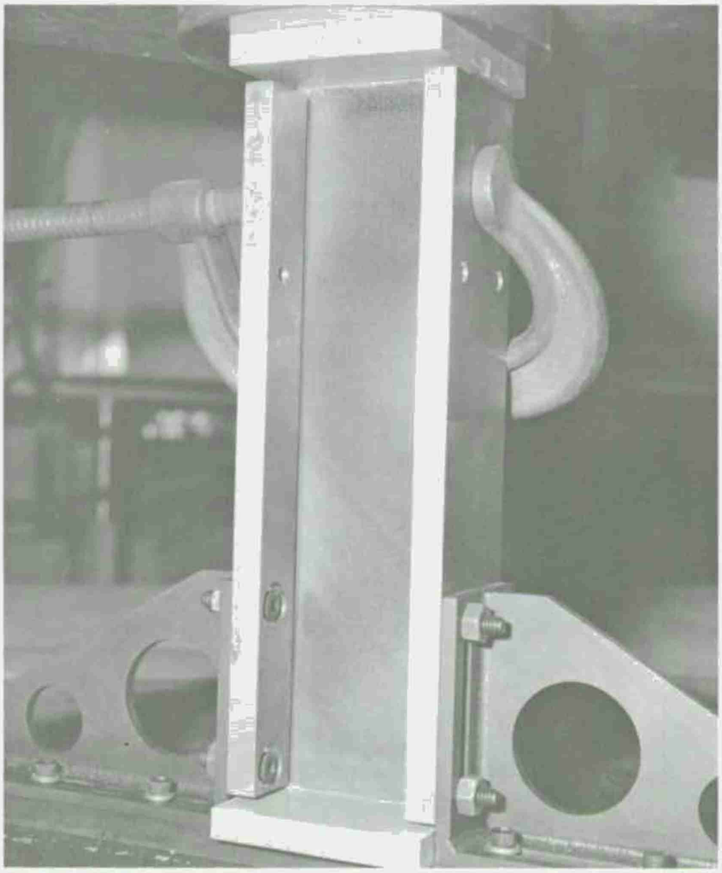

Figure 10. Typical post buckling pattern of the longer laminated plates.

TEST RESULTS FOR THE CHANNELS

Compression test results for graphite/epoxy laminated channels are presented in Table 2. As with plate test results, head displacement is plotted against machine load. Also, photographs were taken during loading. Test results are similarly reported in Tables 1 and 2, including the ratios P_i^{cr}/P^{cr} and P^{cc}/P^{cr}. The values of P^{cr} for the channels were also computed using equations presented by the authors[1]. There is good agreement between incipient and calculated buckling loads for most tests. In all cases, the ultimate or crippling loads exceeded the calculated buckling loads, and the longer channels failed at loads at least double the theoretical buckling loads.

Load displacement for channel specimen 14-3 is shown in Figure 12. The test specimen is shown in Figures 13 and 14 at loads of 9,600 and 10,225 pounds (ultimate load). The flanges buckled only slightly at the lighter load but delaminated and crimped severely at ultimate load. Since most of the damage to the web appears at the damaged corners, it is concluded that the failure mode is governed by interaction of the web and flange.

Load displacement for channel test specimen 16-3 is shown in Figure 15. In Figures 16, 17, and 18, the test specimen is shown at loads of 5,000; 7,750; and 9,325 pounds (ultimate load). At 5,000 pounds, the flanges buckled into two half waves; at 7,750 pounds, the buckling pattern changed to three half waves. This change is plotted in Figure 15 at a displacement slightly greater than 0.05 inch. As seen in Figure 18, crimping and delamination appear to start at the corners. Severe delamination occurred at the free edge of one flange.

Load displacement for test specimen 24-1 is plotted in Figure 19. In Figures 20 and 21, the test specimen is shown at loads of 16,450 and 19,100 pounds. Two views of the specimen at 27,600 pounds (ultimate load) are shown in Figures 22 and 23. The buckling patterns for this specimen are somewhat similar to the previous two, but the mode of failure was much more severe: the web separated from the flanges; one flange sheared apart; and extensive delamination was present.

CONCLUSIONS

Post buckling behavior of graphite/epoxy laminated plates and channels has been presented in machine load versus head travel plots and through photographs of incipient buckling, post buckling, and failure characteristics of the test specimens. Since the buckling patterns of the plates were difficult to photograph, only one is presented. However, many distinct and interesting photographs of channel buckling patterns and ultimate failure or crippling are shown. All laminates exhibited very inelastic behavior in ultimate compressive strength tests.[4]

The classical linearly elastic buckling theory agrees reasonably well with the apparent point of incipient buckling for channels, perhaps because the stress levels were relatively low, being close to the linear portion of the compressive stress-strain curves. Hence, elastic properties are nearly valid for the channels.

Attempts to predict buckling loads for graphite/epoxy plates using a simple theory are futile. Since the stress levels at the lower b/t ratios are clearly in the inelastic range of the compressive stress-strain curves, a reliable plasticity theory for laminated plate elements is needed to predict buckling loads. Until such a theory is developed, the design of minimum weight, graphite/epoxy stiffened panels will depend on the availability of empirical crippling curves. In support of this plate buckling analysis, virtually identical analytical results were obtained by the analysis of a specimen in a computer program [5] using an anisotropic buckling theory and accounting for exact boundary conditions.

ACKNOWLEDGEMENTS

The authors express appreciation to General Dynamics Convair Division and the Norwegian Defence Research Establishment for supporting this research. Appreciation is extended to the following Convair personnel: K.T. Younghusband, design; M. Varlas, V.C. Ryser, and C.W. Smith, fabrication of test specimens; C.R. Maikish, N.J. Callas, F.T. Ferguson, and G.E. Sawyer, machining of test specimens; Dr. N.R. Adsit, M.K. Spencer, and G.L. Hill, testing; and H. McCutchen, Dr. N.R. Adsit, and C.R. Maikish, consulting.

REFERENCES

1. Spier, E.E. and Klouman, F.L., "Empirical Crippling Analysis of Graphite/Epoxy Laminated Plates," paper presented at 4th ASTM Conference on Composite Materials: Testing and Design, Valley Forge, Pennsylvania, May 3-4, 1976.
2. Harris, G.Z , "Buckling and Postbuckling of Orthotropic Laminated Plates," AIAA Paper No. 75-813, 16th AIAA/ASME/SAE Structures, Structural Dynamics, and Materials Conference, Denver, Colorado, May 1975.
3. Stein, M., "Behavior of Buckled Rectangular Plates," J. Engineering Mechanics Division, Proc. American Soc. Civil Engineers, April 1960, 59-76.
4. Spier, E.E. and Klouman, F.L., "Ultimate Compressive Strength and Nonlinear Stress-Strain Curves of Graphite/Epoxy Laminates," paper published in proceedings of 8th SAMPE National Technical Conference, October 12-14, 1976.
5. Ashton, J.E., "Anisotropic Plate Analysis," General Dynamics Fort Worth Division Report FZM-4899, October 12, 1967.

Table 2. Compression test results of $[\pm 45_A/0_B/\mp 45_A]_T$ *laminated channels.*

Geometry							Theoretical Buckling	Test Results			
Specimen No.	v/o %	B	L (in.)	b_f (in.)	b_w (in.)	t (in.)	P^{cr} (lb)	P_i^{cr} (lb)	P_i^{cr}/P^{cr}	P^{cc} (lb)	P^{cc}/P^{cr}
14-1	62	4	5.25	0.749	2.645	0.0727	7,430	7,500	1.01	10,050	1.35
14-2	62	4	5.25	0.750	2.649	0.0714	6,820			9,250	1.36
14-3	62	4	5.25	0.747	2.652	0.0756	8,280	8,100	0.98	10,225	1.23
18-1	62	8	5.25	0.741	2.652	0.0819	9,990	9,300	0.93	12,050	1.21
18-2	62	8	5.25	0.744	2.658	0.0839	10,880	11,250	1.03	13,175	1.21
18-3	62	8	5.25	0.746	2.656	0.0838	10,810	10,500	0.97	13,625	1.26
22-1	62	12	5.25	0.752	2.661	0.0995	17,590	15,000	0.85	20,750	1.18
22-2	62	12	5.25	0.747	2.654	0.1009	17,950	17,500	0.97	21,875	1.22
22-3	62	12	5.25	0.742	2.663	0.1026	18,740	17,500	0.93	22,450	1.20
16-1	58	4	10.50	1.500	5.249	0.0632	2,510	2,600	1.04	9,625	3.83
16-2	58	4	10.50	1.502	5.254	0.0630	2,590	2,600	1.00	9,475	3.66
16-3	58	4	10.50	1.501	5.256	0.0644	2,800	2,550	0.91	9,325	3.33
20-1	59	8	10.50	1.497	5.265	0.0864	6,500	5,000	0.77	17,425	2.68
20-2	59	8	10.50	1.495	5.266	0.0880	6,800	6,250	0.92	17,075	2.51
20-3	59	8	10.50	1.495	5.273	0.0853	5,900	6,500	1.10	18,025	3.06
24-1	58	12	10.50	1.495	5.291	0.1082	12,070	11,100	0.92	27,600	2.29
24-2	58	12	10.50	1.493	5.289	0.1082	11,860	11,500	0.97	27,125	2.29
24-3	58	12	10.50	1.497	5.287	0.1089	12,270	12,500	1.02	25,950	2.11

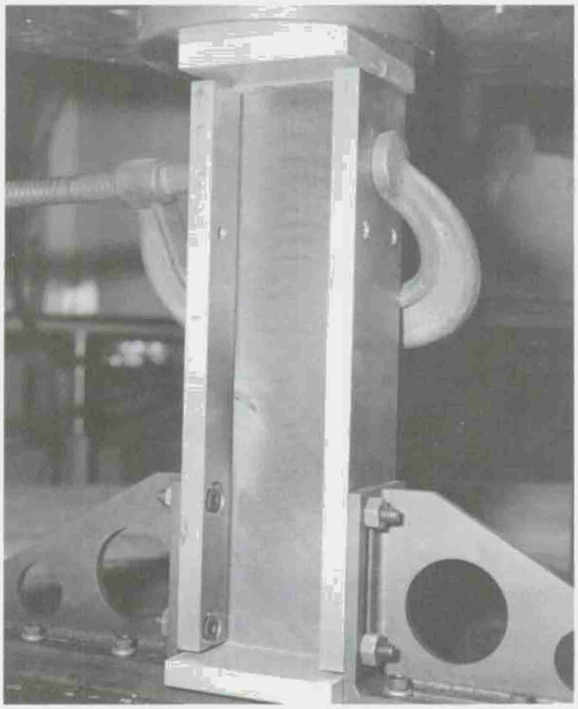

Figure 11. Compression failure of one of the longer laminated plates (shown in Figure 10 in the post buckling state).

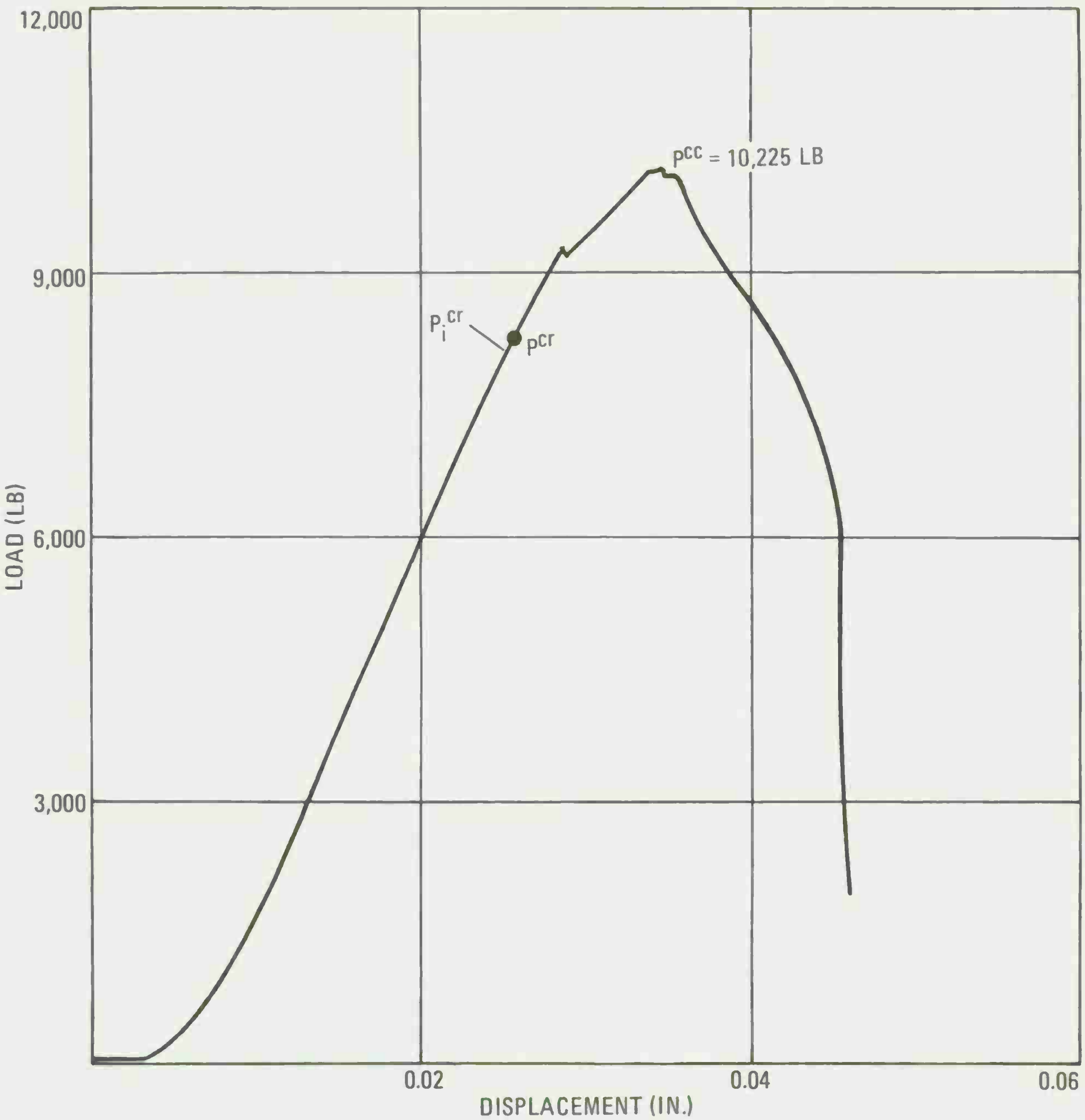

Figure 12. Testing machine load versus head travel for channel specimen 14-3.

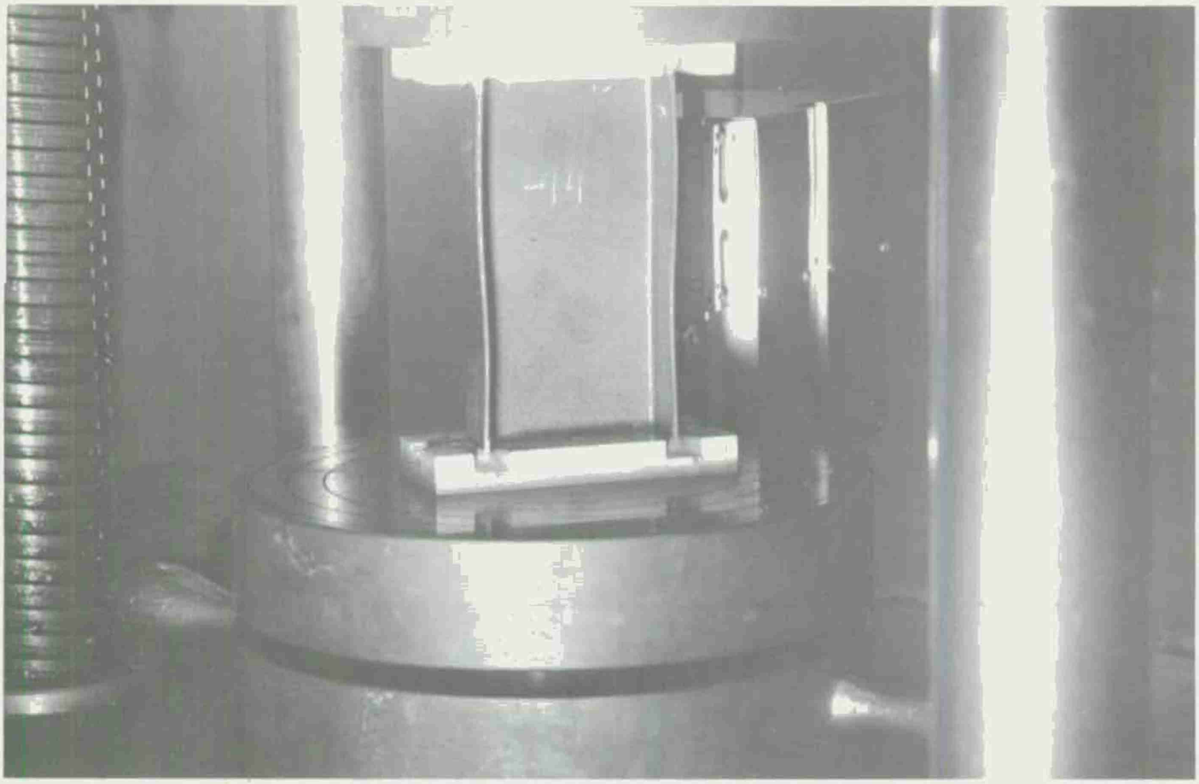

Figure 13. Compression buckling of channel specimen 14-3 at 9,600-lb load.

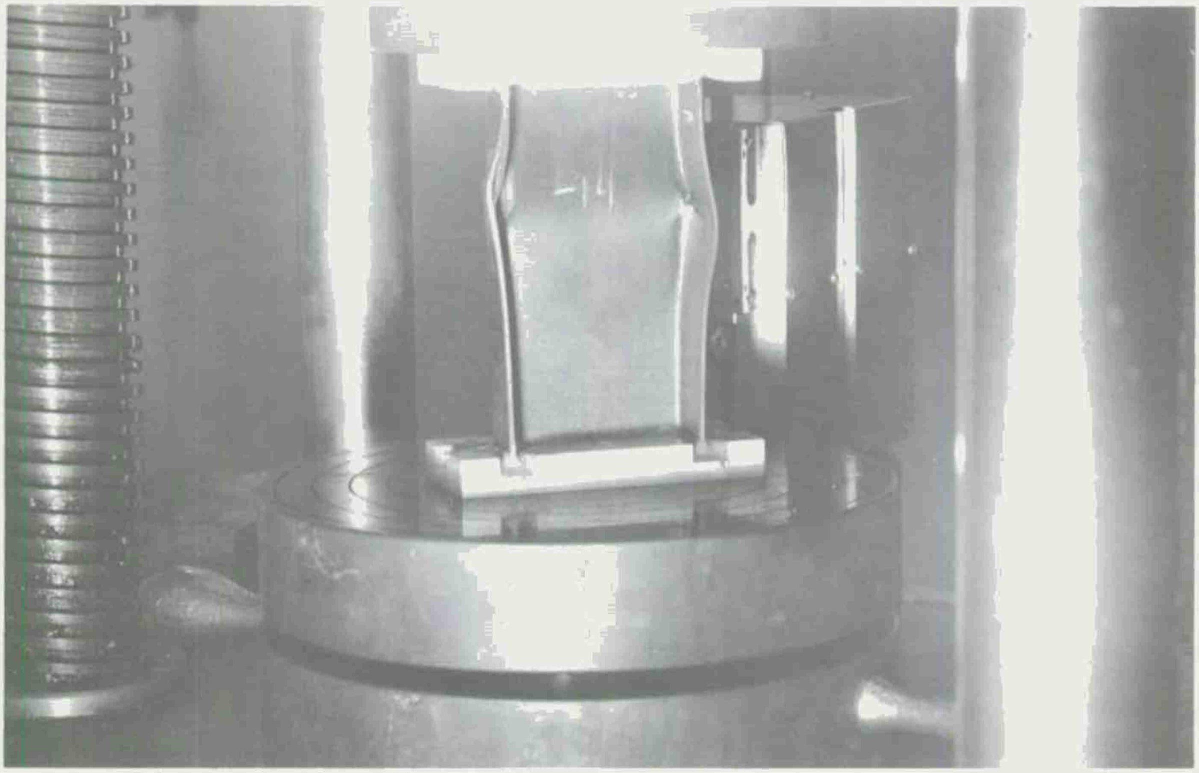

Figure 14. Ultimate compressive failure of channel specimen 14-3 at 10,225-lb load.

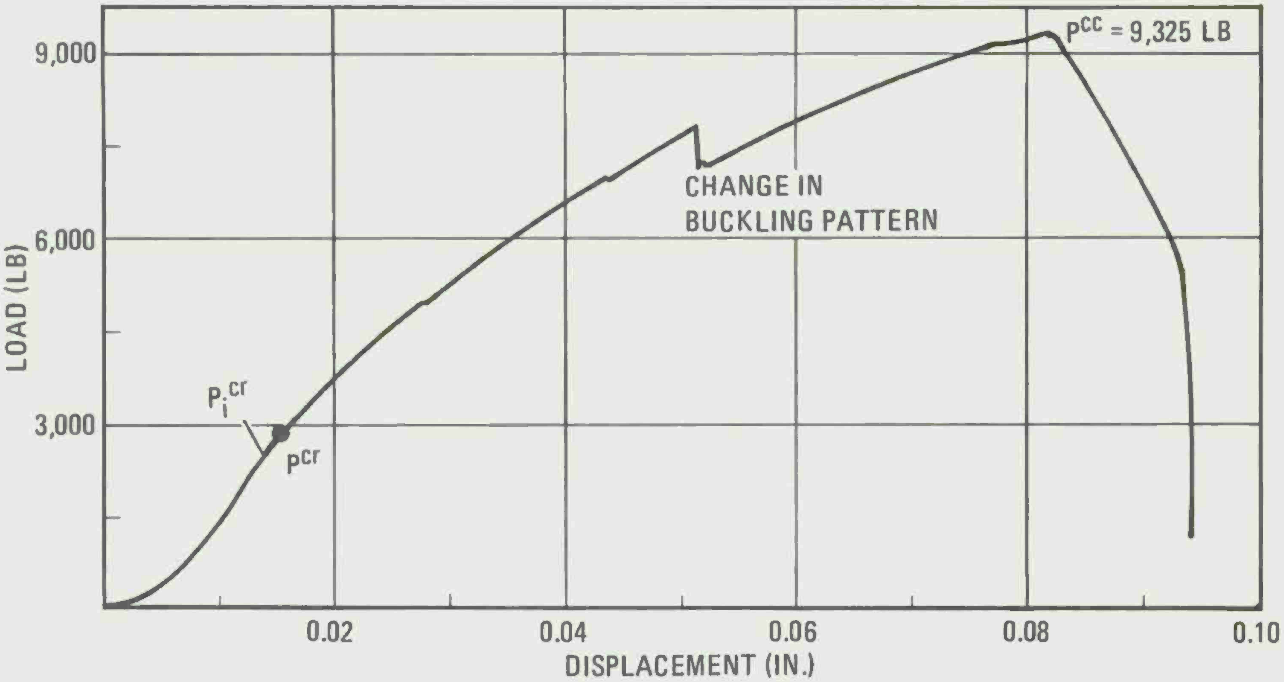

Figure 15. Testing machine load versus head travel for channel specimen 16-3.

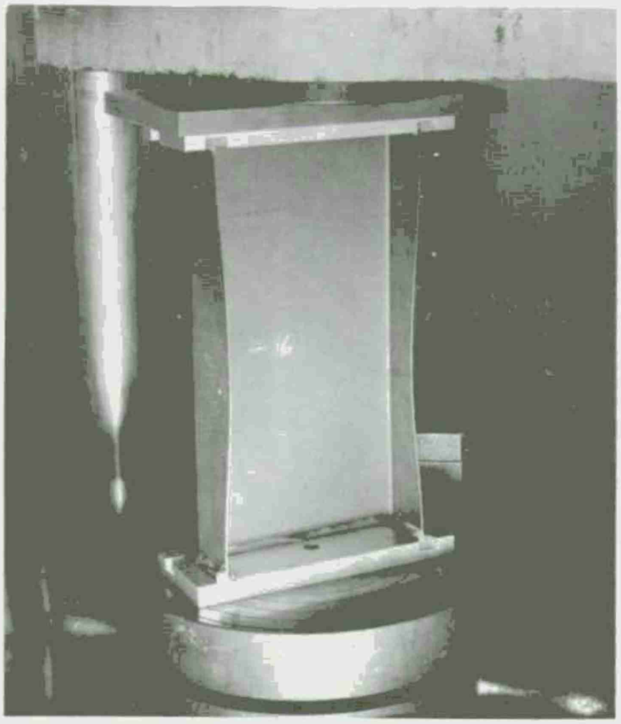

Figure 16. Compression post buckling of channel specimen 16-3 at 5,000-lb load.

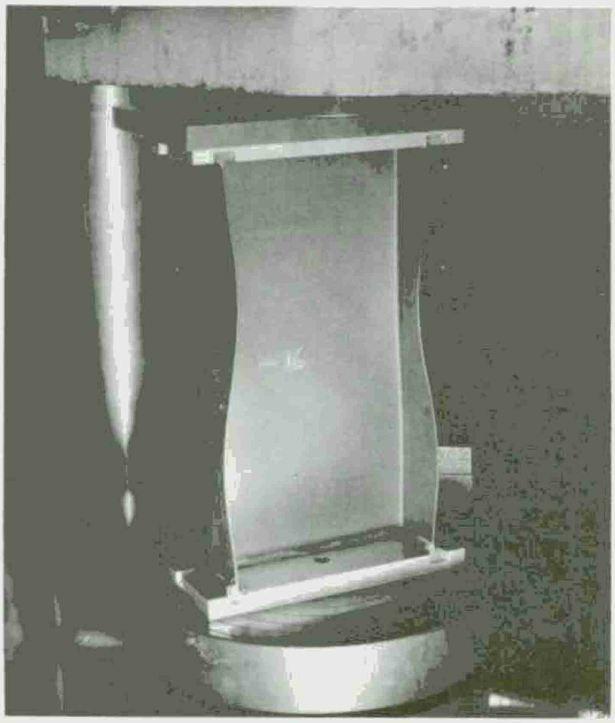

Figure 17. Compression post buckling of channel specimen 16-3 at 7,750-lb load.

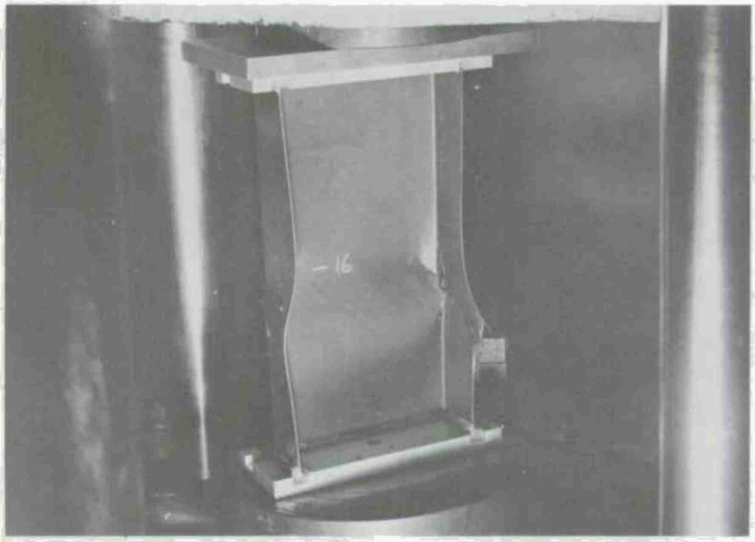

Figure 18. Ultimate compressive failure of channel specimen 16-3 at 9,325-lb load.

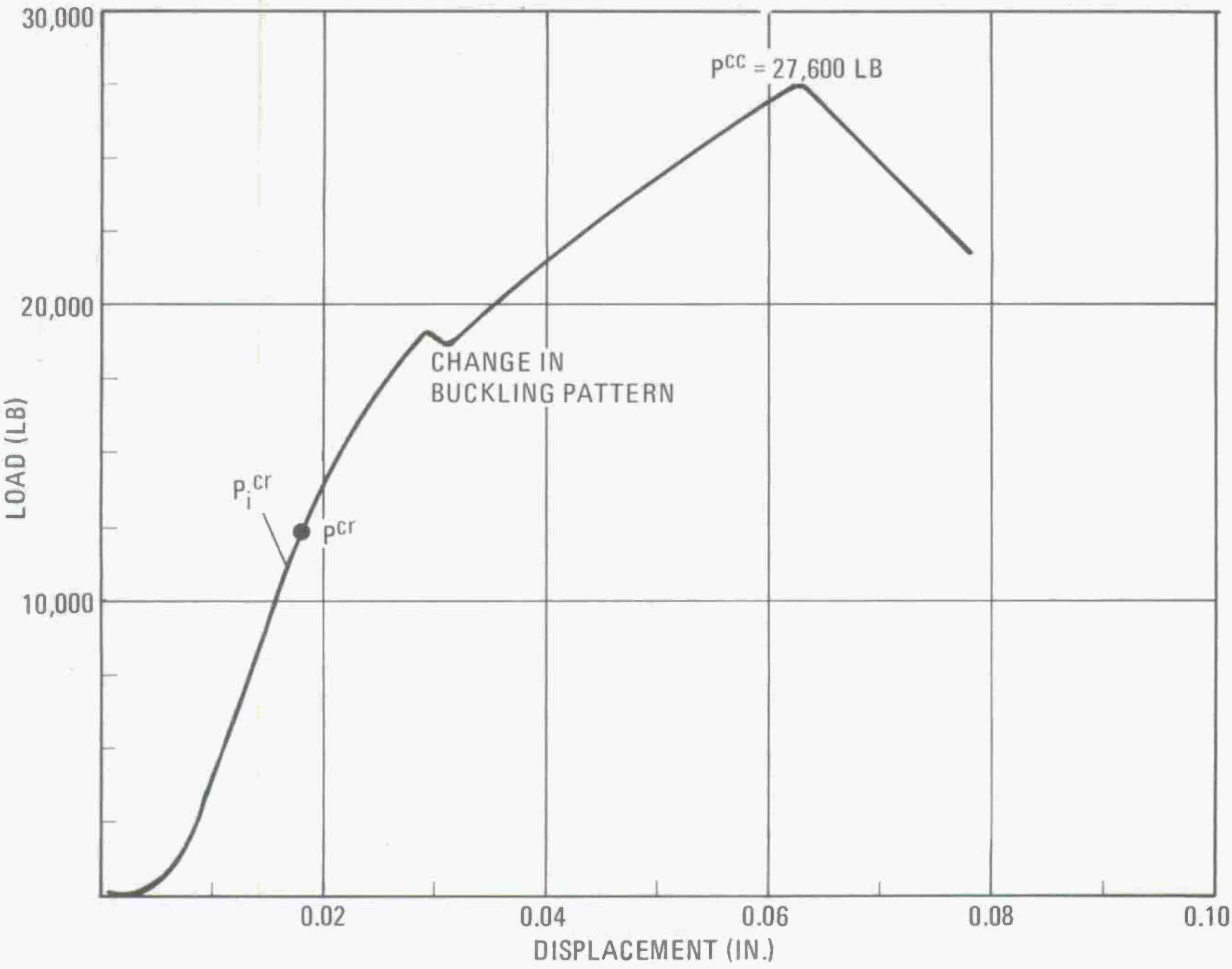

Figure 19. Testing machine load versus head travel for channel specimen 24-1.

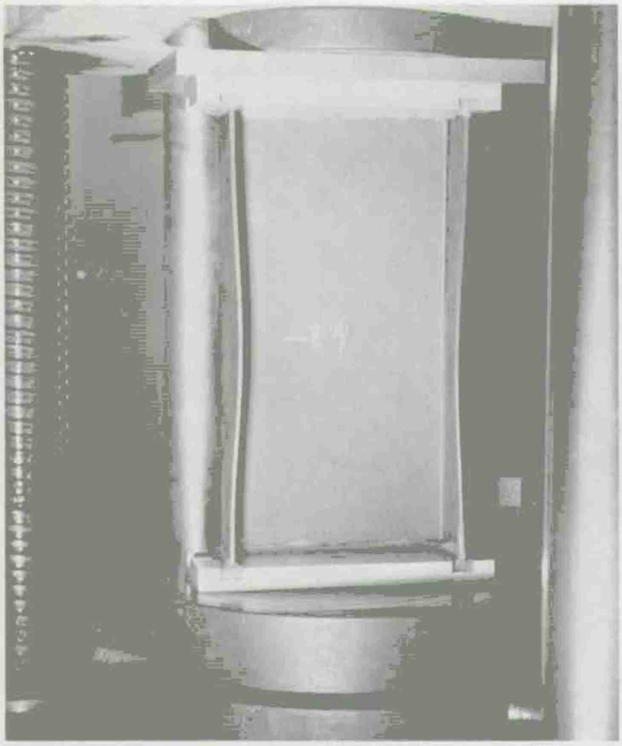

Figure 20. Compressive post buckling of channel specimen 24-1 at 16,450-lb load.

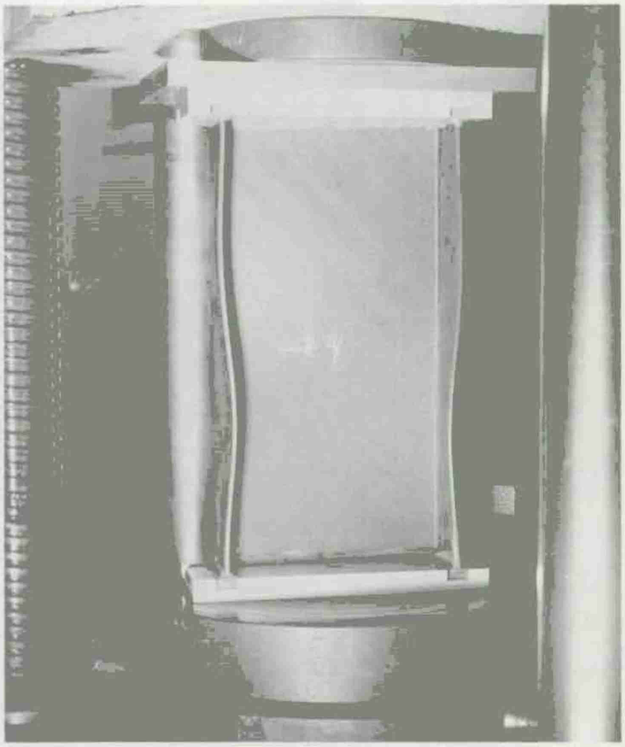

Figure 21. Compressive post buckling of channel specimen 24-1 at 19,100-lb load.

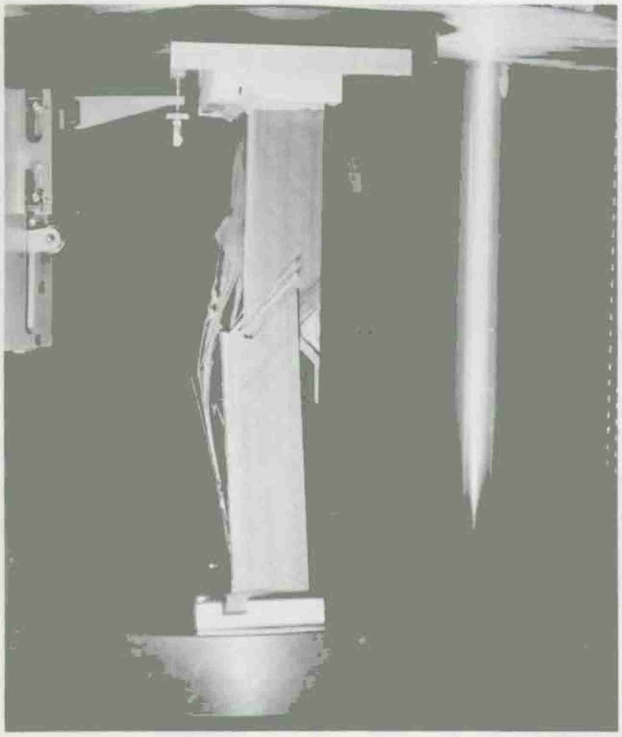

Figure 22. Ultimate compressive failure of channel specimen 24-1 at 27,600-lb load.

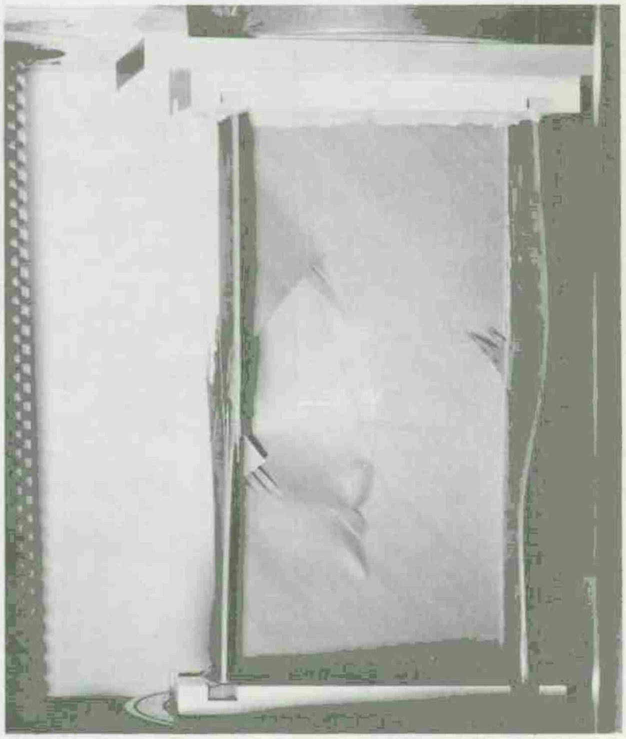

Figure 23. Ultimate compressive failure of channel specimen 24-1 at 27,600-lb load.

SESSION IV: MICROMECHANICS OF CARBON-CARBON COMPOSITES

Chairman: B. W. ROSEN
President, Materials Sciences Corporation

CRACKING IN 3-D CARBON-CARBON COMPOSITES DURING PROCESSING AND EFFECTS ON PERFORMANCE
J. Jortner, McDonnell Douglas Astronautics Company 81

MICROSTRUCTURAL CHARACTERIZATION OF CRACK PROPAGATION AND ANALYTICAL MODELING OF CARBON-CARBON COMPOSITES
J. S. Evangelides, The Aerospace Corporation 98

CRACKING IN 3D CARBON-CARBON COMPOSITES DURING PROCESSING AND EFFECTS ON PERFORMANCE

JULIUS JORTNER
Staff Engineer
McDonnell Douglas Astronautics Company
Huntington Beach, California

ABSTRACT

The microstructure of a three-dimensionally reinforced carbon-carbon composite, such as those being considered for use as reentry vehicle nosetips, is a complex array of impregnated yarn bundles, pockets and pads of matrix material, pores, and cracks. Detailed study of the unit cells in some current materials shows that the crack structure is periodic; that is, the crack locations and orientations in neighboring unit cells are similar. The cracks form a continuous space network within the composite. A conceptual model based on micromechanical reasoning is advanced to explain the formation of the observed crack network during the heat treatment cycles to which such composites are repeatedly subjected in processing. Some quantitative and qualitative correlations with observed behavior appear to validate the general appropriateness of the model. One prediction is that at the temperature of an ablating surface, the crack structure will have been largely closed by differential thermal expansion of the microconstituents. This prediction is supported by photomicrographs of heated samples. Other examples, relating to thermophysical and mechanical behavior, are also discussed. The intent of the paper is to show that, for this class of materials, understanding of the fractures that take place during processing can lead to improved capability to predict behavior during applications and, perhaps, an improved ability to design better composites.

INTRODUCTION

Graphitic materials are of interest to the aerospace community for use as thermal protection in rocket nozzles and reentry vehicles. As a class, such materials exhibit excellent ablation resistance and high-temperature thermostructural properties. Carbon-carbon composites, comprising a carbon (or graphite) matrix reinforced with carbon (or graphite) fibers, offer significant improvements over bulk polycrystalline graphites in terms of thermal stress resistance and strength, with ablation characteristics that are similar to those of bulk graphite [1].

This paper describes some of the details of the structure of three-directionally reinforced (3D) carbon-carbon composites that are being developed as candidates for reentry vehicle nosetips. Some background information is briefly reviewed as to the nature of graphite and its formation in these composites. A qualitative model, based on micromechanical reasoning, is advanced to explain the formation of many of the microstructural features, with emphasis on the effects of the anisotropic thermal expansivities of the constituents during the repeated heat treatment cycles to which such composites are subjected in processing. From the insight gained, some predictions may be made as to the behavior of the composite. This paper shows that actual behavior is in accord with such predictions, with respect to thermal expansion, shear modulus, dimensional growth during processing, and closure of microcracks during heating. The intent of this paper is to help motivate quantitative micromechanical analyses of the processes used to fabricate carbon-carbon composites in the hope that better composites and processes might result from the improved understanding.

BACKGROUND

MICROSTRUCTURE AND PROCESSING OF 3D CARBON-CARBONS

The microstructure of a 3D carbon-carbon composite is a complex array of impregnated yarn bundles, pockets and pads of matrix material, pores, and cracks. The three-dimensional array of reinforcing yarns is illustrated in Figure 1 by a schematic of a frequently used "223" style of weave. Figure 2 shows some typical views of 223 material that has been densified by chemical vapor deposition (CVD) followed by high-pressure pitch processing. Figure 3 shows schematically the nature of this densification process.

WD2694

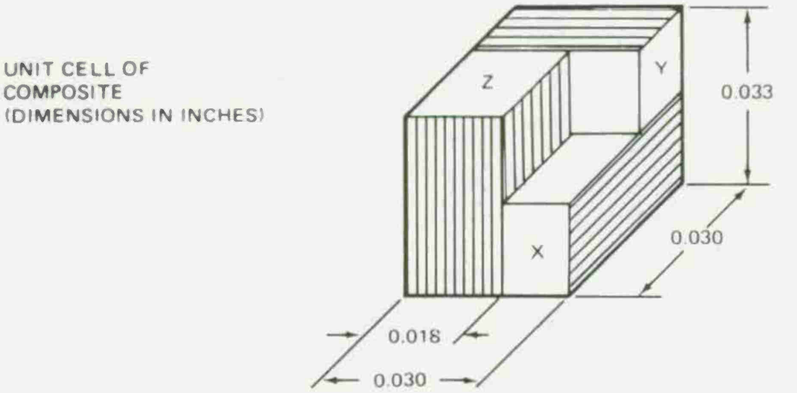

DIRECTION	YARN TYPE	YARN ENDS PER SITE*	REINFORCEMENT VOLUME FRACTION**	BULK DENSITY (g/cc)
X,Y	T-50	2	0.13	——
Z	T-50	3	0.22	——
TOTAL			0.48	0.80

*EACH END CONTAINS 1,440 FILAMENTS

**BASED ON COMPOSITE UNIT CELL DIMENSIONS AND PREPROCESS YARN CROSS-SECTION AREA (6.5 X 10^{-5} IN.^{2} FOR T-50, PER END)

Figure 1. Nominal Weave for 223 Fine-Weave Material

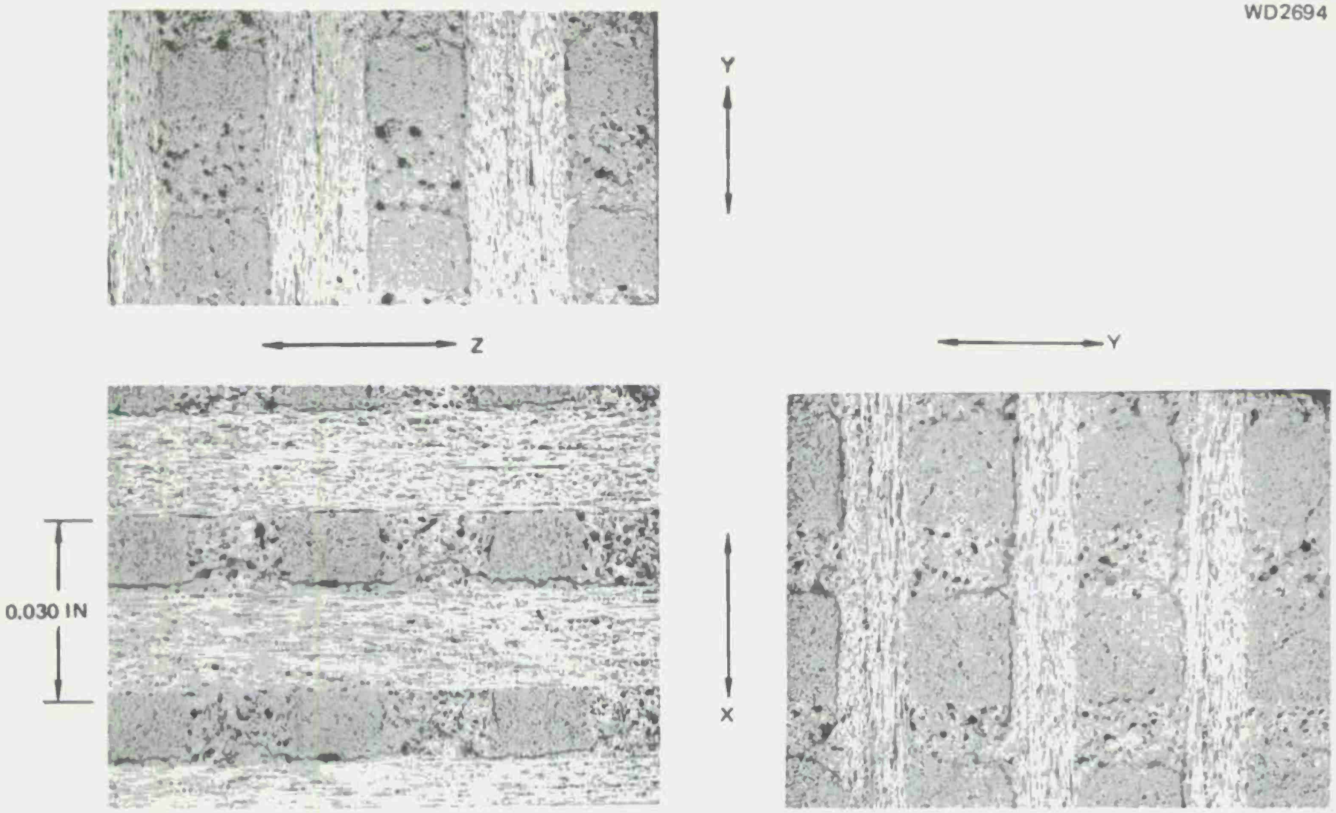
WD2694
Y
Z
Y
0.030 IN
X

Figure 2. Three Orthogonal Views of the Standard 223 Material (GE Billet 331)

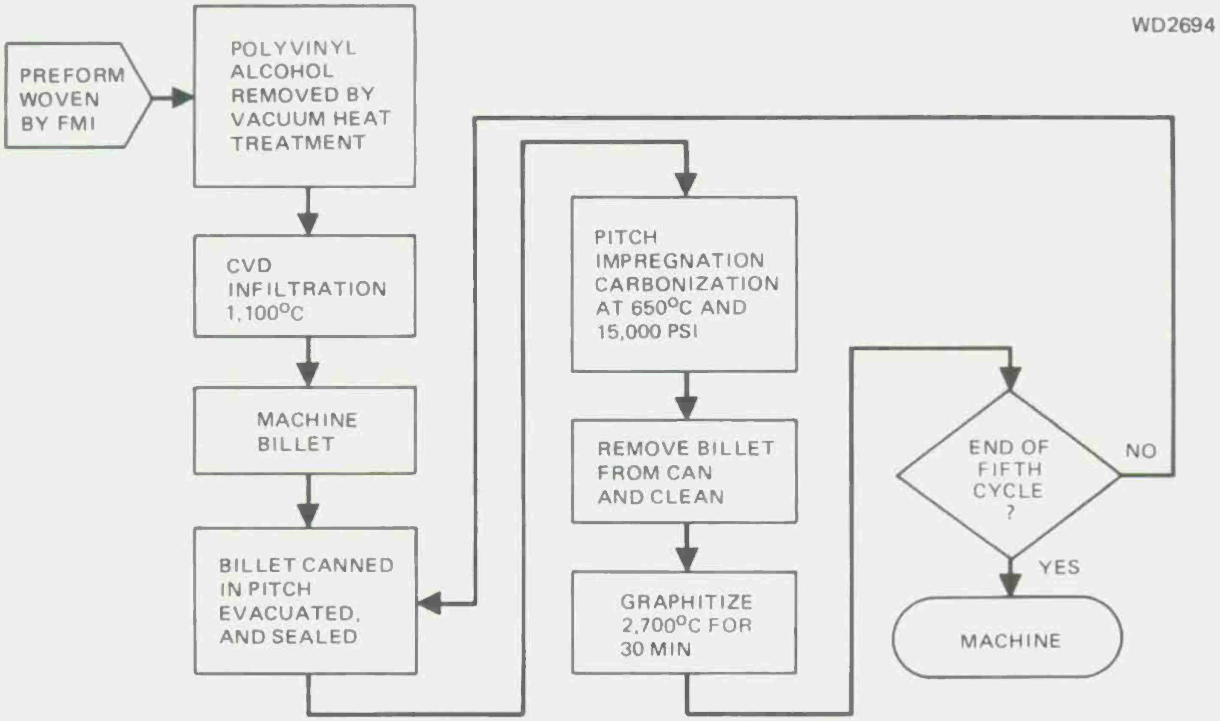
WD2694
PREFORM WOVEN BY FMI
POLYVINYL ALCOHOL REMOVED BY VACUUM HEAT TREATMENT
CVD INFILTRATION 1,100°C
MACHINE BILLET
BILLET CANNED IN PITCH EVACUATED, AND SEALED
PITCH IMPREGNATION CARBONIZATION AT 650°C AND 15,000 PSI
REMOVE BILLET FROM CAN AND CLEAN
GRAPHITIZE 2,700°C FOR 30 MIN
END OF FIFTH CYCLE ?
NO
YES
MACHINE

Figure 3. Processing of Standard 223 Carbon-Carbon (General Electric Process) Using CVD and High-Pressure Pitch Impregnation

Higher magnification views show that many of the yarn-bundle crossing areas are infiltrated with matrix material (Figure 4), and that these matrix layers tend to be cracked. The crack structure tends to be periodic; that is, the crack locations in neighboring unit cells are similar, in terms of being on the right of a yarn bundle rather than on the left, for example. Other 3D carbon-carbons, with different weaves and process histories, show similar tendencies for one-sided crack patterns. The matrix pads between yarns at crossings coincide with the cracks, implying that the repeated infiltrations of matrix materials have occupied the crack space; the cracks then recur, presumably after graphitization (see Discussion). An idealized representation of typical microstructure is shown in Figure 5. Also shown in Figure 5 is the continuous nature of the crack space, a feature which helps explain how new infiltrations of matrix precursor can reach the interior of the billet.

Changes in the details of processing have major effects on the microstructure. Figure 6 shows views of three materials made from the 223 weave but densified with low-pressure pitch processing, with graphitizations to the temperatures indicated under each photo. A schematic of the low-pressure process is provided in Figure 7. It is apparent from Figure 6 that graphitization temperature has an effect on the crack structures. Also striking is a comparison of Figures 2 and 6, which shows significant differences between low-pressure and high-pressure processing in terms of yarn-bundle cross-section shape, "billowing" of the yarn bundles, size of pores in the matrix pockets, thickness of the matrix pads between yarns, and width of the cracks running through the matrix pads.

The transformation of coal-tar pitch to graphite by heat treatment has been extensively studied; for example, see White [2]. It has been found that the graphitic structure forms at surprisingly low temperatures (below 600°C) while the pyrolyzing pitch is still liquid, and that the extent and orientation of the crystallographically aligned regions are the result of many influences including process pressure, rate of temperature change, bubble percolation, stirring, the presence of solid surfaces, etc.

During the formation period of the initial graphitic structure, referred to as the mesophase, the pitch loses a significant portion of its initial mass in evolved gases. These gases must either remain within the composite, or find their way out by diffusion, bubble flow, or direct escape through open passages. Above 600°C, the pyrolyzing pitch is solid and loses very little mass in further volatilization of gases. However, the density (measured by fluid infiltration, so as not to include the volume of pores, cracks, etc.) increases from about 1.4 g/cc to about 2.2 g/cc over the heat treatment from 600°C to 2,800°C, [2]. The decrease in volume of the graphitizing matrix is accommodated by the development of shrinkage cracks on a very fine scale (microns).

The crystal structure of graphite is hexagonal (open, not close-packed) with rather weak bonding between the basal planes. The basal plane is referred to as the a-b plane; the c-axis is defined as being normal to the basal plane. The graphite structure leads to considerable anisotropy;

WD2694

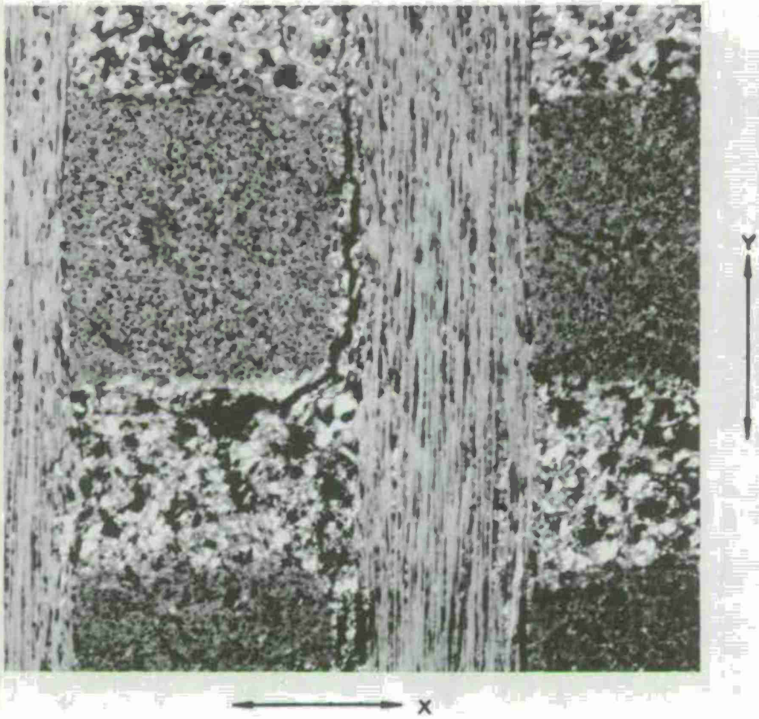

Figure 4. View of 223 Material (GE Billet 331) 80X Under Polarized Light (Note Cracked Matrix Material Between Z and Y Yarns)

WD2694

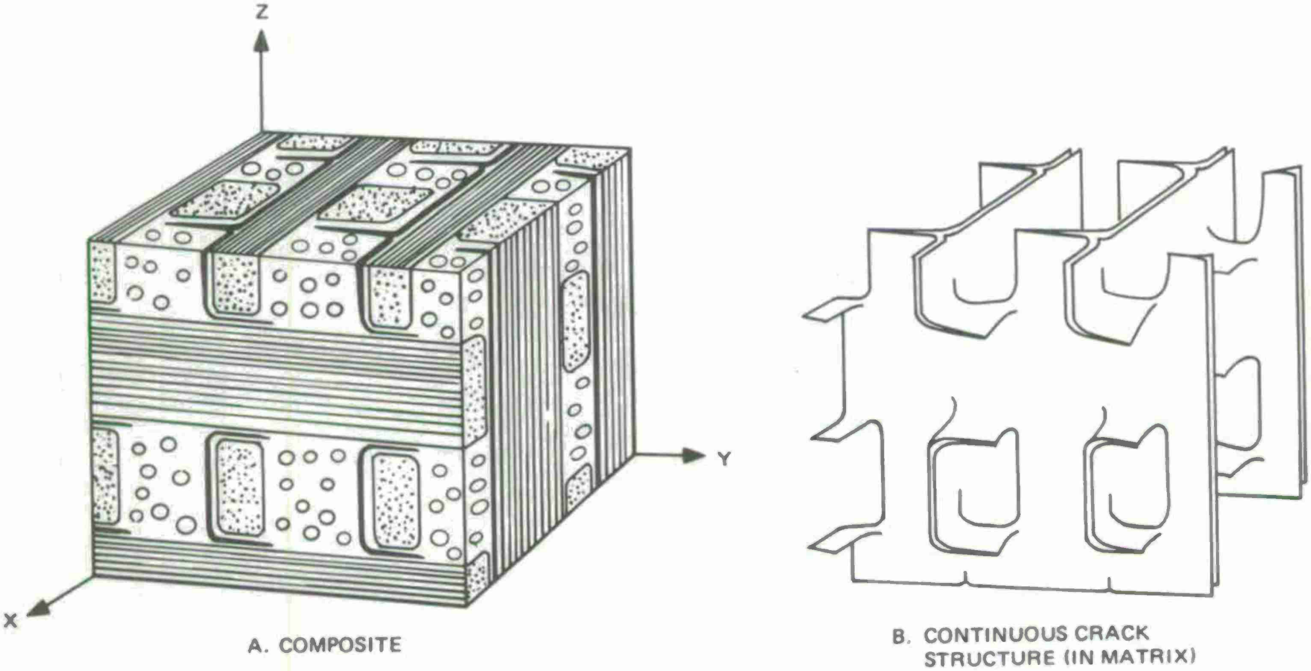

A. COMPOSITE

B. CONTINUOUS CRACK STRUCTURE (IN MATRIX)

Figure 5. Idealized Structure of Standard 223 Carbon-Carbon Composite

WD2694

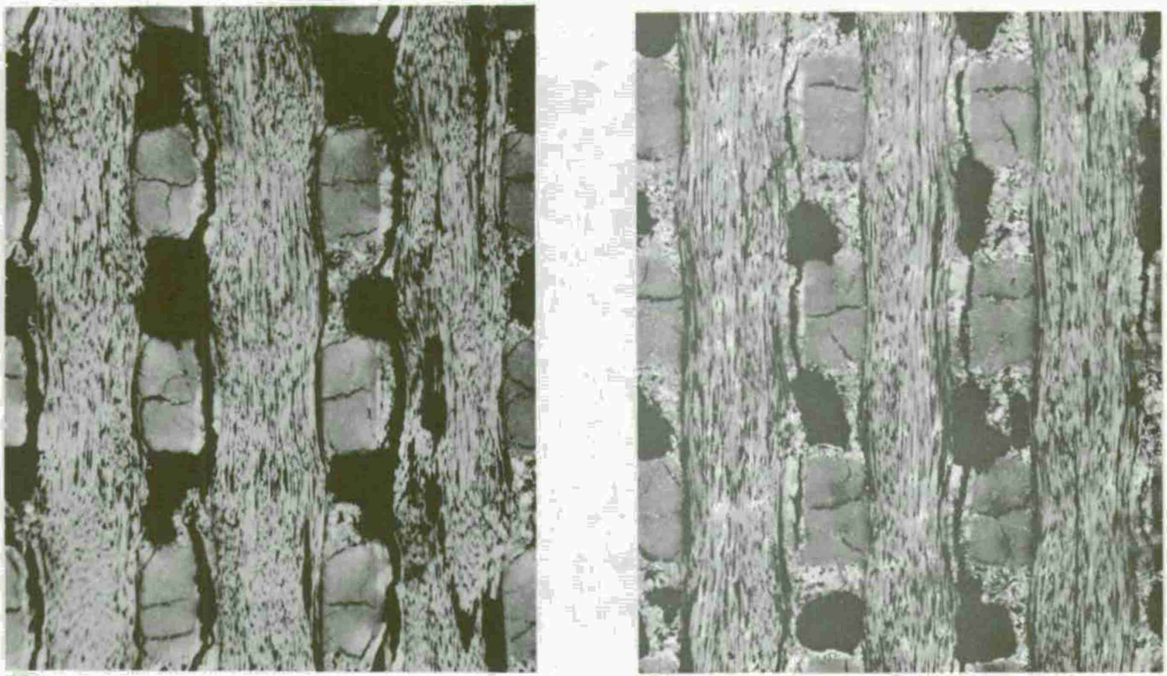

30X T = 2400°C

30X T = 2800°C

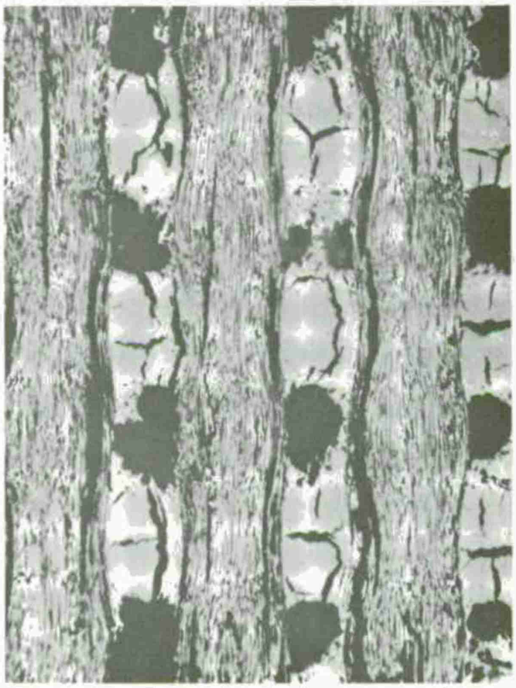

30X T = 3100°C

Figure 6. Microstructural Comparison of Heat-Treatment Temperature Effects in 2-2-3 Carbon-Carbon Densified with Low-Pressure Pitch (Polarized Light)

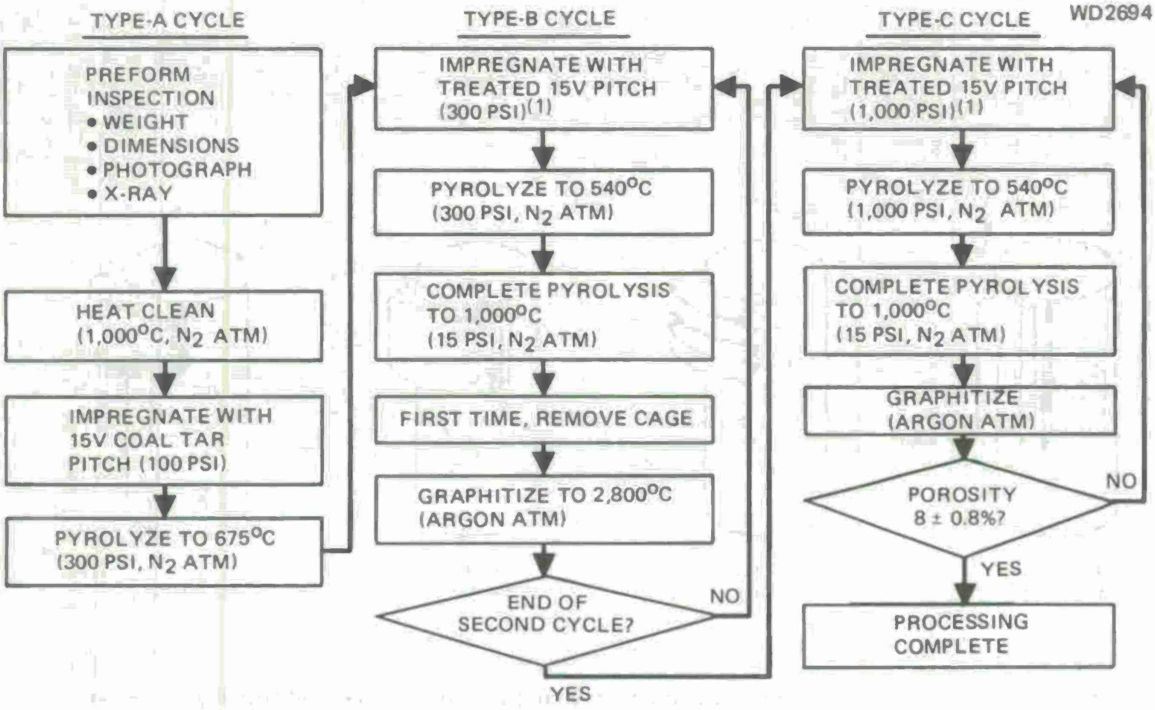
TYPE-A CYCLE
TYPE-B CYCLE
TYPE-C CYCLE
WD2694
PREFORM INSPECTION
• WEIGHT
• DIMENSIONS
• PHOTOGRAPH
• X-RAY
HEAT CLEAN (1,000°C, N2 ATM)
IMPREGNATE WITH 15V COAL TAR PITCH (100 PSI)
PYROLYZE TO 675°C (300 PSI, N2 ATM)
IMPREGNATE WITH TREATED 15V PITCH (300 PSI)(1)
PYROLYZE TO 540°C (300 PSI, N2 ATM)
COMPLETE PYROLYSIS TO 1,000°C (15 PSI, N2 ATM)
FIRST TIME, REMOVE CAGE
GRAPHITIZE TO 2,800°C (ARGON ATM)
END OF SECOND CYCLE?
NO
YES
IMPREGNATE WITH TREATED 15V PITCH (1,000 PSI)(1)
PYROLYZE TO 540°C (1,000 PSI, N2 ATM)
COMPLETE PYROLYSIS TO 1,000°C (15 PSI, N2 ATM)
GRAPHITIZE (ARGON ATM)
POROSITY 8 ± 0.8%?
NO
YES
PROCESSING COMPLETE

(1) FOR TYPE-B AND TYPE-C DENSIFICATION CYCLES, 15V PITCH IS USED THAT HAS BEEN TREATED TO A CONTROLLED CONDITION, BASED ON THERMOGRAVIMETRIC MEASUREMENTS

Figure 7. Low-Pressure Pitch Densification (MDAC Process)

strength, stiffness and thermal conductivity are several times higher within the a-b plane than along the c-axis, while thermal expansion is several times lower. Reynolds [3] and Hodgson [4] provide useful summaries of such basic information.

High-modulus graphite filaments, such as make up the Thornel-50 yarn, are also highly anisotropic. The axis of the yarn is aligned with the high-stiffness direction; strength and conductivity are high along the filament axis; thermal expansion is low along the filament axis and high transverse to the axis. Within a yarn bundle of the finished composite, the matrix graphite can align itself in several basic ways (Figure 8). Study of the material shown in Figure 2 suggests that the matrix alignment is more or less isotropic with a tendency towards c-axis axial, whereas the alignment in the materials of Figure 6 is primarily c-axis radial, as illustrated in Figure 9. In these photographs of etched surfaces, the edges of the layer a-b planes of the graphitic structure are clearly seen. These differences in graphite orientation are expected to influence the thermomechanical situation during processing via differences in transverse thermal expansions of the yarn bundles and other yarn bundle properties.

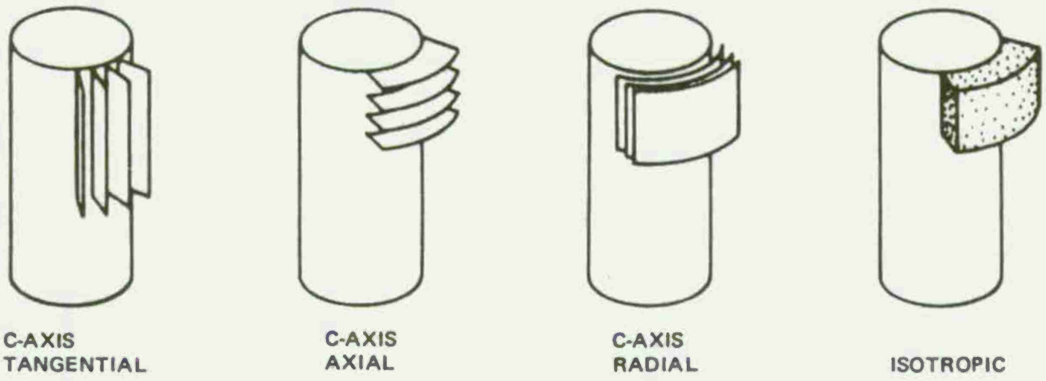

Figure 8. Some Elementary Possibilities for Graphitic Orientation of CVD Layers and Other Matrices on Fibers (Schematic)

DISCUSSION

QUALITATIVE MICROMECHANICAL MODEL

The striking differences in microstructure between composites fabricated with the low-pressure and the high-pressure processes have been previously noted. Comparison of Figures 2 and 6, which show composites made from nominally the same 223 weave by the same preform fabricator, suggests strongly that most of the yarn distortions occur as a result of processing.

Figure 10 presents schematically a sequence of events that might occur during processing and result, mechanistically, in the sort of microstructure seen in Figure 6. Review of Figure 10 will show that among the key factors affecting the microstructure are the yarn bundle thermal expansions (transverse and axial); the ability of the matrix pockets to transfer compressive loads from one yarn to its parallel neighbor; the relative filament volume fractions in the yarn directions; the creep resistance of the yarn bundles; the relative tensile strengths in the transverse direction of the yarn bundle and the matrix material in the matrix pads between yarns; the number of process cycles (or graphitizations); and the graphitization temperature.

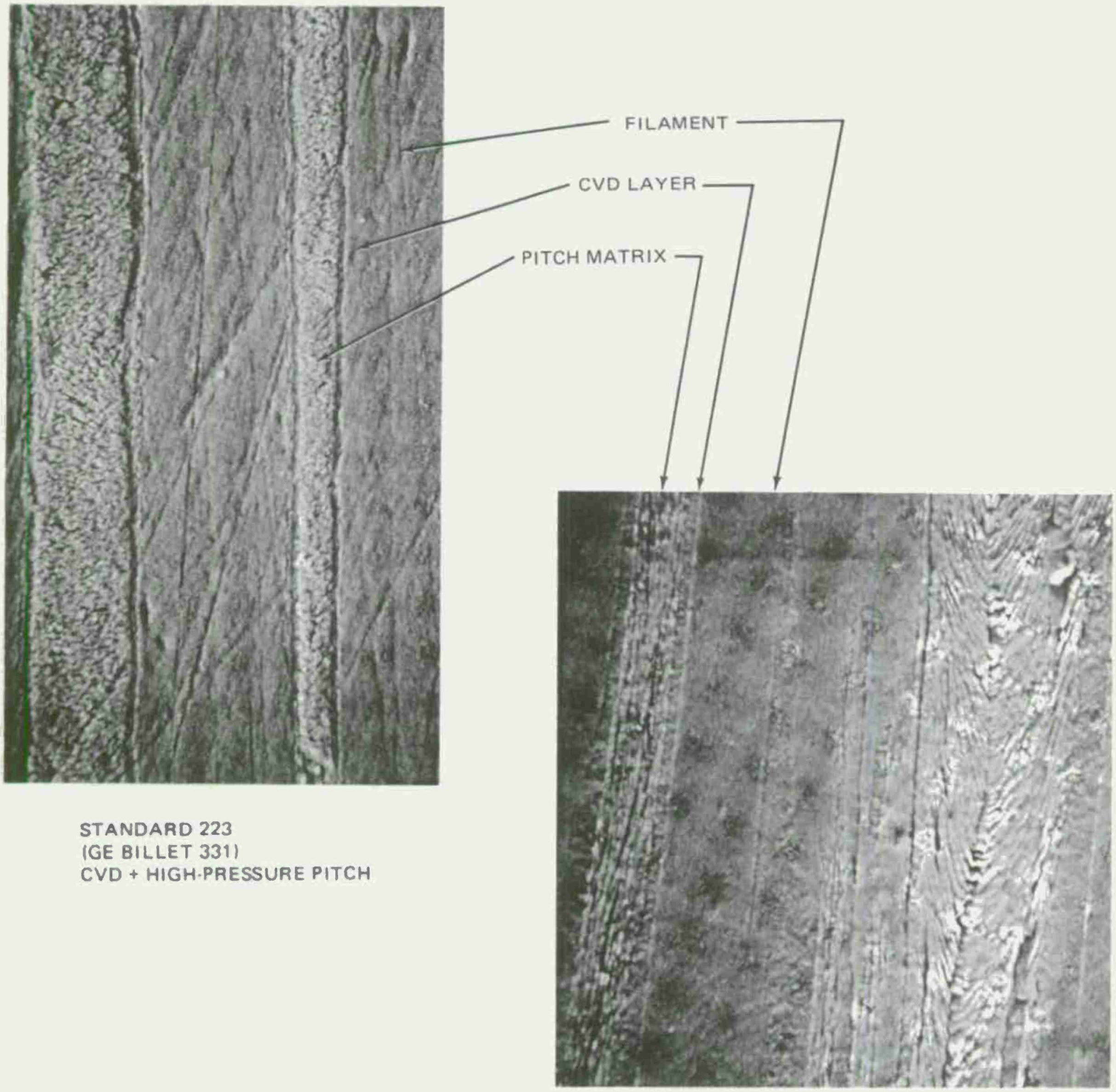
FILAMENT
CVD LAYER
PITCH MATRIX

STANDARD 223
(GE BILLET 331)
CVD + HIGH-PRESSURE PITCH

MDAC/REVMAT 223
(BILLET 432 BC-2)
CVD + LOW-PRESSURE PITCH

Figure 9. Graphitic Layer Structures of Matrix Between Filaments in Yarn Bundles of 3D Carbon-Carbons. SEM photos of etched surfaces. Approximately 5,000 X

WD2694

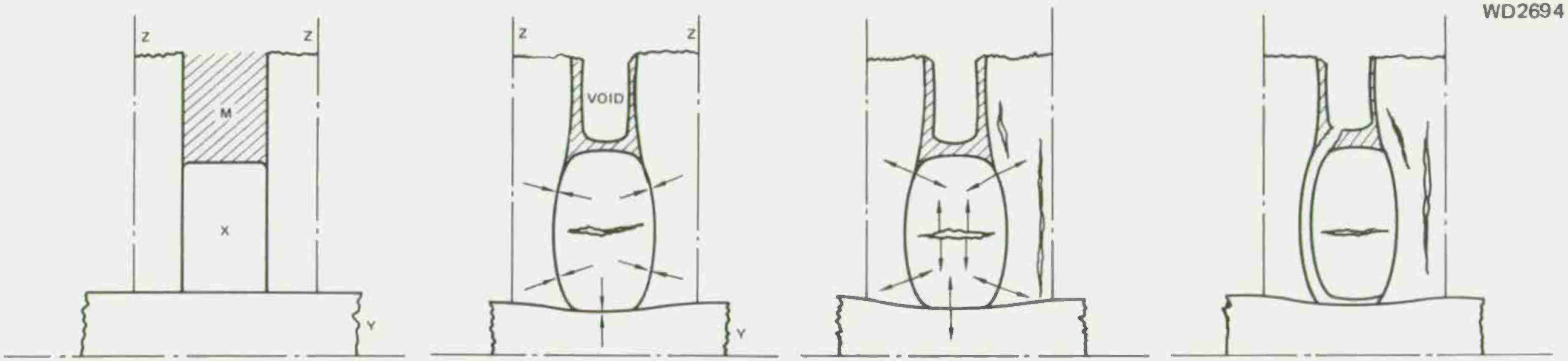

1. FIRST IMPREGNATION OF PREFORM (WITH OR WITHOUT CVD) AT T_I
   - RECTANGULAR YARN SECTIONS
   - IMPREGNATED FULLY

2. FIRST GRAPHITIZATION AT T_G
   - MATRIX POCKET MOSTLY EMPTY
   - YARN CROSSOVERS BONDED
   - ANISOTROPIC YARN EXPANSION:
     - TRANSVERSE COMPRESSION AND HIGH T CREEP OF YARN
     - AXIAL TENSION OF YARN AND FILAMENT CREEP
   - POSSIBILITY OF YARN BUNDLE CRACK (COMPRESSIVE) AT END/PLY INTERFACES
   - YARN BILLOWING INTO MATRIX POCKET VOID

3. COOLDOWN ABOVE T_C
   - ANISOTROPIC YARN CONTRACTION
     - TENSION ACROSS INTERFACES
     - AXIAL COMPRESSION OF YARNS
   - ACCENTUATED BILLOWING?
     - COMPRESSIVE BUCKLING
     - TRANSVERSE TENSILE CREEP
   - FORMATION OR OPENING OF YARN CRACKS?
     - COMPRESSIVE BUCKLING
     - TRANSVERSE TENSION

4. AFTER COOLDOWN AT T_R
   - ONE-SIDED CRACK AT CROSS-OVER
   - ANY YARN CRACKS MAY BE OPENED FURTHER

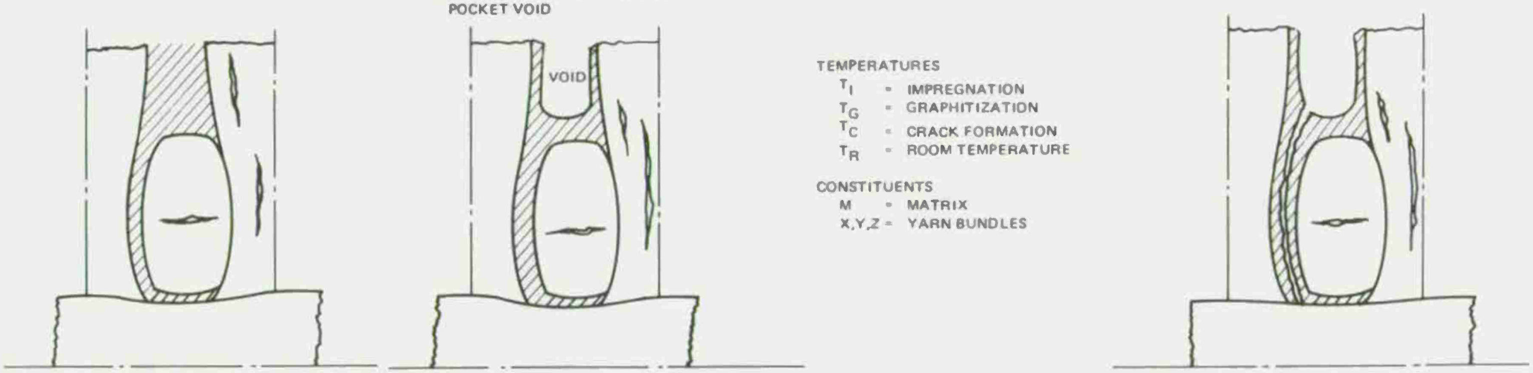

TEMPERATURES

T_I = IMPREGNATION
T_G = GRAPHITIZATION
T_C = CRACK FORMATION
T_R = ROOM TEMPERATURE

CONSTITUENTS

M = MATRIX
X,Y,Z = YARN BUNDLES

5. REIMPREGNATION AT T_I
   - IMPREGNATED FULLY

6. GRAPHITIZATION AT T_G
   - SAME EFFECTS AS FIRST CYCLE
     - POSSIBILITY OF YARN BUNDLE CRACKING
     - ACCENTUATION OF BILLOWING (EARLIER CYCLES)
   - BILLET GROWTH (LATER CYCLES)
     - VOID SPACE LESSENED
     - MATRIX POCKET TRANSMITS COMPRESSION
       - BILLOWING SUPPRESSED
     - TENSILE YARN CREEP MORE LIKELY
       - BILLET GROWTH

7. AFTER COOLDOWN AT T_R
   - MATRIX PAD CRACK, ONE-SIDED
   - ACCENTUATED OR NEW YARN CRACKS
   - REPEATED CYCLES THICKEN MATRIX PAD

Figure 10. Thermomechanical Development of Microstructure in 3D C-C (Low-Pressure Pitch Processing)

The specific microstructural differences observed when comparing a high-pressure (15,000 psi) processed 223 material (Figure 2) to a low-pressure (300 to 1,000 psi) processed 223 material (Figure 6) may be explained in terms of the mechanisms outlined and the following differences in processing:

1. Presence of initial CVD in the high-pressure material, which may strengthen the yarn bundle transversely, thus reducing gross yarn bundle cracks.

2. The orientation of the pitch-precursor matrix within the yarn bundles, which is a consequence of process pressure or of the CVD layer. The orientation in the 223 material processed at high pressure would favor high transverse yarn bundle strength and low transverse expansivity in the yarn bundles. These effects would tend to prevent gross yarn cracking and would tend to decrease the width of the cracks seen in the matrix pads.

3. The high process pressure allows containment of the pyrolysis gases that evolve while the pitch is still liquid. This has several important consequences:

    A. There is no gross outflow of pitch from the preform during pyrolysis, thus the bubbles generated within a given matrix pocket will probably remain within that pocket, leading to a dispersion of small spherical pores rather than the large connected pores seen in the low-pressure pitch materials.

    B. The cracks that serve as connecting paths between unit cells are less affected by the pyrolysis process, as the liquid layers will not be grossly disturbed by the passage of gas.

    C. The matrix pockets remain essentially filled with a porous structure that can transmit at least compressive loads across the matrix pockets. This will tend to suppress much of the yarn billowing into the matrix pockets that is seen in the low-pressure-process materials.

4. The more efficient yield of graphite from the high-pressure process results in a lesser number of process cycles (typically four or five) than the low-pressure process (typically a dozen). Thus, the matrix pads at the yarn crossing will tend to be narrower, and the cumulative creep effects such as yarn billowing and distortion and composite growth will tend to be less.

The micromechanical model illustrated by Figure 10 does not yet include detailed consideration of the events between impregnation and graphitization, although some of the major consequences have been implied (for example the formation of void space in the matrix pocket). The carbonization and graphitization events, such as gas bubble formation;

ejection of liquid infiltrants by excess gas, mesophase formation in the pitch; and changes in mass and dimension of the matrix, are expected to play a significant role in determination of microstructure, especially during the early process cycles. In fact, it is not clear at this time whether or not some of the major cracks, discussed in Figure 10 in terms of shrinkage stresses upon cooling from graphitization, occur during the shrinkages accompanying carbonization. Nevertheless, it appears likely that pyrolysis cracks will have been closed by differential expansion during the graphitization heat-up cycle. In any case, the significant effects of graphitization temperature on the microstructures seen in Figure 10 imply that the graphitization cycle dominates the crack pattern.

A consequence of assuming that the cracks occur on cool-down from graphitization is that they should close upon reheating. Direct observation of the closing of microstructural cracks as temperature is raised is now being attempted. Initial results to a temperature of 1,900°F are shown in Figure 11. Although the temperature reached is only about one-third of the graphitization temperature, significant changes in crack width are apparent.

The mechanism of crack closure may be illustrated in terms of the sketch of a unit cell in Figure 12a and the following approximate equation which relates the temperature-induced change in crack opening width, g, to the differences in thermal expansion of the yarn bundles in their transverse, α_t, and axial, α_a, directions;

$$\frac{\Delta g}{a} = T\,(\alpha_t - \alpha_a) \text{ for } g \ll a \text{ where } a = \text{unit cell width}$$

A fair approximation to the upper limit of transverse yarn expansion of a low-pressure pitch-processed composite might be the c-axis expansion of pyrolytic graphite (approximately 14×10^{-6}/°F, [5]). The axial expansion of the yarn will be less than 0.1 of that. The above equation then predicts that gaps of up to 0.002 inch in a unit cell 0.03-inch wide will be closed by the time the composite reaches graphitization temperature (approximately 5,000°F). Another effect, illustrated in Figure 12b is that differential expansion at an originally flat surface might automatically give an initial surface roughness of one or more mils.

Another consequence of the model outlined in Figure 10 is that graphitization of a partially processed billet may result in dimensional growth. The mechanism is related to the fact that the cracks formed on cool-down from the previous graphitization have been infiltrated with new matrix material. Thus, the transverse thermal expansion of the yarn bundles is no longer accommodated by crack space closure, but results in forces that cause the yarns to creep axially upon heating. Such growth is actually observed (Figure 13) and, in accordance with implications of the model, is greater in directions of lesser fiber area fraction. In some recent process runs, the growth became great enough in the latter stages of densification of the composite to offset any gains in density that might have resulted from the addition of mass to the matrix.

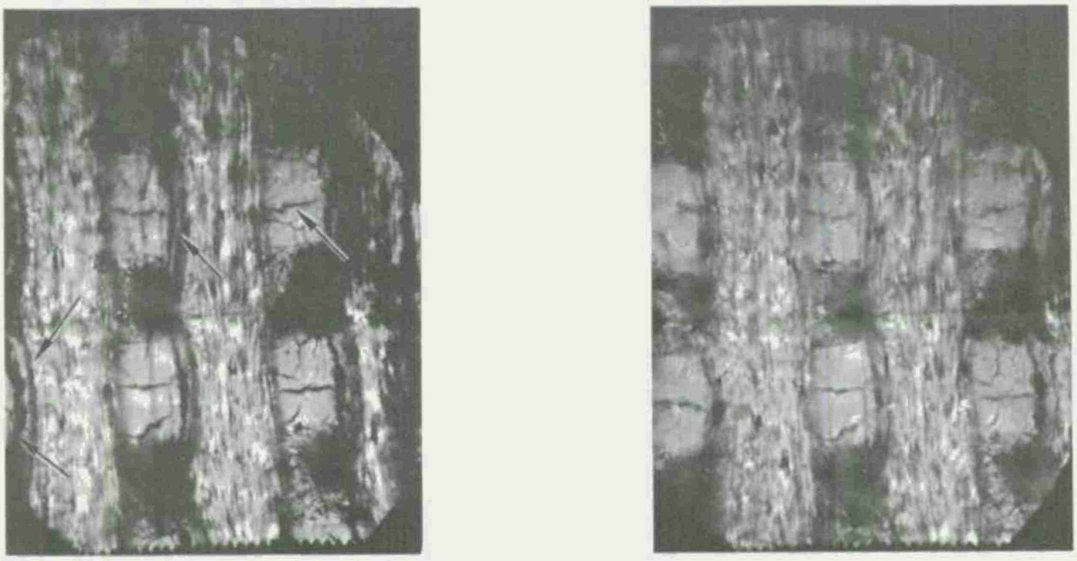

70°F

1,900°F

Figure 11. Photographs of Polished Surfaces of MDAC Material D at Room and Intermediate Elevated Temperatures (Approximately 30X). Note narrowing of most crack features such as those indicated by arrows. Virtually complete closure is expected when graphitization temperature is reached. Material D was processed using low-pressure pitch processing, 2800°C graphitizations, and a standard 223 preform (Thornel 50 yarns).

WD2694

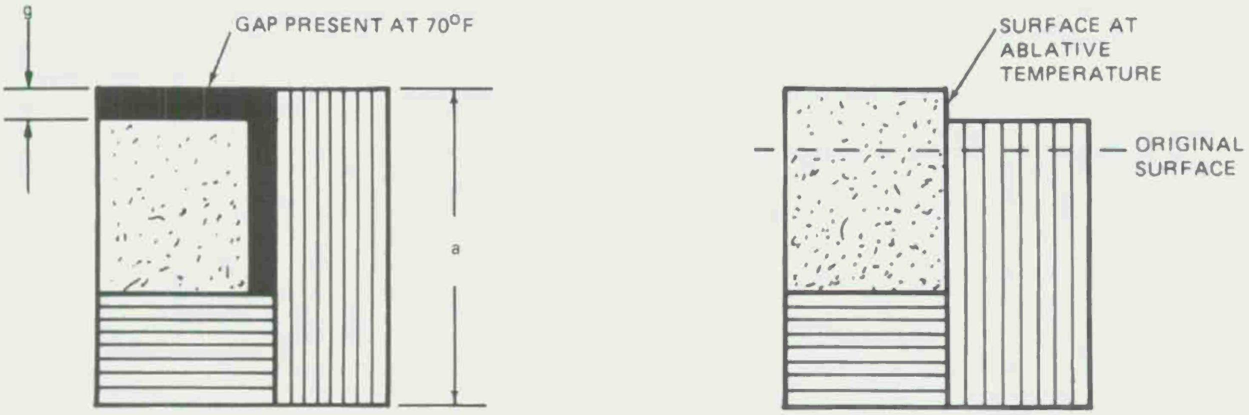
g
GAP PRESENT AT 70°F
a
SURFACE AT ABLATIVE TEMPERATURE
ORIGINAL SURFACE

A. UNIT CELL AND NOMENCLATURE

B. SURFACE EFFECT

Figure 12. Simple Thermal Expansion Model for Unit Cell

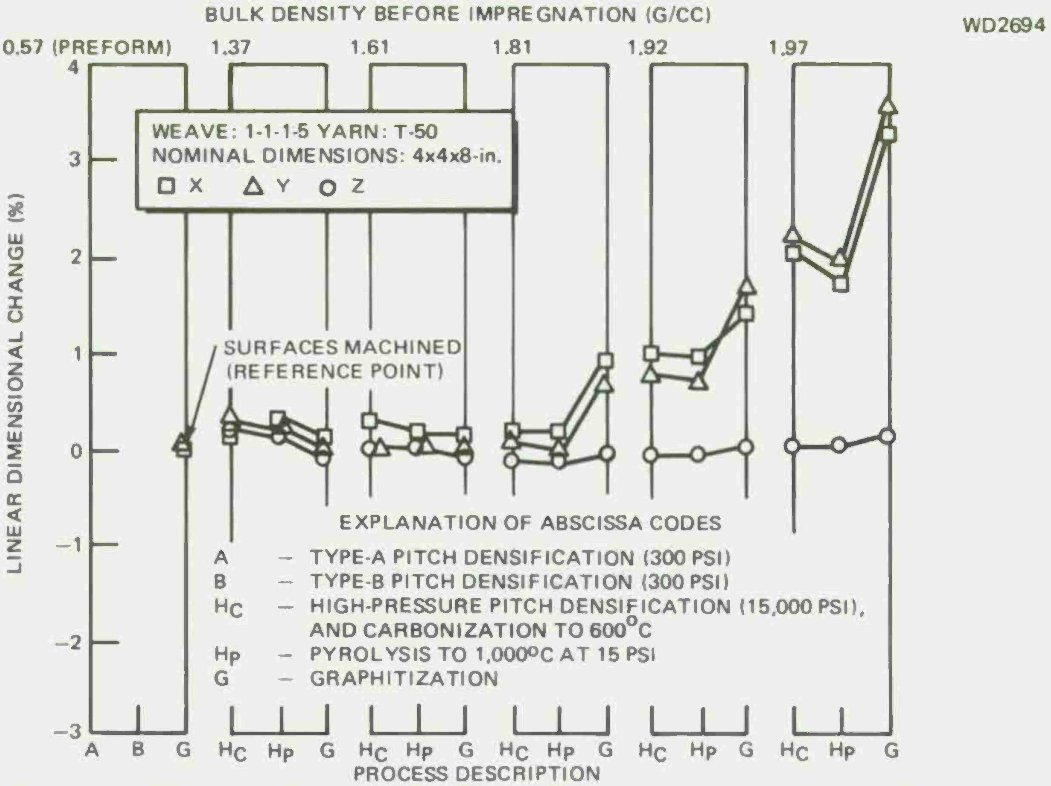

Figure 13. Typical Dimensional Changes as a Function of Individual Carbonization and Graphitization Steps for Billet with High Yarn Fraction in Z Direction

SOME IMPLICATIONS REGARDING PERFORMANCE

The existence and postulated nature of the microstructural crack pattern in graphitized 3D carbon-carbon composites has some obvious implications with regard to the materials' behavior.

The thermal expansion of a 3D composite is influenced by the presence of the crack pattern. The crack space allows the yarn bundles to expand transversely without exerting force on the orthogonally oriented yarns. Thus, up to the temperature at which the cracks are closed, the thermal expansion of the composite may be expected to equal that of a yarn bundle in its axial direction. Recent measurements (on materials like that shown in Figure 6), summarized in Figure 14, fully corroborate this inference. For the 3D composite, the thermal expansion is the same in the Z and X directions (in spite of a two-to-one difference in the respective fiber area fractions) and is equal to that of a unidirectional composite processed in much the same way. Near 5,000°F, the X-direction expansion deviates from the Z-direction expansion, implying that some significant degree of force is transmitted across crack faces at higher temperatures.

It is perhaps of interest to estimate the extent to which conventional analysis, which ignores the existence of open cracks, would err in predicting thermal expansion. To this end, finite-element calculations were recently made (by R. L. Miller, using the SAP IV Code [6]) to predict the

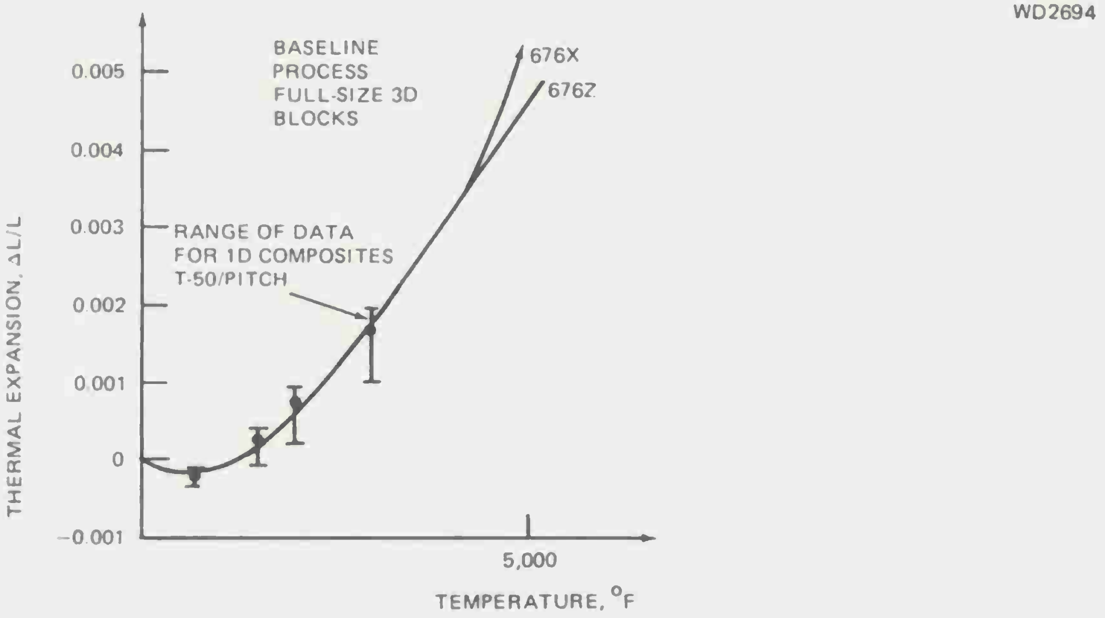

Figure 14. Thermal Expansions of Graphitized 1D and 3D Carbon-Carbon Compsites (REVMAT data)

thermal strain in a 223 carbon-carbon using the estimated constituent properties shown in Table I. In these calculations, the unit cell was modeled with eight elements, two of the elements representing matrix

Table I. Properties Assumed in Calculation of Composite Thermal Expansion

Property		Anisotropic Yarn Bundle	Isotropic Matrix
Young's Moduli 10^6 psi	E_{AA}	36	0.7
	E_{TT}	0.9	
Shear Moduli 10^6 psi	G_{AT}	1.2	0.3
	G_{TT}	0.38	
Poisson's Ratios	ν_{AT}	0.2	0.15
	ν_{TT}	0.2	
Thermal Strain per 1,000°F	α_A	0.001	0.003
	α_T	0.007	
Subscripts: A = Axial; T = Transverse			

pockets and the rest representing portions of yarn bundles. Intimate contact between yarn and matrix and between yarns was assumed. The results predict the X-direction expansion to be 40% higher than in the Z-direction, and 60% higher than measured. Thus, the need to account for the crack structure is apparent.

Study of Figure 5 suggests that the strength and stiffness of the 3D composites, when loaded mechanically along a direction parallel to a set of yarns, will be dominated by the properties of that set of yarn bundles because the continuity of load path through transversely-oriented yarn bundles and matrix material is interrupted by the open crack pattern. Thus, it is not surprising that good linear correlations have been observed between tensile strength (and stiffness) and the fiber area fraction in the direction of loading. Shear behavior, however, depends upon the transfer of force from one set of yarns to another. Given the crack pattern of Figure 5, two orthogonal sets of yarns communicate mechanically only through load paths that are of limited area and somewhat tortuous. As the temperature is raised, and cracks close to the extent that frictional load transfer can take place across them, the shear stiffness of the composite should increase. That such an effect does indeed take place is illustrated by the recent measurements of shear modulus shown in Figure 15. The large increase in stiffness of the composite as temperature is increased is tentatively attributed to the closure of cracks within the material.

WD2694

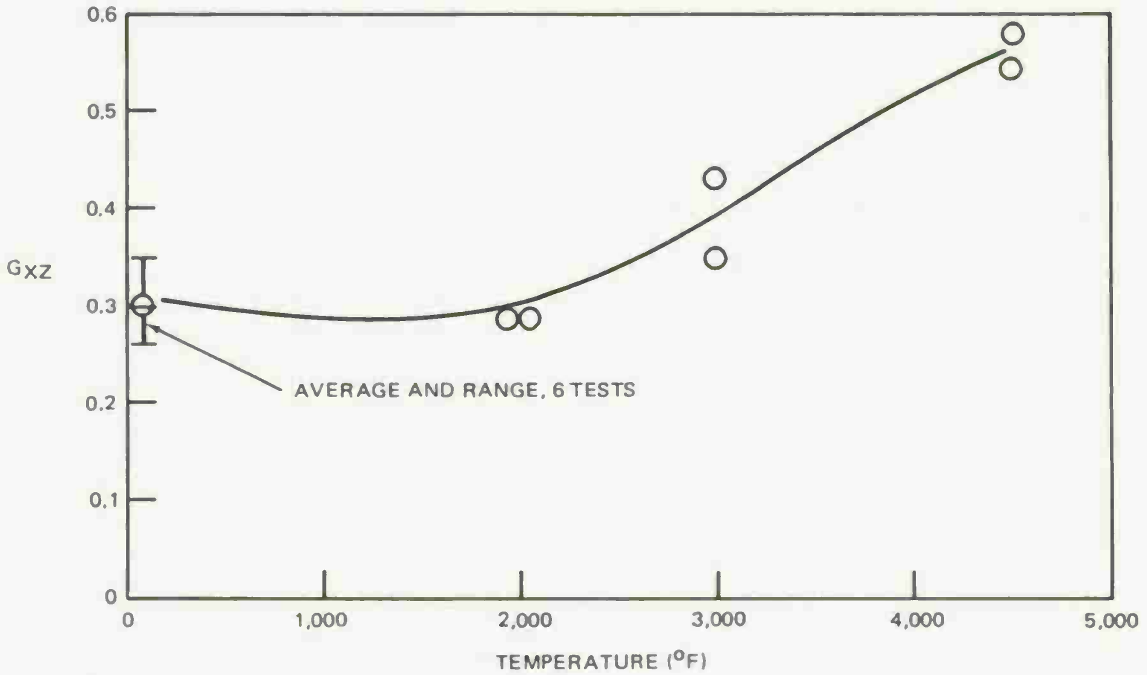

Figure 15. Effect of Temperature on Shear Modulus of 223 Carbon-Carbon (Low-Pressure Pitch Process)

CONCLUSIONS

The processing of orthogonally-reinforced carbon-carbon composites produces microstructural cracking which may be a result of the anisotropic thermal contractions of the yarn bundles upon cooling from the peak process temperature. The temperature dependence of the crack width may account for some ot the thermomechanical behavior of the finished composite. The details of the crack pattern are dependent on the details of the densification process and the thermomechanical nature of the reinforcement yarns. Analytical modeling of the densification process for such carbon-carbon composites, using micromechanical approaches, would appear to be a promising avenue for developing positive approaches to the design and processing of improved materials.

ACKNOWLEDGMENT

The results presented were derived from work sponsored by the Naval Surface Weapons Center (under REVMAT, Contract N60921-74-C-0241) and by McDonnell Douglas (Independent R&D Account 1W1AA115).

REFERENCES

1. Kratsch, K. M., Schutzler, J. C., and Eitman, D. A. "Carbon-Carbon 3D Orthogonal Material Behavior;" paper presented to AIAA/ASME/SAE 13th Structures, Structural Dynamics and Materials Conference, AIAA Paper No. 72-365, April 1972.

2. White, J. L. "The Formation of Microstructure in Graphitizable Carbons;" Air Force Report No. SAMSO-TR-74-93, also Aerospace Corporation Report No. TR-0074 (4250-40)-1, 15 April 1975.

3. Reynolds, W. N. Physical Properties of Graphite, Elsevier Publishing Co., Ltd, London, 1968.

4. Hodgson, Jr., E. W. "Carbon for Aerospace Applications, A Tutorial Review;" Cornell Aeronautical Laboratories Report to NASA, Contract NAS7-742, Report No. DM-2270-E-6, 1 August 1972.

5. Dollof, R. T., and Meers, J. T. "Status and Future of Graphite and Refractory Compounds;" J. of Metals, v. 14, May 1962, 351-354.

6. Bathe, K., Wilson, E. L., and Peterson, F. E. "SAP IV, A Structural Analysis Program for Static and Dynamic Response of Linear Systems" University of California Report No. EERC 73-11, June 1973, revised April 1974.

MICROSTRUCTURAL CHARACTERISTICS OF CRACK PROPAGATION AND ANALYTICAL MODELING OF CARBON-CARBON COMPOSITES

J. S. EVANGELIDES
The Aerospace Corporation
El Segundo, California

ABSTRACT

The use of carbon-carbon composites for thermostructural application requires a basic understanding of the microstructural characteristics that control properties. The objective of this effort was to identify those microstructural factors that contribute to failure of carbon-carbon composites and to apply these data in developing an analytical model for composite tensile behavior. The experimental approach was to observe crack initiation and propagation in unidirectional and multidirectional composites while under load in the scanning electron microscope. The crack propagation studies have shown that the crack path was controlled by highly oriented lamina in the matrix and that fracturing occurred not at the fiber-matrix interface, but within the matrix. The analytical model satisfactorily predicted experimental stress-strain curves only when the filaments were assumed bent and surrounded by a kinked matrix sheath.

INTRODUCTION

The development of advanced carbon-carbon composite systems requires an understanding of the influence of many composite microstructural variables: filaments, matrixes, filament-matrix interactions, construction parameters and processing procedures on composite properties. The need for characterizing microstructure became quite apparent when one attempted to explain the differences in stress-strain behavior of composites fabricated by various procedures. In particular, the measured longitudinal tensile modulus of unidirectional composites fabricated by low-pressure procedures were 67 to 85% greater than that which would have been predicted by the rule of mixtures. Crack propagation studies were conducted to determine by what mode and sequence constituent failures contribute to composite fracture. The identification of microstructural parameters that control crack initiation and propagation in uni- and multidirectional composites was accomplished with miniature notched tensile and double-cantelever wedge specimens. The development and refinement of surface preparation techniques was vital to the observation of matrix structure and composite failure modes.

The analytical tensile model being developed uses the identified microstructural characteristics with micromechanical principles to predict the stress-strain behavior of a carbon-carbon composite. The physical model of the composite system consists of three or more phases: filament, highly aligned matrix sheath, and an isotropic bulk matrix. All model input parameters were obtained from experimental measurements or observations in order to eliminate the necessity for estimating parameters. Such a model combined with the experimental proof of validity can provide a valuable means of predicting optimum microstructural features. Therefore, the model can provide guidance for materials research and development and inputs to structural analyses.

DISCUSSION

EXPERIMENTAL PROCEDURES

Surface preparation techniques were developed to investigate the microstructural characteristics of the carbon-carbon composites. The matrix structure of interest, crystallographic orientation of graphite basal planes, and microcracking were enhanced for interpretation by ion etching techniques. Specimens were first metallographically polished and then etched with xenon [1]. With this technique, a significant amount of surface detail that would otherwise have been lost was revealed (Figure 1). The matrix flow lines that were indicative of graphite basal plane orientation and shrinkage cracks were evident only in the scanning electron micrograph taken after ion etching. The structural appearance that was obtained after ion etching was not only a function of the degree of crystallographic orientation, but also the angle at which the graphite basal planes intersected the free surface [2]. Those materials that did not graphitize had a smooth glass-like appearance after ion etching (Figure 2a). When the graphite basal planes intersected the surface at a near normal angle, the etched appearance was well defined lamina, whereas a parallel orientation yielded a flat planar surface. Intermediate orientations yielded a "fish scale" appearance (Figure 2b).

Test specimens for crack propagation studies were selected for controlled slow crack growth. Unidirectional composites were tested in the transverse direction with use of a notched rectangular specimen bonded between steel doublers (Figure 3a), whereas multidirectional composites were tested with a miniature double-cantelever wedge specimen (Figure 3b). Specimens were polished, ion etched, and then loaded in the tensile stage for loading in the scanning electron microscope (SEM). The most detailed micrographs were obtained at SEM operating voltages of 5 to 7 kV.

MICROSTRUCTURAL CHARACTERIZATION

The microstructures of the matrix phase in carbon-carbon composites will affect crack propagation modes and failure mechanisms. Consequently, it was of interest to characterize the microstructure of carbon-carbon composites prior to crack propagation studies. The matrix structure developed was basically dependent on the impregnation and pyrolysis processing pressure as well as the type of matrix and filament precursor. The effect of pressure was particularly evident between individual filaments of a fiber bundle. One series of composites were fabricated with Thornel 50 yarn, both with and without a chemical vapor deposited (CVD) carbon coating and with coal tar pitch (Allied Chemical 15 V) matrix processed under low

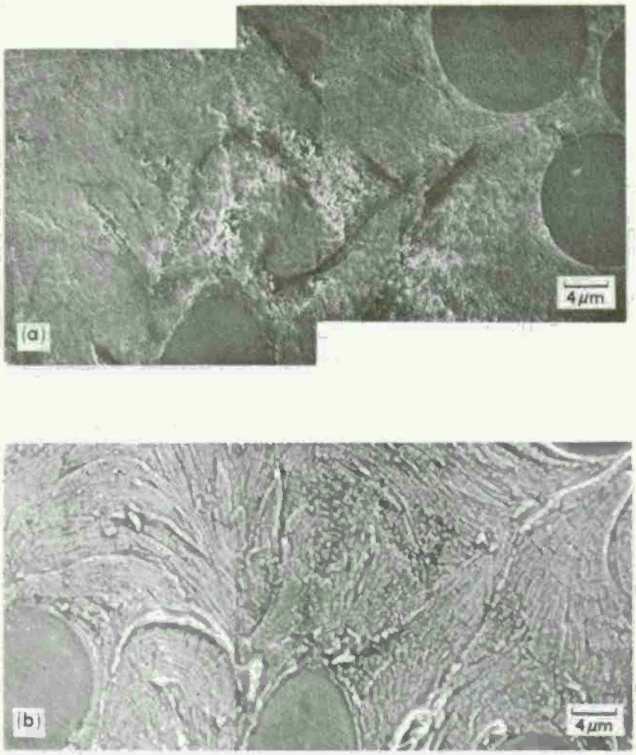

Figure 1 Scanning Electron Micrographs of Carbon-Carbon Composite in Transverse Direction with Effect of Xenon Ion Etching Shown. (a) As polished. (b) Ion etched.

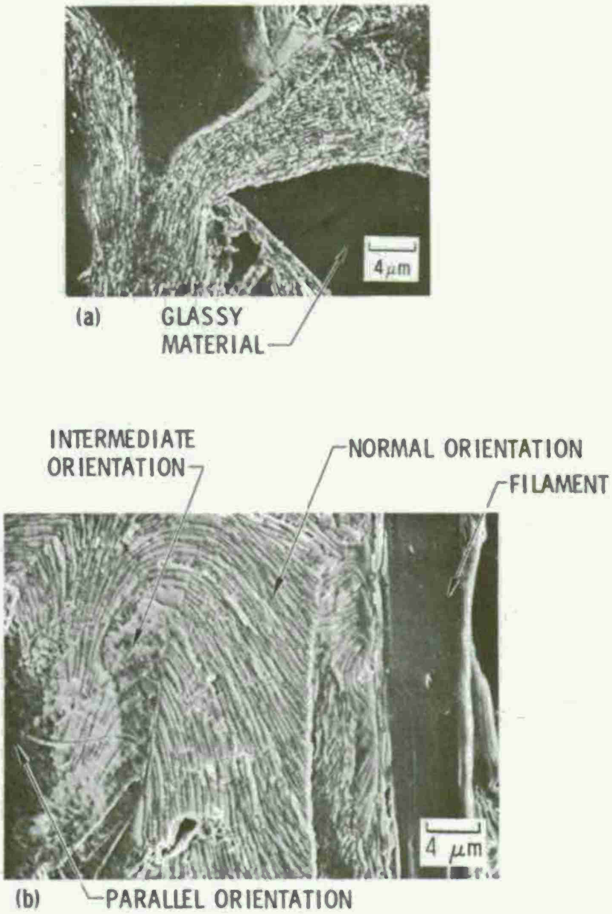
4 μm
(a)
GLASSY MATERIAL
INTERMEDIATE ORIENTATION
NORMAL ORIENTATION
FILAMENT
4 μm
(b)
PARALLEL ORIENTATION

Figure 2 Scanning Electro Micrographs of Carbon-Carbon Composites with Different Matrix Precursors and with Range of Etch Structure Shown. (a) SC1008 phenolic matrix. (b) Petroleum pitch matrix.

pressure (≤1000 psi) impregnation and pyrolysis procedures.* The second series of composites examined was with Thornel 50 yarns fabricated with an initial CVD carbon coating followed by high-pressure (15,000 psi) impregnation and pyrolysis procedures.†

Low-pressure processing resulted in the matrix structure that surrounded the filaments becoming highly aligned such that the graphite layer planes laid parallel to the filament surface, as indicated by the etched lamina (Figure 4). This sheath of graphite basal planes was characterized by slight curvature or waviness [3]. Progressing away from the filament and sheath, the matrix structure became more complex or intertwined and, as such, more isotropic.

A significantly different pitch microstructure was developed with the high-pressure processing. Within a fiber bundle, the graphite basal planes were no longer completely parallel to the filament surface, but were more randomly oriented (Figure 5). In addition, this structure did not have the long-range order of the low-pressure composites. Immediately, at the CVD-pitch interface, the basal planes were oriented at angles from 0 to 90 deg with the 0 deg or parallel orientation predominating; for example, at locations A and B of Figure 5. In a region where the interfilament distance was less than 2 μm, the basal planes were parallel to the filaments (Figure 5 location C). A combination of transversely oriented graphite and parallel alignment at the CVD-pitch interface is shown in Figure 6.

CRACK PROPAGATION

The crack propagation studies were conducted on unidirectional and multidirectional composites fabricated by low- and high-pressure procedures, respectively. Microcrack initiation in the unidirectional composites loaded in the transverse direction occurred at the prepared specimen notch (Figure 3), at large pores (60 μm diam), and at those locations where the graphite basal plane orientation was perpendicular to the tensile axis. The crack propagation path was coincident with the highly oriented basal planes of the matrix (Figure 7). Since the basal plane direction represents the strong direction of the graphite crystal, those planes oriented parallel to the local tensile stress were the most difficult to fracture. Therefore, as the crack propagated through the matrix and encountered unfavorably oriented basal planes, the crack path deviated by as much as 90 deg. Further specimen loading resulted in crack coalescence and multiple fracturing, as indicated by comparing the micrographs in Figure 7.

In the multidirectional composites, tensile cracks occurred initially between the x-bundles and the adjoining bulk matrix pockets (Figure 8).

---

*Fabricated by McDonnell Douglas Astronautics Company

†Fabricated by General Electric Company

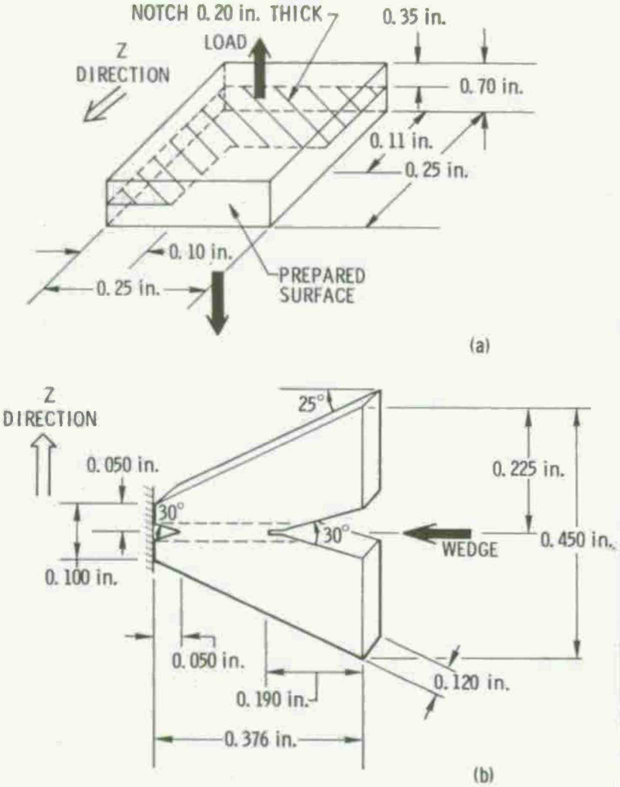
NOTCH 0.20 in. THICK
0.35 in.
Z
DIRECTION
LOAD
0.70 in.
0.11 in.
0.25 in.
0.10 in.
0.25 in.
PREPARED
SURFACE
(a)
Z
DIRECTION
25°
0.050 in.
0.225 in.
30°
30°
WEDGE
0.450 in.
0.100 in.
0.050 in.
0.190 in.
0.120 in.
0.376 in.
(b)

Figure 3 Crack Propagation Specimens for Unidirectional and Multidirectional composites. (a) Unidirectional transverse tension. (b) Multidirectional wedge.

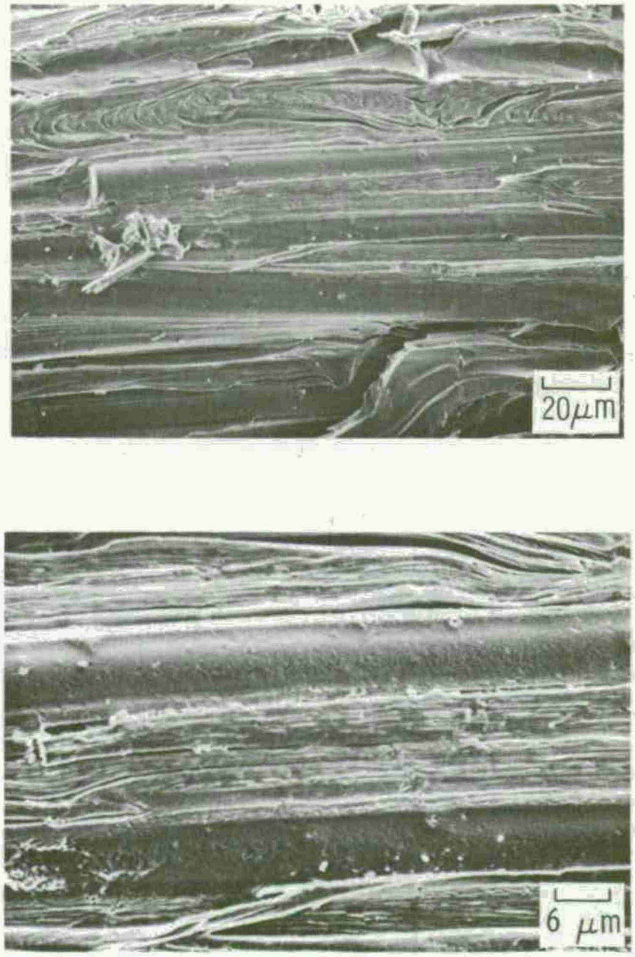

Figure 4 Scanning Electron Micrographs of Typical Microstructures of Carbon-Carbon Composites Fabricated with Low-Pressure Procedures

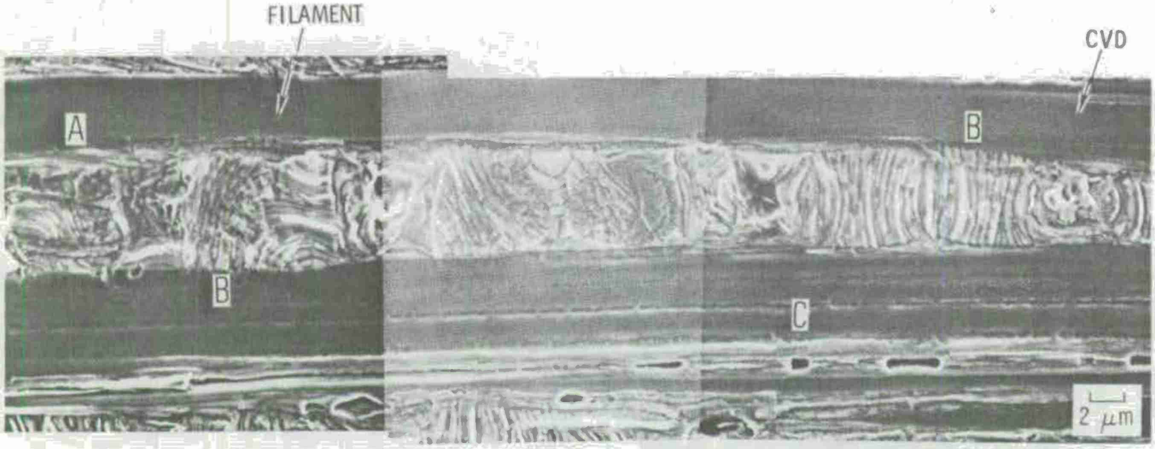

Figure 5 Scanning Electron Micrographs of Carbon-Carbon Composite Processed with High-Pressure Impregnation Procedures

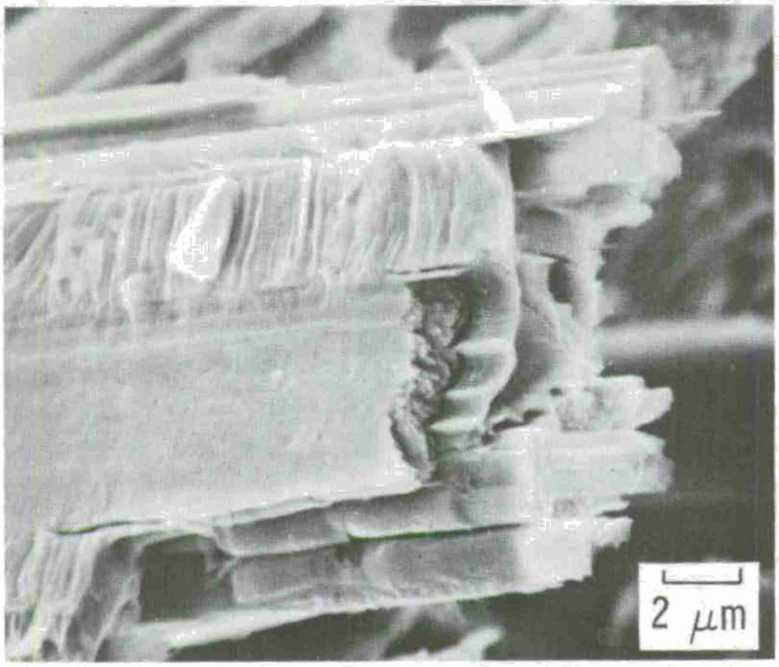

Figure 6 Scanning Electron Micrograph of Matrix Structure Due to High-Pressure Impregnation Procedures

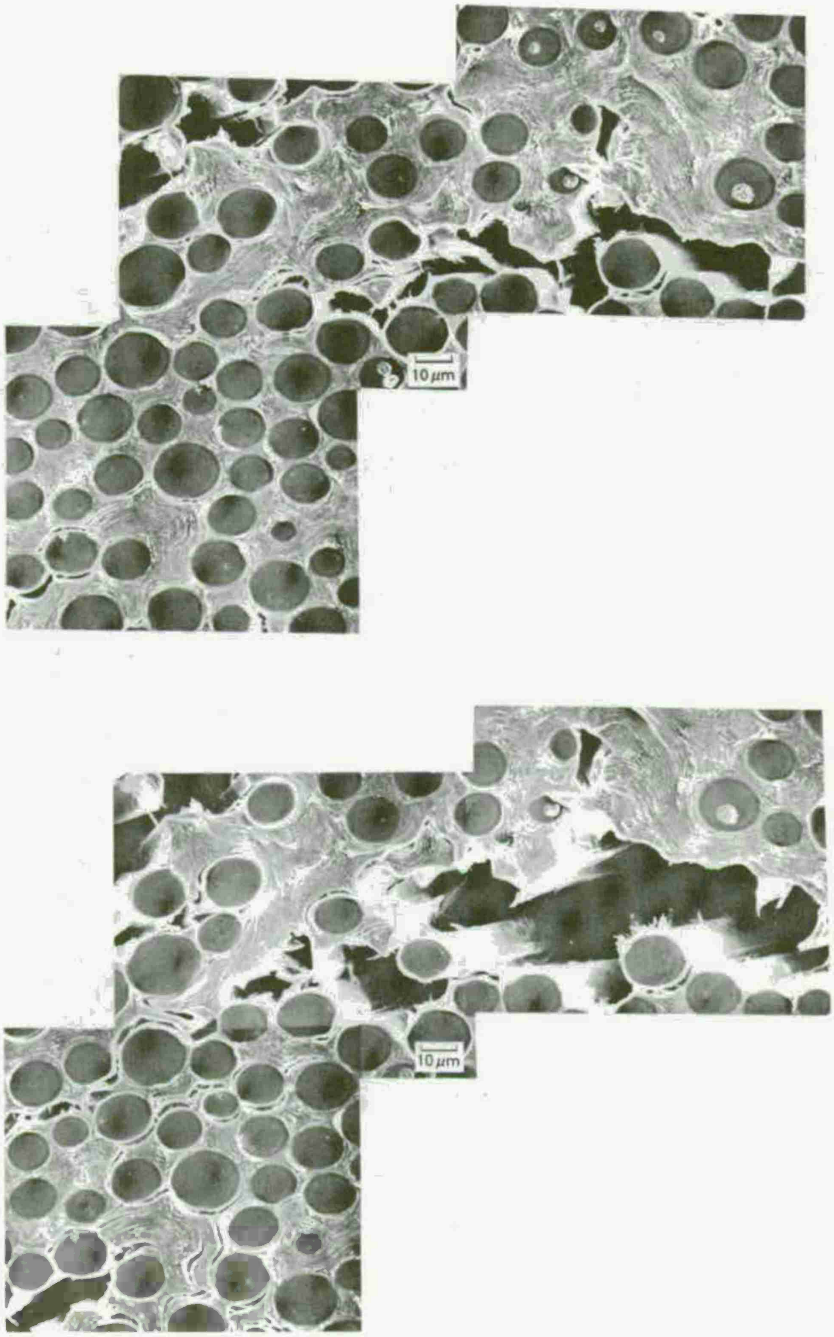

Figure 7 Scanning Electron Micrographs of Crack Propagation and Coalescence in Unidirectional Composite Loaded in Transverse Direction. (a) Initial loading. (b) Final loading.

Generally, filament tensile failures occurred at these matrix fractures, as shown in the top portion of Figure 8. The Thornel 50 fiber used in these composites is a two-ply twisted fiber (1.5 twists per in.). Individual filament fractures within a bundle began at the intersection of the twisted plies and not at random within the plies (Figure 9). Matrix tensile fractures did not always occur at filament fracture sites (Figure 10a, b). However, when they did occur, they were parallel to the graphite basal planes (Figure 10c, d). Generally, matrix shear failures accompanied filament tensile failures; however, there were examples that indicated filament fracture without any matrix failure (Figure 10d). Matrix shear failures could be advantageous in inhibiting continued crack propagation. Figure 11 shows an area of filament and matrix tensile crack that has been temporarily arrested by a matrix shear failure adjacent to, but not at, the filament matrix interface.

ANALYTICAL MODELING

The microstructural and crack propagation studies have provided the basis for developing an analytical tensile model. Through the microstructural analyses, the exceptionally high modulus of composites fabricated by various low-pressure impregnation procedures was attributed to the highly aligned graphitic planes laying parallel to the filaments. This sheath was characterized by a slight waviness or curvature of the aligned graphitic planes (kinks). Progressing away from the filament and sheath, the matrix phase was found to be more complex or intertwined and, as such, more isotropic.

The uniaxial tensile model was developed for a pore-free unidirectional composite consisting of a minimum of three phases: filament, highly aligned sheath and bulk matrix. The constituents were assumed to behave elastically with composite strain equaling the strain of each constituent. It was also assumed that once a filament or sheath fractured, it no longer contributed to composite properties. The load axis was taken parallel to the filament/sheath axis.

The physical model of the composite was initially taken as having straight filaments with a kinked sheath (Figure 12). Filament properties required as input to the model were diameter D_f, tensile E_f and shear G_f moduli, volume fraction V_f, and Weibull distribution parameters. The Weibull distribution was selected to describe the statistical nature of filament strengths [4]

$$G(\sigma) = 1 - \exp\left[-W\left(\frac{\sigma - \sigma_u}{\sigma_o}\right)^m\right] \qquad (1)$$

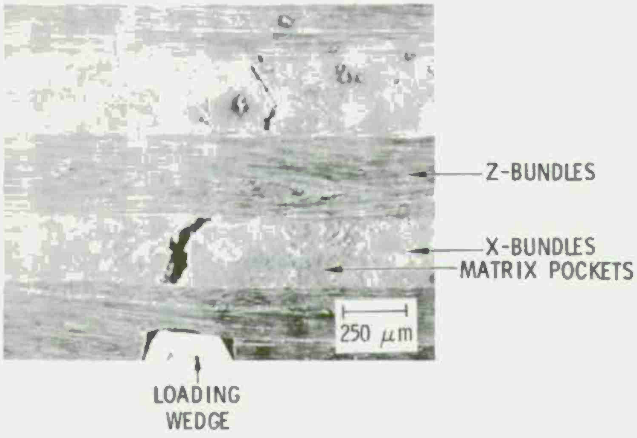
Z-BUNDLES
X-BUNDLES
MATRIX POCKETS
250 μm
LOADING WEDGE

Figure 8 Scanning Electron Micrograph of Multidirectional Composite Wedge Specimen

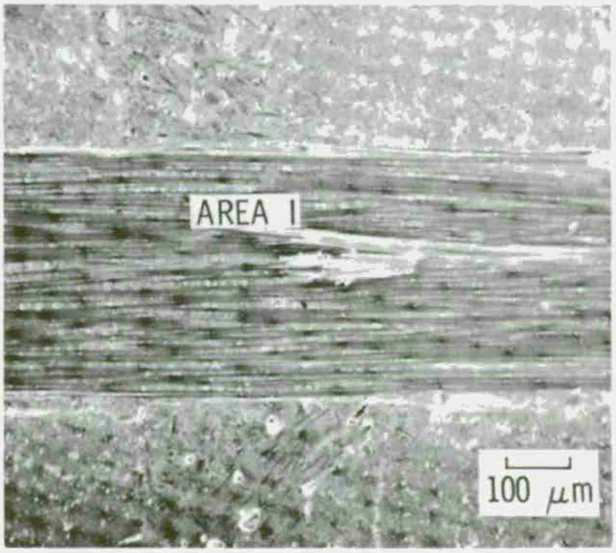
AREA I
100 μm

Figure 9 Scanning Electron Micrograph of Filament Fractures at Ply Intersection

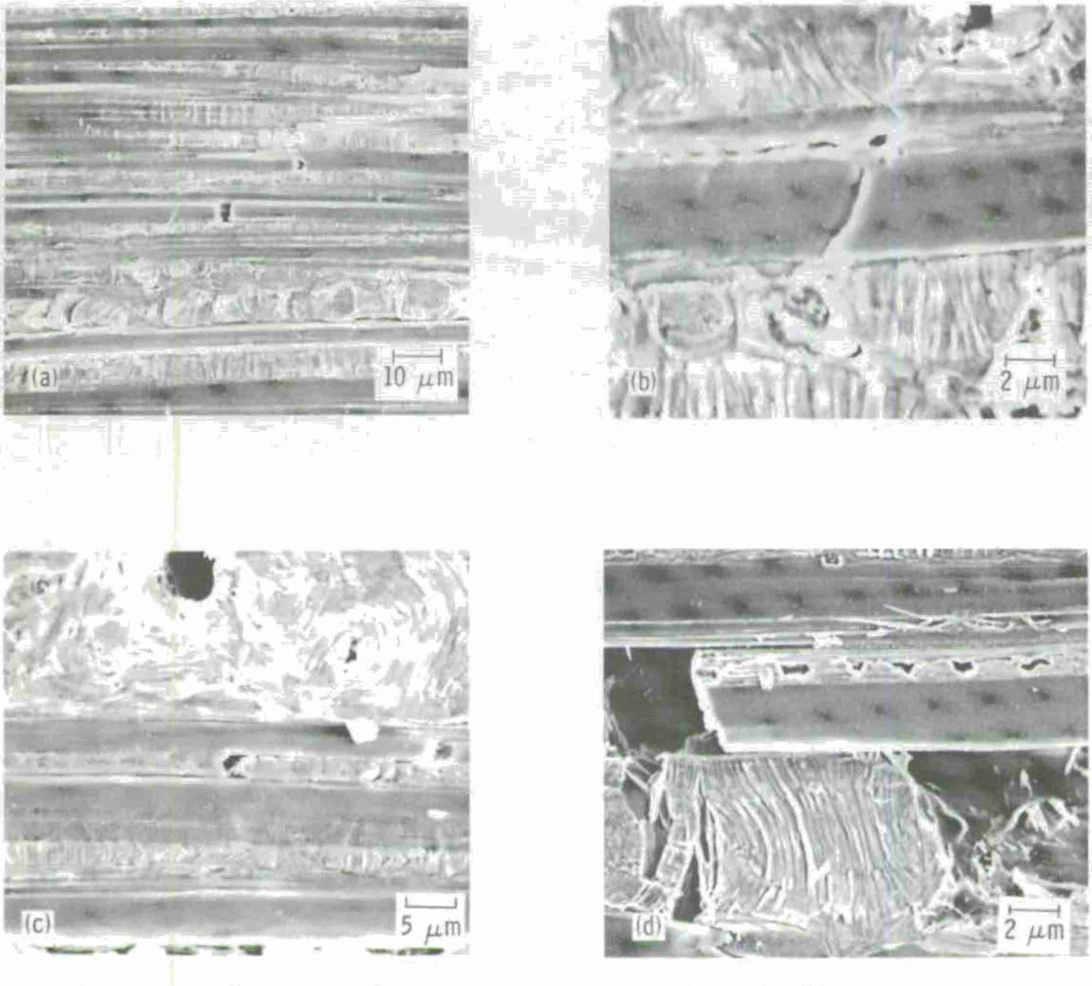
(a)
10 μm
(b)
2 μm
(c)
5 μm
(d)
2 μm

Figure 10 Scanning Electron Micrographs of Filament and Matrix Failures

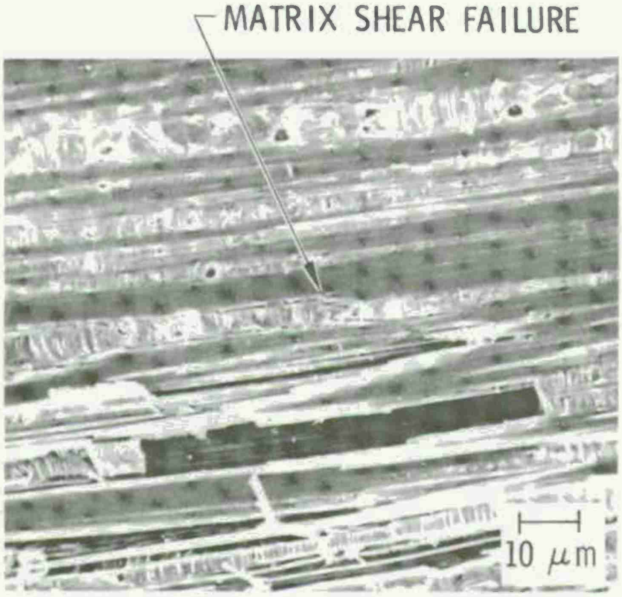
MATRIX SHEAR FAILURE
10 μm

Figure 11 Scanning Electron Micrograph of Filament-Matrix Tensile Crack Arrest

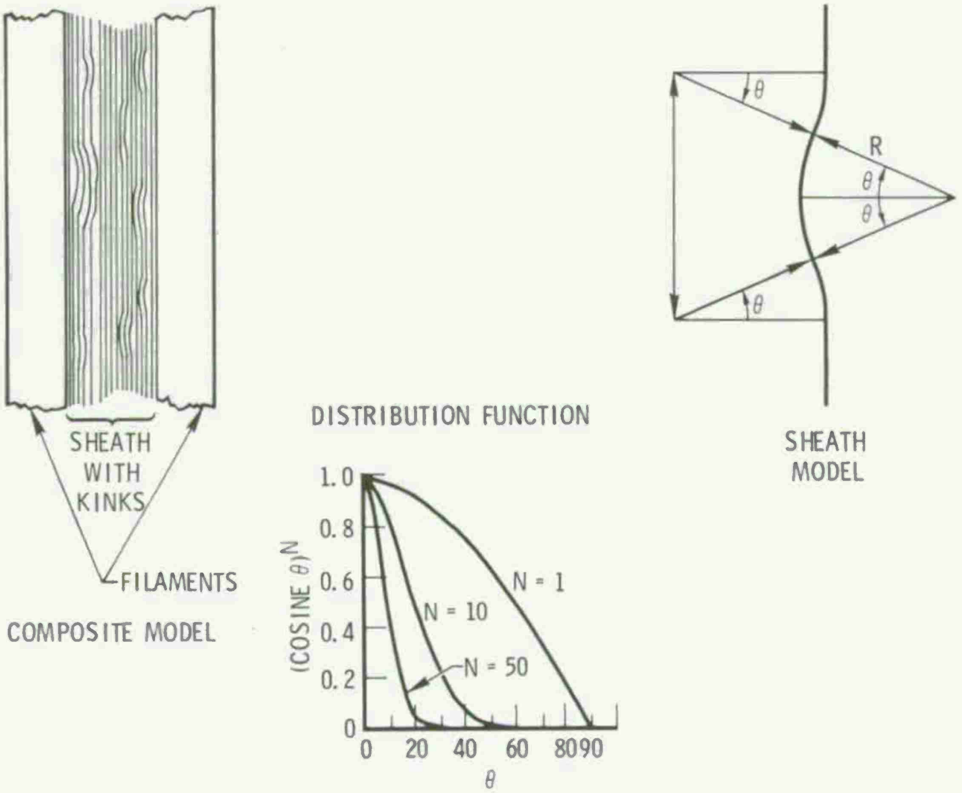
SHEATH WITH KINKS
FILAMENTS
COMPOSITE MODEL
DISTRIBUTION FUNCTION
1.0
0.8
0.6
0.4
0.2
0
(COSINE θ)^N
N = 1
N = 10
N = 50
0
20
40
60
80
90
θ
θ
R
θ
θ
θ
SHEATH MODEL

Figure 12 Composite Tensile Model

where

$W = L/L_o$ = normalized filament length
L = filament length
L_o = 1.0 in.
σ_u = lower limiting strength below which fracture will not occur
σ_o = scale parameter
m = parameter describing data scatter
σ = actual stress on specimen

Ultimate tensile strengths of individual Thornel 50 filaments were experimentally measured at 1.0-in. guage lengths to obtain the Weibull parameters for the model [5].

The required properties for the matrix sheath included thickness T_s, kink radius R, kink angle θ, percent of sheath kinked PER, kink distribution function, graphite single-crystal tensile E_T, and shear G_T moduli, and single-crystal ultimate tensile strength U_{TS}. The distribution of kink angles θ was described by a distribution function of the type $\cos^N\theta$. The exponent N defined the shape of the distribution of kink angles as determined from experimental observation. It is important to emphasize that these are not arbitrary parameters, but were obtained from microstructural characterization of the composites.

Single crystal moduli were taken to be 150.0 and 0.6×10^6 psi for the tensile and shear modulus, respectively [6]. The ultimate strength was taken to be less than the 2800 ksi reported in Ref. 6 because of the large number of defects that were microscopically observed in the sheath structure.

The bulk matrix phase was assumed isotropic with a tensile modulus E_B of 1.0×10^6 psi and an ultimate strength U_{TB} of 1.0 ksi. This phase contributed very little to the overall composite tensile properties.

The maximum angle in the distribution of kink angles was limited by the distance between curved segments of the sheath and the maximum distance between filaments. If the filaments are assumed in a square array, this distance was

$$D_B = D_f \left[\left(\frac{\pi}{4V_f} \right)^{1/2} - 1 \right] \tag{2}$$

The distance between curved segments of the sheath for a given radius R and angle θ was

$$B = 2R\,(1 - \cos\theta) + T_s \tag{3}$$

If this distance was assumed to be equal to or less than half the distance between filaments, the maximum kink angle was

$$\theta_M \le \cos^{-1}\left(1 - \frac{D_B - 2T_s}{4R}\right) \tag{4}$$

Therefore, the distribution function shown in Figure 12 would be truncated at θ_M. The half-distance limit was selected because, between each filament, there are two thicknesses of sheath, and the kink development on each was considered independent.

The portion of sheath with kinks of angle θ_i was obtained from the probability of having angle θ_i, kink length, and the percent of the sheath length that was kinked. The probability was obtained from the distribution function and was given by

$$P_i = \frac{\int_{\theta_i}^{\theta_i+\Delta\theta} \cos^N\theta \, d\theta}{\int_o^{\theta_m} \cos^N\theta \, d\theta} \tag{5}$$

All calculations were done for θ_i increments of 2 deg ($\Delta\theta$). The length of a kink of angle θ_i was given by

$$L_i = 4R \sin \theta_i \tag{6}$$

The portion of sheath with kinks of angle θ_i was given by [7]

$$S_i = P_i \, L_i \, \frac{PER}{\sum_{i=1}^{M} P_i \, L_i} \tag{7}$$

where M was the integer number of 2-deg increments in θ_M.

The effective modulus of the sheath was calculated from the contribution of straight and kinked segments. Taking the kinked sheath as a curved beam, and using the beam theory under plain strain conditions, we derived the modulus by [8]

$$ESB_i = E_T \sin\theta_i \left[\theta_i\,(C1) - \frac{1}{4}\,(C2)\,\sin 2\theta_i\right]^{-1} \tag{8}$$

where

$$C1 = \frac{R}{K}\left(\frac{3}{2} + 2\cos^2\theta_i - 2\cos\theta_i\right) + \frac{1}{2}\left(3 + \alpha\,\frac{E_T}{G_T}\right)$$

$$C2 = 1 + \frac{3R}{K} + \alpha\,\frac{E_T}{G_T}$$

$$K = R - T_s/\ln[(R + T_s/2)/(R - T_s/2)]$$

ESB_i = modulus of kinked sheath containing angle θ_i

α = geometric constant

= 3/2 for rectangular cross section

The effective modulus of a sheath with θ_i angles, where i goes from 1 to M, was given by

$$E_s = \frac{E_T \prod_{i=1}^{M} ESB_i}{\left(\prod_{i=1}^{M} ESB_i\right)\left(1 - \sum_{i=1}^{M} S_i\right) + E_T\left[\sum_{i=1}^{M}\left(S_i\left[\frac{1}{ESB_i}\prod_{j=1}^{M} ESB_j\right]\right)\right]}$$

The composite modulus was then calculated from the rule of mixtures

$$E_C = E_f\,V_f + E_s\,V_s + E_B\,V_B \tag{10}$$

where V_s is volume fraction of sheath and V_B is volume fraction of bulk matrix. The volume fraction of sheath was calculated from filament diameter, sheath thickness, and filament volume fraction

$$V_s = A_s/A_T \tag{11}$$

where

A_s = sheath cross-sectional area
$= \pi(D_f T_s + T_s^2)$
A_T = total cross-sectional area
$= A_f/V_f$
A_f = filament cross-sectional area
$= \pi D_f^2/4$

The maximum stress for a kink of angle θ_i occurs at the point of maximum curvature and was given by [8]

$$\sigma_{M_i} = \left[\frac{2T_s (1 - \cos\theta_i)}{B(2R - T_s)} + 2\cos\theta_i - 1\right]\sigma_s \tag{12}$$

where

σ_s = stress on sheath due to applied stress $\sigma_a = \frac{E_s}{E_c}\sigma_a$
$B = \frac{R}{T_s}\ln\frac{R + T_s/2}{R - T_s/2} - 1$

Sheath failure will occur when σ_{M_i} is greater than the ultimate strength of the single crystal. For an applied stress σ_a, failure will occur in sheaths with kink angles greater than a critical angle θ_c. This angle was derived from the above equation by letting $\sigma_{M_i} = U_{TS}$ and solving for θ_c

$$\theta_c = \cos^{-1}\left[\frac{\gamma Q + Q - 2T_s}{2(Q - T_s)}\right] \tag{13}$$

where Q is $B(2R - T_s)$, and γ is U_{TS}/σ_s.

The probability of failure depends on the probability of having an angle equal to or greater than θ_c. This was given by

$$PSF = \frac{\int_{\theta_c}^{\theta_M} \cos^N\theta \, d\theta}{\int_{o}^{\theta_M} \cos^N\theta \, d\theta} \tag{14}$$

The probability of filament failure was given by the Weibull distribution [Eq. (1)], where σ was set equal to σ_f $(E_f \sigma_a / E_c)$. The probability of bulk matrix failure was

$$\mathrm{PBMF} = \begin{cases} 1 & \sigma_B \geq U_{TB} \\ 0 & \sigma_B < U_{TB} \end{cases} \tag{15}$$

where

$$\sigma_B = \frac{E_B}{E_c} \sigma_a$$

Composite failure required that all constituents fail. The crack propagation results would suggest that some independence of constituent failure exists. Therefore, the probability of composite failure was taken as the product of the constituent failure probabilities. However, future model refinements will include the more rigorous filament/matrix failure interactions. When a filament, sheath, or bulk matrix fractured, the load it was carrying was assumed to be evenly redistributed over the remaining elements (local stress concentrations assumed small). Consequently, the stress carried by the remaining elements was continually increasing as filaments, sheaths, and bulk matrix fractured. A stress redistribution factor was defined for filaments as

$$\mathrm{FRF} = \frac{\mathrm{TN}}{\mathrm{TN} - \mathrm{BF}} = \frac{1}{1 - \mathrm{PFF}} \tag{16}$$

where TN was total number of filaments, and BF was the number of fractured filaments, TN (PFF). A similar stress redistribution factor (SRF) was defined for the sheath. Since it was assumed that a fractured constituent did not contribute to composite properties, constituent volume fractions were reduced as the applied stress was incremented. Filament and sheath volume fractions were recalculated based on the remaining number of filaments or sheaths and the original specimen cross-sectional area. Bulk matrix volume fraction was constant until fracture, at which point it was set equal to zero. By using these new volume fractions, composite modulus was recalculated after each stress increment. The stresses applied to the remaining filaments and sheaths were then calculated by taking into account the change in modulus and the stress redistribution factors, e.g.,

$$\sigma_f = \frac{E_f}{E_c} \mathrm{FRF} \, \sigma_a \tag{17}$$

These stresses were used to calculate composite failure probability in 5 ksi increments. Composite strain at each stress increment was the quotient of stress and composite modulus. Composite failure was taken as the stress at which the total probability of failure was 0.90.

Analytical predictions of stress-strain curves were made for a composite described by the input parameters of Table I. Probability of failure as a function of applied stress for several composites having different input parameters is shown in Figure 13. The effect of varying input parameters on the resulting composite properties is summarized in Table II. Because of the restriction on the maximum permissible kink angle, a variation of two orders of magnitude in the distribution function exponent (NEX) resulted in negligible changes to the stress-strain behavior. The maximum kink angle restriction also resulted in the increase of strength and modulus with an increase in kink radius R. This was due to the fact that, with a larger R, the maximum angle permitted was reduced. This reduction in θ had a much greater affect than the increase in R.

The stress-strain curves for changes in sheath thickness, single crystal ultimate strength, and Weibull parameters (σ_u, σ_o, and m) are shown in Figure 14. A sheath thickness of 0.1 μm had only a minor effect on the tensile behavior of unidirectional composites. However, a thickness of 0.3 μm resulted in a 51% increase in modulus, 19% increase in strength, and 32% decrease in strain to failure. Improvements in composite strength and strain to failure were noted for filaments that had strengths with less scatter (larger m), higher minimum strengths (larger σ_u), and higher-scale parameters (larger σ_o).

Table I Composite Model Input Parameters for Composite I

Filament	Sheath	Bulk Matrix
$D_f = 5.5\ \mu m$	$T_s = 0.30\ \mu m$	$E_B = 1.0 \times 10^6$ psi
$E_f = 60 \times 10^6$ psi	$V_s = 0.14$	$U_{TB} = 1.0$ psi
$G_f = 0.60 \times 10^6$ psi	$R = 10.0\ \mu m$	$V_B = 0.26$
$V_f = 0.60$	$PER = 0.20$	
$\sigma_u = 75.0$ ksi	$N = 10$	
$\sigma_u = 259.0$ ksi	$E_T = 150 \times 10^6$ psi	
$m = 2.2$	$G_T = 0.60 \times 10^6$ psi	
	$U_{TS} = 500$ ksi	

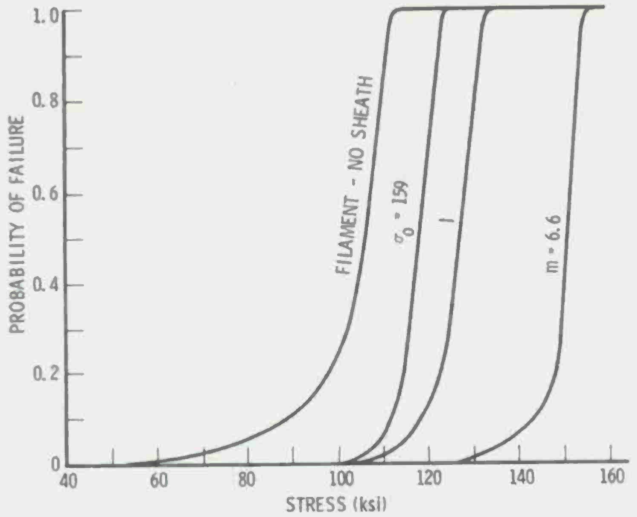

Figure 13 Probability of Failure as a Function of Stress for Composites Listed in Table I

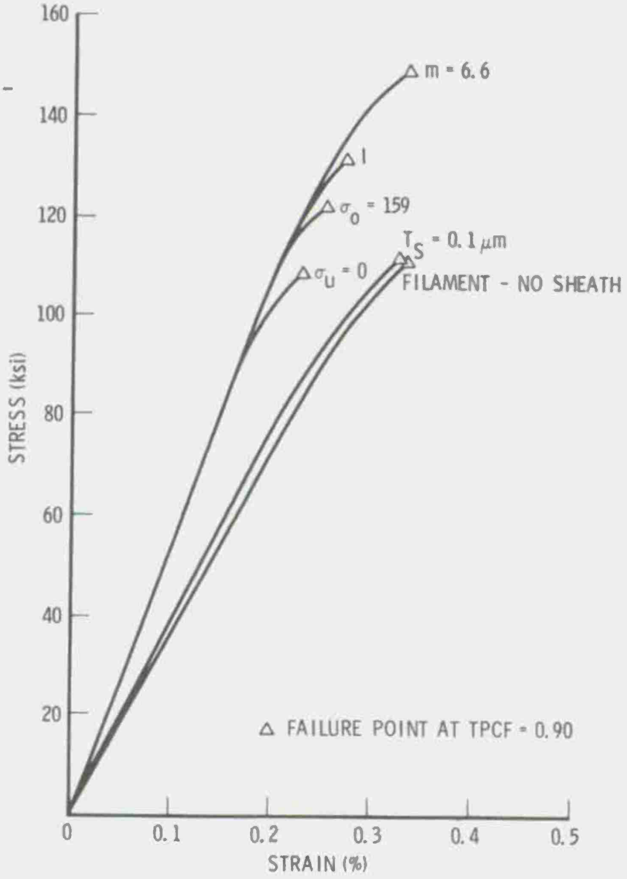

Figure 14 Predicted Stress-Strain Curves for Unidirectional Composites (Table I)

Table II Effect of Varying Composite Input Parameters

Composite Variable	Percent Change With Respect to Composite I		
	Initial Modulus	Failure Strength	Strain to Failure
NEX = 1	0	0	0
NEX = 50	0.2	0.4	0.7
NEX = 90	0.2	0.8	1.8
R = 20	2.4	12.1	10.9
ST = 0	-33.7	-15.9	21.8
ST = 0.1	-29.7	-15.9	18.2
TS = 1000	0	28.8	27.3
$\sigma_u = 0$	0	-17.4	-21.1
$\sigma_o = 159$	0	-7.6	-7.3
M = 6.6	0	16.7	20.0

The stress-strain curve for a composite fabricated by high-pressure impregnation procedures was predicted by taking the majority of the matrix phase as being isotropic with only a thin 0.01 μm sheath thickness, as was suggested from the microstructural characteristics. As expected, the predicted curve was essentially the same as the one with all bulk matrix (no sheath) shown in Figure 14.

In any composite system, there is the possibility of having bent or curved filaments. This was modeled by treating the filament and sheath separately as a curved beam similar to that which was done for the sheath kinks. The filament/sheath bends were on the order of 100 μm as compared with 10 μm for the sheath kinks. The first case considered was one of a single-bend radius RB, angle ϕ, and percentage of filament length that was bent PERB. The probability of having a bend was taken as PB. The equations for constituent properties were redefined to account for this probability of bent constituents. The redefinition of volume fractions was

$$V_{fs} + V_{fb} + V_{ss} + V_{sb} + V_B = 1.0 \tag{18}$$

where

$$V_{fs} = V_f(1 - PB)(1 - PFS) = A_f \frac{TN(1 - PB)(1 - PFS)}{SAT} \tag{19}$$

where V_{fs} = volume fraction of straight filaments

$$V_{fb} = V_f(PB)(1 - PFB) = A_f \frac{TN(PB)(1 - PFB)}{SAT} \tag{20}$$

where V_{fb} = volume fraction of bent filaments and similarly for V_{ss} and V_{sb}. The probability of bent PFB and straight PFS filament failure was as described in Eq. (1) with

$$\sigma_f = \frac{E_f}{E_c} (FRF)\, \sigma_a \qquad \text{straight filaments} \tag{21a}$$

$$\sigma_f = \frac{E_{fb}}{E_c} (FRFB)(SCF)\, \sigma_a \qquad \text{bent filaments} \tag{21b}$$

where

$$FRFB = \frac{1}{1 - PFB}$$

$$SCF = \frac{2D_f (1 - \cos \phi)}{C_f (2RB - D_f)} + 2 \cos \phi - 1$$

$$C_f = \frac{RB}{D_f} \ln\left(\frac{RB + D_f/2}{RB - D_f/2}\right)$$

$$E_{fb} = \frac{E_{fbb} E_f}{E_{fbb} (1 - PERB) + E_f (PERB)}$$

The bent filament modulus E_{fbb} was calculated from Eqs. (8) and (9) by substituting in the appropriate filament bend properties for a single angle. The factor SCF in Eq. (21b) was similar to that in brackets in Eq. (12).

It was assumed that bends in the sheath occurred in straight sections and was not coincident with the kinks. The equations that describe kinked and bent sheath failure were developed as was done for the filaments. The modulus of a bent and kinked sheath was calculated from Eqs. (8) and (9) with the additional angle ϕ of radius RB and portion PERB included. The probability of kinked and bent sheath failure was the sum of that due to the kinks, as described by Eq. (14), and that due to the bend

$$\mathrm{PSFB} = \mathrm{PSF} + \mathrm{PSFBB} \tag{22}$$

where

$$\mathrm{PSFBB} = \begin{cases} 1 & \sigma_{msb} \geq U_{TS} \\ 0 & \sigma_{msb} < U_{TS} \end{cases} \tag{23}$$

The bent sheath stress σ_{msb} was calculated from Eq. (12) by substituting RB for R and ϕ for θ_i.

The equations that describe the tensile behavior of a composite with some fraction of bent filaments and sheaths are now

$$\mathrm{TPCF} = (\mathrm{PFS})\,(\mathrm{PFB})\,(\mathrm{PSF})\,(\mathrm{PSFB})\,(\mathrm{PBMF}) \tag{24}$$

$$E_c = (V_{fs})\,E_f + (V_{fb})\,E_{fb} + (V_{ss})\,E_s + (V_{sb})\,E_{sb} + V_B\,E_B \tag{25}$$

where strain is the quotient of applied stress and composite modulus.

Stress-strain curves were predicted for unidirectional composites with different bend probabilities (Figure 15). If all filaments/sheaths were assumed bent (PB = 100%), the failure stress was reduced by 29%, and the strain-to-failure by 27% for a sheath thickness of 0.7 μm. For a slightly thicker sheath, 0.8 μm, the reduction in strain to failure was the same, whereas the strength was reduced by only 11%.

In order to aid in establishing the validity of this modeling approach, experimental stress strain curves were sought for comparisons. The carbon-carbon unidirectional composites that have been tested and reported have suffered from some degree of filament-load axis misalignment. It has been shown analytically that a misalignment of 1 deg will reduce the strength, 54%, and modulus, 10%, from that of a well-aligned composite [9]. In a study where filament misalignment was measured, a specimen with 1 deg misalignment had a strength of 40.3 ksi, modulus of 55×10^6 psi, and was essentially linear to failure [10]. By applying these strength and modulus reduction factors, a predicted stress-strain curve was obtained for a PB of 100% (Figure 16). The agreement achieved suggests that refinements to the micromechanical modeling effort and further microstructural studies to establish input parameters are definitely warranted.

CONCLUSIONS

The combination of microstructural analyses to characterize composite structure and crack propagation modes, and of micromechanical principles to describe the stress and strain within a material can be used to develop a physically based composite model. The analytical tensile model being developed can predict the experimental stress-strain curves only when (1) the filaments are bent and surrounded by a highly aligned kinked matrix sheath, and (2) filament misalignment is considered. Further analytical modeling is being conducted to include off-axis loading and to consider the filament/sheath bend as a curved beam of two materials. Additional microstructural analyses are needed to establish the microstructural input parameters such as sheath thickness and criteria for maximum kink angle.

ACKNOWLEDGEMENT

The author wishes to acknowledge the support of the Navy REVMAT Program under Air Force Contract No. F04701-75-C-0076.

REFERENCES

1. Meyer, R. A., Zimmer, J. E. and Almon, M.C., "Final Report, Micromechanics of Failure in Carbon System," The Aerospace Corporation Report ATR 74(7408)-2, March 1974.

2. Reiswig, R. D., et al., "Optical and Electron Microscopy of Carbonaceous Materials," Carbon, V.5, 1967.

3. Zimmer, J.E., White, J. L., Evangelides, J. S. and Meyer, R. A., "Carbon Nose-Tip Materials Technology: Microstructure and Fracture of Carbon Materials," The Aerospace Corporation, Report TOR-0076(6726-02)-2, Vol I, September 1975.

4. Weibull, W., "The Phenomenon of Rupture in Solids," Ing. Vetenskaps Akad Handl., No. 153, 1939.

5. Sullivan, P., The Aerospace Corporation, unpublished data.

6. Walker, P. L. and Thrower, P. A., Chemistry and Physics of Carbon, Marcel Dekker, Inc., New York, 1973, Vol. 9.

7. Evangelides, J. S., Meyer, R. A., White, J. L. and Zimmer, J. E., "Carbon Nose Tip Materials Technology: Microstructure and Fracture of Carbon Materials," The Aerospace Corporation, Report TOR-0076(6726-02)-6, Vol. I, September 1976.

8. Timoshenko, S., Strength of Materials, D. Van Nostrand, Inc., Princeton, N.J., 1955, Part 1, 3rd ed.

9. Eitman, D. A., Greszczuk, L. B., and Jortner, J., "Exploratory Development Leading to Improved Carbon/Carbon Composites," McDonnell Douglas Astronautics Company, Report MDC G4730, July 1973.

10. Eitman, D. A., Greszczuk, L. B. and Zelik, J. A., "Exploratory Development Leading to Improved Carbon/Carbon Composites," McDonnell Douglas Astronautics Company, Report MDC G5423, July 1974.

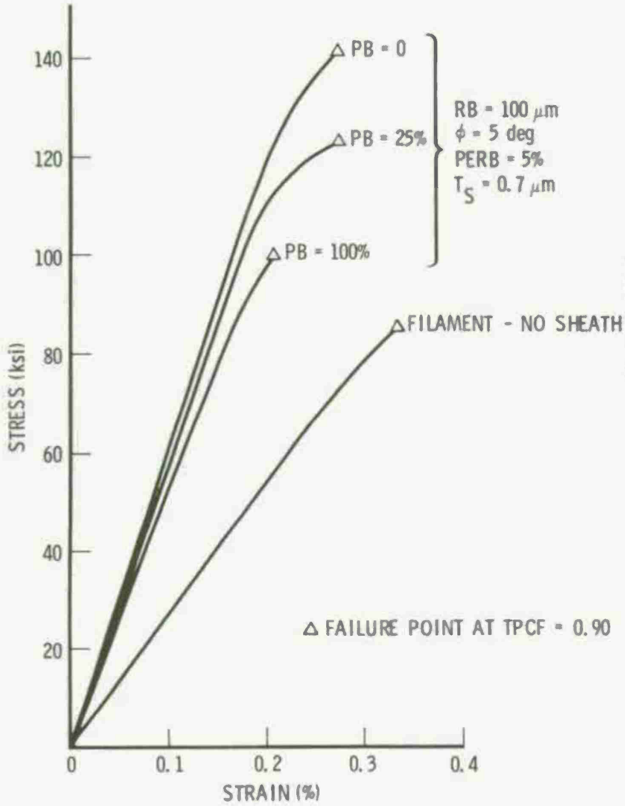

Figure 15 Predicted Stress-Strain Curves for Bent Filament/Sheath

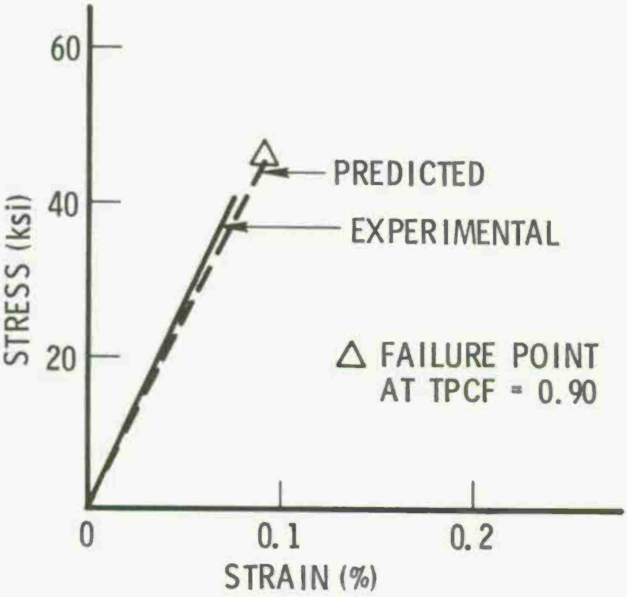

Figure 16 Predicted and Experimental Stress-Strain Curves for Unidirectional Carbon-Carbon Composite Tested in Tension

SESSION V: COMPOSITE APPLICATIONS AND DESIGN CONSIDERATIONS

Chairman: R. A. Pride
Head, Composites Section, Materials Division
NASA-Langley Research Center

EFFECTS OF MANUFACTURING AND IN-SERVICE DEFECTS ON COMPOSITE MATERIALS
R. M. Verette, Northrop Corporation, and E. Demuts, Air Force Flight Dynamics Laboratory 123

DAMAGE TOLERANT STRUCTURAL CONCEPTS FOR FIBER COMPOSITES
J. G. Avery and T. R. Porter, The Boeing Company 138

FAIL-SAFE COMPOSITE ROTOR HUB
R. J. Mayerjak, Kaman Aerospace Corporation, and G. T. Singley, III, Eustis Directorate, Army Air Mobility R&D Laboratory 153

EFFECT OF VARIABILITY OF DESIGN PARAMETERS ON STRESS CONCENTRATION ESTIMATES
E. M. Lenoe and D. M. Neal, Army Materials and Mechanics Research Center 171

EFFECTS OF MANUFACTURING AND IN-SERVICE DEFECTS ON COMPOSITE MATERIALS

RALPH M. VERETTE

Northrop Corporation

EDVINS DEMUTS

Air Force Flight Dynamics Laboratory

ABSTRACT

A number of defects likely to be encountered during the manufacture and in-service use of graphite/epoxy laminates are examined in this paper. Defects studied include errors in curing, those associated with machining operations, errors in assembly, and flaws introduced during service. The consequences of the various defects are examined with regard to the effects they have on static tensile and compressive strength as well as on residual tensile and compressive strength following spectrum fatigue exposure. Three multidirectional laminates typical of aircraft construction are examined in detail. The bulk of the tests are conducted in a moisture saturated condition. Guidelines are given as to the severity of flaws or defects which can be tolerated with acceptably small strength loss resulting.

NOMENCLATURE

2 LT T = 2 lifetimes of tension-dominated fatigue (where 1 lifetime = 4000 hours).
2 LT C = 2 lifetimes of compression-dominated fatigue.
Laminate 1 = $[0/\pm 45_2/0/\pm 45]_s$
Laminate 2 = $[0_2/\pm 45/0_2/90/0]_s$
Laminate 3 = $[0/\pm 45/90]_{2s}$
RTD = room temperature dry
RTW = room temperature wet, where wet means saturated as obtained by continued immersion in 180F deionized water.

INTRODUCTION

Static and residual strengths of composite materials have been examined for a number of years. The bulk of the data presently available are for unflawed laminates. Some data on notched strengths of composites do exist, but these are usually for the case of through-the-thickness slots or holes. Relatively few papers have been presented dealing exclusively with manufacturing or in-service induced defects in composites. These "real-life" defects are characteristically difficult to analyze since they frequently are three dimensional in character. It is important, however, to quantify the effects of realistically occurring defects in laminates. Composites actually produced and placed in service will have to withstand those types of defects which can occur despite our best efforts to preclude their occurrence.

In tracing the various steps which comprise the sequence of events leading from a design concept involving composites to a successful, complete fleet experience of twenty or more years of service (in the case of fighter, transport or bomber aircraft), it is readily apparent that numerous opportunities exist for defects to occur. The defects can be of various kinds. For example, the design itself can be defective; it can specify an inadequate number of plies for strength requirements, inadequate edge distances, overlap lengths, etc. for joining requirements, inadequate stiffness for aeroelastic or flutter prevention requirements, and so on. Design deficiencies can usually be revealed by in-depth analyses and/or design verification tests. Having a validated design, however, is only a necessary but not a sufficient condition for trouble-free performance in service. Many events can occur which make parts produced inferior to those called for in the drawings. The material used in making composite parts may be of inferior quality. Incoming quality control checks can reveal cases where an entire roll of prepreg is substandard and hence a rejection is indicated, but subtleties such as extreme intra-roll variability can exist, giving rise to situations where the incoming quality control requirements are met and substandard material finds its way into composite parts anyway.

There are several ways in which good prepreg material can be improperly stored or handled, thus giving rise to defective composite parts. One may perform incoming quality control and find the material to be satisfactory and, merely as a result of exceeding specified shelf life (typically six months at 0F for graphite/epoxy) prior to layup and cure, one may suffer losses in material properties. Also, by inadvertently exceeding a material's "out time" (time out of the 0F environment), the prepreg can degrade (a typical "out time" is fourteen days for graphite/epoxy). Prepreg used which has been improperly stored can be subject to poor resin flow, creating laminates with variable void, resin, and fiber percentages.

The deficiencies mentioned above can largely be prevented by adequate quality control and proper bookkeeping and therefore will not be emphasized in this paper. It is possible to start with good prepreg at the time of layup and by improper curing produce laminates of inferior quality. Although this can be minimized by maintaining continuous automatically generated autoclave records of temperature and pressure versus time, curing errors of this kind can be made and will be examined below.

After layup and cure, composite parts are machined. At this time, edge cuts are made, contours are formed, bevels and scarfs are introduced, holes are drilled, etc. These operations may be done imperfectly and the consequences of such imperfections are discussed below. After the various parts are machined, they are commonly brought together and assembled to form a completed unit. It is possible to commit errors in assembling the completed parts which can affect structural characteristics. Defects such as edge bruises and poor fastener installation techniques will be discussed below.

Finally, one could perform "flawless" fabrication, but flaws can be introduced during normal maintenance and use. Examples are inadvertent weight drops and surface scratches. These will be the final flaw types to be treated.

In the balance of this paper the effects of several defects are examined for a currently used graphite/epoxy material, AS/3501-5. The properties investigated are the tensile and compressive strengths of unidirectional and multidirectional laminates.

Tensile strengths are determined using straight-sided, tab-ended coupons. Compression strengths are determined using compression test fixtures similar to the one shown in Figure 1, unless otherwise noted. These fixtures are used in conjunction with straight-sided, untabbed compression coupons.

The majority of the data contained in this paper are for laminates which were previously moisture conditioned by continuous immersion in 180F deionized water until saturation, as evidenced by a condition of no further weight gain, was attained. This step was taken to incorporate into the data the moisture effects which would naturally occur over a 20 year (or greater) service life. A typical weight gain curve is shown in Figure 2.

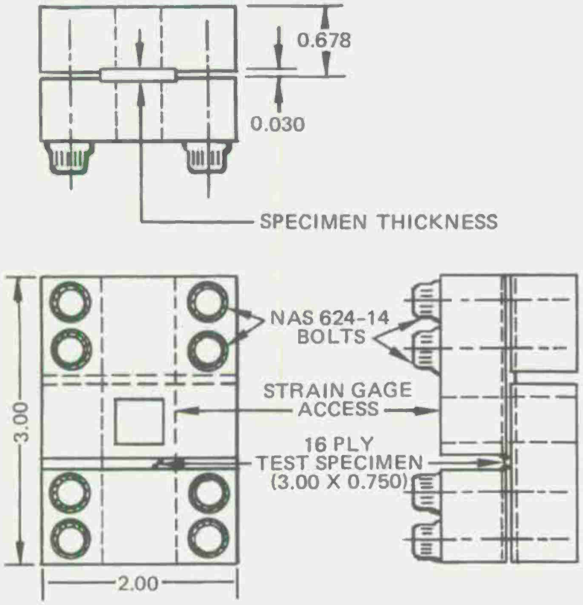

FIGURE 1. COMPRESSION TEST FIXTURE

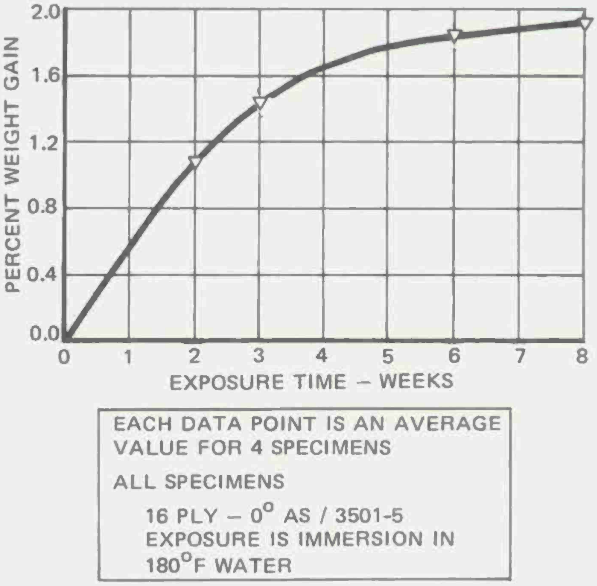

FIGURE 2. WEIGHT GAIN DUE TO MOISTURE CONDITIONING

Three 16-ply midplane symmetric multidirectional laminates typical of aircraft construction are examined in detail in this paper. They are: (1) a laminate containing 25% 0° plies and 75% ± 45° plies; (2) a laminate consisting of 62-1/2% 0° plies, 12-1/2% 90° plies, and 25% ± 45° plies; and (3) a $\Pi/4$ laminate, consisting of equal percentages of 0°, 90°, +45° and -45° plies. In the subsequent portions of this paper these laminates will be referred to as laminates 1, 2, and 3, respectively. In general, all data presented are averages of at least three individual test results, except where specifically noted to the contrary.

The spectrum utilized in this paper is derived from that applicable to the F-5E wing root location. The F-5E has an assumed mission mix of 85% air-to-air usage and 15% air-to-ground. Both tension and compression dominated fatigue spectra are employed. A tension-dominated spectrum is typified by that experienced by lower wing skins. It contains predominantly tension loads although some small infrequently occurring compression loads are present. The compression dominated spectrum is very nearly a mirror image of the tension dominated spectrum. Scaling is such that the maximum spectrum load is adjusted to the lower of (1) the load which will produce the B-basis matrix failure strain in any ply or (2) the load which will produce 83% of the B-basis fiber failure strain in any ply.

PROCESSING DEFECTS

UNIFORMLY HIGH VOIDS

To study the effects of committing processing errors on composites, two conditions were examined. In one series of tests, a standard cure cycle for AS/3501-5 graphite/epoxy, consisting of a single stage cure involving 30 minutes at 350F and 100 psi, was perturbed. The standard cure cycle provides laminates having voids typically well under 1%. The perturbations involved keeping the times and temperatures the same as in the standard cure, but decreasing the maximum pressure from 100 psi to 50 psi in one case (laminate 3 only) and to 30 psi in another case (all three laminates). The laminates produced using the reduced pressures contained more voids, typically 2% for the 50 psi case and from 7% to 8% for the 30 psi case. The voids were uniformly distributed throughout the laminate thickness and throughout the laminate planform. The "undercured" laminates were 8% (50 psi) and 14% (30 psi) thicker than the standard cure laminates. Also they showed evidence of porosity along the machined edges and appeared dry on the laminate top surfaces.

Figure 3 shows the influence of these "undercures" on the room temperature wet (RTW) tensile and compressive strengths of the three multidirectional laminates discussed above. The wet condition is achieved, as discussed above, by accelerated moisture conditioning. In general, Figure 3 shows that (1) compressive strengths are more severely reduced by low pressure cures (i.e., voids) than are tensile strengths; (2) the 50 psi pressure cure laminates (2% voids) are nearly equivalent to the 100 psi cure laminates (~0.5% voids) in strength; (3) laminates containing 7-8% voids are generally weaker statically than are void-free laminates, and spectrum fatigue corresponding to a typical fighter appears to reduce the residual compressive strengths of the high void content laminates more than the "void-free" laminates. In reviewing the data presented in Figure 3 and throughout this paper, values very close to 100% (±5%) are considered to be due to data scatter rather than to any real phenomenological effect.

Figure 4 shows the influence of uniformly high voids on 265F wet* compression strength for $[0]_{16}$ unidirectional laminates tested in the fixture of Figure 1. Heating was provided by quartz lamp heaters which heated the fixture directly and heated the specimens by conduction through the fixture. A uniform state of temperature was achieved throughout the test specimen. Dwell time at temperature was 10 minutes. The void content, 6.7%, was achieved by using the standard cure cycle except that the maximum pressure used was 30 psi instead of 100 psi. Note that uniformly distributed voids up to 6.7% do not affect the average value of longitudinal compression strength although data scatter increased.

---

*In this case, "wet" was 30 days immersion in 180F water.

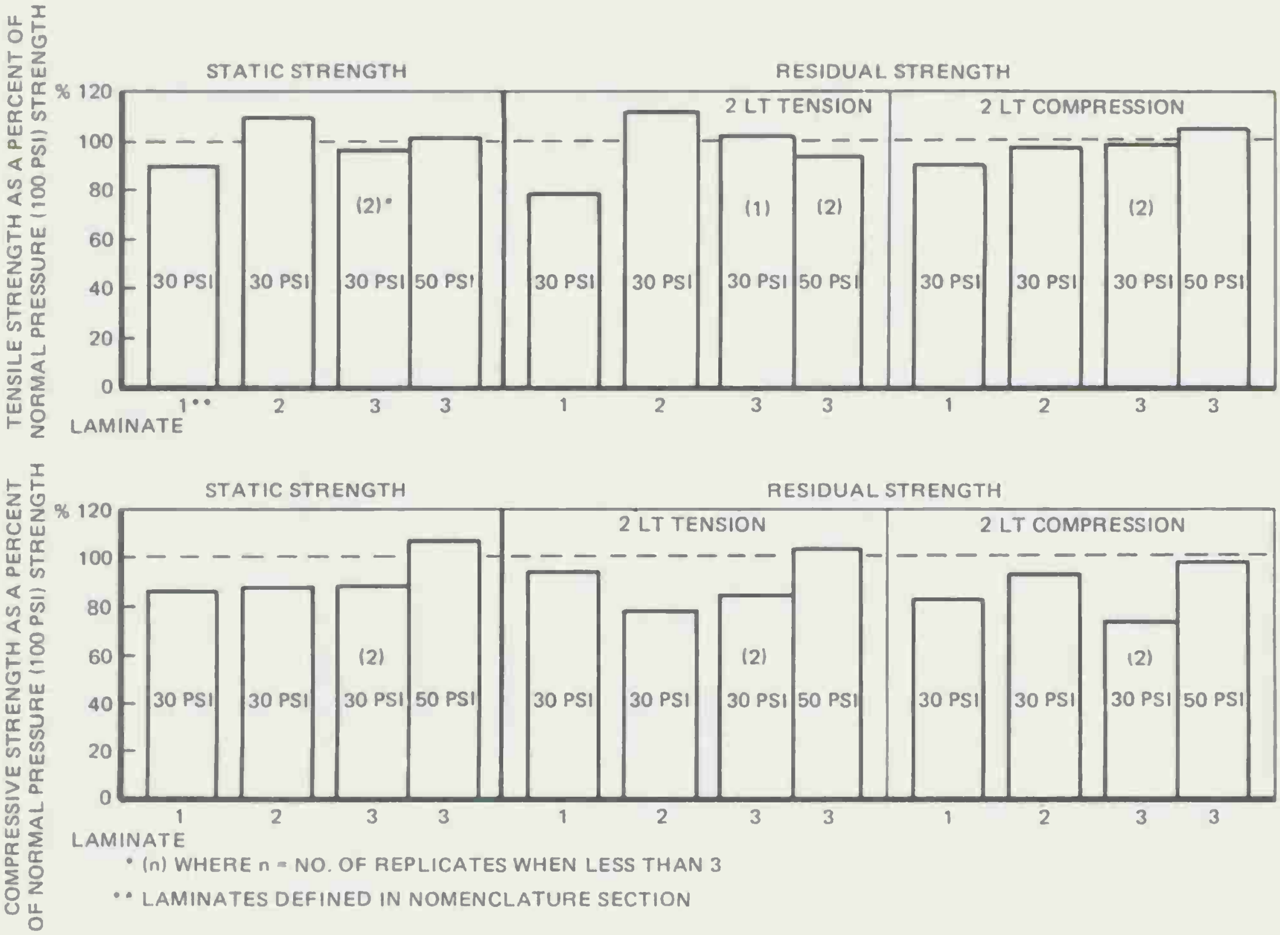

* (n) WHERE n = NO. OF REPLICATES WHEN LESS THAN 3

** LAMINATES DEFINED IN NOMENCLATURE SECTION

FIGURE 3. EFFECT OF UNDERCURE (LOW PRESSURE) ON RTW TENSILE AND COMPRESSIVE STRENGTHS

NONUNIFORMLY DISTRIBUTED VOIDS

A rare case of processing and incoming material quality-induced error can result in nonuniformly distributed voids (through-the-thickness) in composite laminates. On a current research program, one panel out of many hundreds which have been produced had the nonuniform distribution of voids through-the-thickness shown in the photomicrograph of Figure 5. This panel had an average void content, as determined by acid digestion samples taken at several locations around the panel, of about 3.5%. The in-plane void content variation was very slight, but the through-the-thickness nonuniformity was extreme, as shown in Figure 5. It appears that a combination of three factors may have produced this panel: (1) a low quality region of an otherwise acceptable roll of prepreg, (2) poor layup technique resulting in entrapped air bubbles, and (3) improper synchronization of pressure and temperature application during cure. Results for this panel are compared to void-free (less than 0.5% voids) results for the case of longitudinal compression in Figure 6. Note that mild strength reduction occurs because of the presence of the nonuniform voids except for the 265W condition. Here, the specimens with the nonuniform voids exhibit strengths less than 25% of their "void-free" counterparts. The 265W results of Figure 6 are in marked contrast with the uniformly distributed voids results of Figure 4.

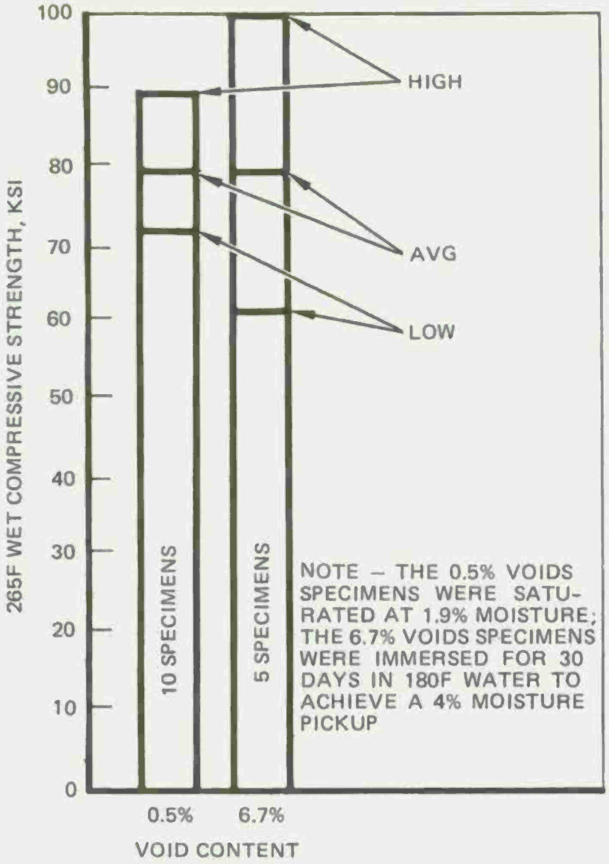

FIGURE 4. EFFECT OF UNIFORMLY DISTRIBUTED VOIDS (BOTH IN-PLANE AND THROUGH-THE-THICKNESS) ON 265F WET LONGITUDINAL COMPRESSIVE STRENGTH

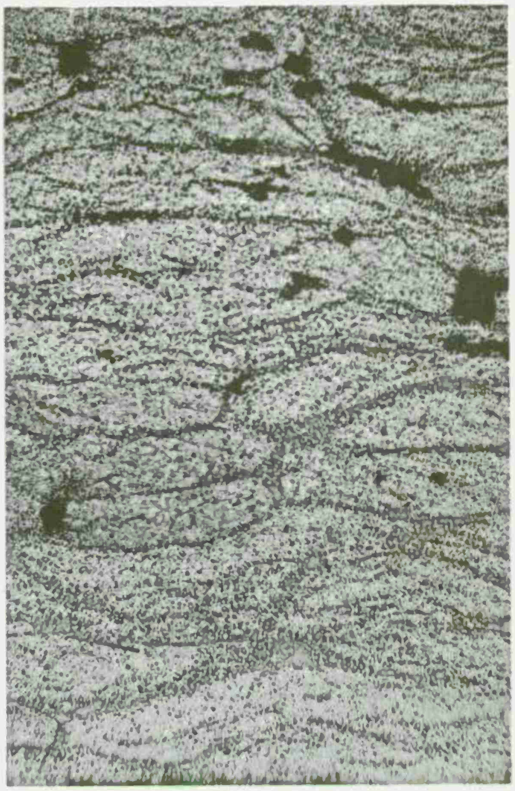

FIGURE 5. PHOTOMICROGRAPH SHOWING NONUNIFORM VOID DISTRIBUTION

MACHINING DEFECTS

When cured graphite/epoxy laminates are machined, several defect types can be introduced. In this paper, two such defects, delaminations at holes and oversized holes are discussed.

DELAMINATIONS AT HOLES

In drilling fastener holes, a defect type which has been observed is the case of a delamination at the exit side of the drilled hole, typically several plies into the laminate. This defect can result because of improper drill speed, improper feed of the part to the drill, or improper backing of the composite part. A series of tests was conducted simulating delaminations by using embedded teflon disks between the second and third plies, counting from the non-countersunk side, of specimens similar to those shown in Figure 7. Note that the specimens contained two countersunk fastener holes, one being a normal hole and one containing a simulated delamination. Test results showing the influence of the simulated delamination on the static and residual

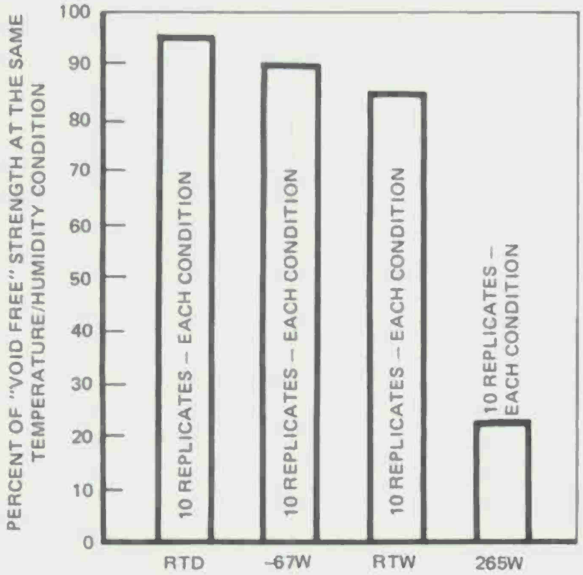

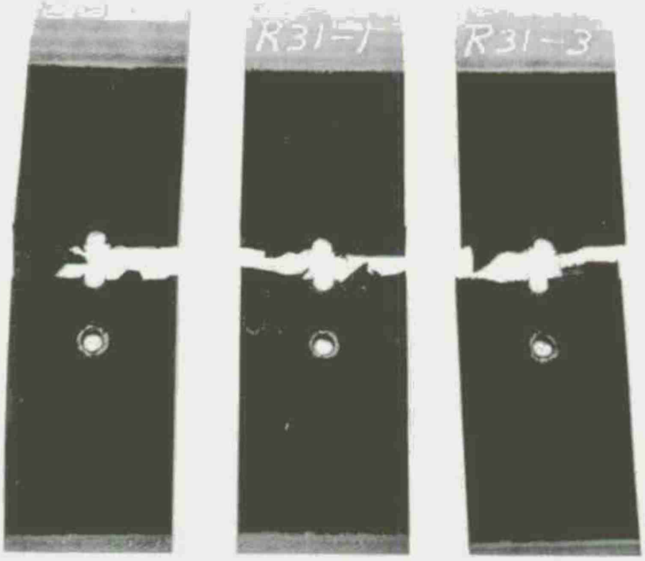

FIGURE 6. EFFECT OF NONUNIFORM DISTRIBUTION OF VOIDS THROUGH-THE-THICKNESS ON LONGITUDINAL COMPRESSION STRENGTH FOR $[0]_{16}$ LAMINATES

FIGURE 7. TYPICAL SPECIMENS CONTAINING FASTENER HOLES

strengths of specimens are given in Figure 8. These data are for the case of filled (i.e., fasteners installed but unloaded) holes. This figure contains information for three different types of hole configurations. One type, unreinforced holes, is the case where holes are drilled into laminates containing no special features in the hole region to accommodate the holes. Another type, reinforced holes, is the case where laminates contain buildups of interleaved plies at the hole location. The buildup produces laminates twice as thick at the hole as in the basic laminate. The ply stacking order is preserved exactly the same, ply-for-ply, in the reinforced area as in the basic laminate. Further, the buildup occurs in such a way as to produce one smooth surface and the other with a "bulge." The last hole configuration studied was the case of softened holes, where the 0° graphite plies in the hole region are replaced by unidirectional E glass/epoxy. In the softened case the ply stacking order was revised slightly to put 45° plies on the outer surfaces. The static results show that the delamination at a hole defect is more detrimental in compression than in tension. The residual strength results show that the application of fatigue does not appear to materially increase the effect of the delamination as compared to the static results.

OVERSIZE HOLES

Another machining error which can be made is the case where holes are drilled too large (larger than called for in the design drawings). This creates an excessively loose fit and may be detrimental to strength. To examine this effect, static and fatigue tests were conducted using specimens containing two holes as shown in Figure 7 where one hole was sized properly and one hole had a fastener/hole clearance five times as

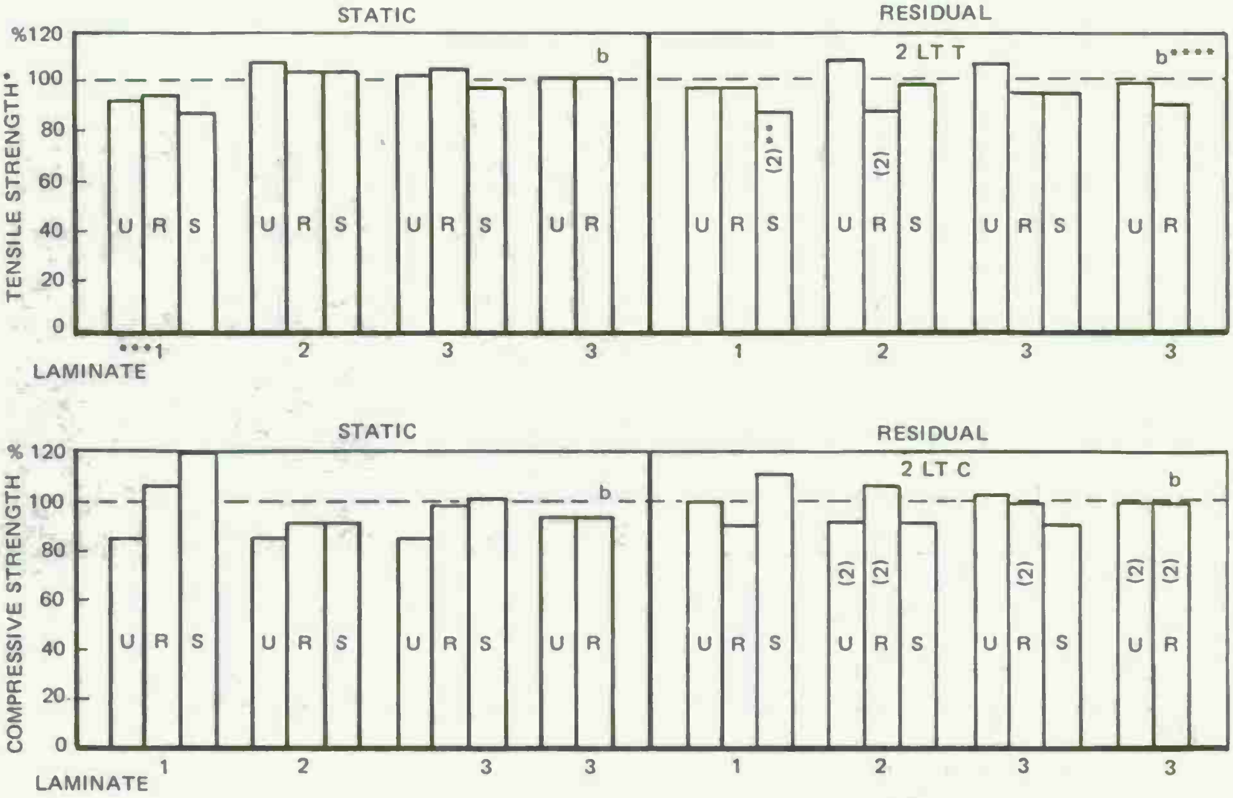

* PERCENTAGES GIVEN ARE PERCENTS OF IDENTICAL TESTS RUN ON NO-DELAMINATION SPECIMENS

** (n) WHERE n = NO. OF REPLICATES WHEN LESS THAN 3

*** DEFINED IN NOMENCLATURE SECTION U = UNREINFORCED, R = REINFORCED, S = SOFTENED

**** b = HOLES NORMAL TO LOAD, ALL OTHERS AS SHOWN IN FIGURE 7

FIGURE 8. EFFECT OF DELAMINATIONS AT HOLES ON RTW TENSILE AND COMPRESSIVE STRENGTHS OF SPECIMENS CONTAINING UNLOADED HOLES

large as the standard clearance. The specimens were tested using the fixture of Figure 9 in which 25% of the load is taken out at the two fasteners. The photo of Figure 9 shows a single loaded fastener. The specimens of Figure 7 were tested using another loading beam which permits two fasteners to be loaded. Figure 10 shows test results for the unreinforced, reinforced and softened cases as discussed previously. The presence of an oversized hole has a negligible effect on the static strength of specimens as shown in Figure 10. Also, as indicated, the residual loaded hole tensile strength is not reduced for a softened specimen compared to the static loaded hole tensile strength. To examine the consequences of a specimen where 100% of the load is taken in bearing, several reinforced specimens were tested containing one oversize and one standard size hole. The results again show no sensitivity to the oversized hole as shown in Figure 10.

ASSEMBLY DEFECTS

Two defects which can arise during assembly of composite parts are treated in this paper. They are overtorqued fasteners and edge delaminations and are discussed below.

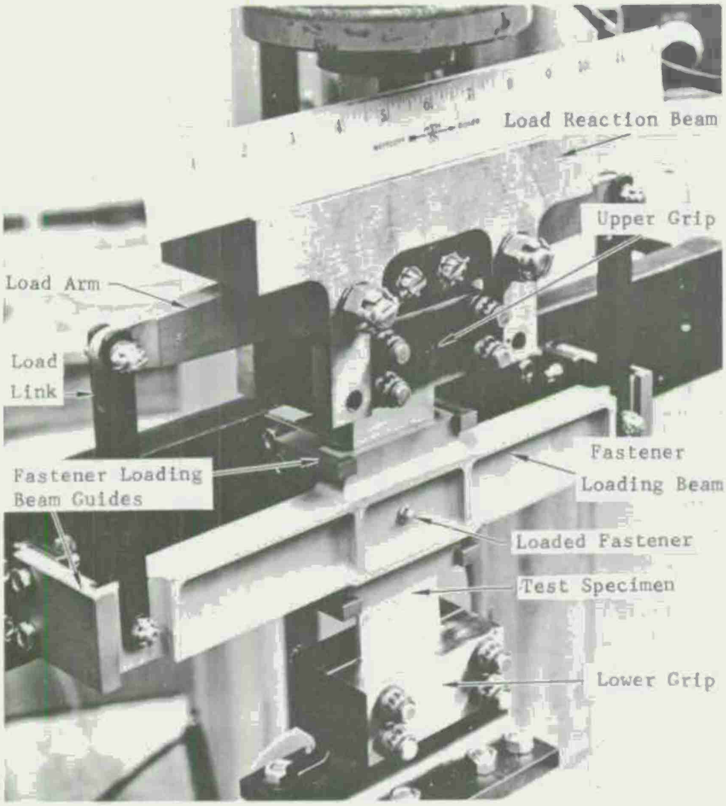

FIGURE 9. LOADED HOLE TEST FIXTURE

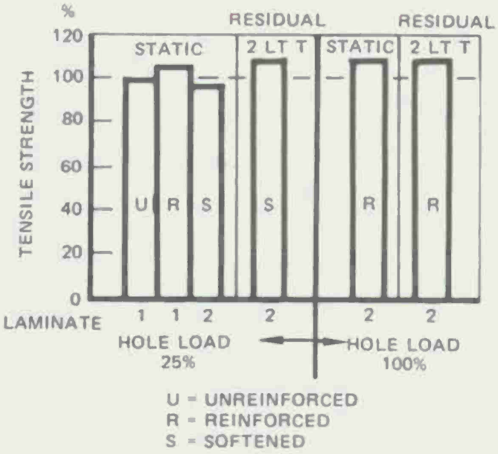

FIGURE 10. EFFECT OF OVERSIZED HOLES ON RTW STRENGTH (IN % OF STANDARD SIZE LOADED HOLE STATIC STRENGTH)

OVERTORQUED FASTENERS

Normal installation procedures for fastening 16-ply graphite/epoxy skins to substructures using 3/16-inch fasteners call for fastener/nut tightening using up to 25 inch pounds of torque. To investigate the possible detrimental effect of overtorquing the fasteners, a series of tests was performed on moisture preconditioned specimens similar to those shown in Figure 7. In the tests, one fastener was torqued to the "standard" 25 inch pound value while the other was torqued to 70 inch pounds, a value selected by trial as being slightly above the onset of noticeable fastener head dimpling, or to a value of torque at which pull through of 0.005 inch was experienced, whichever occurred first. Results of the tests are given in Figure 11. Notice that unreinforced static strengths are degraded more than reinforced or softened static strengths because of the overtorquing. Fatigue exposure seems to increase the sensitivity of the laminates to the presence of an overtorqued fastener.

EDGE DELAMINATIONS

In handling composite parts prior to or during final assembly, the possibility exists that part edges may be bumped or bruised. To assess the influence of edge delaminations, specimens similar to those shown in Figure 12 were tested. These specimens are two inches wide and contain simulated delaminations along one edge. Edge delaminations were simulated by embedding semicircular teflon disks at the laminate quarter thicknesses. Two radii, 0.3 inch and 0.6 inch were used. The resulting RTW strengths are shown in Figure 13. The edge delaminations affect static

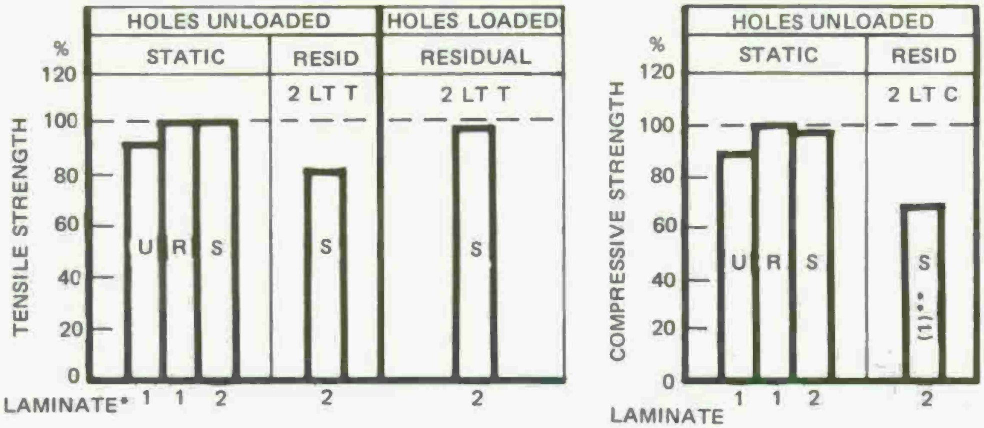

* DEFINED IN NOMENCLATURE SECTION

U = UNREINFORCED R = REINFORCED S = SOFTENED

** TWO SPECIMENS FAILED IN FATIGUE

FIGURE 11. EFFECT OF OVERTORQUED FASTENERS ON RTW STRENGTH (VALUES QUOTED IN % OF UNFLAWED STRENGTH)

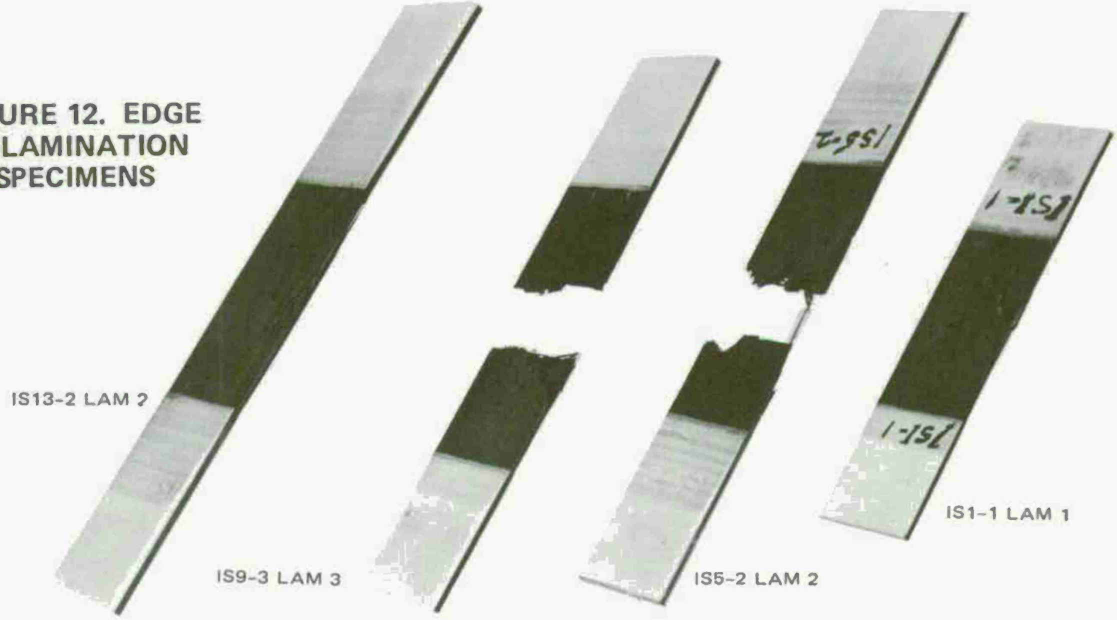

FIGURE 12. EDGE DELAMINATION SPECIMENS

compressive strengths more than static tensile strengths. Also, large delaminations are more detrimental than small delaminations. The tensile fatigue exposure appears to enhance the residual tensile strength, but the compressive fatigue exposure often failed specimens during fatigue as noted in Figure 13.

IN-SERVICE DEFECTS

Two types of in-service defects — surface scratches and foreign object damage — are examined. They are discussed separately below.

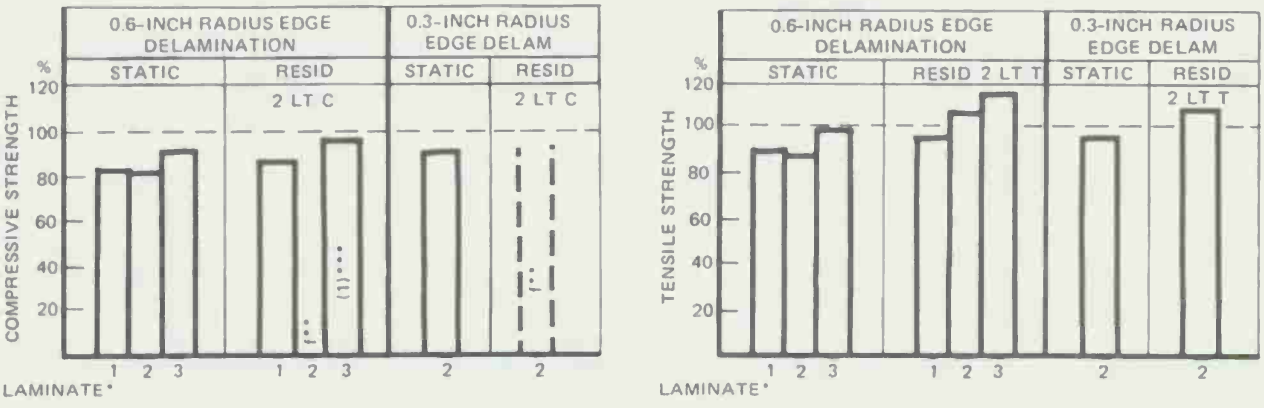

* SEE NOMENCLATURE SECTION

** SPECIMENS FAILED DURING FATIGUE

*** ONE REPLICATE FAILED DURING FATIGUE

FIGURE 13. EFFECT OF EDGE DELAMINATIONS ON RTW STRENGTH (VALUES QUOTED IN % OF UNFLAWED STRENGTH)

SURFACE SCRATCHES

In the course of maintenance and aircraft use, occasions arise in which exposed graphite/epoxy surfaces are inadvertently scratched by tools or other objects. To study this effect, a series of tests was run on specimens containing V-notch scratches of various lengths and depths. The specimens were two inches wide and the scratch lengths were one-half inch and one inch oriented normally to the applied uniaxial load. Typical scratches are shown in Figure 14. Results are shown in Figures 15 and 16. The tensile results were obtained using two inch wide specimens similar to those shown in Figure 17. As can be seen by examining Figures 15 and 16, scratches are detrimental in tension, particularly if they are deep or located along a specimen edge. It should be noted that the specimens tested all had 0° plies cut as shown in Figure 14; no attempt was made to "bury" the 0° plies, and thereby cut only the less critical load carrying plies.

The compression results appear to be less severely affected than the tensile results due to the presence of the scratch. A typical surface scratch compression specimen is shown in Figure 18. This two inch wide specimen is used in conjunction with a stabilization fixture similar to the one shown in Figure 1. The fixture precludes significant out-of-plane motion of the specimen. To get a feel for the influence of test specimen geometry on the sensitivity to surface scratches, several two inch wide sandwich beams containing central scratches were tested. These specimens displayed more out-of-plane motion at failure as shown in Figure 19, and the lack of lateral constraint is thought to be the reason why this specimen shows more sensitivity to scratches than the compression coupon (See Figure 15 for comparison).

FOREIGN OBJECT DAMAGE

To study the effect of Foreign Object Damage (F.O.D.) on laminate strength, a series of tests was conducted on two inch wide specimens. Two impact energy levels

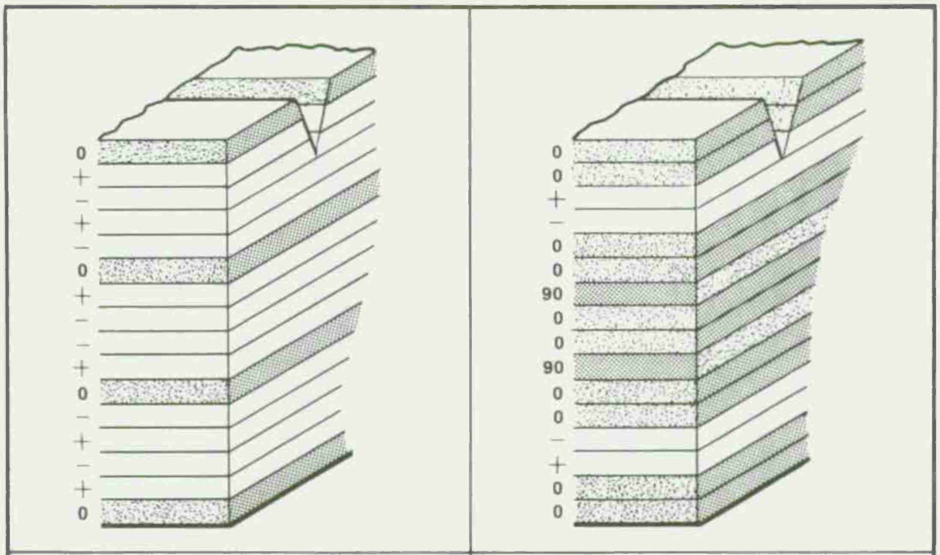

LAMINATE NO. 1
$[0/\pm 45_2/0/\pm 45]_s$ – 3 PLY DEEP

LAMINATE NO. 2
$[0_2/\pm 45/0_2/90/0]_s$ – 3 PLY DEEP

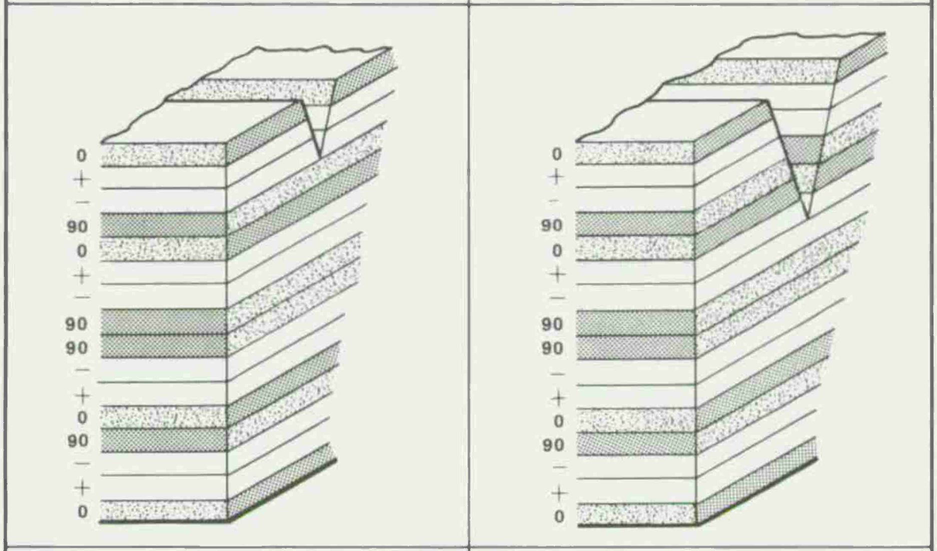

LAMINATE NO. 3
$[(0/\pm 45/90)_2]_s$ – 3 PLY DEEP

LAMINATE NO. 3
$[(0/\pm 45/90)_2]_s$ – 6 PLY DEEP

FIGURE 14. STACKING ORDERS FOR SURFACE SCRATCH SPECIMENS

were defined: energy level 1 is the amount of energy required to cause incipient back face fiber failure while the impacted face, although indented, has no fiber failure; energy level 2 is at the threshold of causing front face fiber failure (it causes substantial back face damage). A spherical indenter was used on specimens resting on a ring support and the energy levels were determined independently for each laminate. The results are shown in Figure 20. Notice that severely reduced strengths are observed, both for the higher energy level and the level which was just barely visible on the non-impacted face and virtually non-detectable (by visual examination) on the impacted face (energy level 1).

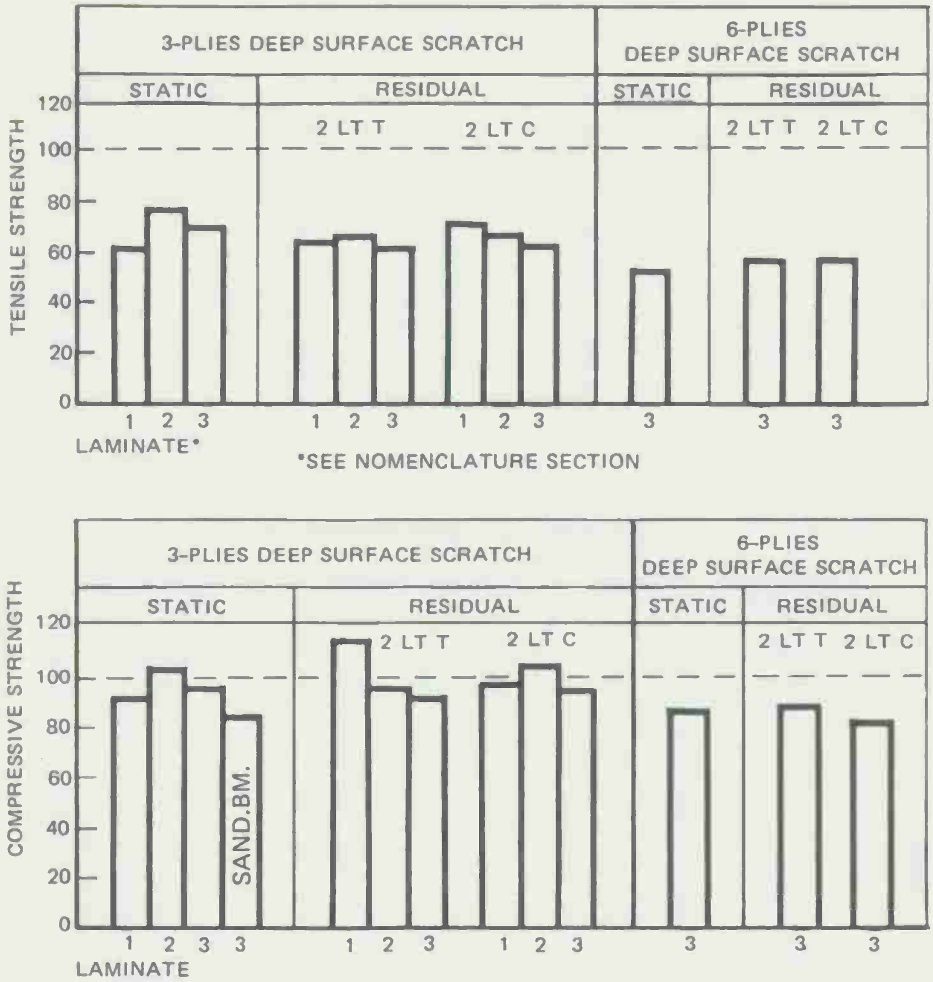

FIGURE 15. EFFECT OF CENTRAL 1-INCH SURFACE SCRATCH ON RTW STRENGTHS (EXPRESSED IN % OF UNFLAWED STRENGTH)

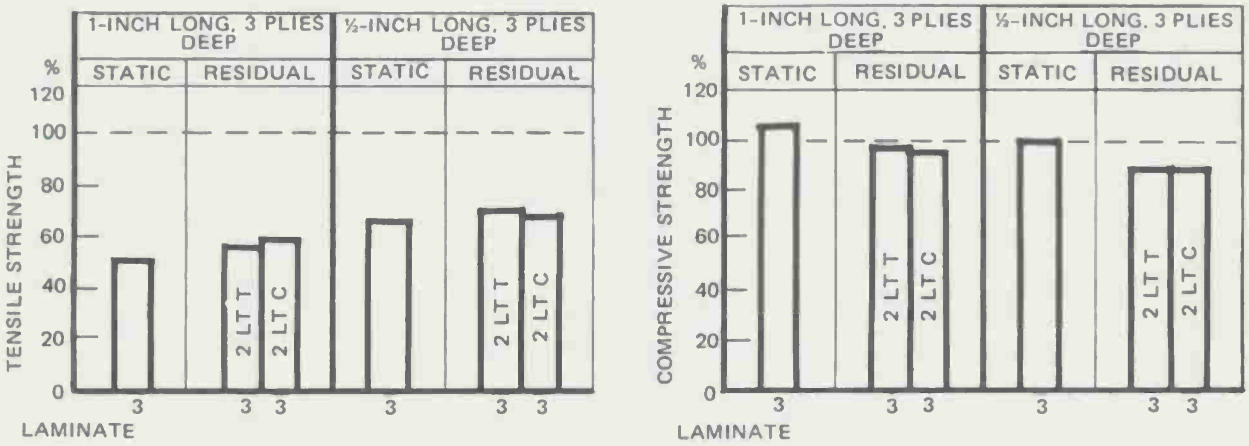

FIGURE 16. EFFECT OF SURFACE SCRATCH AT EDGE ON RTW STRENGTHS (EXPRESSED IN % OF UNFLAWED STRENGTH)

14-61
IC-30
14-68

Laminate No. 1

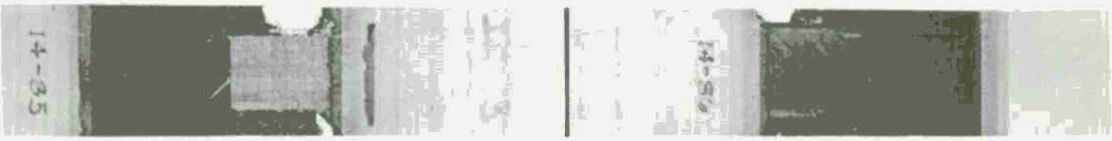

Laminate No. 2

Laminate No. 3

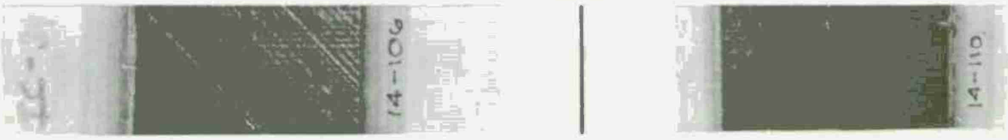
14-106
14-110

FIGURE 17. FAILED 3 PLY DEEP CENTER SCRATCH SPECIMENS

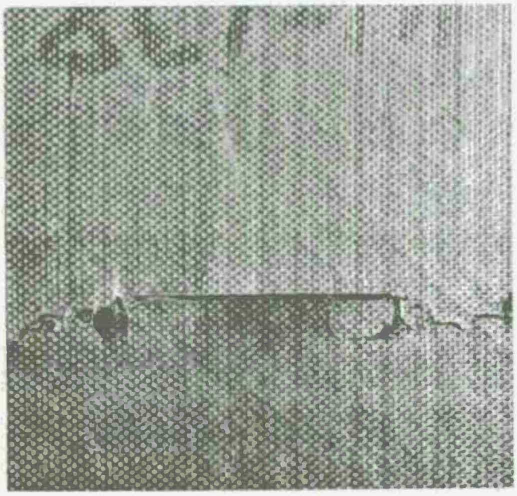

FIGURE 18. FAILED COMPRESSION SPECIMEN CONTAINING A SURFACE SCRATCH

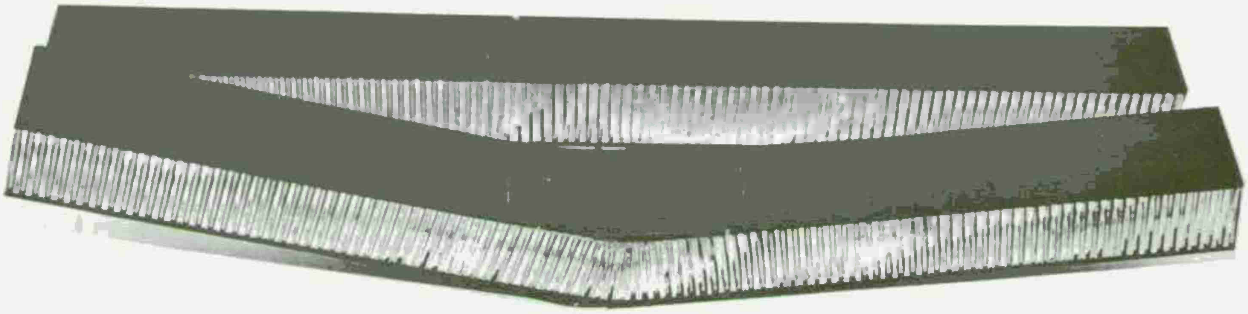

FIGURE 19. SANDWICH BEAM CONTAINING SURFACE SCRATCH

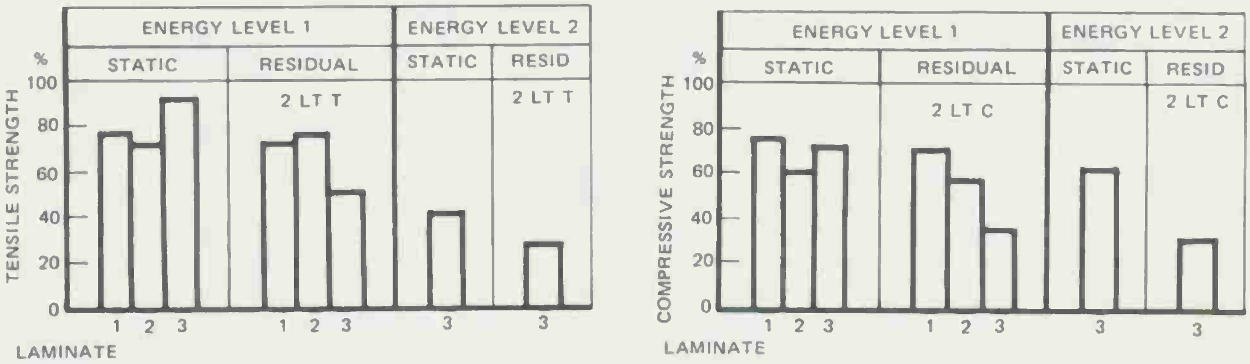

ENERGY LEVEL 1 = INCIPIENT BACK FACE FIBER FAILURE

ENERGY LEVEL 2 = INCIPIENT FRONT FACE FIBER FAILURE

FIGURE 20. EFFECT OF FOREIGN OBJECT DAMAGE ON RTW STRENGTH (EXPRESSED IN % OF UNFLAWED STRENGTH)

CONCLUSIONS

Data presented in this paper suggest that certain of the flaws investigated are more detrimental than others. At the coupon level, uniformly distributed voids, edge delaminations, oversized holes and overtorqued fasteners were not found to be particularly detrimental. Scratches, foreign object damage, and nonuniformly distributed voids were found to significantly reduce "unflawed" strengths. Most flaws resulted in static strength reductions with little or no further reduction in residual strength after the specific spectrum fatigue exposure. It was found that certain flaw types are more detrimental in tension than compression (e.g., scratches). The reason appears to be that these flaws can tolerate compression loading by something like a crack closing mechanism. Other flaws (e.g., delaminations) appear to be more critical in compression. The local decrease in bending stiffness at a delamination is the probable cause of compression strength loss.

RECOMMENDATIONS

It is suggested that the results obtained here be checked for more complex loading situations (e.g., biaxial loading, shear, etc.). Also analytical methodology should be developed so that coupon results can be extrapolated to components. Test data are needed on more complex assemblies where fitup, load paths, etc., are more intricate than at the coupon level. Having earmarked "critical flaw types," NDE methods should be perfected to provide assurance that all flaws of a given type above a certain critical size can be detected.

ACKNOWLEDGEMENT

The authors acknowledge the support of the Air Force for the work reported herein, conducted under Contract Number F33615-74-C-5182, "Structural Criteria for Advanced Composites." Also some of the data were generated under Northrop IRAD Project Number 75-R-1059, "Advanced Composites Structures Design Analysis Methods Development."

DAMAGE TOLERANT STRUCTURAL CONCEPTS FOR FIBER COMPOSITES

J. G. AVERY

and

T. R. PORTER

Boeing Aerospace Company
Seattle, Washington

ABSTRACT

Special layup concepts have been developed in order to meet damage tolerant objectives in fiber composite structure. Two concepts discussed are "softening strip" and "low-modulus skin" designs. Each of these concepts takes advantage of the versatility of fiber composite materials by using a mix of layups and/or material to provide low-stress/high-toughness regions for crack arrest. The test data presented illustrates the potential advantages of these concepts, and the influence of material combinations on failure modes and damage tolerance capability.

INTRODUCTION

Combat statistics show that a significant percentage of combat aircraft losses were caused by structure-related failures. To counter this, new aircraft procurements are requesting higher levels of survivability, including stringent operational requirements after damage from high-explosive threats. This increased emphasis on survivability, and the development of fiber composites for primary structure, highlights the need for survivable composite structural concepts.

In order to meet battle damage tolerant design objectives, several structural design concepts are being studied. Two of these are "softening strip" and "low-modulus skin" designs.

Softening strip panels rely on discrete low-stress regions in the panel to arrest a propagating crack. The softening strips are produced during layup by substituting a low-stiffness material, such as ±45 laminate or fiberglass, for high stiffness 0° fibers contained in the basic skin.

In the low modulus skin concept, most of the uniaxial load is carried by discrete stiffening elements. The basic skin is a low axial modulus layup (±45°, for example) designed to react shear and internal pressure loadings. In this manner, the skin can be tailored to have a high allowable axial strain even when damaged.

Several completed and current research programs at Boeing address the development of these concepts for battle damage tolerance. These include development of low modulus skin concepts (1), Boeing in-house studies, and a current program for developing battle damage tolerant wing structure (2).

FRACTURE RESPONSE OF SIMPLE LAMINATES

Several research programs (3-7) have been sponsored by industry and government to establish the battle damage tolerance of fiber composite structure. These programs developed data on damage characteristics due to ballistic impact and fracture reponse in the presence of ballistic damage. Boeing used this available data to develop analysis models for damage and residual strength of damaged graphite and boron laminates. These models were included in the Design Handbook for Survivable Combat Aircraft Structure (6).

The results showed that the effective ballistic damage size is directly related to the projected size of the projectile in the plane of the laminate as illustrated in Figure 1. The additive constant of 0.2-inches shown in the figure is an average value for residual strength correlation found from available test data.

The second step in the development of the analysis models was to relate the fracture stress to the damage size. The relationship given by fracture mechanics, wherein the failure stress is proportional to the damage size to the 1/2 power, was assumed for this purpose. Figure 2 shows a reduction of the available data compared with this damage size-fracture stress relationship. As implied by Figure 2, normalizing the data to the undamaged strength (F_{tu}) consolidates the majority of layups and materials onto this single line with slope of minus one-half. The data used in this development consisted of the 0°, $\pm 45^o$, and 90° layup family.

Carrying the analysis of the data one step further, all of the available data was used to develop an allowable fracture response line. This was performed by computing the .95 confidence, .90 probability value using normal population parameters. This is analogous to "B" value allowables used in aerospace structural design. A line representing this allowable is also presented in Figure 2 for comparison.

Combining the models for damage and fracture and using the allowable (0.95 confidence, 0.9 probability) fracture stress line gives the potential structural strength degradations shown in Figure 3. As indicated, the potential strength loss due to an impact from a single small caliber projectile can be severe.

Because of the versatility of composite materials, simple panel response data is not sufficient. This was illustrated by Boeing studies (7) where comparisons between metallic and composite structure were made. It was pointed out that aircraft structural response can be much different than simple panel response because of fracture containment design. Composite materials, because of their versatility in layup, have the potential to be

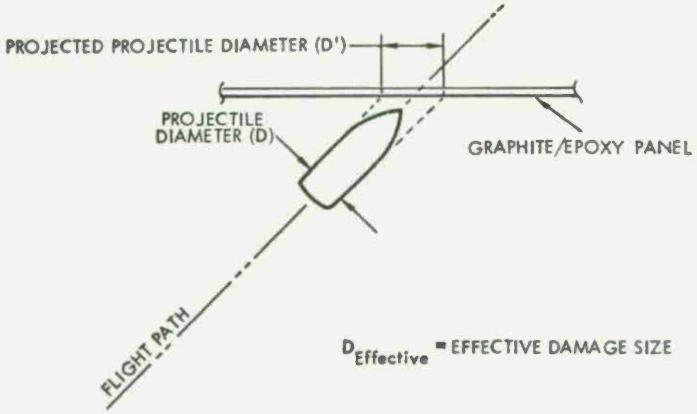
PROJECTED PROJECTILE DIAMETER (D')
PROJECTILE DIAMETER (D)
GRAPHITE/EPOXY PANEL
FLIGHT PATH
D_{Effective} = EFFECTIVE DAMAGE SIZE

Figure 1. Effective damage size from projectile impact.

FOR THIN PANELS : $D_{Effective} = D' + 0.2$ (INCHES)

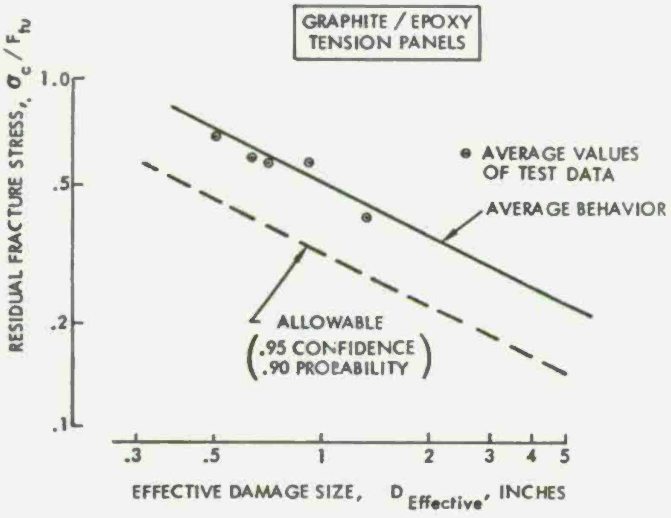

Figure 2. Residual strength data for graphite/epoxy panels containing projectile damage.

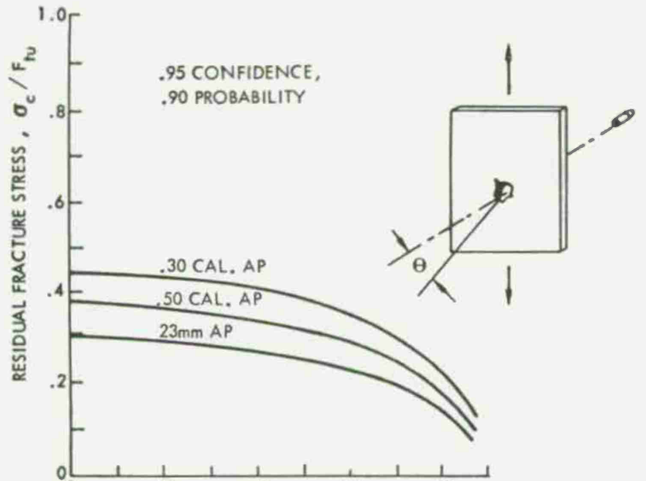

Figure 3. Allowable residual strength of advanced fiber composite panels.

configured in a structural design having superior battle damage tolerance. It is for this purpose that the current studies were directed.

SOFTENING STRIP DESIGN CONCEPTS

Initial studies of softening strip design concepts were presented by Eisenmann (8) in boron/epoxy laminates. His approach was to substitute ±45 material for the 0° and 90° fiber material at discrete locations, producing a low-stiffness (softening) strip in the laminate as illustrated in Figure 4. The regions of low stress can arrest a propagating crack. The panel retains full shear capability and, if the 90° plies are retained, has full transverse strength. The loss of axial strength depends on the relative widths of the softening strips and the basic layup.

As an illustration of the effect of softening strips on stress distribution, the results of a finite element analysis of a cracked panel are shown in Figure 5. A $(0_2/\pm45/90)$ HTS graphite/epoxy panel was analyzed. The softening strips were formed by replacing the (0_2) graphite with (0_2) S-glass. In this coarse grid example shown to illustrate the trends, the mesh size ranged down to 0.1-inch around the crack tip. The analysis used an orthotropic constant strain element with properties reflecting the layup and materials.

Stress distributions are shown for panels with and without softening strips. The values of the peak stresses depend on the mesh size and are only approximate, but the relative stress distributions reflect actual behavior. There is a significant drop in the peak stress near the crack tip in the softening strip panel. This is illustrated by the stress distribution at a plane 0.1-inch away from the crack, selected to minimize the errors near the crack tip singularity. The remote stress field, shown to be approached when $Y = 4.0$ in., illustrates the effect of the softening strip on the uncracked panel stresses.

Consideration of the stress distribution near the crack in the softening strip panels shows a secondary stress peak adjacent to the strip. The width of the softening strip must be sufficient to maintain the magnitude of this secondary peak below the level that will initiate failure in the base laminate beyond the softening strip.

Several panels were constructed and tested in tension as shown in Figure 6 to evaluate the damage containment capability of softening strip concepts. Initial damage was simulated by a 2-inch long central saw-cut. In order to measure crack growth during loading, a crack opening displacement gage was placed across the center of the crack with the output recorded on a load versus displacement plot. This instrumentation accurately indicated the load at crack propagation.

Two softening strip concepts were tested. In one concept, the (0_2) graphite was replaced with (±45) graphite in the softening strip. In the

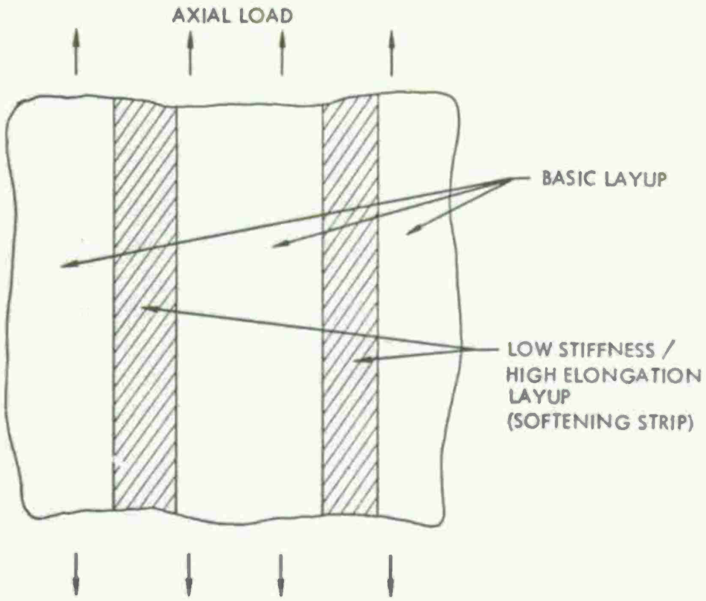
AXIAL LOAD
BASIC LAYUP
LOW STIFFNESS / HIGH ELONGATION LAYUP (SOFTENING STRIP)

Figure 4. Softening strip concept.

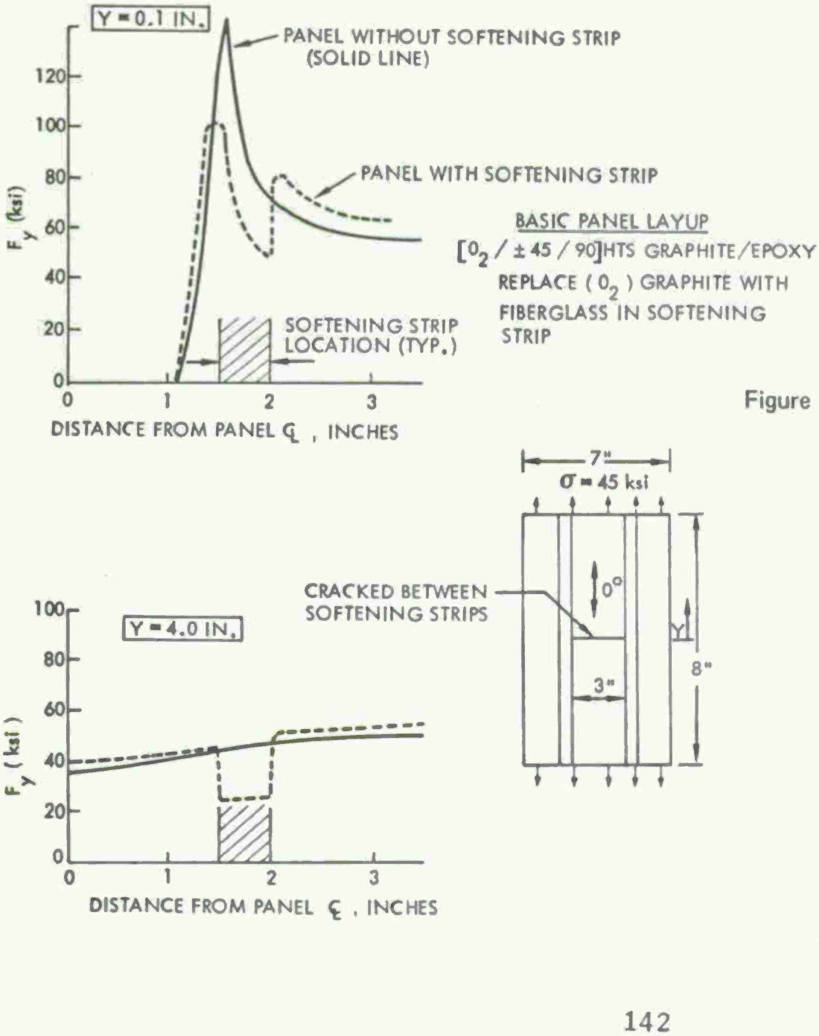

Figure 5. Finite element analysis results of typical softening strip panel.

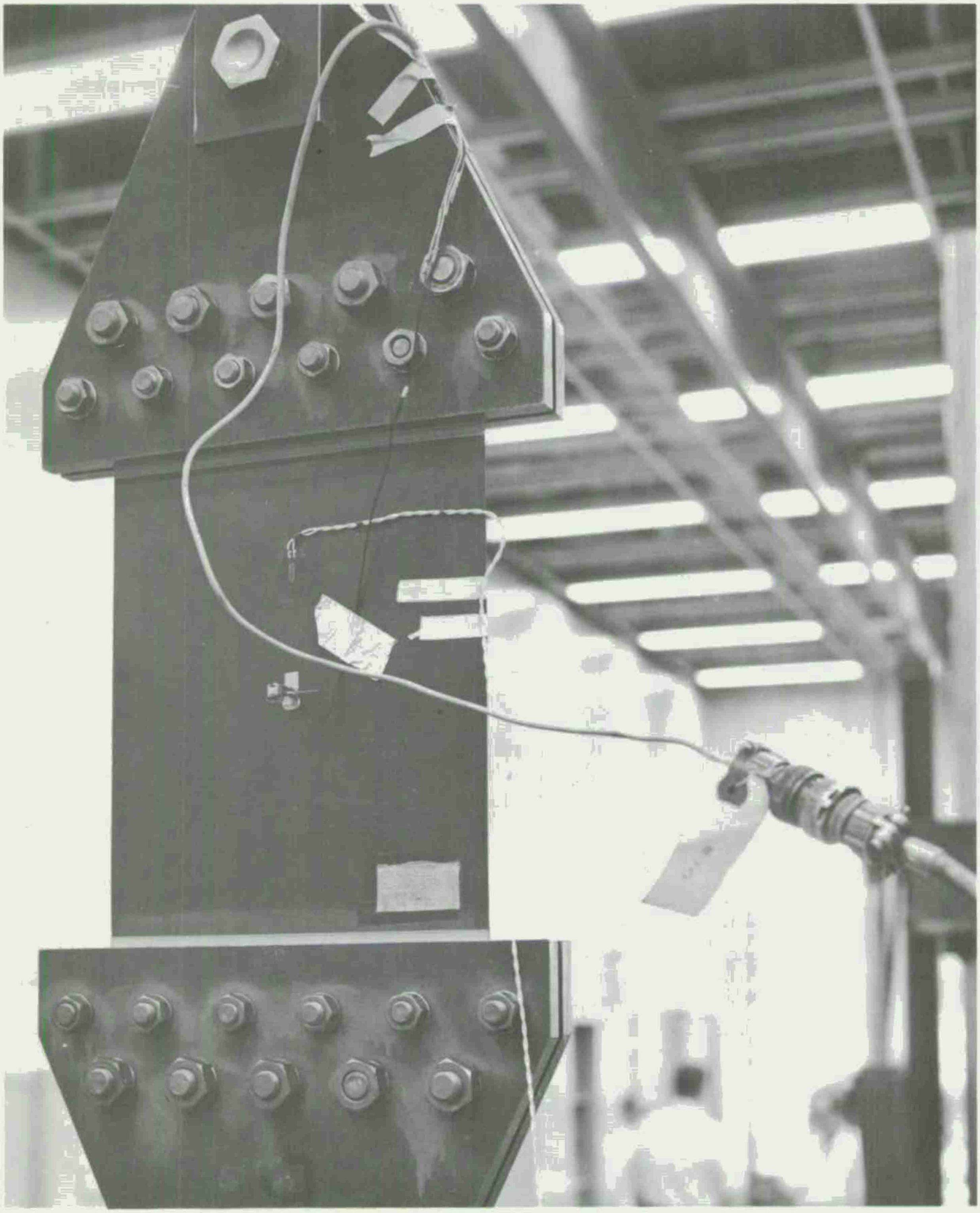

Figure 6. Damage tolerant panel test setup.

other concept, the (O_2) graphite was replaced with (O_2) E-glass. The (±45) and (90) plies in the basic lamiante were continuous across the panels.

A comparison of the two softening strip concepts with basic laminate fracture results is presented in Figure 7. The open symbols indicate the damage size and stress at initial crack propagation and the solid symbols indicate panel separation. The stress at crack propagation was correlated to the fracture toughness of the basic laminate, as found from separate basic laminate fracture tests. The test data from the base laminate fracture tests are shown as solid dots in the figure. The smooth curve through these data extrapolated to the larger damage sizes reflects the analysis method presented previously in Figure 2. Both softening strip concepts arrested the crack, but the final failure loads for the E-glass softening strip panel was significantly higher than in the ±45 softening strip panel.

Figures 8 and 9 are photographs of the two panels, and a difference in fracture appearance can be seen. In the E-glass concept, there is significant fiber pull-out and crack branching, indicating higher toughness than shown by the ±45 concept.

In current studies (2), a fracture comparison between graphite/glass hybrids and graphite laminates has been performed. The results, shown in Figure 10, demonstrate why the glass substitution in the softening strip was a superior design. In Figure 10, the critical strain (gross area) in a test panel containing a central slit is shown to be a function of the percent S-glass. The results show an increase in critical strain levels for (±45) graphite over quasi-isotropic graphite, and even greater critical strain levels for (±45) graphite/(0) glass hybrids.

The results of another hybrid composite softening strip concept are shown in Figure 11. The test data is from a boron/graphite panel that had an all-graphite softening strip. As shown in the figure, crack arrest was achieved, resulting in a significant increase in panel failure stress. Figure 12 is a photograph of the failed test panel.

The use of softening strips in a damage tolerant structural wing design was explored by Boeing (9). In this study, a wing box conceptual design was developed using graphite/epoxy skin with regularly spaced S-glass softening strips. The softening strips provided both crack arrest capability and low stress regions for fastening. By using the softening strips for a double purpose, the weight penalty associated with providing damage tolerance was minimized.

LOW MODULUS SKIN DESIGN CONCEPTS

Boeing has studied (1 and 2) an alternate method of designing composite structure for damage tolerance. This method is referred to here as the low-modulus skin concept, wherein the primary axial loads are carried by discrete, high-modulus stiffening elements such as straps or spar chords. The

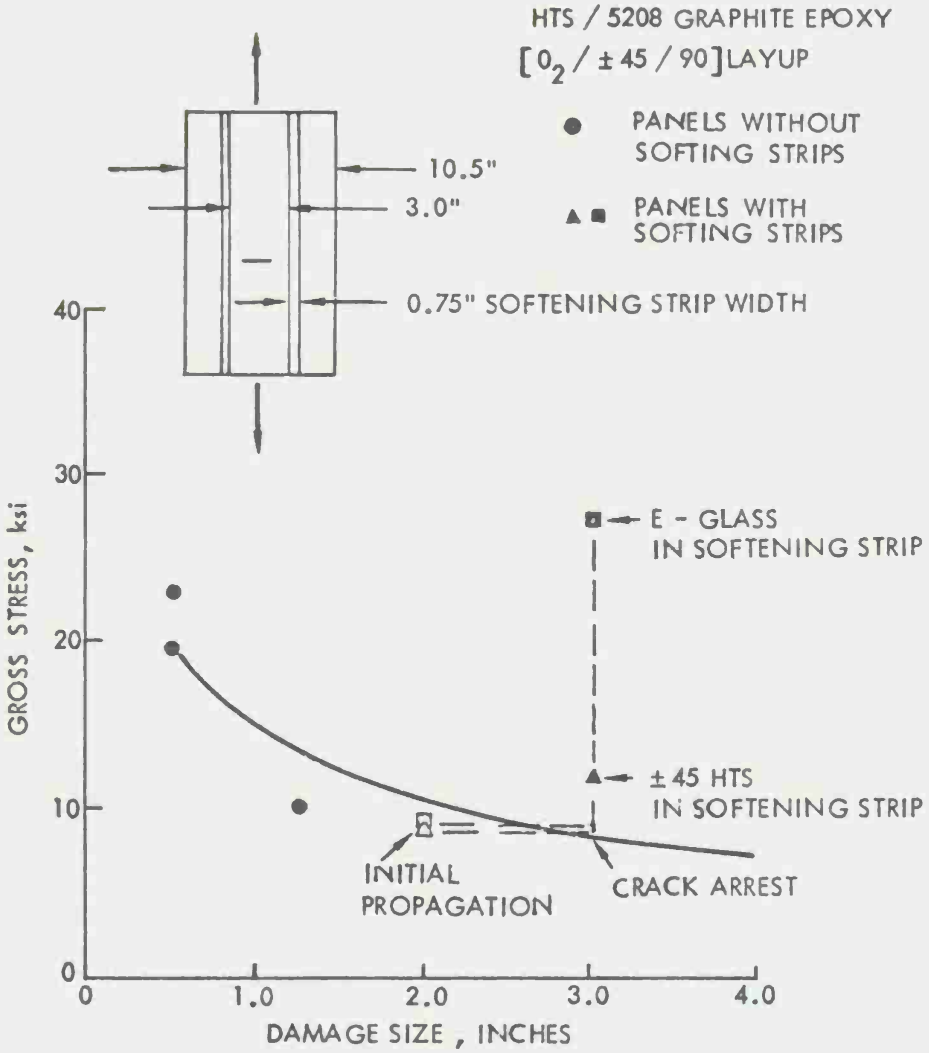

Figure 7. Comparison of base laminate and softening strip fracture stress.

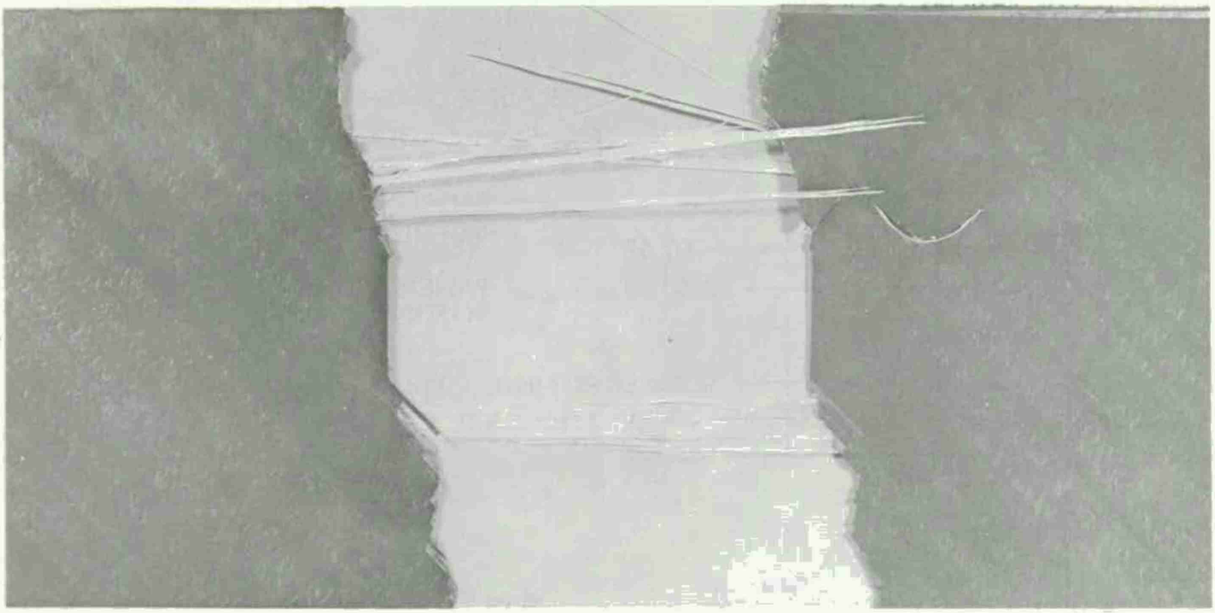

Figure 8. Fractured E-glass substitution softening strip panel.

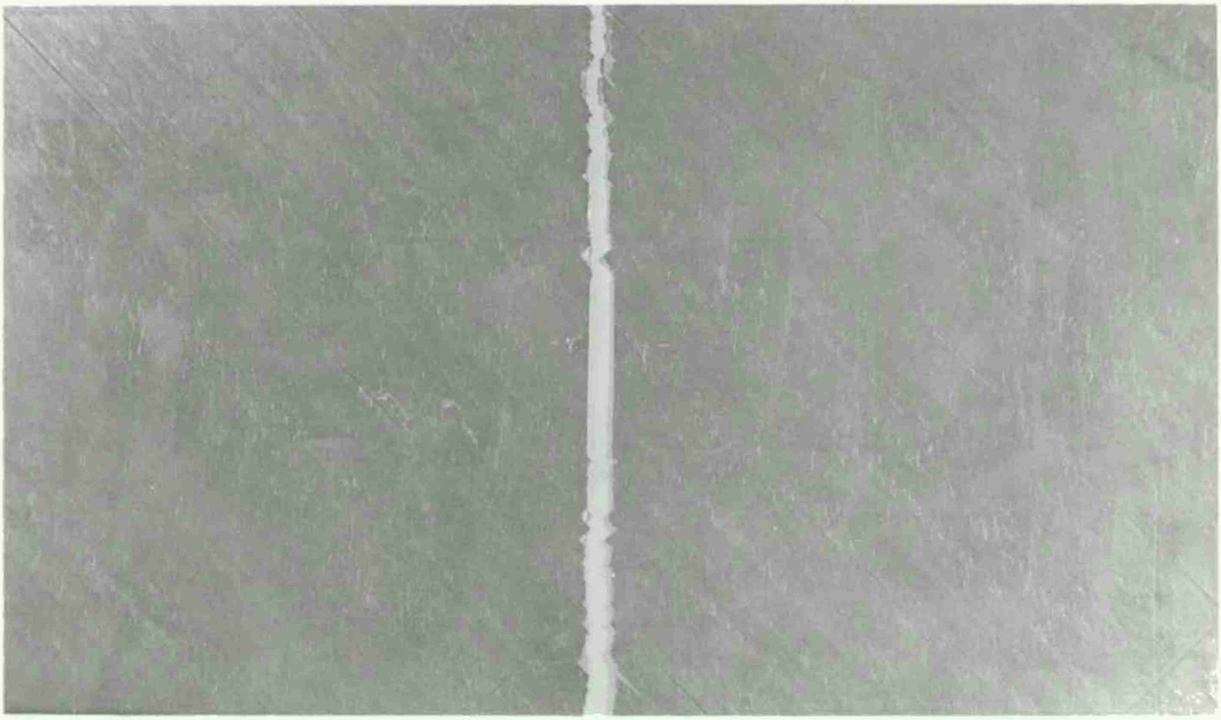

Figure 9. Fractured ±45° substitution softening strip panel.

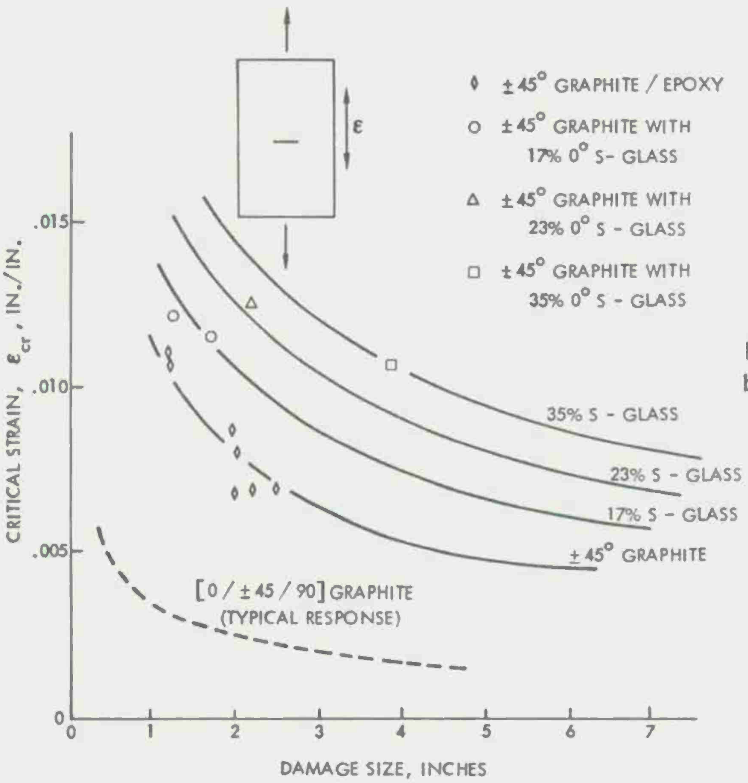

Figure 10. Damage containment improvement by adding 0° S-glass to ±45° graphite.

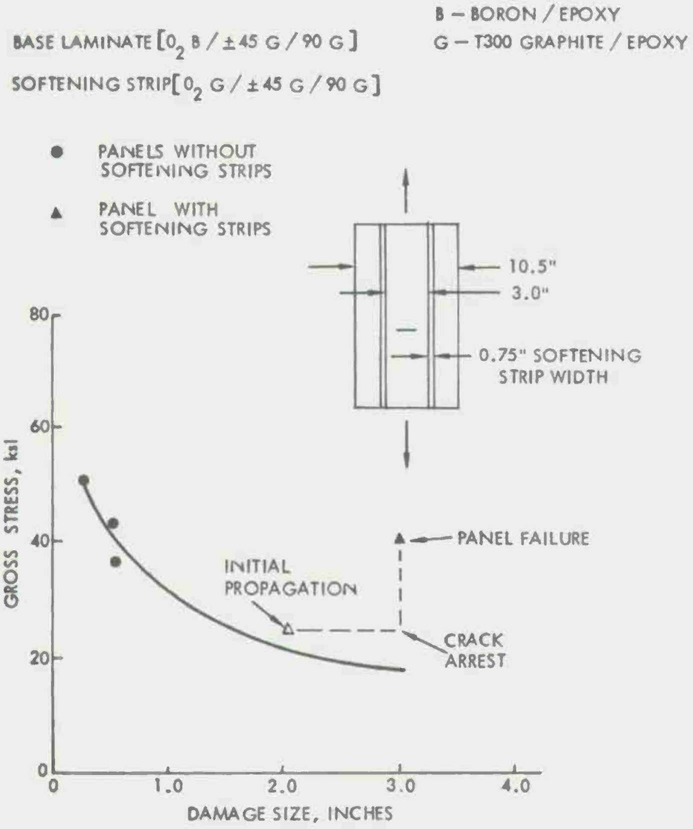

Figure 11. Fracture stress in boron/ graphite hybrid softening strip panel.

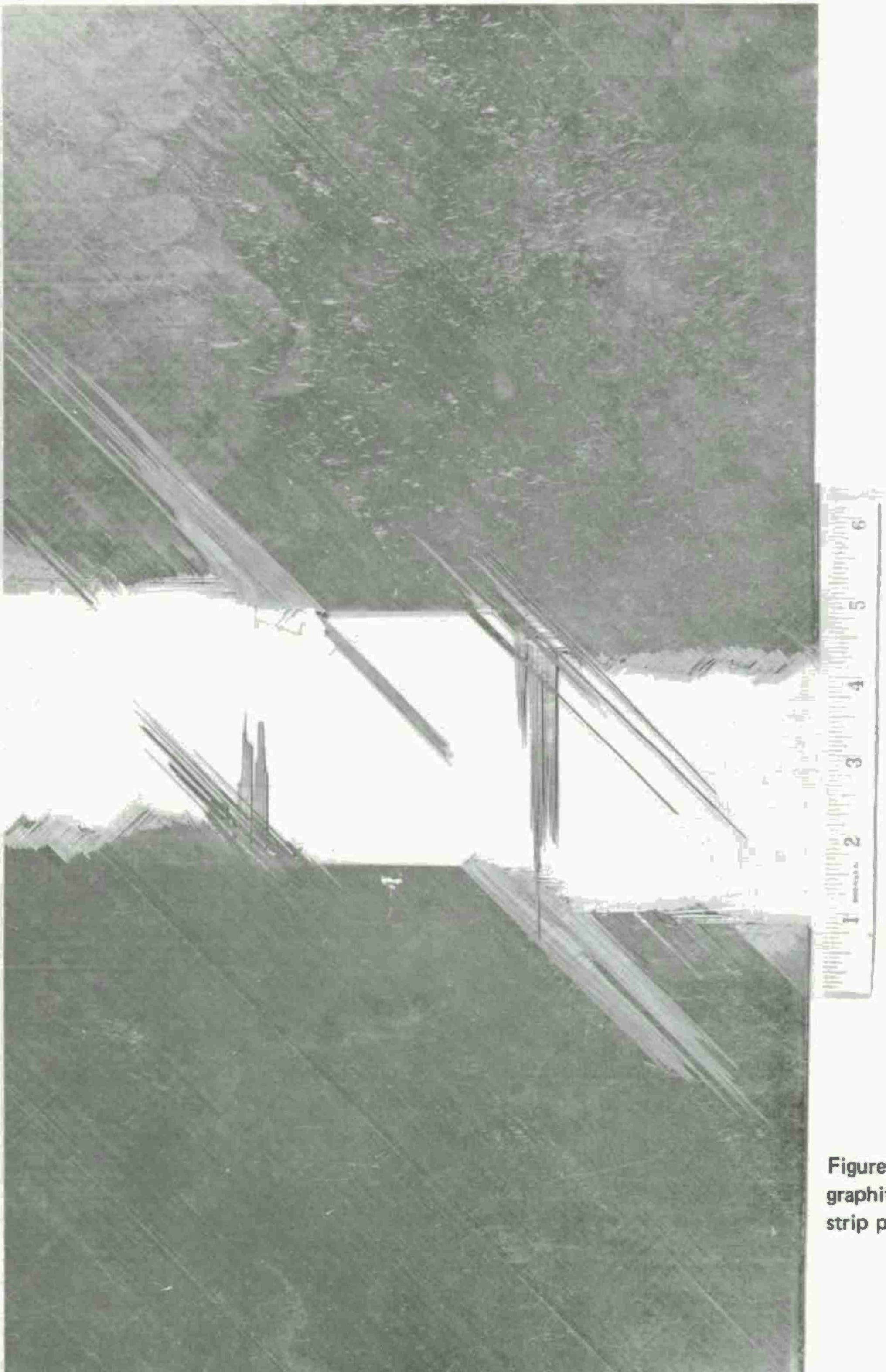

Figure 12. Fractured boron/graphite hybrid softening strip panel.

skin is sized to meet torsional and internal pressure requirements and is constructed of materials and layups that provide a high elongation prior to fracture. Figure 13 is a schematic diagram of a wing-box design using low modulus skins.

As a demonstration of this method, tests were performed to compare with the softening strip results described above. The same overall panel configuration was used. However, instead of a softening strip laminate, external (0) straps were bonded to a ($\pm$45/90) skin. The number of 0° fibers in the straps was nearly equal to those distributed in the softening strip panels so the undamaged strength would be equivalent.

An example of the test results is presented in Figure 14. The line and solid dots are the same baseline fracture data presented in Figure 7 for (0_2/±45/90) panel. The squares indicate the results found for the low-modulus skin panel. As shown, the stress at crack propagation is considerably above the basic laminate fracture response. This is consistent with the comparison of strain at crack run shown for (±45) laminates and laminates containing 0° fiber shown in Figure 10. In addition, the crack was arrested at the straps and carried still greater loading prior to failure. A photograph of a failed low-modulus skin panel is shown in Figure 15.

Further improvements in the fracture resistance of this concept can be realized by adding glass fiber to the skin laminates, as demonstrated by the data in Figure 10.

CONCLUSIONS

Two design approaches for providing damage tolerance in composite structures are discussed. Both concepts provide crack containment capability and can be used in the design of tension panels. In both concepts, the use of hybrid laminates can be used to advantage to increase the damage tolerant capability.

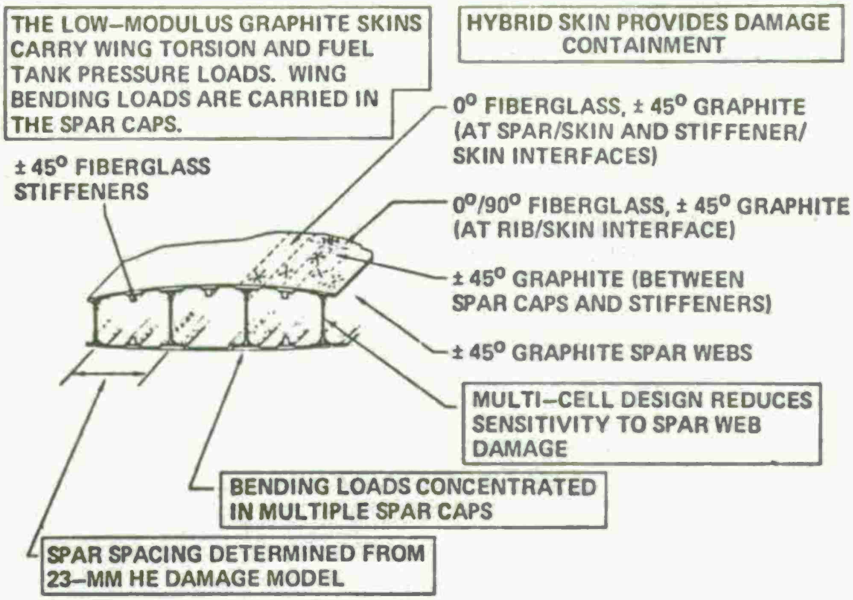
THE LOW–MODULUS GRAPHITE SKINS CARRY WING TORSION AND FUEL TANK PRESSURE LOADS. WING BENDING LOADS ARE CARRIED IN THE SPAR CAPS.
HYBRID SKIN PROVIDES DAMAGE CONTAINMENT
0° FIBERGLASS, ± 45° GRAPHITE (AT SPAR/SKIN AND STIFFENER/ SKIN INTERFACES)
± 45° FIBERGLASS STIFFENERS
0°/90° FIBERGLASS, ± 45° GRAPHITE (AT RIB/SKIN INTERFACE)
± 45° GRAPHITE (BETWEEN SPAR CAPS AND STIFFENERS)
± 45° GRAPHITE SPAR WEBS
MULTI–CELL DESIGN REDUCES SENSITIVITY TO SPAR WEB DAMAGE
BENDING LOADS CONCENTRATED IN MULTIPLE SPAR CAPS
SPAR SPACING DETERMINED FROM 23–MM HE DAMAGE MODEL

Figure 13. Design concept to provide improved damage tolerance using low modulus skin design.

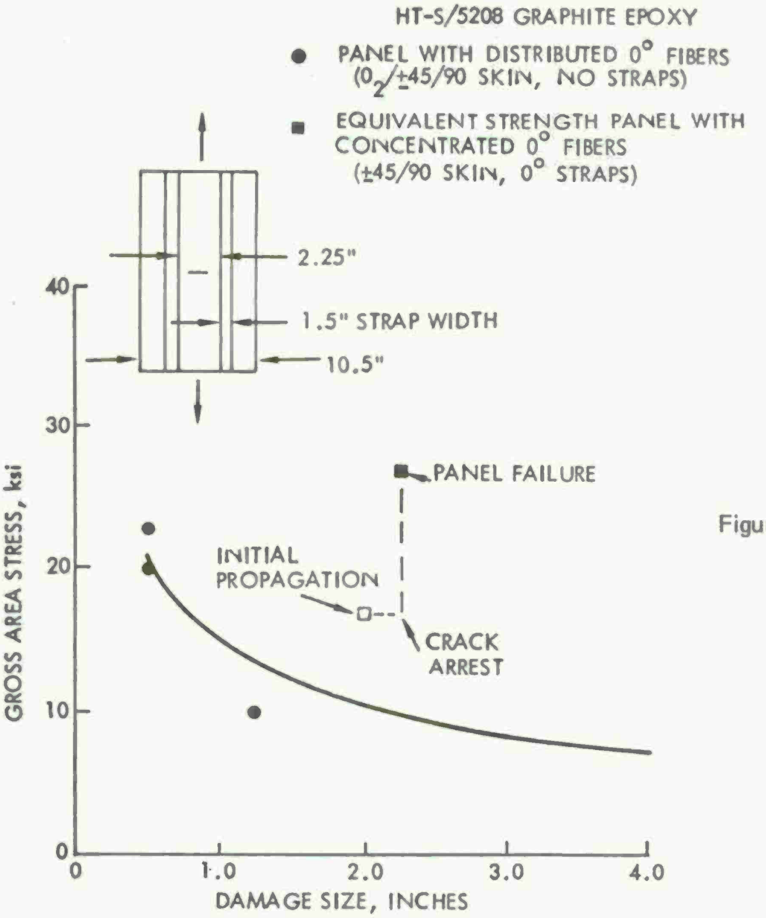

Figure 14. Comparison of base laminate panels and soft skin panel.

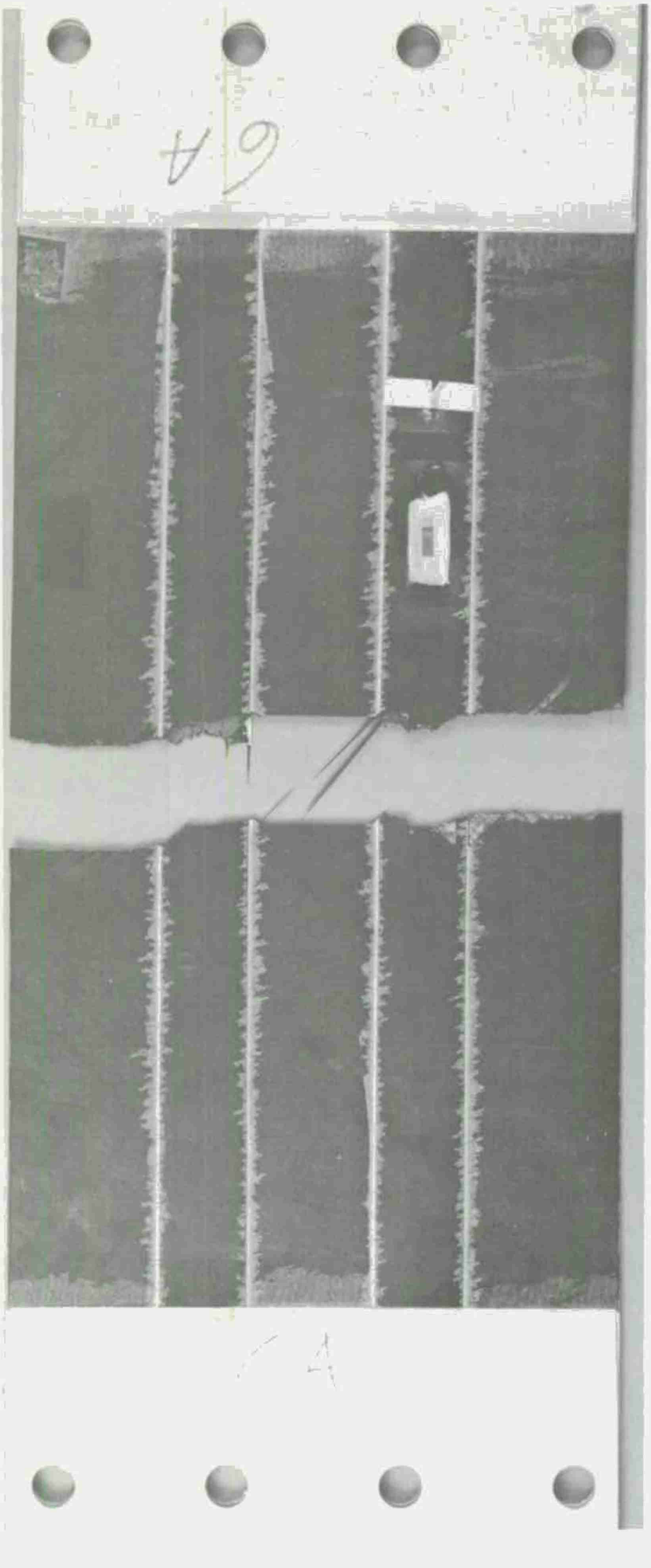

Figure 15. Fractured graphite low-modulus skin panel.

REFERENCES

1. Blichfeldt, B., and McCarty, J. E., "Analytical and Experimental Investigation of Aircraft Metal Structures Reinforced with Filamentary Composites," Boeing Contract with NASA, NASA CR-2039, June 1972.

2. Avery, J. G., et al, "Battle Damage Tolerant Wing Structure Development Program," Quarterly Report for NASC Contract N00019-75-C-0178, July 1975.

3. Olster, E. F., and Woodbury, H. A., "Evaluation of Ballistic Damage Resistance and Failure Mechanisms of Composite Materials," Air Force Contract F33615-70-C-1570, AVCO Corporation, AFML-TR-72-79, April 1972.

4. Suarez, J. A., "Vulnerability of Composite Aircraft Structures," Air Force Contract F33615-71-C-1111, Grumman Aerospace Corporation, AFFDL-TR-72-8, February 1972.

5. Hayes, R. D., et al, "Flightworthy Graphite Fiber Reinforced Composite Aircraft Primary Structural Assemblies," Air Force Contract F33615-69-C-1490 (Project 6169), Northrup Corporation, AFML-TR-71-276, April 1972.

6. Avery, J. G., and Porter, T. R., "Survivability Combat Aircraft Structures Design Guidelines and Criteria - Design Handbook," AFFDL-TR-74-50, April 1974.

7. Avery, J. G., and Porter, T. R., "Comparison of the Battle Damage Response of Fiber Composites and Metals," Foreign Object Impact Damage to Composites, ASTM-STP-568, 1974.

8. Eisenmann, J. R., and Kaminski, B. E., "Fracture Control for Composite Structures," Engineering Fracture Mechanics, Vol. 4, 1972, 907-913.

9. McKinney, M. E., Porter, T. R., Sedlacek, C. J., "Battle Damage Tolerant Wing Study," Boeing Contract with NASC Final Report, Contract N00019-72-C-0433, D180-15150-1, October 1972.

FAIL-SAFE COMPOSITE ROTOR HUB

ROBERT J. MAYERJAK
Engineer
Kaman Aerospace Corporation
Bloomfield, Connecticut

GEORGE T. SINGLEY, III
Aerospace Engineer
Eustis Directorate
U. S. Army Air Mobility
Research and Development Laboratory
Fort Eustis, Virginia

ABSTRACT

The U. S. Army Air Mobility Research and Development Laboratory (USAAMRDL) is supporting a program to develop an improved rotor hub constructed from composite materials. The purpose of the program is to develop practical new structural concepts that will exploit the theoretical potentials of composite materials to provide a broad spectrum of improvement in cost, weight, fail-safety, radar detectability, vulnerability, reliability, and maintainability. It is believed that helicopters of all weight classes can benefit from composite hubs; however, the need is greatest for large helicopters, where the large size of conventional hubs approaches the limits of forging feasibility. Accordingly, the USAAMRDL has selected the CH-54B rotor hub as the baseline for the design. This paper reviews the composite hub structure, describing: the rationale for its configuration, the analysis of its structural integrity, the testing completed to date, and the characteristics of its performance.

INTRODUCTION

The Army's efforts to reduce helicopter costs and to exploit the potential benefits of structures made from composite materials have lead to the search for an improved composite rotor hub. Composite rotor hubs appear to offer improvements in the following characteristics in comparison to conventional metal rotor hubs: cost, weight, fail-safety, detectability, vulnerability, reliability, and maintainability.

The trend toward high rotor hub costs and weights for large helicopters, shown in Table I, was the impetus for the R&D effort discussed in this paper. Recently the trend in metal rotor hub materials has been toward titanium alloys which provide a high strength-to-weight ratio and good corrosion resistance. Although lighter than their steel counterparts, titanium alloy hubs are more costly. Conventional metal hubs are machined from large forgings, and they are plagued by high machining waste. For example, the CH-47C hub was machined in 77 operations from a 790 lb 4340-steel forging with over 80% machining waste. Composite materials offer the opportunity to avoid such losses.

TABLE I. WEIGHT AND COST OF ROTOR HUBS FOR LARGE HELICOPTERS

	CH-46F	CH-47C	CH-54B	HLH
Number of Main Rotors	2	2	1	2
Hub Material	Steel	Steel	Titanium	Titanium
Design Gross Weight, lbs	21519	33000	47000	118000
Empty Weight, lbs	13435	20085	19685	64878
Hub Weight, Housing, lbs	100	225	345	1847
Hub Weight, Assembly, lbs	1002	1496	1799	7034
Hub Cost, Housing, $1000s	8.4	20.2	34.0	112.1
Hub Cost, Assembly, $1000s	109.9	102.4	144.6	511.2

NOTES:

1. Costs for the CH-46F, CH-47C and CH-54B were developed from the price last paid for the particular item adjusted to the value of 1976 dollars. The HLH costs are estimates based upon HLH prototype aircraft experience adjusted to 1976 dollars. The CH-46F, CH-47C, and the CH-54B costs are for the 600th hub; and the HLH costs, for the 250th hub.
2. Weights are actual measured values taken from weight and balance reports for each aircraft.
3. Weights and costs for the tandem rotor helicopter are for one ship set.
4. The rotor hub housing is defined as the finish machined hub forgings alone.
5. The rotor hub assembly includes all rotor head components between the rotor blade root end fittings and the rotor shaft, except for blade folding hardware.

Although it is believed that helicopters of all weight classes can benefit from composite rotor hubs, the need is greatest for large helicopters, where the conventional hub size approaches the limits of forging feasibility. Because the improvements should be greatest for the larger helicopters, the CH-54B rotor hub was selected as the baseline for the composite rotor hub design effort. The CH-54B is a heavy lift helicopter which has a single main rotor with six articulated rotor blades. Its titanium alloy main rotor hub is five-feet-wide and one-foot-high. The hub is subjected to steady and vibratory loads in several directions. The following partial list of its design loads provides a measure of its strength:

Centrifugal force	82 tons (ultimate) from each of 6 blades
Lift	64 tons (ultimate)
Torque	142 foot-tons (ultimate)
Head moment	94 foot-tons (ultimate)
Head moment	± 33 foot-tons (fatigue) for millions of cycles

The existing production hub has two structural elements: an upper hub and a lower plate, as shown in Figure 1. The upper hub consists of six cantilevered beams that radiate from a hollow central cylinder. The lower

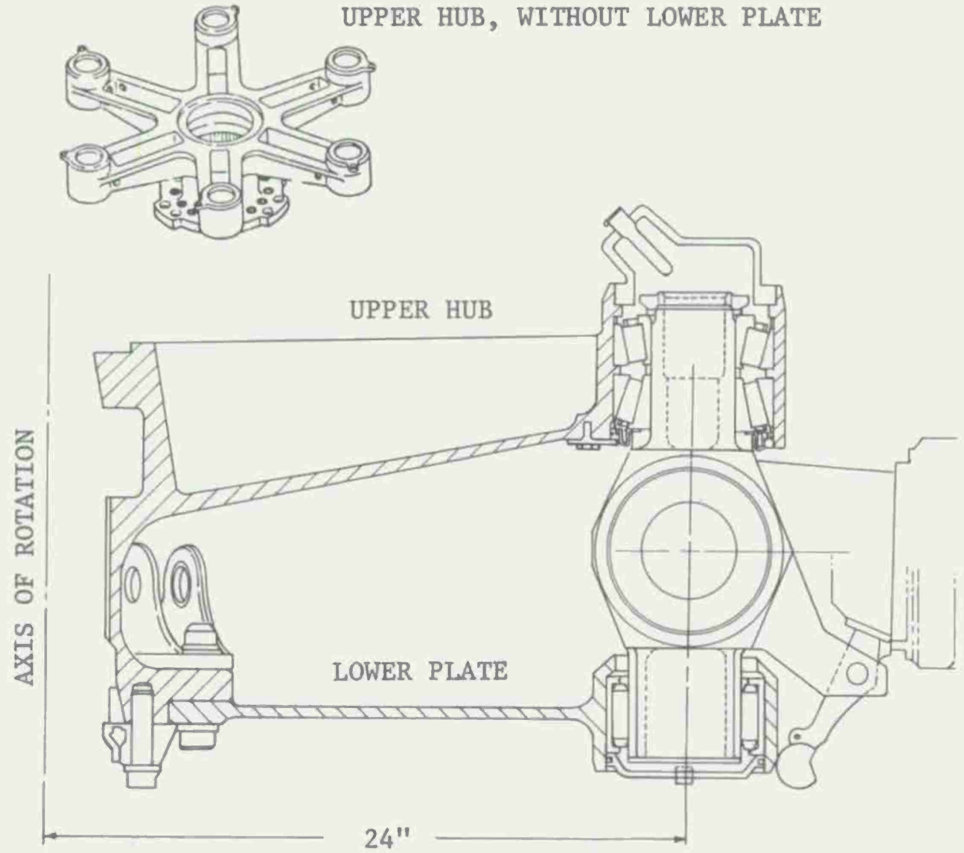

Figure 1. Existing Titanium Hub for CH-54B

plate is similarly star-shaped but much thinner. The upper hub and the lower plate share the support of centrifugal force and the transmission of torque. The beams of the upper hub alone support shears from lift and control moments. The hub is connected to the drive shaft by splines for torque transfer, cone seats for moment and a threaded nut for axial force. This configuration is efficient in metal. It provides compact load paths that are appropriate for a dense material that exhibits high strength in any direction of loading. However, these conventional load paths do not appear to be well-suited for composite materials, which have low inter-laminar tensile and shear strengths.

Pioneering efforts to apply composites to the CH-54B hub began in 1971 (References 1 and 2). These designs investigated the conventional load path, which can be called the center-beam concept. The design featured many narrow, continuous loops of composite material, each of which connected two opposite blades. At the center, the loops passed by the sides of a hollow central cylinder. When stacked together and enclosed by shear webs, these loops formed radial beams similar to those of the production hub. This concept is attractive in principle but difficult to implement efficiently. After detailed study, the investigators concluded that such a composite upper hub would be 270 lbs, (122%) heavier than its titanium counterpart. It is believed that the high weight is attributable in unknown proportions to at least three factors: an inherent low capacity of the concept to transfer shear forces; parasitic weight introduced by spacers required to accommodate geometrical interferences of the loops which must overlap each other at the central cylinder; and the design requirement that the hub should mate to existing hardware. These results stimulated efforts to find an alternative concept for a composite hub.

DESCRIPTION AND MECHANICS OF THE NEW COMPOSITE HUB

CONFIGURATION AND LOAD PATHS

Figures 2 and 3 show a new fail-safe composite hub that has been designed to match or exceed the static and fatigue strengths of the existing CH-54B titanium hub. It consists of three composite plates: an upper plate, a pan plate and a lower plate. Both the upper and lower plates are flat, except in areas of local reinforcement. The pan plate is cone-shaped, with a circular flange at its center and six lugs projecting from its perimeter. The upper plate and the pan plate are joined semi-permanently by six bearing housing and nut assemblies. Each lead-lag pin is held into a bearing housing by the tapered-roller upper bearings and the retaining nut at the top end of the lead-lag pin. The straight-roller lower bearings are free to float axially on the lead-lag pins. The lower plate is supported at its center by bolts which connect the pan plate and lower plate to the main rotor shaft. The dampers are supported by six bolts between the pan and the lower plates. In order to present the maximum information in a single view, the cross-section shown in Figure 2 shows the center bolts coplanar with the damper bolts. The true position of the center bolts is 15° away, as shown in Figure 3.

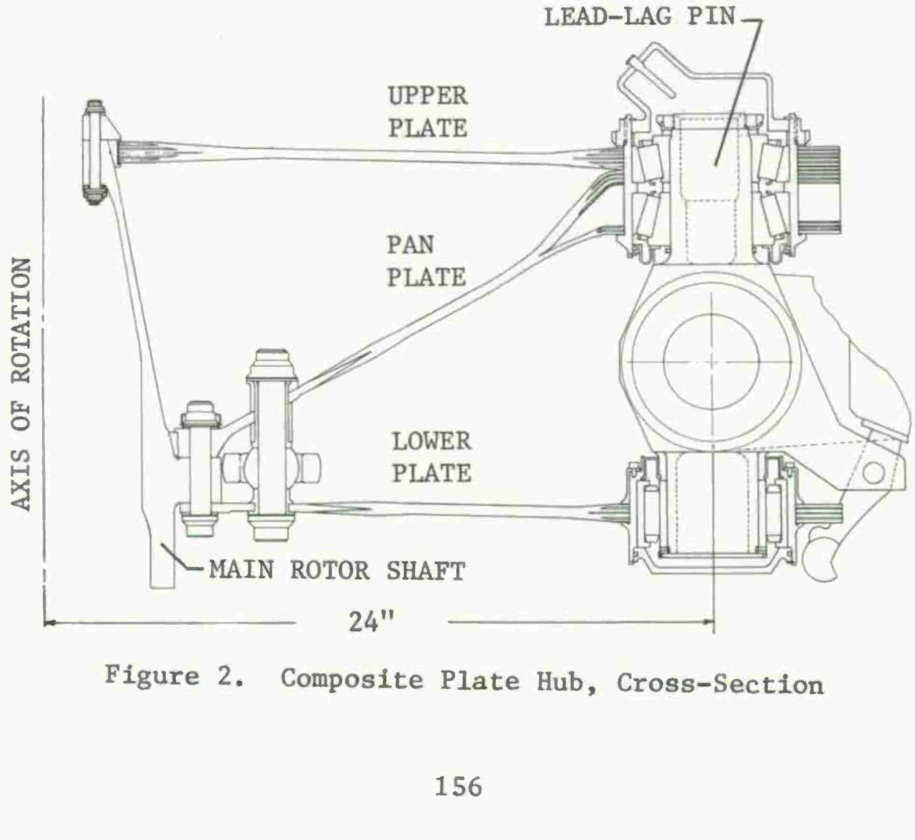

Figure 2. Composite Plate Hub, Cross-Section

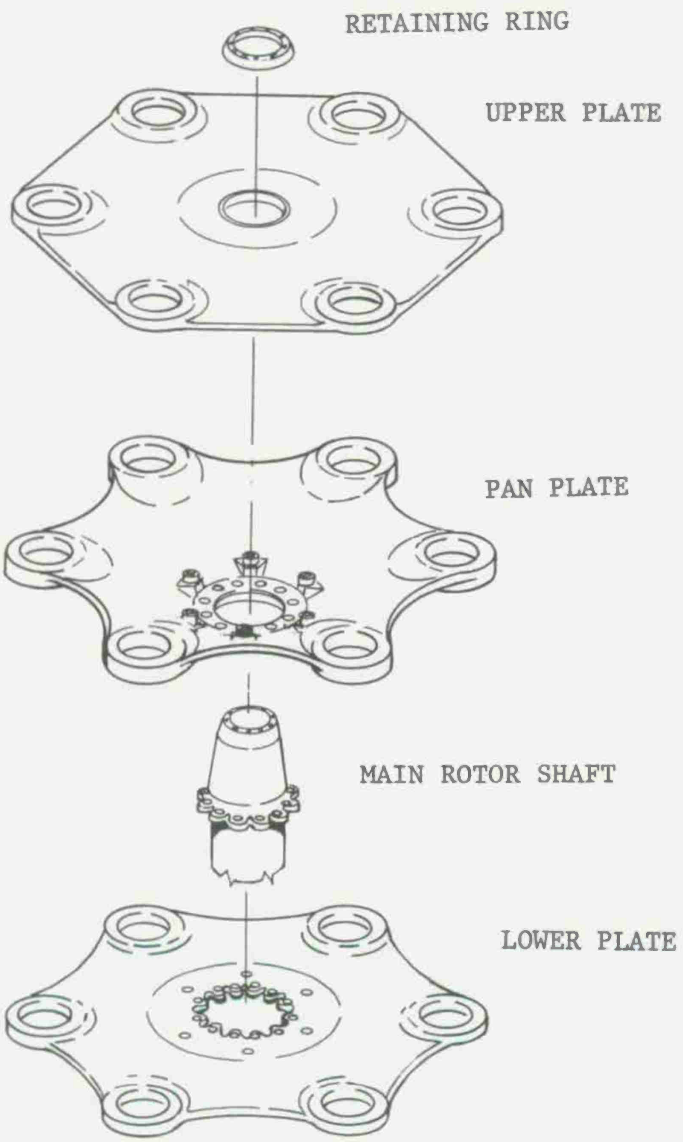

Figure 3. Composite Plate Hub, Exploded View

Major loads are transmitted primarily by direct stresses and shears in the planes of the plates which lie along efficient load paths for the support of the three principal loadings: centrifugal force, torque and transverse loads.

The centrifugal force is bridged by the lead-lag pins to the planes of the upper and lower plates. There, the loads are introduced into the composite plies by interleaved metal shims which provide a durable surface for contact with the housing and a large area of bond surface for the composite. Once into the plates, the loads spread out, following highly redundant paths.

Load diffusion is fostered by the pattern of reinforcement which provides equal stiffness load paths in both the perimeter and radial directions. The hub provides a new direct load path for torque without using the splines and the central cylinder of the conventional hub. Torque is transferred from a scalloped flange on the drive shaft to metal fittings in the pan and lower plates by twelve bolts which are loaded in double shear. Balanced-stiffness scarf joints transfer the torque from the fittings to the composite plates. The upper plate does not participate in the torque path.

Transverse loads (vertical shears) lie parallel to the centerline of the main rotor drive shaft and transverse to the top and bottom plates of the hub. Important transverse loads at the offset flapping hinges are produced when the pilot controls the aircraft by causing the axis of rotation of the rotor to tilt relative to the axis of rotation of the drive shaft, as shown in Figure 4. Such tilts, particularly during forward flight, cause the blades to undergo complex vibratory flapping motions which produce transverse dynamic loads on the hub. The most significant of these loads for the hub structure is a 1 per rev vibratory loading (at 185 rpm for the CH-54B) that can be approximated as the product of blade centrifugal force and the sine of the flapping angle at the flapping pin. Figure 4 shows that these loads are antisymmetrical and, because of the 24-inch offset, that they produce a large moment called the hub moment. Lift also produces transverse loads; however, they are symmetrical, essentially static, and less significant than those from rotor tilt.

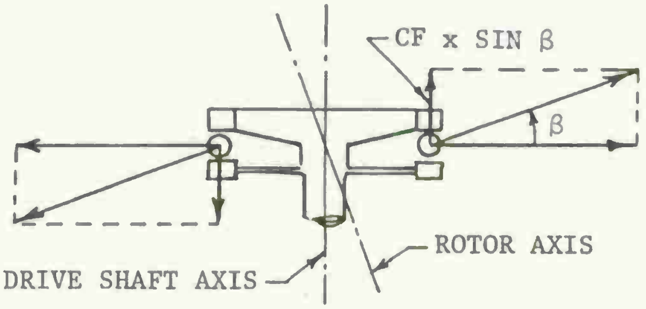

Figure 4. Origin of Hub Moment

At the outboard lugs, the upper bearings transfer the transverse load from the lead-lag pin to the upper housing and the nut. The latter bear against the upper and pan plates to complete the load transfer into the hub. The upper and pan plates support the transverse loads by the truss action of the in-plane forces in each plate. Transverse loads also produce local inter-laminar shearing stresses in the lugs of the pan plate. The lugs are thick to control these stresses.

At the center of the hub, three-quarters of the hub moment is transferred from the upper and pan plates to the rotor shaft by a pair of equal and opposite radial forces at the cones; the remainder is transferred by a pair of transverse loads on the flange. The cones are preloaded as the bolts are tightened during assembly. Lift forces are transferred from the pan plate to the flange on the rotor shaft.

MATERIALS

A constant-thickness construction with fibers in the 0/± 60 directions is used throughout because it provides multiaxial strength and economical fabrication. The orientation is appropriate for a 6-bladed rotor because it produces a symmetrical pattern of reinforcement that coincides with the perimeter and center load paths. Four fiber materials were considered: S-glass, Kevlar, a blend of Kevlar and alumina, and all graphite.

Initially, S-glass was favored because of its low cost, low radar detectability, and high impact strength. Glass was eliminated, however, because of its low modulus, low fatigue strength in the quasi-isotropic state, and high density. Stress analysis showed that significant compressions (11 ksi, ultimate) would be developed in the plates under maneuver conditions; thus, buckling became a design consideration, and the low modulus of glass, a liability. It is believed that a composite hub using glass could be designed to weigh less than the existing titanium hub; however, a glass hub would be heavier than one made from advanced materials. Of the advanced materials, graphite is most attractive. In the quasi-isotropic layup, it provides the highest absolute strength, specific strength and specific stiffness. Figure 5 shows a calculated interaction diagram for typical ultimate strengths of a graphite-epoxy laminate. The ultimate strength was defined as the stress that causes failure of the most critical ply. A limiting strain theory of failure was used.

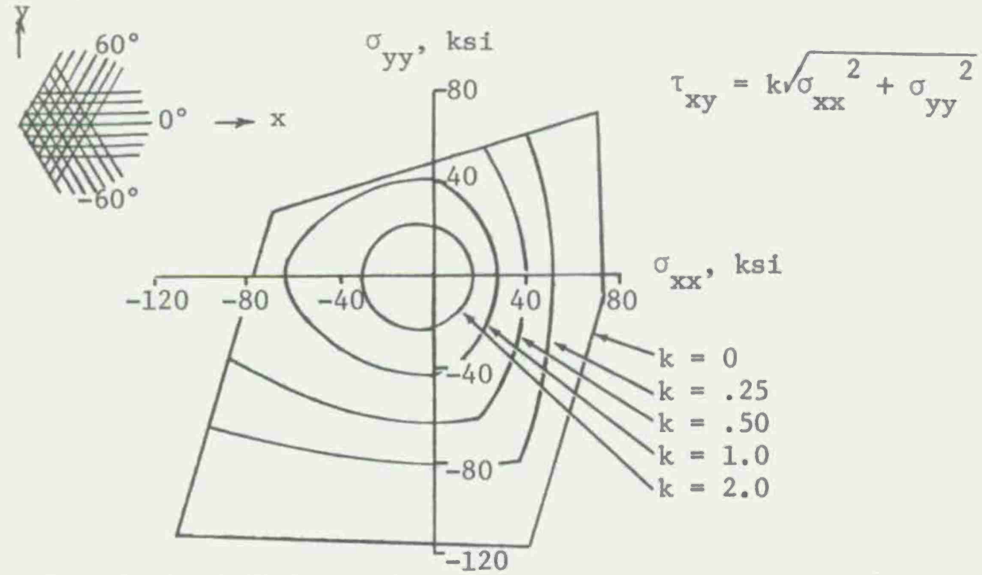

Figure 5. Typical Ultimate Strength for Graphite-Epoxy, 0/±60

The metallic components of the new hub were selected to provide the best compromise, considering performance, weight and cost. Titanium 6Al4V is used for the larger elements: the retaining ring at the top of the rotor shaft, the disc fittings, the upper and lower housings, and the large retaining nuts for the upper housing. The cones are aluminum-bronze in order to minimize the possibility of fretting of the drive shaft. The reinforcement laminae are steel, 17-7 PH. The fasteners and bushings are high-strength, low-alloy steel.

METAL LAMINAE REINFORCED JOINTS

Nineteen of the holes in the new hub are reinforced with multiple metal laminae. The metal laminae provide local multiaxial strength that allows the use of simple, low-cost layups for the plates and narrow edge distances at the holes. The metal laminae also provide wear resistance to local chafing, both in the holes and on contacting faces adjacent to the holes. In addition, at the center hole of the top plate, the metal plates provide resistance to creep, which assures retention of an initial preload. The integrity of these joints is a prime concern, and this program includes both analytical and experimental evaluations of these joints.

Six modes of failure were considered. They were static and fatigue failures of:

the composite at the edge of each reinforced area
the composite at the edge of each hole
the metal at the edge of each hole
the bond of composite to metal
the tapered tip of metal
the bearing surface within each hole (interlaminar splitting).

The first three modes of failure were analyzed using linear-elastic, two-dimensional, finite-element models lying in the plane of the plate. Figure 6 shows a portion of the finite element model for the upper plate in the vicinity of the outer joint.

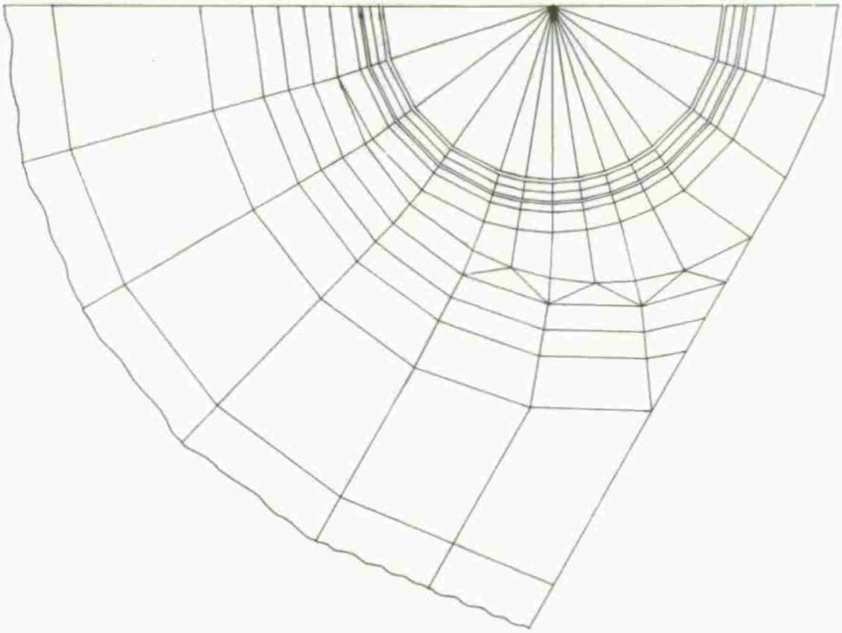

Figure 6. Inplane Finite Element Model for a Joint

The fourth and fifth modes of failure were analyzed using a linear-elastic, two-dimensional finite-element model of a unit-width cross-section through the thickness, as shown in Figure 7.

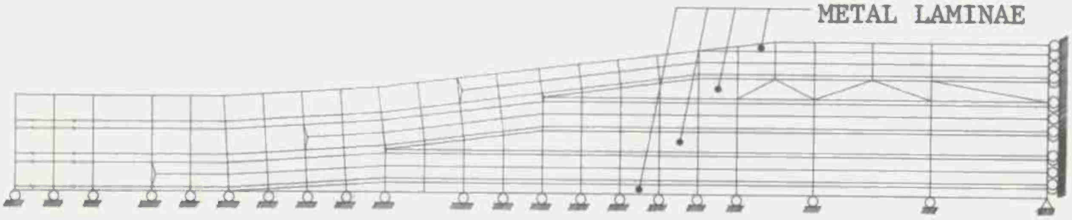

Figure 7. Cross-Sectional Finite Element Model for a Joint

The sixth mode, interlaminar splitting, is not amenable to direct analysis. It will be precluded from occurring by provisions at every joint for an initial clamp-up through the thickness, to produce a compressive preload on the interlaminar surfaces.

The finite-element analysis provided detailed knowledge of the biaxial states of stress throughout the structure for both the static and the fatigue design conditions. Corresponding data, to predict the strength of the materials when subjected to such stresses, were not considered reliable, and for this reason, the program included static and fatigue testing to determine failure strengths and working allowables under similar states of stress. Figure 8 shows the test specimen. Each end of the specimen contains an exact 1/2-scale model of the joint in the upper plate. A finite-element analysis of the specimen showed that the stresses in the vicinity of the joints of the test specimen are generally similar in pattern and magnitude to those in the hub for scaled loads.

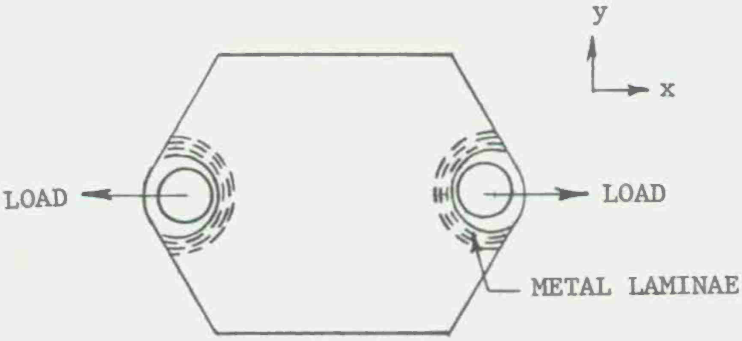

Figure 8. Specimen for Element Tests

The static test showed that the ultimate strength of a full-sized joint would be 176 kips, which is 1.95 times the required strength for the most critical loading. Figure 9 shows that the metal shims successfully transferred the load into the composite and that the composite supported the load. The primary mode of failure appeared to be rupture of the steel reinforcement at point A which is close to the minimum cross-section for the steel. The specimen exhibited fail-safe characteristics by surviving four individual failures which preceeded the final failure. As the loads were increasing at a uniform rate, loud reports were heard at 93, 95, 97 and 99% of the failure

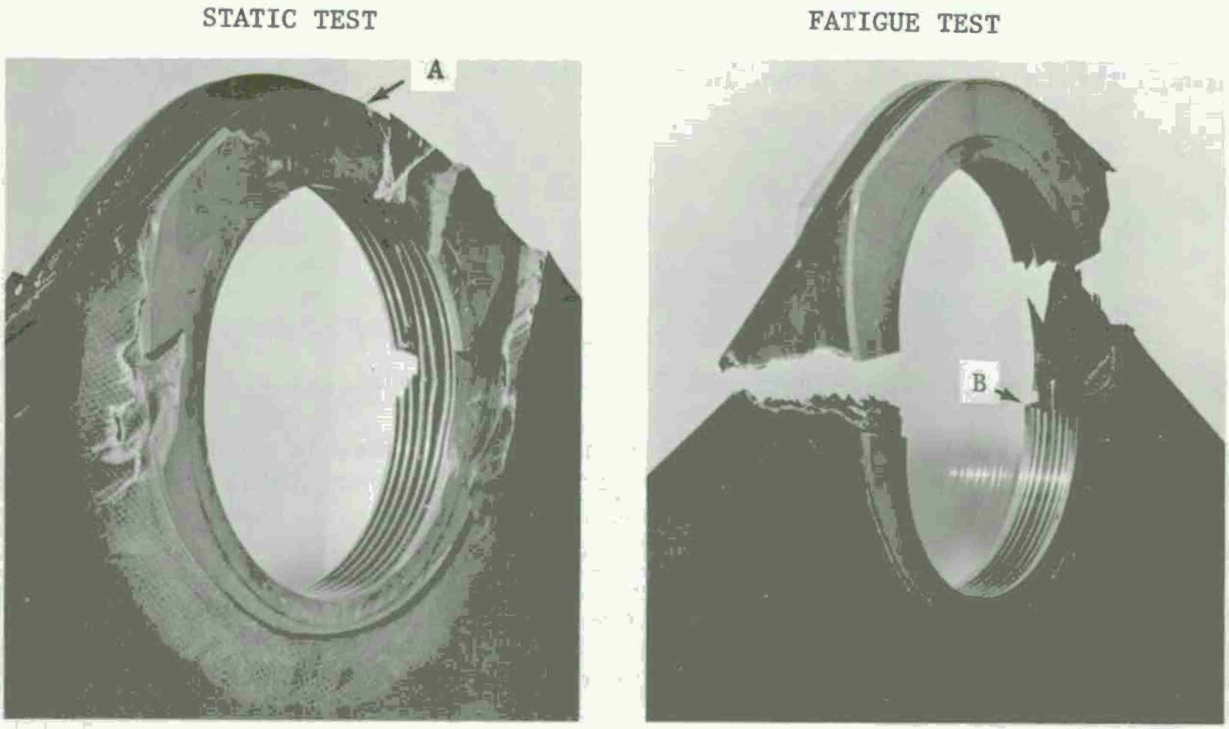

Figure 9. Element Specimens After Tests to Failure

load. The following stresses were calculated using the elastic finite-element model and the final failure load:

Composite at inner edge of reinforced area	38.7 ksi, σxx
	2.0 ksi, σyy
	17.7 ksi, τxy
Composite at inner edge of hole	58.9 ksi
Metal at inner edge of hole	217. ksi
Bond of composite to metal	2.0 ksi
Tapered tip of metal	61.5 ksi
Metal at failure origin (outer edge)	194. ksi
Composite at failure origin (outer edge)	10.3 ksi, σxx
	39.6 ksi, σyy
	- 20.2 ksi, τxy

A fatigue test was performed upon a second specimen using R = .1, maximum load/minimum load. The specimen was subjected to the following conditions:

1 million cycles at peak load = 25.0% of static failure load
1 million cycles at peak load = 30.7% of static failure load
.26 million cycles at peak load = 38.6% of static failure load

Stresses corresponding to these loads are directly proportional to the stresses shown for the static test. The origin of failure in the fatigue test was fatigue of the metal laminae at the inner edge of the hole at point B, shown in Figure 9. The fatigue strength of this joint is about 7% higher than that required to match the fatigue strength of the existing titanium hub.

Additional tests will be performed upon a one-half scale model of the hub assembly. The planned program includes static, fatigue endurance and ballistics damage tests.

CHARACTERISTICS AND PERFORMANCE

WEIGHT

Table II compares the estimated weight of the new composite hub and the actual weight of the existing CH-54B titanium hub. Weights for the new design were calculated from detail drawings. The new composite hub and its attachments are 105.89 lbs (26%) lighter than the existing production counterparts. Because the new rotor shaft is also lighter by 22.19 lbs, the total weight saving for the hub and rotor shaft is 128.08 lbs (25%).

TABLE II. WEIGHTS, EXISTING HUB AND NEW COMPOSITE HUB

EXISTING TITANIUM HUB	
Upper hub assembly	221.80 lbs
Lower plate assembly	70.50
Other (Brackets, fasteners, rings, cones, etc.)	111.90
TOTAL, HUB PROPER	404.20 lbs
Rotor shaft segment (calculated)	97.03
TOTAL, HUB AND ROTOR SHAFT	501.23 lbs
NEW COMPOSITE HUB	
Upper plate	63.23 lbs
Pan plate	91.77
Lower plate	56.79
Other (housings, fasteners, rings, cones, etc.)	86.52
TOTAL, HUB PROPER	298.31 lbs
Rotor shaft segment	74.84
TOTAL, HUB AND ROTOR SHAFT	373.15 lbs

NOTE: The table includes the weight of the segment of shaft above Water Line 250.95 to provide a valid basis for comparisons, because the shafts above that level are different in each design.

COST

Detailed estimates were prepared for the average price in a total production run of 1000 assemblies. Table III summarizes the results. It shows that the initial acquisition price is $17,114 per assembly with no credit for lower weight. If weight savings were valued at only $50 per pound, the adjusted price would be $11,228 per assembly. These prices are based upon a 1976 quotation of $35/lb for graphite-epoxy prepregs. If the cost were $20/lb (a projected future cost stated in 1976 dollars), the weight-adjusted price would be $7,870.

The price for the corresponding existing titanium hub is estimated to be $36,000. (This price includes $34,000 for the hub housing, as shown in Table I, plus $2,000 for 59 lbs of required fasteners and supports.) Based upon this price, the composite hub provides the following savings in initial acquisition costs alone:

52%, with no credit for weight savings
68%, if weight savings were valued at $50/lb
78%, if weight savings were valued at $50/lb, and if graphite were available at $20/lb in the acquisition time period.

TABLE III. SUMMARY OF ESTIMATED PRODUCTION COSTS IN 1976

COMPONENT	MATERIAL	COST	SEE NOTE
Doublers	CRES	$ 171	1
Center Fittings	Titanium	1,068	
Plates	Graphite-Epoxy	5,140	2
Other	Miscellaneous	1,208	
TOTAL Material and Purchased Components		$ 7,587	
Material Burden Factor		x 1.524	3
Through Price for Materials		$11,563	4
Production Labor, 246.7 hrs.		5,551	
TOTAL Production Price		$17,114	6

NOTES:

1. All costs are average costs for a production run of 1000 hubs.
2. Using 1976 prices, $35/lb for 5209 T-300 system.
3. Typical for a competitive company.
4. Price to the customer, including all burdens and a 12% profit.
5. Hours based upon an 87% learning curve.
   Rate = $22.50/hr, typical for a competitive company.
6. Price to the customer, including all materials and labor, fully burdened with a 12% profit.

PRODUCIBILITY

The composite hub is designed for uncomplicated and efficient production using hand layups of preimpregnated materials. The layups are exceptionally simple, permitting placement with a minimum of handling. Each plate is basically uniform in thickness. Thus, a single steel rule die for each plate can be used to cut the entire pattern, including the holes, in one operation. The plies and local reinforcements can then be stacked in sequence to achieve the desired interleaving. The bonding tool can contain standing plugs at each hole to assist placement. A nearly exact 0 ± 60 orientation can be used in the top and bottom plates which are flat. The orientation in the pan plate will be an approximate 0 ± 60 which results when the flat patterns are layed over a conical mold.

FAIL-SAFETY AND BALLISTICS TOLERANCE

The new composite hub enjoys a high degree of fail-safety and ballistics tolerance in full accordance with AR-56, which requires that no failure of a single structural element cause catastrophic failure or preclude safe continuous flight to a normal destination.

The plate hub concept provides inherent redundancy. Each plate can be envisioned as closely spaced elements providing multiple and alternative load paths. Such plates can survive ballistically-induced holes arbitrarily located. Olster and Roy performed tests to determine the ballistics survivability of graphite composites and observed that failure will not occur upon impact if the stress at the time of impact is below a characteristic threshold strength and that failure will not occur upon subsequent loadings of the damaged plate if the stresses are below a characteristic residual strength (Reference 3). Their conclusions included the following:

"1. The threshold strength and residual strength of the laminates were found to be approximately 55 and 62%, respectively, of the ultimate tensile strength, implying that ply orientation is the most significant factor.
2. For the two velocities considered, the residual strength was independent of both the preload and the projectile velocity.
3. Both the residual strength and threshold strength show a correspondence with the fracture toughness of the laminates.
4. Based upon very limited results, it appears that 50-caliber AP projectiles have only a slightly more detrimental effect than 30-caliber projectiles."

Stress analyses show that, in the fatigue design condition, the peak stresses in the upper and pan plates are less than 11 ksi, and in the lower plate, less than 13 ksi. These values are well below the threshold strength of 30.1 ksi and the residual strength of 34.6 ksi reported for 0/± 60 laminates of graphite following 30-caliber projectile hits. A residual strength of 29.4 ksi was reported following a 50-caliber hit. Thus, it is concluded that the plates will be ballistics tolerant even to multiple hits.

In addition, it is believed that there exists a significant survival probability following 23-mm HE attack, but no convincing analysis is possible. Experimental verification would be necessary to establish 23-mm survivability.

It is also expected that significant fatigue performance will be still available following 30-caliber or 50-caliber attack. Freeman and Keubeler have shown that graphite structures exhibit fatigue strengths that are exceptionally large fractions of their static strength, even in the prsence of sharp notches (Reference 4). For example, HT graphite, with various fiber orientations, exhibits the fatigue performance shown in Table IV.

TABLE IV. FATIGUE PERFORMANCE OF HT* GRAPHITE

FIBER ORIENTATION	STATIC ULTIMATE STRESS ksi	MAXIMUM STRESS, R = 0.1 NOTCHED $K_t = 3$ 10^4 cycles	10^7 cycles
0	165	70	60
0, 90	110	63	60
0, 90, ± 45	58	32	30

*HT = High tensile strength, high elongation, intermediate modulus, intermediate cost, graphite fiber.

RELIABILITY AND MAINTAINABILITY (R&M)

The composite plates are rugged and simple and have highly redundant load paths and low notch sensitivity. They are inherently reliable and maintainable. Therefore, the design efforts concentrated upon the joint details, where R&M had a great influence upon the final configuration. The simplicity, low parts count and producibility of the present joints are, in large measure, the results of repeated design changes to improve reliability and maintainability. A desirable consequence was also a corresponding lowering of cost. The R&M characteristics will be presented in future reports; herein, the maintainability requirements are listed, and the installation and removal procedures are described.

The maintainability requirements were stated as the following qualitative goals and objectives:

1. Minimize the maintenance manhours per flight hour for both scheduled maintenance and unscheduled corrective maintenance
2. Minimize the probability of maintenance being required above field level
3. Ensure the simplicity of installation and removal
4. Ensure that there are positive removal procedures, even in the presence of extensive corrosion and/or fretting
5. Ensure that the installation and removal of the hub assembly requires no disassembly of hub components

6. Ensure the ease of inspection of critical parts
7. Provide maximum accessibility to mounting hardware
8. Ensure that all components subject to corrosion, fretting or wear can be refurbished or replaced
9. Ensure that the maintenance manpower requirements will be compatible with the CH-54 maintenance program
10. Ensure that the skill levels required for field repairs are compatible with the training of the Army personnel.

The hub is installed and removed as a complete unit, with no buildup or disassembly at the Direct Support level. For installation, first the damper bolts are loosened two turns, then the hub is lowered over the drive shaft until the bottom plate approaches the flange on the drive shaft. The hub is turned to align the scallops, lowered to rest on the cone seats, and turned again to align the bolt holes, and then the lower bolts are inserted. The ring at the top of the shaft is positioned, and the upper bolts are inserted. All bolts are then torqued to standard levels. As the bolts tighten, they will draw the aluminum-bronze cones down to positive stops and induce a tight preload.

The upper and lower cone seats are cut at an angle of 14 degrees, which will normally allow self-release and ease of removal. In the event of abnormal seizing due to corrosion or fretting, positive removal is still assured by provisions for forcing separation by applying hydraulic pressure to the upper cone and by applying mechanical jacking to the lower cone. Assembly and removal require only common hand tools. The mounting bolts are all easily accessible.

RADAR DETECTABILITY

Radar cross-section (RCS) measurements were made using one-half scale models of the existing production hub and several versions of the new plate hub. These versions included hubs constructed from bare, nonconducting (fiberglass) composites, from nonconducting composites coated selectively with a magnetic absorber, and from a conducting composite, such as graphite. The latter was simulated by covering the fiberglass model with aluminum foil. The magnetic absorber material is a special paint consisting of a polyurethane vehicle with finely divided ferrous and ferrite pigments. It is applied with conventional spray equipment.

The new plate hub provides reduced radar detectability to the following extents:

1. A 38% reduction in RCS was achieved by shape alone, comparing the current hub and the plate hub covered with aluminum.
2. A 76% reduction in RCS was achieved through the combination of shape and the use of nonconducting composites.
3. A 93% reduction in RCS was achieved through the combination of shape, nonconducting composite materials, and the application of the magnetic absorber to the improved hub.
4. Use of conductive (graphite) composites will change the RCS treatments required. It will be necessary to cover larger areas with the magnetic absorber.

ADDITIONAL CONSIDERATIONS

Lightning. Graphite composites can be seriously damaged if they become the primary electrical path. This will be precluded in the new plate hub by radial, metallic conductors between the main rotor shaft and each bearing housing.

Impact. Graphite-epoxy composites are susceptible to foreign object damage (FOD) involving low-velocity impacts, such as those from falling objects; however, the actual service threat and the corresponding design criteria are not well-defined, particularly in the case of a rotor hub, which is located high-up on the aircraft and which is relatively unexposed. It is believed that the present design is rugged and that, if required, it could be protected to any degree desired by the use of energy-absorbing covers on selected exposed surfaces. In the most exposed positions, at the blade joints, the graphite composite is already reinforced by steel doublers, which should provide ample resistance to impact damage. Away from the joints, the plates are thick, 0.338 inch, and should possess adequate inherent impact resistance. The FOD problem is widely recognized, and it is anticipated that, in the future, material suppliers will develop new matrix systems that will provide increased impact resistance.

Debris. The space between the rotor shaft and the pan plate will not become a trap for water, sand or other debris. It will be cleansed by centrifugal force which will expel any material through the openings that exist between the pan and upper plates at the positions between the blades. In addition, the lower cone will be grooved to provide drainage paths at the lowest point.

OTHER APPLICATIONS

In the design for the CH-54B, the pan plate, which provides the load path for transverse shear, is located in the intermediate position. This is not the only possible configuration. The pan plate could also be located either above or below the flat plates. Figure 10 shows a sketch of an alternate design (for a four-bladed rotor) in which the pan plate (2) is on top. In addition, the plates (1 and 3) are also shown with a shallow cone corresponding to the steady 1-g cone angle of the blade. The load paths in this design are similar to those described earlier except for the transmission of torque which, in this design, is shared by plates 1 and 3.

The principal advantage of this configuration is the clear envelope it provides inboard of the bearings. The entire annular space between plates 1 and 3 is open. Figure 10 shows an elastomeric articulation in this space. A spherical bearing (4) provides the lead-lag and flapping motions; a chevron-stack thrust bearing (5) allows feathering motions. The outboard end of the spherical bearing receives attachment bolts that hold it to the hub. The rotor blade shank (6) extends inboard for contact with flapping stops and attachment of a damper.

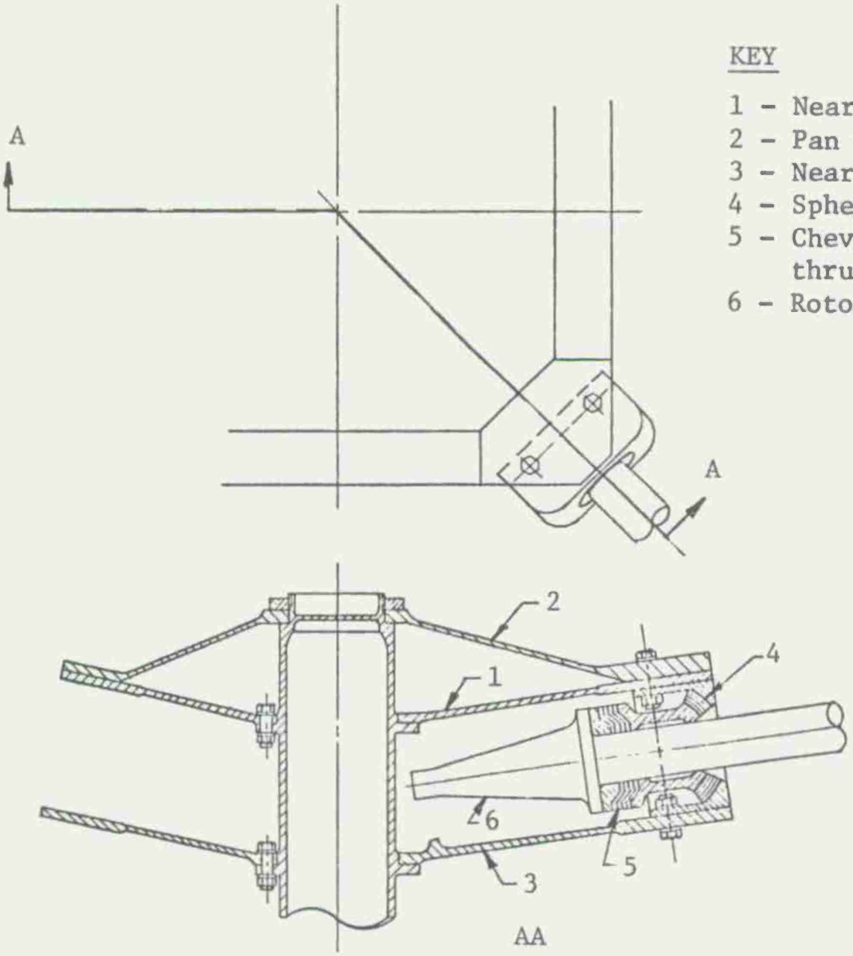

KEY

1 - Nearly flat plate
2 - Pan plate
3 - Nearly flat plate
4 - Spherical bearing
5 - Chevron-stack thrust bearing
6 - Rotor blade shank

Figure 10. An Alternative Plate Hub Configuration

CONCLUSIONS

1. The composite plate hub is producible, fail-safe, ballistically tolerant, reliable, maintainable, low in radar detectability, low in weight, and low in cost.
2. A composite hub designed for the CH-54B offers the following specific advantages:

   a. The composite hub weighs 105.89 lbs (26%) less than the existing titanium hub.
   b. The composite hub and rotor shaft assembly weighs 128.08 lbs (25%) less than the corresponding titanium hub and rotor shaft assembly.
   c. The initial acquisition price of the composite design is $17,114 per assembly, with no credit for lower weight. If weight savings were valued at $50/pound and if graphite were $20/pound, the

adjusted initial price would be $7,870 per assembly. These costs correspond to savings of 52% and 78% of the price of the existing titanium hub.

d. The composite design provides increased ballistics tolerance, fail-safety, and reliability.

e. The composite design provides a 38% reduction in radar cross section by shape alone. Using limited applications of a spray-on magnetic absorber, a 93% reduction is feasible.

f. The composite design provides good maintainability, with particularly simple procedures for installation and removal that require no special tools.

REFERENCES

1. Faiz, R. L., "A Design Analysis of a CH-54B Main Rotor Hub Fabricated From Composite Materials", Whittaker Corporation; USAAMRDL TR 73-14, U. S. Army Air Mobility Research and Development Laboratory, Fort Eustis, Virginia, 1973.
2. Levenetz, B., "Composite-Material Helicopter Rotor Hubs", Sikorsky Aircraft Division; USAAMRDL TR 73-49, U. S. Army Air Mobility Research and Development Laboratory, Fort Eustis, Virginia, 1973.
3. Olster, E. F., and Roy, P. A., "Tolerance of Advanced Composites to Ballistics Damage", presented at the Third Conference on Composite Materials: Testing and Design; ASTM STP 546, Philadelphia, Pennsylvania, 1973.
4. Freeman, W. T., and Kuebeler, G. C., "Mechanical and Physical Properties of Advanced Composites", presented at the Third Conference on Composite Materials: Testing and Design; ASTM STP 546, Philadelphia, Pennsylvania, 1973.

ACKNOWLEDGEMENTS

This project is sponsored by the U. S. Army Air Mobility Reasearch and Development Laboratory, Eustis Directorate, under Contract DAAJ02-75-C-0013. The writers wish to acknowledge the foresight of Mr. Arthur Gustafson of USAAMRDL, who recognized early the potential advantages of composite rotor hubs and initiated the program. Several persons have made significant contributions. Mr. Richard Hollrock, Kaman Aerospace Corporation, contributed to the structural design and prepared the project drawings. Mr. Robert Gilchrist, Kaman Aerospace Corporation, performed reliability and maintainability analyses and contributed to design improvements. Mr. John R. Carver, Tulsa Division of Rockwell International, performed the radar measurements and analyses.

EFFECT OF VARIABILITY OF DESIGN PARAMETERS ON STRESS CONCENTRATION ESTIMATES

E. M. LENOE
Chief, Mechanics of Materials Division

D. M. NEAL
Research Mathematician

Army Materials and Mechanics Research Center
Watertown, Massachusetts

ABSTRACT

This paper presents a statistical evaluation of stress concentration factors (SCF) of finite and infinite width anisotropic plates, subjected to uniaxial loads and containing various types of central cutouts. SCF for finite plates are determined from a modified mapping collocation technique as applied to orthotropic plate analysis. Influence of variability in material moduli is investigated by application of the Monte Carlo method. Glass, boron and graphite reinforced $[0/\pm 45/0/\overline{90}]_s$ epoxy laminates are considered. Sensitivity analysis of the influence of increasing variability in moduli is completed. Scatter in shear modulus is shown to dominate scatter of the probability distribution of stress concentration. Comparison of the calculated distribution function with available experimental data demonstrates the success of the theoretical estimates for strain concentration. However, strength estimates remain problematical, partly due to lack of data from which to formulate appropriate failure criteria, and also due to requirements in further development of ply-by-ply fracture analysis. This is particularly true for materials and angle ply configurations capable of large deformations.

INTRODUCTION

In recent years, various development and design studies have produced data and tentative philosophy for design of composite structures, but discontinuities, joints and cutouts are still not well understood. Classical and numerical analysis procedures can predict elastic stress-strain distribution and concentration factors reasonably well. Predicted deformation patterns are also in reasonable agreement with experimentation. However, failure stress estimates cannot be made with great exactness and the tendency is to considerably underestimate composite structural load capacity. This is partly related to the fact that even in the case of plane stress, sufficient test data are ordinarily not available to select a preferred failure criterion with confidence. It is generally observed [1] that elastic laminate ply-by-ply analysis leads to measured strength reduction factors (SRF) $\geqslant$ theoretical stress concentration factors (SCF). Numerous experimental investigations have shown that the failure process is dominated by unloading mechanisms which utilize available parallel unloading paths. For instance, Whiteside, et al [2] reports that during monotonic loading of quasi-isotropic composite panels containing cutouts, audible fracturing commenced at 60 to 70% of the ultimate failure load in boron and glass laminates, and near 85% in graphite epoxy constructions. Both boron and glass composites displayed delamination due to tensile cracking as well as interlaminar shear failure of individual plies. Thus, not only is the failure criteria data lacking, but also the procedures to calculate local fracture modes and sequences are in developmental stages. Fortunately, existing analytical treatments of failure are ordinarily conservative. However, in the interest of more efficient utilization of composites, as well as the necessity to develop statistical methods, several problems were treated during this study.

The first problem is primarily concerned with examination of the effects of moduli uncertainty and variability on stress analysis of anisotropic structures. Abundant literature documents the experimental difficulties of accurate characterization of fiber reinforced materials. Certain properties are rather easily obtained whereas others are troublesome to measure. For instance, uniaxial moduli such as longitudinal and transverse moduli in composites generally exhibit less scatter than experimentally determined shear modulus. Furthermore, the mean value of shear modulus is markedly affected by the test method [3,4,5]. Thus in this case, the influence of moduli variability on predicted stress variation was established. Calculated variations compared reasonably well with experimental data reported in the open literature.

The second problem deals with attempts to calculate ply-by-ply failure response of the quasi-isotropic laminates. Comparison of these calculated strength distributions with results obtained on various angle ply configurations emphasizes the importance of further study of failure theories and the necessity for generating design data for the composite system under consideration.

HOMOGENEOUS ANISOTROPIC PLATE ANALYSIS

Stress analysis of filamentary composite plates requires anisotropic, inhomogeneous and inelastic considerations in order to represent the actual physical problem. In order to avoid these extreme analysis problems, the simplest composite representation consisting of homogeneous anisotropic medium is analyzed. The actual homogeneous solution involves determining stresses in an orthotropic, mid-plane symmetrical laminate subjected to plane stress conditions. The method of solution for the infinite sheet was developed by Refs. 6 and 7. For finite sheets, a modification of the above method was developed by using the Modified Mapping Collocation technique [8]. This procedure provides a means of solving finite orthotropic plate problems for various configurations subjected to cutouts, cracks and cutouts with cracks.

The basic equation for the 2-dimensional problem is

$$a_{22} \frac{\partial^4 U}{\partial x^4} - 2\, a_{26} \frac{\partial^4 U}{\partial x^3 \partial y} + (2\, a_{12} + a_{66}) \frac{\partial^4 U}{\partial x^2 \partial y^2} \tag{1}$$

$$- 2\, a_{16} \frac{\partial^4 U}{\partial x \partial y^3} + a_{11} \frac{\partial^4 U}{\partial y^4} = 0$$

where a_{ij} are elastic constants from generalized Hooke's law.

U is a stress function of the form

$$U(x,y) = 2\, R_e \left[F_1(z_1) + F_2(z_2)\right] \tag{2}$$

where

$$F_1(z_1) \text{ and } F_2(z_2)$$

are arbitrary functions of the complex variables

$$z_1 = x + s_1 y \text{ and } z_2 = x + s_2 y.$$

The complex constants s_1 and s_2 are determined from assuming unequal roots of the characteristic equation.

$$a_{11} s^4 - 2 a_{16} s^3 + (2 a_{12} + a_{66}) s^2 - 2 a_{26} s + a_{22} = 0 \tag{3}$$

and are of the form

$$s_1 = \alpha_1 + i \beta_1 \qquad s_3 = \alpha_1 - i \beta_1$$
$$s_2 = \alpha_2 + i \beta_2 \qquad s_4 = \alpha_2 - i \beta_2$$

where α_1, α_2, β_1 and β_2 are real constants

and $\beta_1 > 0, \beta_2 > 0; \beta_1 \neq \beta_2$

The stress components can be defined by means of two analytic functions, ϕ, ψ. Introducing the stress equations

$$\sigma_x = \frac{\partial^2 U}{\partial y^2}, \ \sigma_y = \frac{\partial^2 U}{\partial x^2} \text{ and } \tau_{xy} = -\frac{\partial^2 U}{\partial x \partial y} \tag{4}$$

with the definitions

$$\frac{dF_1}{dz_1} = \phi(z_1) ; \frac{dF_2}{dz_2} = \psi(z_2)$$

one then obtains the general expression for stress components by means of two analytic functions ϕ and ψ in the form:

$$\begin{aligned}
\sigma_x &= 2R_e\,[s_1^2\,\phi'(z_1) + s_2^2\,\psi'(z_2)] \\
\sigma_y &= 2R_e\,[\phi'(z_1) + \psi'(z_2)] \qquad (5) \\
\tau_{xy} &= -2R_e\,[s_1\,\phi'(z_1) + s_2\,\psi'(z_2)]
\end{aligned}$$

Defining $x_n ds$ and $y_n ds$ as horizontal and vertical forces acting on an element of arc ds with normal n, the force resultant along the arc can be written as [9]

$$\begin{aligned}
&(1 + s_1)\,\phi(z_1) + (1 + is_2)\,\psi(z_2) + (1 + i\,\overline{s}_1)\,\overline{\phi(z_1)} \\
&\qquad + (1 + i\,\overline{s}_2)\,\overline{\psi(z_2)} = i\int^{s} (x_n + i\,y_n)\,ds \qquad (6)
\end{aligned}$$

For orthotropic plate analysis a_{26} and $a_{16} = 0$ in Eq. (1), the anisotropic material will therefore contain three planes of elastic symmetry.

From Eq. (1) orthotropic plate equation can be written as,

$$\frac{1}{E_2}\,\frac{\partial^4 U}{\partial x^4} + \left(\frac{1}{G_{12}} - \frac{2\nu_{12}}{E_1}\right)\frac{\partial^4 U}{\partial x^2 \partial y^2} + \frac{1}{E_1}\,\frac{\partial^4 U}{\partial y^4} = 0 \qquad (7)$$

with characteristic equation

$$\frac{s^4}{E_1} + \left(\frac{1}{G_{12}} - \frac{2\nu_{12}}{E_1}\right) s^2 + \frac{1}{E_2} = 0 \qquad (8)$$

and moduli values are defined in Fig. 1.

MODIFIED MAPPING COLLOCATION TECHNIQUE

The Modified Mapping Collocation technique is applied to the anisotropic plate analysis in a manner described in [8]. The method provides stress functions while ensuring traction free conditions on the cutout surface by using the Mushkelishvili-type extension arguments of analytic functions theory.

The stress function is represented by a Laurent expansion of the form

$$F\ (\zeta)\ = T \sum_{-\infty}^{\infty} (a_n + i\ b_n)\zeta^n \tag{9}$$

where a_n and b_n are real and ζ is a complex variable defined in auxiliary ζ plane (see Fig. 2).

The other boundary conditions are satisfied by choosing a finite number of boundary stations in the z-plane (Fig. 2) and prescribing proper stress and force conditions at these points. The a_n's and b_n's for the truncated series (Eq. 9) are determined by satisfying the above conditions. The coefficients are determined in a least squares sense in that the number of conditions exceeds the degrees of freedom by a ratio of two to one. This is done in order to obtain desired accuracy of solution.

INFINITE ORTHOTROPIC PLATE ANALYSIS

The simpler analytical problem considered is the infinite anisotropic plate, subjected to uniaxial tensile loads and containing a center hole. In this instance, the hoop stress, σ_θ, is calculated from [7]

$$\sigma_\theta = T\frac{E_\theta}{E_1}\left[-\ K\ \cos^2\theta + (1+n)\ \sin^2\theta\right] \tag{10}$$

where

$$K = \sqrt{E_1/E_2}\ , \qquad n = \sqrt{2\ (\ (E_1/E_2)^{1/2} - \nu_{12} + E_1/G_{12})}\ ,$$

$$T = \text{Applied tensile stress}$$

and

$$\frac{1}{E_\theta} = \frac{\sin^4\theta}{E_1} + \left(\frac{1}{G_{12}} - \frac{2\nu_1}{E_1}\right)\ \sin^2\theta\cos^2\theta\ +\ \frac{\cos^4\theta}{E_2}$$

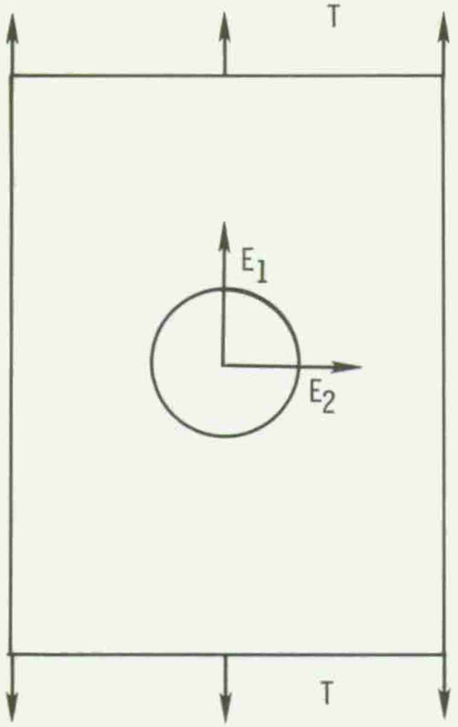

E_1 = Young's Modulus (more rigid principal direction)

E_2 = Young's Modulus (other in-plane principal direction)

ν_{21}, ν_{12} = Poisson's ratios

G_{12} = Shear Modulus

Figure 1. ORTHOTROPIC PLATE WITH CUTOUT

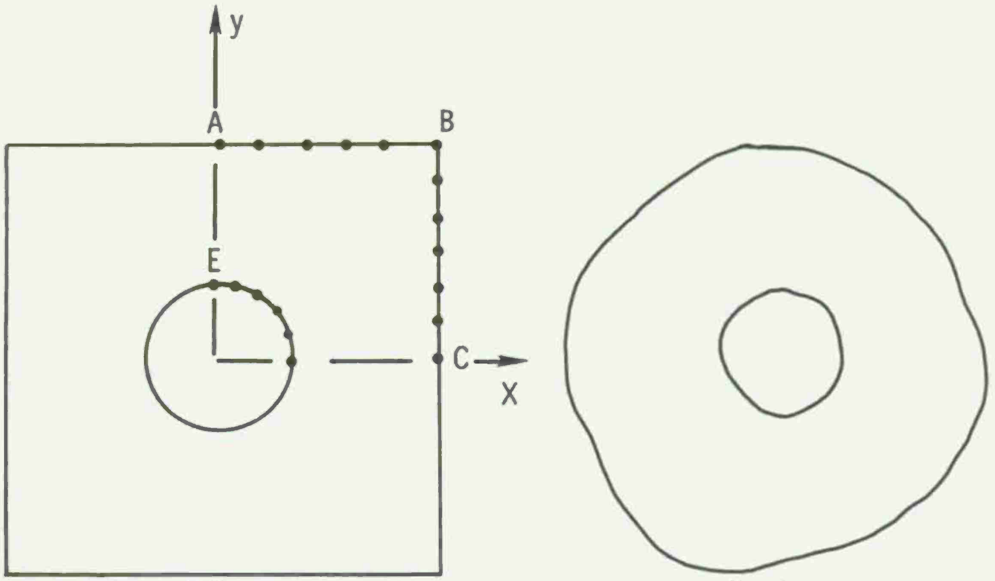

Z-Plane

ζ-Plane

$\widehat{ED}$

$$\sigma_n + i\tau_n = 0$$

AB

$$\sigma_x + i\tau_{xy} = T$$

BC

$$\sigma_y - i\tau_{xy} = 0$$

Figure 2. MAPPING PLANES

STRESS CONCENTRATION FACTORS

The Stress Concentration Factors (SCF) are defined as follows:

$$\mathrm{SCF} = \sigma_{max}/T \qquad (11)$$

where σ_{max} is the peak stress commonly evaluated at point D if Fig. 2. T is the applied tensile stress as shown in Fig. 1.

MONTE CARLO METHOD

The Monte Carlo method was applied in order to simulate the inherent variability of the controlling parameters, E_1, E_2, G_{12} and ν_{12} in determining SCF for the composite plate. The relative complexity of the functional relationship further suggests the need for the Monte Carlo method. The method avoids restrictions on the exact specification of the statistical distributions of the variables since simple approximating functions can serve well in the scheme. In general, this prevents formulation of incorrect frequency distributions for the quantities of interest.

In this paper determination of SCF values by the Monte Carlo method involves representing each of the independent variables by a set of normally distributed random numbers. Justification for using normal distributions is provided by results in Figure 3. Use of normal distributions is not a requirement. However, due to resulting simplifications, normal distributions were used in this initial phase of our work. The pertinent equation, including shear modulus G_{12}, commonly applied for SCF estimates is:

$$\frac{s^4}{E_1} + \left(\frac{1}{G_{12}} - \frac{2\nu_{12}}{E_1}\right)s^2 + \frac{1}{E_2} = 0 \qquad (12)$$

A value is specified for each variable by choosing a number at random from its corresponding distribution. The resulting value for SCF is determined for each set of randomly selected variables. The computation is repeated and a probability distribution is obtained for the SCF values.

The normally distributed random numbers were generated by a Univac 1108 subroutine. The procedure is simply one of generating uniform random numbers and solving for X in the relation

$$\int_{-\infty}^{X} f_i \, dx = R \qquad (13)$$

where R = uniform random number and

f_i = normal frequency distribution.

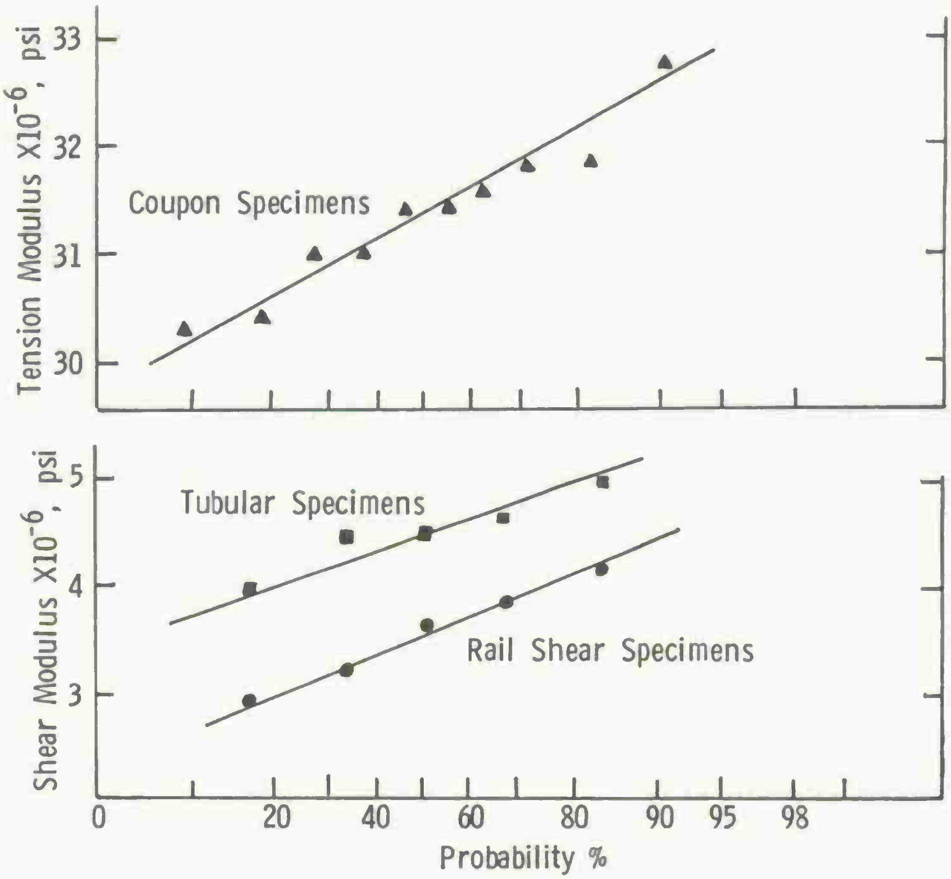

Figure 3. TENSION AND TORSION MODULUS OF 0^0 BORON EPOXY, NOMINAL 50% REINFORCEMENT REFERENCE [9]

As noted previously, if the probability distributions of the controlling variables are known from some experimental results or from an analytical basis, then the appropriate distribution function f_i may be used.

The roots evaluated in Eq. 12 are substituted into the analysis described previously. Values for σ_y are then tabulated for the composite system with maximum stress σ_{max} inserted in Eq. 11 in order to obtain SCF values. The number of SCF values equals the random numbers generated for each parameter.

STATISTICAL PARAMETERS

The mean, dispersion and distortion parameters are defined as follows:

$$\overline{W} \quad \text{(mean)} \quad = \quad \frac{1}{N} \sum_{i=1}^{N} W_i$$

$$\text{S.D. (standard deviation)} = \left[\frac{1}{N} \sum (W_i - \overline{W})^2 \right]^{1/2} \qquad (14)$$

$$g_1 \quad \text{(skewness)} = U_3 \; U_2^{-3/2}$$

$$g_2 \quad \text{(kurtosis)} = U_4 \; U_2^{-2} \quad -3$$

where W_i = i^{th} simulation of SCF

and

$$U_j = \frac{1}{N} \sum_{i=1}^{N} (W_i - \overline{W})^j$$

In order to generate the random numbers in the Monte Carlo application, the standard deviation (S.D.) is determined from the relation:

$$\text{S. D.} \quad = \quad M_x \; V_x \qquad (15)$$

where M_x = Mean

and V_x is an assigned percentage. The discussion "variation" in the figures and tables are V_x values.

RESULTS AND DISCUSSION OF STRESS CONCENTRATION ESTIMATES

For the three materials, graphite, glass and boron fibers, the composite was taken to have a $[0/\pm 45/0/\overline{90}]_s$ laminate construction.

The selection of optimum number of coefficients in the stress function (Equation 9) is made by minimizing errors on boundary collocation points and maintaining desirable solution accuracy for the system of equations in the stress computation. The bimodal frequency distributions shown in Figures 4a and 4b are the result of unacceptable solutions of the systems. In Figure 4a and 4b there are an insufficient and excessive number of coefficients respectively. For most of the computations, 12 to 18 positive and negative coefficients were necessary for satisfactory solutions.

The orthotropic SCF depends on the material constants, unlike the isotropic case which is independent of moduli values. The effect of large variations (30 to 40%) in modulus values combined with high stress gradients (SCF = 6.0) make it difficult to accurately assign acceptable number of coefficients for the mapping function. The infinite plate solution does not experience the above problem since the solution is quite simple compared to finite plate analysis.

A sensitivity analysis (Fig. 5) was made in order to determine the effects of variations in individual moduli values for the case of an elliptical cutout. In this problem the plate has a length and width of 20 and 10 inches respectively. The cutout is an ellipse with major and minor axes of 2.0 and 1.0 inches respectively.

In the case of all parameters with 5% variations (Fig. 5a), and for ν_{12} (Poisson's ratio) with variation of 30% (5d) there is slight variation in SCF values. For Young's modulus E_1 (Fig. 5c) and shear modulus G_{12} with variations of 30% (Fig. 5b) there is a large variation in SCF. This is not an important consideration for E_1 since experimental determinations are usually quite accurate and at the most in error by 10% or less. G_{12} values, however, are difficult to obtain experimentally and can have large uncertainties [3, 4, 5].

In design and analysis such variations can result in considerable problems since the designer may not have sufficient test data to recognize potential variation in stress states due to inherent material property variation. In the selection of material the designer must often proceed without being able to assess the effects of variations in material properties. Error bounds can be made for deterministic values obtained in the analytic solution of composites but these are only crude approximations.

On the other hand, the development of a probability density function (PDF) by the Monte Carlo technique allows one to obtain realistic probability numbers for SCF of the structure, while limited test data obtained from the experimental approach usually fails to provide accurate (PDF) curves.

In Tables I, II and III the effects of moduli variations on mean, standard deviation, skewness and kurtosis parameters are summarized. It should be noted that for relatively large variations in moduli the mean SCF varies by less than 2%, while dispersion and shape parameters increase considerably, particularly for the kurtosis measurement. Since the actual variations in observed G_{12} and other moduli can approximate 25% and 5% respectively then examination of results indicate care should be taken in arbitrarily assigning PDF values, particularly of the Gaussian form. The skewed right distribution could produce highly conservative estimates for SCF range of data.

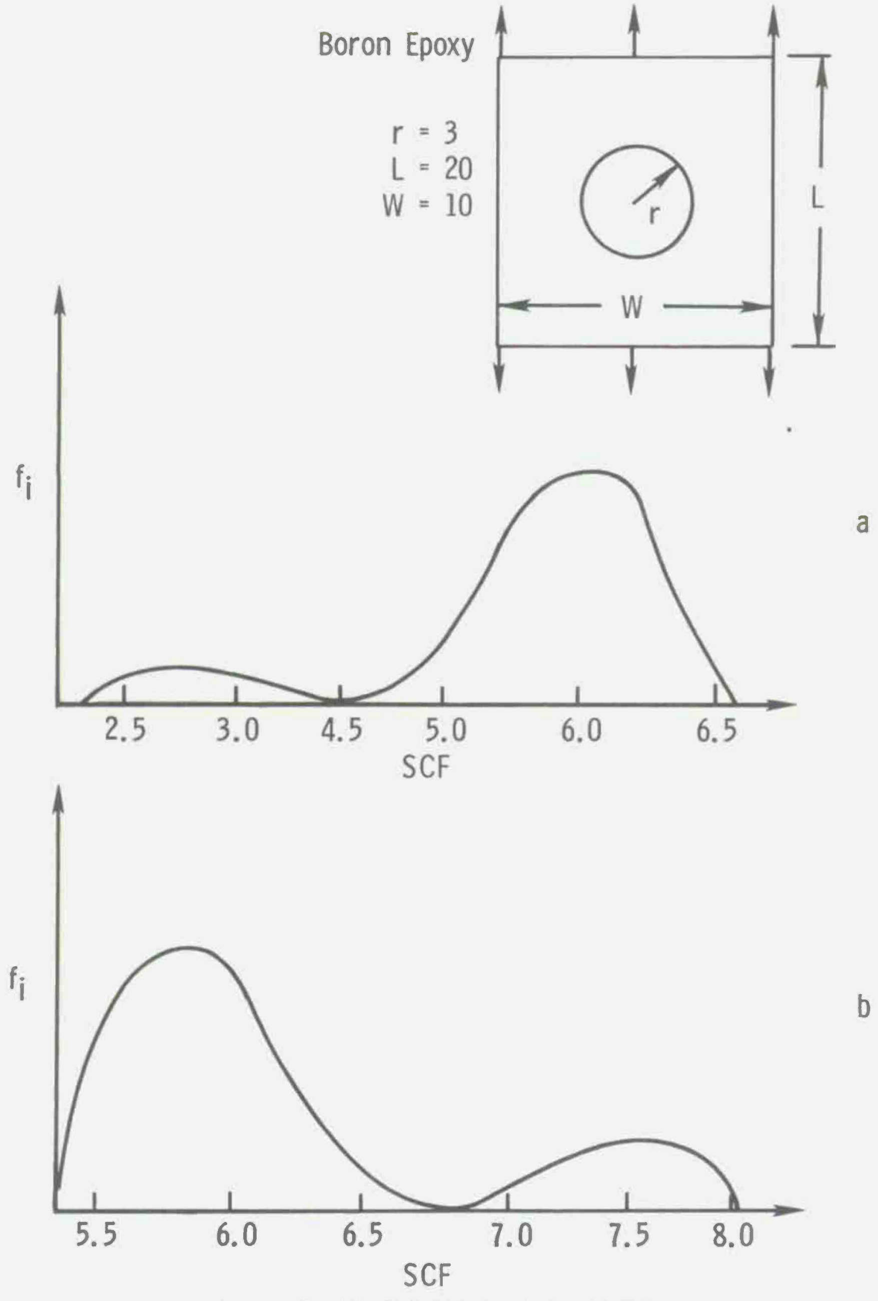

Figure 4. FINITE PLATE SOLUTION

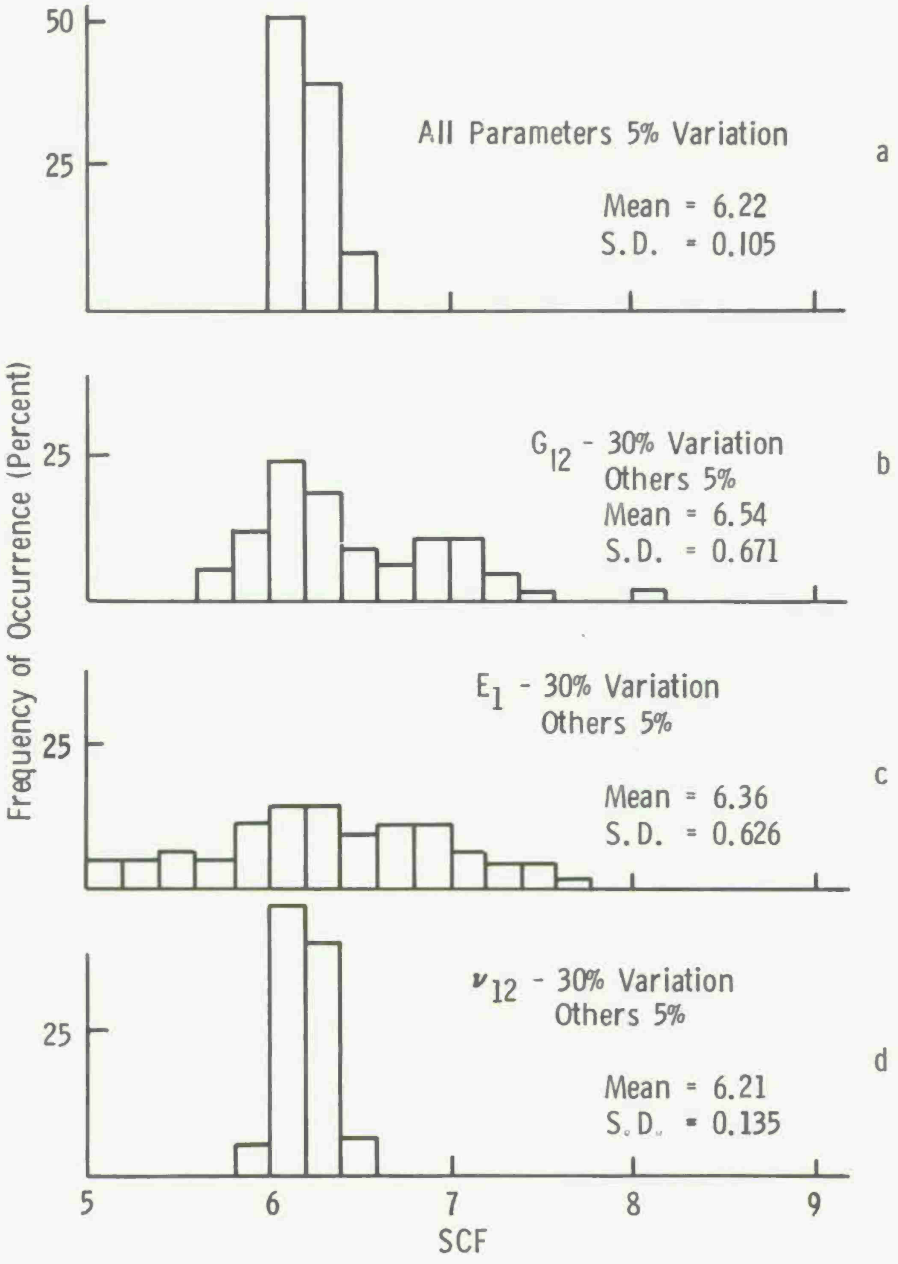

Illustrating Moduli Sensitivity

Figure 5. BORON EPOXY (ELLIPTICAL CUT-OUT)

TABLE I. SUMMARY OF BORON EPOXY COMPUTATIONS

SCF* = 3.438 $E_1 = 15.80\times10^6$ $E_2 = 7.26\times10^6$ $G_{12} = 4.28\times10^6$ $\nu_{12} = 0.450$

	Percent Variation of Moduli: E_1, E_2, G_{12} and ν_{12}			Variance in G_{12} when E_1, E_2 and ν_{12} have 5% Variation			
	5%	10%	15%	10%	15%	20%	25%
SCF†	3.397	3.401	3.408	3.402	3.412	3.426	3.448
Standard Deviation	0.0687	0.1390	0.2131	0.0976	0.1366	0.18701	0.2651
Skewness	0.1488	0.1794	0.2306	0.3689	0.732	1.3171	3.0042
Kurtosis	0.2600	0.3424	0.5354	0.2732	1.217	4.184	22.589

*Finite Plate Solution (No Variations) L = 20.0, W = 10.0 and r = 0.5
†Infinite Plate Solution - 1500 Trials
Moduli in pounds per square inch

TABLE II. SUMMARY OF GLASS EPOXY COMPUTATIONS

SCF* = 3.157 $E_1 = 3.75\times10^6$ $E_2 = 2.83\times10^6$ $G_{12} = 1.29\times10^6$ $\nu_{12} = 0.360$

	Percent Variation of Moduli: E_1, E_2, G_{12} and ν_{12}			Variance in G_{12} when E_1, E_2 and ν_{12} have 5% Variation		
	5%	10%	15%	15%	20%	25%
Standard Deviation	0.0610	0.1217	0.1894	0.1215	0.1664	0.2359
SCF†	3.119	3.119	3.129	3.133	3.140	3.165

*Finite Plate Solution (No Variations) L = 20.0, W = 10.0, and r = 0.5
†Infinite Plate Solution - 1500 Trials
Moduli in pounds per square inch

TABLE III. SUMMARY OF GRAPHITE EPOXY COMPUTATIONS

SCF* = 3.624 $E_1 = 10.25\times10^6$ $E_2 = 4.69\times10^6$ $G_{12} = 2.27\times10^6$ $\nu_{12} = 0.42$

	Percent Variation of Moduli: E_1, E_2, G_{12} and ν_{12}			Variance in G_{12} when E_1, E_2 and ν_{12} have 5% Variation			
	5%	10%	15%	10%	15%	20%	25%
SCF†	3.576	3.580	3.588	3.582	3.593	3.609	3.633
Standard Deviation	0.0747	0.1513	0.2321	0.1087	0.1536	0.2110	0.2991
Skewness	0.1521	0.1959	0.2620	0.3789	0.7403	1.3155	2.9630
Kurtosis	0.1832	0.2750	0.4853	0.2604	1.231	4.1580	22.0050

*Finite Plate Solution (No Variations) L = 20.0, W = 10.0 and r = 0.5
†Infinite Plate Solution - 1500 Trials
Moduli in pounds per square inch

The results for 1500 "random tests" described in the tables combined with appropriate PDF provides a good analytic tool for determining predictable range of SCF values with corresponding probabilities.

The predicted dispersions shown in the tables are consistent with Whiteside's experimental data [2] for the same model described in Fig. 1. For limited data of three similar Boron specimens, SCF values were 3.08, 3.34 and 3.58 using a strain gage measurement. There were similar dispersions for graphite and glass epoxy. Calculated distributions of strain concentrations are shown in Figure 6.

PLY FAILURE ANALYSIS

In principle, failure criteria can be applied on a ply-by-ply basis and compared to the stress state in the vicinity of a free edge or notch. There are a number of difficulties associated with this notion. First of all, the choice of empirical failure criteria is problematical. Secondly, the general state of stress is not easily determined.

Regardless of these troubles, we sought to establish the relative accuracy of failure predictive capability for the problem defined in Figure 7a, using widely accepted failure theories, but restricting consideration to linear analysis procedures.

The method of analysis involves treating each layer as an anisotropic continuum and defining failure in relation to each layer. This requires use of a modified plasticity yield criterion which is basically a quadratic interaction formula involving stress components.

The stress in each layer is determined by considering the laminate to be a homogeneous anisotropic elastic plate where plane stress at a point produce uniform strain through the thickness. The strain and stress values in each layer (Fig. 7b) are determined from relations of this type, (0° layer)

$$\sigma_{\ell} = \sigma_x \left(\frac{Q_{12} - \nu_{xy}\, Q_{11}}{E_x} \right) + \sigma_y \left(\frac{Q_{11}}{E_y} - \frac{\nu_{xy} Q_{12}}{E_x} \right)$$

$$\tau_{\ell t} = \sigma_x \left(\frac{Q_{12} - \nu_{xy} Q_{12}}{E_x} \right) + \sigma_y \left(\frac{Q_{12}}{E_y} - \frac{\nu_{xy} Q_{22}}{E_x} \right)$$

$$\tau_{\ell t} = \tau_{xy} \frac{Q_{66}}{G_{xy}} \qquad (16)$$

where Q's – reduced layer stiffnesses

σ_{ℓ}, σ_t – fiber stresses in longitudinal and transverse direction respectively.

ν_{xy} – Poisson ratio

$\tau_{\ell t}$ – shear stress in layer

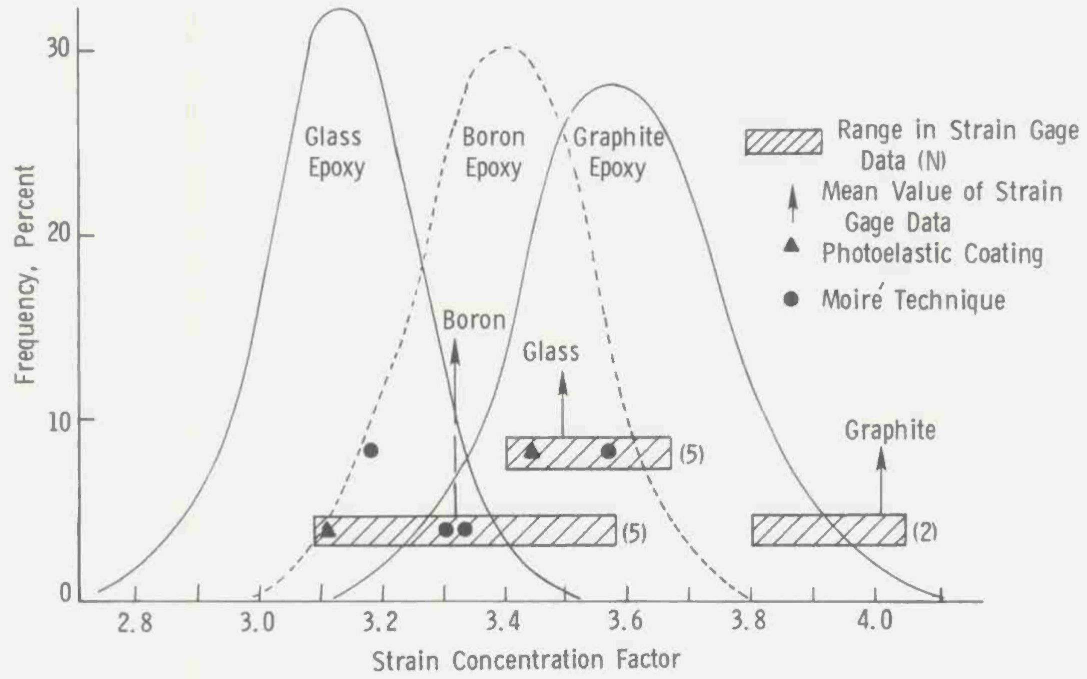

Figure 6. COMPARISON OF CALCULATED AND OBSERVED PROBABILITY DISTRIBUTIONS OF STRAIN CONCENTRATION FACTORS

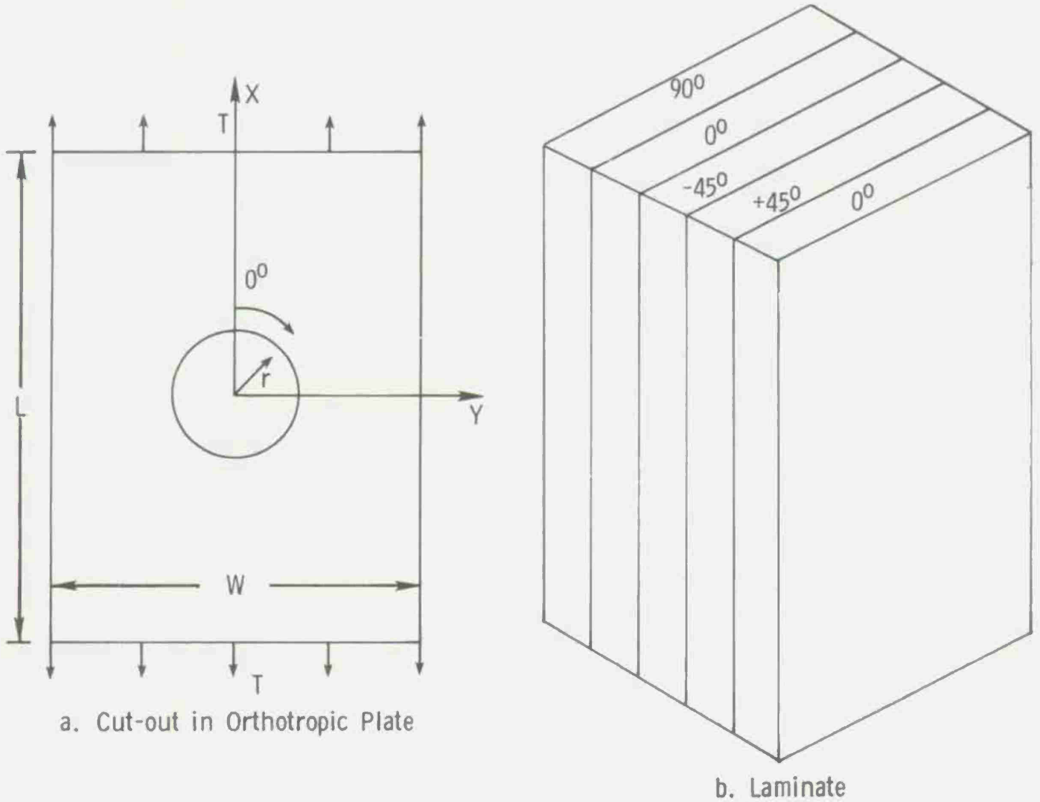

a. Cut-out in Orthotropic Plate

b. Laminate

Figure 7. PLY ORIENTATION $(0/\pm45/0/\overline{90})_s$

and σ_x, σ_y, τ_{xy} are determined stresses from orthotropic laminate solution.

With the ability to determine stresses and their locations one may determine failure loads and locations of failure using various criteria such as Hill-Von Mises, Tsai-Wu and Hoffman. The model selected (Fig. 7a) with geometric parameters L = 20, W = 10 and r = .5, for evaluation of point stress failure law, involves compressive and tensile stresses in the solution. For this stress state, the Hoffman criterion was applied to the model in order to include both stresses and is of the form:

$$\frac{\sigma_\ell^{\,2}}{X_T X_c} + \frac{\sigma_t^{\,2}}{Y_T Y_c} - \frac{\sigma_\ell \sigma_t}{X_T X_c} + \left(\frac{X_c - X_T}{X_T X_c}\right)\sigma_\ell + \left(\frac{Y_c - Y_T}{Y_T \; Y_c}\right)\sigma_t + \frac{\tau_{\ell t}^{\,2}}{s^2} = 1 \qquad (17)$$

where ultimate strengths are defined as:

X_T - tension (direction of fiber),

X_c - compression (direction of fiber),

Y_T - tension (transverse),

Y_c - compression (transverse)

and

s - Shear Strength

The failure stresses FL tabulated in Tables IV to VI are determined from solution of the quadratic equation (17). Stresses are initially computed for unit loads, then magnified as determined from solutions of Eq. 17. Strength values are obtained from Whiteside's tabulated strength data [2].

In the development of the referenced tables, the stresses are determined systematically so that contour representation of stress field is made for each ply. Tables IV to VI are abbreviated versions of a more complete representation of the stress field. Only the more relevant data is presented. Zero degree ply designates fibers oriented in the direction of the load. The other ply orientations are consistent with rotations from zero orientation. The X-Y coordinates indicate location of stresses.

In examining Tables IV to VI it becomes obvious from experimental results that minimum FL values are not sufficient for measuring failure loads of the composite. Two other criteria were used in establishing failure location and loads. Initially from the Hoffman criterion load FL is determined. The layer stress σ_ℓ in direction of fiber for each layer is evaluated for this load, then the ratio σ_ℓ / X_T is calculated. The combination of $\sigma_\ell / X_T > 1$ and corresponding minimum FL values determine the layer, failure load and location of failure.

With this assumption one estimates that failure load using this approach for graphite material (Table V) is 25.7 ksi for 0° ply at location X = .5 and y = 0, since σ_ℓ / X_T is max and the

TABLE IV* GLASS

PLY°	X	Y	σ_ℓ	σ_t	$\tau_{\ell t}$	σ_ℓ/X_T	$\sigma_\ell/{-X_c}$	σ_T/Y_T	$\sigma_t/{-Y_c}$	$\tau_{\ell t}/s$	FL(KSI)
0	.50	0	4.94	-.17	0	1.01	-1.80	-.29	.14	0	23.0
45	.50	0	1.81	.73	.77	.28	- .51	.95	-.47	.46	17.00
-45	.50	0	1.81	.73	- .77	.28	- .51	.95	-.47	.46	17.0
0	.50	0	4.94	-.17	0	1.01	-1.80	-.29	.14	0	23.0
90	.50	0	-1.31	1.64	0	-.09	.16	.93	-.46	0	7.60
0	.494	.078	4.56	-.10	-.28	.99	-1.76	-.18	.91	.23	24.0
45	.494	.078	2.89	.38	.69	.62	-1.11	.67	-.33	.57	24.0
-45	.494	.078	.62	1.04	-.69	.07	- .125	.98	-.49	.30	12.6
0	.494	.078	4.56	-.10	-.28	.99	-1.76	-.18	.09	.23	24.0
90	.494	.078	-1.05	1.52	.28	-.08	.14	.94	-.47	.08	8.24
0	.476	.155	3.57	.06	-.46	.90	-1.61	.13	-.06	.44	27.9
45	.476	.155	3.45	.10	.49	.88	-1.56	.21	-.10	.48	28.0
-45	.476	.155	-.28	1.18	-.49	-.03	.05	.96	-.48	.18	10.9
0	.476	.155	3.57	.06	-.46	.90	-1.61	.13	-.07	.44	27.9
90	.476	.155	-.41	1.21	.46	-.04	.07	.95	-.48	.17	10.5

$E_x = 4.04\text{X}10^6$ $E_y = 2.80\text{X}10^6$ $G_{xy} = 1.21\text{X}10^6$ $\nu_{xy} = .261$

$X_T = 110.0$ KSI $Y_T = 13.4$ KSI $s = 29.0$ KSI

$X_c = 62.0$ KSI $Y_c = 26.0$ KSI

Failure Load (PSI)(Whiteside) = $31.5\text{X}10^3$

* Distance and Stresses in inches and KSI, respectively, moduli in PSI

TABLE V* GRAPHITE

PLY°	X	Y	σ_ℓ	σ_t	$\tau_{\ell t}$	σ_ℓ/X_T	$\sigma_\ell/-X_c$	σ_T/Y_t	$\sigma_t/-Y_c$	$\tau_{\ell t}/s$	FL(KSI)
0	.50	0	6.28	-.13	0	1.15	-1.35	-.68	.178	0	25.7
45	.50	0	1.91	..24	.33	.22	-.25	.76	-.19	.52	15.9
-45	.50	0	1.91	.24	-.33	.22	-.25	.76	-.19	.52	15.9
0	.50	0	6.28	-.13	0	1.15	-1.35	-.68	.17	0	25.7
90	.50	0	-2.46	.61	0	-.14	.16	.96	-.24	0	7.88
0	.494	.078	5.70	-.09	-.14	1.07	-1.25	-.49	.12	.35	26.3
45	.494	.078	3.66	.08	.29	.58	.68	.36	-.09	.64	22.2
-45	.494	.078	.08	.38	-.29	.01	-.01	.91	-.23	.34	11.8
0	.494	.078	5.70	-.09	-.14	1.07	-1.25	-.49	.12	.35	26.3
90	.494	.078	-1.96	.56	.14	-.12	.14	.96	-.24	.12	8.57
0	.476	.155	4.26	0	-.21	.83	-.97	.04	0	.58	27.2
45	.476	.155	4.56	-.02	.19	.91	-1.06	-.14	.03	.53	27.9
-45	.476	.155	-1.09	.46	-.19	-.08	.09	.95	-.24	.20	10.4
0	.476	.155	4.26	0	-.21	.83	-.97	.04	0	.58	27.2
90	.476	.155	-.79	.43	.21	-.06	.07	.94	-.24	.23	11.0

$E_x = 11.03X10^6$ $E_y = 5.51X10^6$ $G_{xy} = 2.78X10^6$ $\nu_{xy} = .408$

$X_T = 140.0$ KSI $Y_T = 4.9$ KSI $s = 120.0$ KSI

$X_c = 120.0$ KSI $Y_c = 19.0$ KSI

Failure Load (PSI)(Whiteside) = $23.8X10^3$

* Distance and Stresses in inches and KSI, respectively, moduli in PSI

TABLE VI* BORON

PLY°	X	Y	σ_ℓ	σ_t	$\tau_{\ell t}$	σ_ℓ/X_T	$\sigma_\ell/-X_c$	σ_t/Y_T	$\sigma_t/-Y_c$	$\tau_{\ell t}/s$	FL(KSI)
0	.50	0	6.50	-.12	0	1.15	-.82	-.54	.17	0	31.5
45	.50	0	1.86	.21	.22	.30	-.22	.88	-.27	.09	28.8
-45	.50	0	1.86	.21	-.22	.30	-.22	-.54	-.27	.09	28.8
0	.50	0	6.50	-.72	0	1.15	-.82	1.02	.17	0	31.5
90	.50	0	-2.77	.55	0	-.20	.14	-.40	-.31	0	13.0
0	.494	.078	5.88	-.08	-.09	1.12	-.80	.39	.12	.04	33.9
45	.494	.078	3.74	.07	.20	.80	-.57	1.00	-.12	.10	38.0
-45	.494	.078	-.09	.35	-.20	-.01	-.01	-.40	.30	.05	26.1
0	.494	.078	5.88	-.08	-.09	1.12	-.80	1.02	.12	.04	33.9
90	.494	.078	-2.23	.50	.09	-.18	.13	.02	.31	.02	14.2
0	.476	.155	4.36	0	-.14	.99	-.70	-.13	.01	.08	40.4
45	.476	.155	4.71	-.02	.13	1.04	-.74	1.02	.04	.07	39.4
-45	.476	.155	-1.31	.41	-.13	-.13	.09	.02	-.31	.03	17.2
0	.476	.155	4.36	0	-.14	.99	-.70	1.01	-.01	.08	46.4
90	.476	.155	-.96	.39	.14	-.10	.07	.56	.31	.04	18.3

$E_x = 16.41X10^6$ $E_y = 8.06X10^6$ $G_{xy} = 3.96X10^6$ $\nu_{xy} = .444$

$X_T =$ 178.0 KSI $Y_T = 7.0$ KSI

$X_c =$ 250.0 KSI $Y_c = 23.0$ KSI

s = 73.0 KSI

Failure Load (PSI)(Whiteside) = $42.2X10^3$

* Distance and Stresses in inches and KSI, respectively, moduli in PSI

corresponding FL is 25.7 ksi. The 25.7 ksi result is consistent with Whiteside's experimental results of 23.8 ksi. The fact that graphite stress strain response is linear may account for the excellent correlation of analytic and experimental results. Experimental and analytical FL values for boron and glass vary by about 35%. This difference could be due to the nonlinearity of material response. It is probably necessary to consider a three-dimensional stress analysis and also to revise the assumption of linear behavior for a more accurate determination of failure loads for these composites. A statistical approach including volume effects could also be considered as an alternative method for evaluation of FL. Incorporation of statistical variability of the strength constants would be a cumbersome procedure, and in many cases the required experimental data is lacking. Therefore it is expedient to use confidence limits and deterministic computation at the present time.

CONCLUSIONS

The Monte Carlo technique was found to be an excellent analytical tool for assessing the controlling influence of materials variability of SCF. Fortunately, for relatively large variations in moduli the mean values of stress concentration factor were found to vary by less than 2%. Predominating influences were variability of longitudinal and shear moduli.

While mean values were not very sensitive to variability of input parameters, the probability distributions were markedly affected. Dispersion and shape parameters of SCF depend strongly on increasing variability in moduli. Obviously this has important implications in designing to prescribed reliability levels.

The failure criterion presented and the linear elastic laminate analysis was found to predict graphite composite failure response reasonably well. Estimated failure loads for glass and boron were not as consistent with reported experimental results. Currently a nonlinear, incremental ply-by-ply failure analysis is being conducted to further explore improved failure theories.

REFERENCES

1. Composite Materials, Volume 7, Structural Design & Analysis, Part I; Volume 8, Structural Design & Analysis, Part II, Edited by C. C. Chamis, Academic Press, 1975.

2. J. B. Whiteside, R. E. Rowlands and I. M. Daniels, "The Behavior of Advanced Filamentary Composite Plates with Cutouts", AFFDL-TR-73-48, June 1973.

3. Composite Materials: Testing & Design, ASTM STP 460, February 1969.

4. Composite Reliability, ASTM STP 580, April 1974.

5. E. M. Lenoe, Testing and Design of Advanced Composite Materials, Journal of the Engineering Mechanics Division, Proceedings of the American Society of Civil Engineers, December 1970, pp. 809-823.

6. S. G. Lekhnitskii, Theory of Elasticity of an Anisotropic Body, Holden Day, San Francisco, 1965.

7. S. G. Lekhnitskii, Anisotropic Plates, Gordon & Breach, Science Publishers, New York, London and Paris, 1968.

8. O. L. Bowie, C. Freese; Central Crack in Plane Orthotropic Rectangular Sheet. International Journal of Fracture Mechanics, Vol. 8, March 1972.

9. G. N. Savin, Stress Concentration Around Holes, Pergamon Press, New York, 1961.

SESSION VIa: FAILURE MODES

Chairman: J. P. WASZCZAK
Senior Structures Engineer
Convair Division, General Dynamics

FAILURE MECHANICS OF FIBER COMPOSITE NOTCHED CHARPY SPECIMENS
C. C. Chamis, NASA-Lewis Research Center. 193

FATIGUE DAMAGE IN NOTCHED COMPOSITE LAMINATES
R. B. Pipes, University of Delaware, and S. V. Kulkarni and
P. V. McLaughlin, Materials Science Corporation 212

FRACTURE BEHAVIOR OF CROSS-PLY COMPOSITE MATERIALS
J. M. Slepetz, Army Materials and Mechanics Research Center . . 223

FAILURE MECHANICS OF FIBER COMPOSITE

NOTCHED CHARPY SPECIMENS

C. C. Chamis
Lewis Research Center
Cleveland, Ohio

ABSTRACT

A finite element stress analysis was performed to determine the stress variation in the vicinity of the notch and far field of fiber composites Charpy specimens (ASTM Standard). NASTRAN was used for the finite element analysis assuming linear behavior and equivalent static load. The unidirectional composites investigated ranged from T75/E to S-Glass/E with the fiber direction parallel to the long dimension of the specimen. The results indicate a biaxial stress state exists in (1) the notch vicinity which is dominated by transverse tensile and interlaminar shear and (2) near the load application point which is dominated by transverse compression and interlaminar shear The results also lead to the postulation of hypotheses for the predominant failure modes, the fracture initiation, and the fracture process. Finally, the results indicate that the notched Charpy test specimen is not suitable for assessing the impact resistance of nonmetallic fiber composites directly.

INTRODUCTION

The notched Charpy test method has been used extensively to assess the impact resistance and the notch sensitivity of unidirectional composites under impact load. The use of the notched Charpy test method for assessing composite impact resistance has three attractive features: (1) simplicity, (2) established test procedures (ASTM Standard E23-73), and (3) commonality with a successful method for assessing conventional metal notch sensitivity. However, the geometry and load application of the notched Charpy composite test specimen are such that the specimen is in a biaxial stress state and is loaded primarily in short beam shear (interlaminar shear stress). This type of load and the relatively low shear strength of unidirectional composites results in a high probability of interlaminar shear stress failures. This type of failure does not fracture fibers which provide the maximum impact resistance and, therefore, the test may not be suitable for assessing impacting resistance in nonmetallic fiber composites.

Although the notched Charpy test specimen has been used for years in testing metals and recently in testing composites, no analysis has been performed to determine the detailed stress state variation in the notch vicinity. In general, the physical problem of the notched Charpy test specimen is dynamic and nonlinear; solution of this problem is difficult. However, a good first order approximation may be obtained by determining the stress variation in the notch vicinity by assuming linear behavior and an equivalent static load. The detailed stress variation near the notch obtained from such a solution should help provide insight and possible identification of predominant fracture modes, fracture initiation, and fracture processes. Therefore, it is the objective of this investigation to carry out a detailed stress analysis using NASTRAN to determine the stress variation in the notch vicinity of the notched Charpy composite test specimen assuming linear behavior and equivalent static load.

The type of analysis performed, the results obtained, and the interpretation of these results relative to fracture modes, fracture initiation, and fracture process of the notched Charpy composite test specimen and its utility in assessing composite impact resistance are described herein.

ANALYSIS

The specimen geometry, the finite element representation, the finite element analysis method, and the composite systems analyzed are described in this section.

Specimen Geometry

The geometry of the Charpy test specimen (ASTM STD E23-7) is depicted in figure 1. As can be seen in this figure, the overall length of the specimen is 2.164 inches and the length between supports is 1.574 inches. The specimen width is 0.394 inch. The specimen unnotched depth is 0.394 inch and the depth at the notch is 0.315 inch. The notch is 0.079 inch deep and has a 45° opening symmetric about the specimen midlength.

Finite Element Representation

The specimen is assumed to be symmetric with respect to both geometry and loading about its midlength for analysis purposes. The material properties are uniform, orthotropic, and obey a linear stress strain law throughout the analysis. In addition, the specimen is assumed to be in a state of plane stress. That is, the stresses are permitted to vary along the specimen length and through the thickness but not through the width. This reduces the stresses to be calculated to three, two normal and one shear.

With these assumptions, plane stress finite elements can be used to model the Charpy test specimen and only one-half of its length need be used in the finite element representation. The finite element representation of the specimen and the boundary conditions prescribed are shown in figure 2. As can be seen in this figure, all of the elements are quadrilateral except for one triangular element at the notch. Note that the displacement boundary conditions do not permit displacements in the x direction at the line of symmetry (x = 0) and y displacements at the support points. The specimen is assumed to be subjected to static concentrated load at its midlength.

The statistics of the finite element representation are as follows:

Number of nodes or grid points	197
Number of displacement degrees of freedom (DOF) (2 degrees of freedom per node)	394
Number of elements	168
DOF eliminated using the boundary conditions (7 from u = 0 and 1 from v = 0)	8
Number of free DOF (394-8)	386

Finite Element Analysis Method

The NASTRAN general purpose structural analysis finite element computer program was used for the finite element analysis method. The specific elements used are identified as CQDMEM and CTRMEM in the NASTRAN library-resident elements. The triangular element is a constant strain plane element and the quadrilateral combines four triangular elements, the stiffness of which is generated using the four constant strain triangular elements internally in NASTRAN together with the appropriate anisotropic material properties. NASTRAN obtains the solution using a displacement formulation via rigid format 1. Only one-half of the concentrated load is needed with the half-length of the specimen modeled in the finite element representation.

Composite Systems Analyzed

Charpy test specimens made from six different composite systems were analyzed. Namely: Thornel 75/epoxy (T75/E), Modmor I/epoxy (MOD I/E), boron/epoxy (B/E), Modmor II/epoxy (MOD II/E), Kevlar 49/E (KEV 49/E), and S-glass/epoxy (S-G/E). The specimens were all unidirectional composites with the fibers parallel to the length (x-axis, fig. 1) of the specimen.

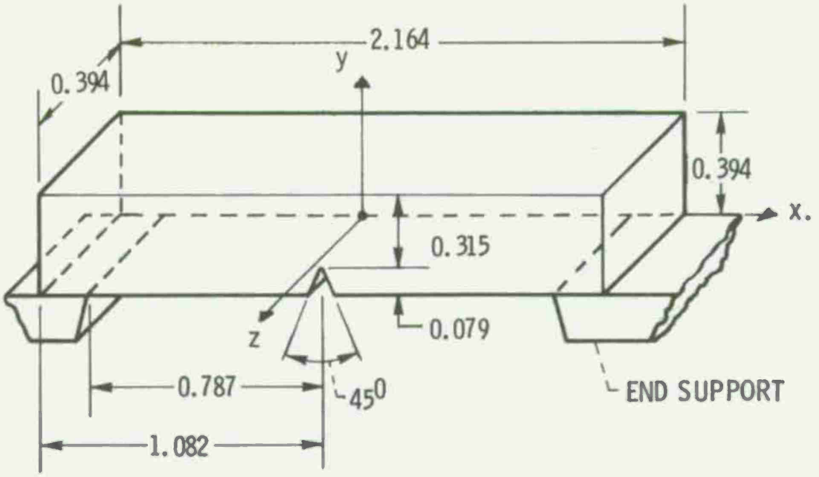
2.164
y
0.394
0.394
x.
0.315
0.079
z
0.787
45⁰
1.082
END SUPPORT

Figure 1. Geometry of ASTM Charpy test specimen (all dimensions in inches)

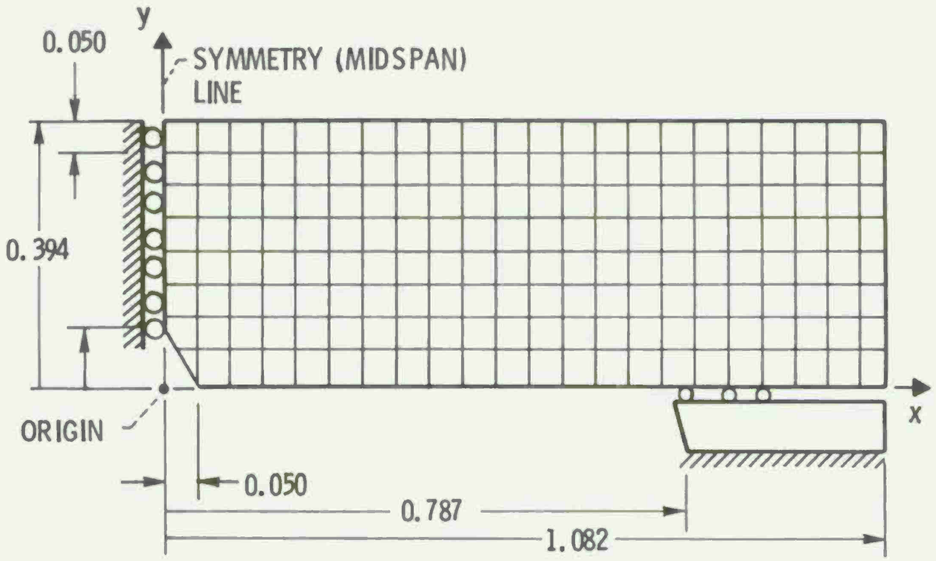
y
0.050
SYMMETRY (MIDSPAN) LINE
0.394
ORIGIN
0.050
0.787
1.082
x

FINITE ELEMENT STATISTICS:

NODES	197
D.O.F./NODE	2
ELEMENTS	168
B.C's	u = 0 AT SYM. LINE; v = 0 AT x = 0.787 AND y = 0
MATERIAL	ORTHOTROPIC, FIBERS PARALLEL TO X-AXIS
LOAD POINT	x = 0; y = 0.394

Figure 2. ASTM Charpy test specimen - finite element representation (all dimensions in inches)

The composite systems listed were selected because characterization data and Charpy test data for these composites were reported in reference 1. Tensile and shear fracture stress ranges of these composites reported in reference 1 are summarized in table I. Typical values for compression fracture stresses and Poisson's ratios are shown in table II. The plane stress-strain relationship (stiffness) coefficients required for input to NASTRAN are summarized in table III. The values in table III were obtained from the moduli data reported in reference 1 and the Poisson's ratio values shown in table II for these composite systems.

The relationships between the NASTRAN stiffness coefficients (G's), and the usual engineering constants are:

$$G_{11} = E_{\ell 11}/(1 - \nu_{\ell 12}\nu_{\ell 21}) \tag{1}$$

$$G_{12} = \nu_{\ell 21}G_{11} = \nu_{\ell 12}G_{22} = G_{21} \tag{2}$$

$$G_{22} = E_{\ell 22}/(1 - \nu_{\ell 12}\nu_{\ell 21}) \tag{3}$$

$$G_{33} = G_{\ell 12} \tag{4}$$

The notation in equations (1) to (4) is as follows: $E_{\ell 11}$ denotes the longitudinal modulus, $E_{\ell 22}$ the transvers modulus, $G_{\ell 12}$ the shear modulus, $\nu_{\ell 12}$ the major Poisson's, and $\nu_{\ell 21}$ the minor Poisson's ratios. For an elastic material, the two Poisson's ratios are related by the well known relation.

$$\nu_{\ell 21} = \nu_{\ell 12}E_{\ell 22}/E_{\ell 11} \tag{5}$$

RESULTS AND DISCUSSION

The load conditions used for the analysis and the various stress results obtained are described in this section. The stress results include: (1) stress variation in the notch vicinity and comparisons with those predicted by simple beam theory; (2) typical interlaminar shear stress contours; and (3) typical bearing stress variation near the support.

Load Conditions

Two sets of loads were used in determining stress variations near the notch. The

TABLE I. - MEASURED FRACTURE STRESS RANGES (KSI) (REF. 1)

Composite system	Longitudinal tensile		Transverse tensile		Interlaminar shear			
					Short beam		Torsional rod	
	High	Low	High	Low	High	Low	High	Low
Thornel 75/epoxy (T75/E)	154	142	4.5	3.8	7.8	7.8	7.3	7.0
Modmore I/epoxy (MOD I/E)	146	129	5.1	5.0	8.4	8.2	7.2	6.8
Boron/epoxy (B/E)	222	205	9.3	7.2	15.3	14.7	13.2	12.8
Modmore II/epoxy (MOD II/E)	161	146	6.0	5.8	10.3	9.4	10.8	10.0
Kevlar 49/epoxy (KEV 49/E)	170	154	3.7	2.4	6.9	6.8	5.0	4.0
S-glass/Epoxy (S-G/E)	222	216	14.0	12.0	14.0	12.6	17.1	16.7

TABLE II. - TYPICAL COMPRESSION FRACTURE STRESSES AND POISSON'S RATIO

Composite system	Compression fracture stress		Poisson's ratio
	Longitudinal (ksi)	Transverse (ksi)	
T75/E	130	20	0.36
MOD I/E	128	28	.34
B/E	232	18	.41
MOD II/E	180	30	.35
KEV 49/E	42	9	.46
S-G/E	110	25	.36

TABLE III. - NASTRAN PLANE STRESS-STRAIN RELATIONSHIPS

Composite system	Stress-strain coefficient (10^6 psi)				Orthotropy ratio, G_{11}/G_{22}
	G_{11}	$G_{11} = G_{12}$	G_{22}	G_{33}	
T75/E	38.0	0.41	1.16	0.63	33
MOD I/E	30.6	.40	1.17	.70	26
B/E	30.6	2.10	5.14	1.95	6
MOD II/E	19.4	.40	1.13	.59	17
KEV 49/E	11.5	.39	.85	.39	14
S-G/E	8.79	1.17	3.26	1.27	3

$$\begin{Bmatrix} \sigma_x \\ \sigma_y \\ \sigma_{xy} \end{Bmatrix} = \begin{bmatrix} G_{11} & G_{12} & 0 \\ G_{21} & G_{22} & 0 \\ 0 & 0 & G_{33} \end{bmatrix} \begin{Bmatrix} \epsilon_x \\ \epsilon_y \\ \epsilon_{xy} \end{Bmatrix} \text{(For orthotropic material)}$$

first set of loads was selected to produce fracture in the specimen under an equivalent static load. The stress state generated from this load can then be compared to the fracture stress of the composite. The procedure for selecting this load is as follows:

1. Assume the longitudinal tensile stress at the notch root produces fracture.
2. Use the simple beam formula

$$P = (bh^2/6\ell)S_{\ell 11T} \tag{6}$$

where P is the load used for the NASTRAN stress analysis; b is the specimen width and is equal to 0.394 inch; h is the specimen thickness at the root and is equal to 0.315 inch; ℓ is the specimen length to the edge of the support and is equal to 0.787 inch; and $S_{\ell 11T}$ is the longitudinal tensile-fracture stress of the composite.

Substituting these numerical values in equation (6) yields

$$P = 0.00828\ S_{\ell 11T} \tag{7}$$

3. Substitute for $S_{\ell 11T}$ in equation (7) the longitudinal fracture stress from table I. The results for the composite systems investigated (rounded to the nearest "5") are: (stress variations for other loads are obtained by direct ratio).

Composite system	Equivalent static fracture load, lb	Value selected from table I
T75/E	1275	High value
MOD I/E	1070	Low value
B/E	1770	Average
MOD II/E	1270	Average
KEV 49/E	1340	Average
S-G/E	1810	Average

The second load set was assumed to be constant (1320 lb) for all composite specimens. This constant load was selected in order to compare the stress state variation near the notch root and thereby assess the influence of the different composite systems.

Stress Variation in the Notch Vicinity

The stress variation produced by the equivalent static fracture load for T75/E is plotted in figure 3 (a - longitudinal; b - transverse; c - shear). In this and subsequent figures the specimen depth is plotted as ordinate and the stress magnitude as abscissa. Each stress is plotted at three different span sections near the notch vicinity denoted by x = 0.025, 0.075, and 0.125 inch, respectively. The notch root is at x = 0 (fig. 2).

Both the composite transverse fracture stresses tensile (low value (table I) and compression (table II)) are shown in figure 3(b). The interlaminar shear fracture stress is shown in figure 3(c). The corresponding longitudinal fracture stresses are not shown because they are beyond the scale of figure 3(a).

The important points to be observed from the calculated results in figure 3 on a comparative basis and in conjunction with the data from tables I and II are:

1. The longitudinal stress (fig. 3(a)) near the notch root is tensile and is about 50 percent of the corresponding fracture stress (72 ksi compared to 142 ksi, low value table I). This relatively low longitudinal tensile stress will not produce fiber fractures.

2. Longitudinal tensile stress (fig. 3(a)) of considerable magnitude is present in the notch vicinity below the notch root line.

3. The transverse stress (fig. 3(b)) is tensile in the notch root vicinity and exceeds the composite corresponding fracture stress.

4. Relatively high longitudinal compressive stresses are present near the load application point (fig. 3(a)) (140 ksi versus approximately 130 ksi for the corresponding fracture stresses).

5. The transverse stress (fig. 3(b)) is compressive near the load application point and its magnitude exceeds the corresponding composite fracture stress.

6. The interlaminar shear stress has magnitudes which exceed the corresponding fracture stress below and above the notch line and especially near the load application point (fig. 3(c)).

The high compressive stresses near the load application point, the high transverse tensile stress near the notch root, the interlaminar shear stress sign reversal, and the large magnitude of the interlaminar shear stress are not intuitively obvious results from simple beam theory.

The important conclusion from the above observations is that the equivalent static load is sufficient to cause fracture near the notch root and near the load application point. Near the notch root the critical stresses are transverse tensile and interlaminar shear. Near the load application point the critical stresses are transverse compression and interlaminar shear. Both of these combinations are likely to produce local delaminations prior to fiber fractures.

The stress variations near the notch root and near the load application points corresponding to figure 3 are shown in figure 4 for MOD I/E, in figure 5 for KEV 49/E, and in figure 6 for S-G/E. The corresponding fracture stresses are shown in a similar manner as in figure 3. Though stress variations are not shown here, those for B/E are similar to MOD I/E and those for type A/E are similar to MOD II/E.

As can be observed from the plots in figures 4 to 6 the stress variations are similar to corresponding ones in figure 3. It is important to observe, however, the large stresses (longitudinal compression, transverse compression, and intralaminar shear) in the KEV 49/E specimen (fig. 5) relative to the corresponding fracture stresses. Based on the conclusions following the discussion of the results in figure 3, the KEV 49/E specimen would probably start delaminating at very low values of the equivalent static load. Observe, also, the relatively high stresses in the S-G/E specimen (fig. 6) for transverse compression and interlaminar shear compared to corresponding fracture stresses. This specimen, too, will probably start delaminating at low values of the equivalent static load.

Interlaminar Shear Stress Contours

It was noted in the previous discussion that the interlaminar shear stress is important in initiating fracture by delamination in Charpy composite specimens. It is of interest, therefore, to see the variation of this stress through the thickness and along the length of the specimen. Such a variation is best illustrated graphically by stress contour plots.

The interlaminar shear stress contour plot for KEV 49/E is shown in figure 7. Peak values are noted with an asterisk in this figure. As can be observed in figure 7 the interlaminar shear stresses are relatively high compared to the corresponding fracture stress of 6.8 ksi from table I. A possible conclusion from this observation is that once delamination is initiated it is probably driven subsequently by the high interlaminar shear stress present through the whole length of the specimen.

Interlaminar shear stress contour plots for the other specimens are similar to that of the KEV 49/E and are not shown here. The magnitudes of the stress contours depend on the load. However, the observations and conclusions are the same as those already made for the KEV 49/E specimen.

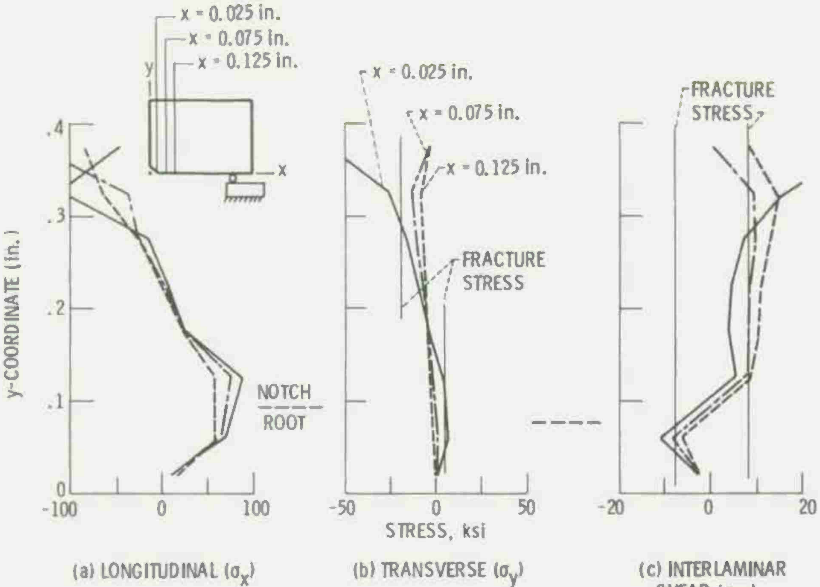

(a) LONGITUDINAL (σ_x)

(b) TRANSVERSE (σ_y)

(c) INTERLAMINAR SHEAR (σ_{xy})

Figure 3. T75/E ASTM Charpy test specimen: variation of stresses at sections in the vicinity of notch (static load = 1275 lb)

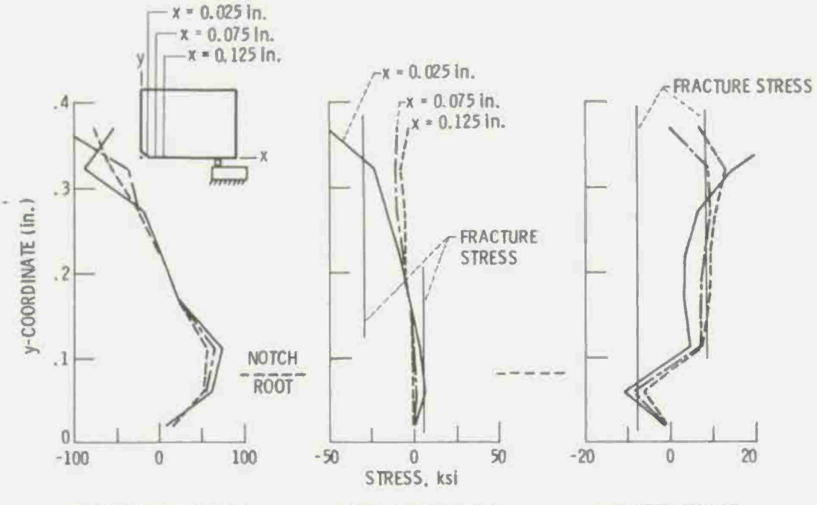

(a) LONGITUDINAL (σ_x)

(b) TRANSVERSE (σ_y)

(c) INTERLAMINAR SHEAR (σ_{xy})

Figure 4. Mod I/E ASTM Charpy test specimen: variation of stresses at sections in the vicinity of notch (static load = 2152 lb)

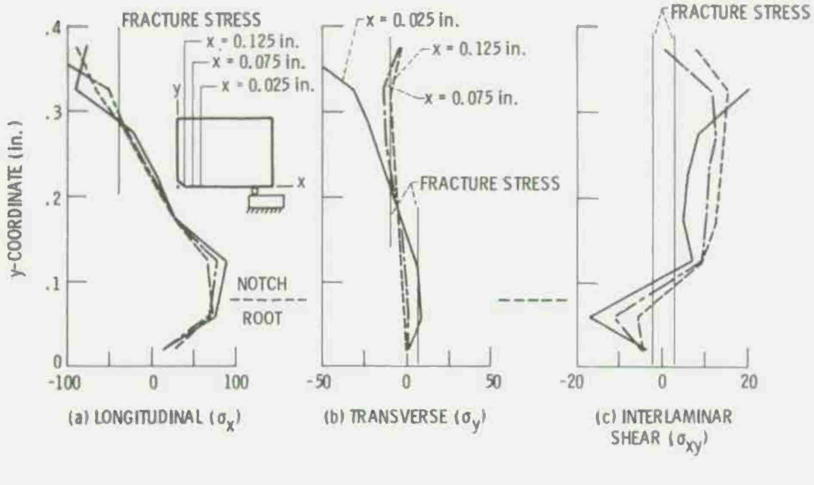

(a) LONGITUDINAL (σ_x)

(b) TRANSVERSE (σ_y)

(c) INTERLAMINAR SHEAR (σ_{xy})

Figure 5. KEV 49/E ASTM Charpy test specimen: variation of stresses at sections in the vicinity of notch (static load = 1341 lb)

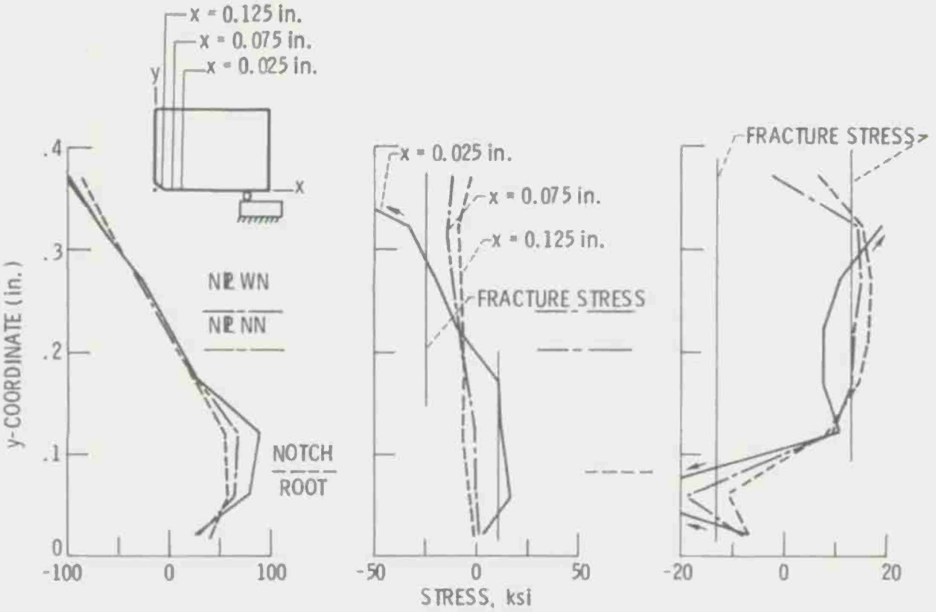

(a) LONGITUDINAL (σ_x) (b) TRANSVERSE (σ_x) (c) INTERLAMINAR SHEAR (σ_{xy})

Figure 6. S-GL/E ASTM Charpy test specimen: variation of stresses at sections in the vicinity of notch (static load = 2640 lb)

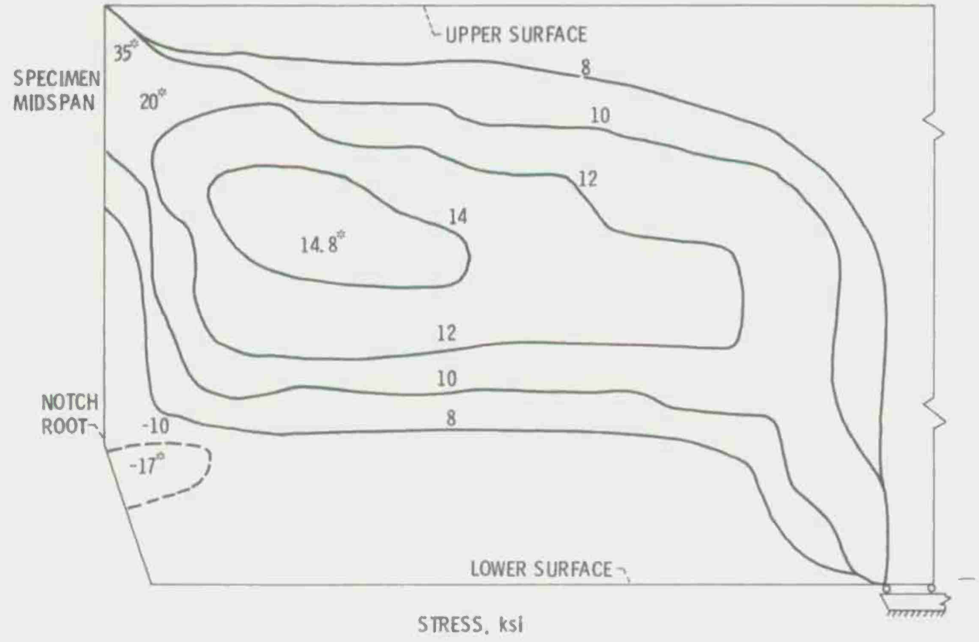
UPPER SURFACE
SPECIMEN MIDSPAN
35*
20*
8
10
12
14
14.8*
12
10
8
NOTCH ROOT
-10
-17*
LOWER SURFACE
STRESS, ksi

Figure 7. KEV 49/E ASTM Charpy test specimen: interlaminar shear stress contours through the specimen thickness (static load = 1341 lb) (* denotes peak stress within contour)

Comparisons with Simple Beam Theory

Stress variations in the notch vicinity predicted by the finite elemen stress analysis for the composite specimens investigated and for the same load are compared with those predicted using simple beam theory. Stress variation based on both full and reduced sections are calculated using the simple beam theory.

Comparison results for the longitudinal stress are presented in figure 8 for two vertical sections: $x = 0.025$ inch, figure 8(a) and $x = 0.075$ inch, figure 8(b). In this figure, the stress variations predicted by the simple beam theory equation

$$\sigma_x = 12\ P(0.787 - x)3/bh^2 \tag{8}$$

are shown by straight lines for both the full and reduced sections. The important points to be observed from the results in figure 8 are:

1. The longitudinal stress variation predicted by the finite element is approximately the same for all the composite systems.
2. The simple beam theory predicts stress variations, relative to those of the finite element, which are:
   a. Unconservative above the notch root when the full section is used.
   b. Conservative below the neutral plane and near the top when the reduced section is used.

The conclusion from the above observations is that simple beam theory predicts longitudinal stress variations in the notch vicinity of Charpy specimens which are in considerable error (as much as 100 percent) when compared to finite element results, and this theory is therefore inadequate to predict these stresses.

Comparison results for the interlaminar shear stress are presented in figure 9 for two vertical sections: $x = 0.025$ inch in figure 9(a), and $x = 0.125$ inch in figure 9(b). Note in these figures the stress variations predicted by the simple beam theory equation

$$\tau_{xy} = \frac{1.5\ P}{bh}\left[1 - \left(\frac{2y}{h}\right)^2\right] \tag{9}$$

using the reduced section only, are shown as parabolas. The important points to be observed from the results in figure 9 are:

1. The interlaminar shear variation nearest the notch ($x = 0.025$ in. or less than the notch depth, fig. 2), depends on the composite system, and appears to be inversely

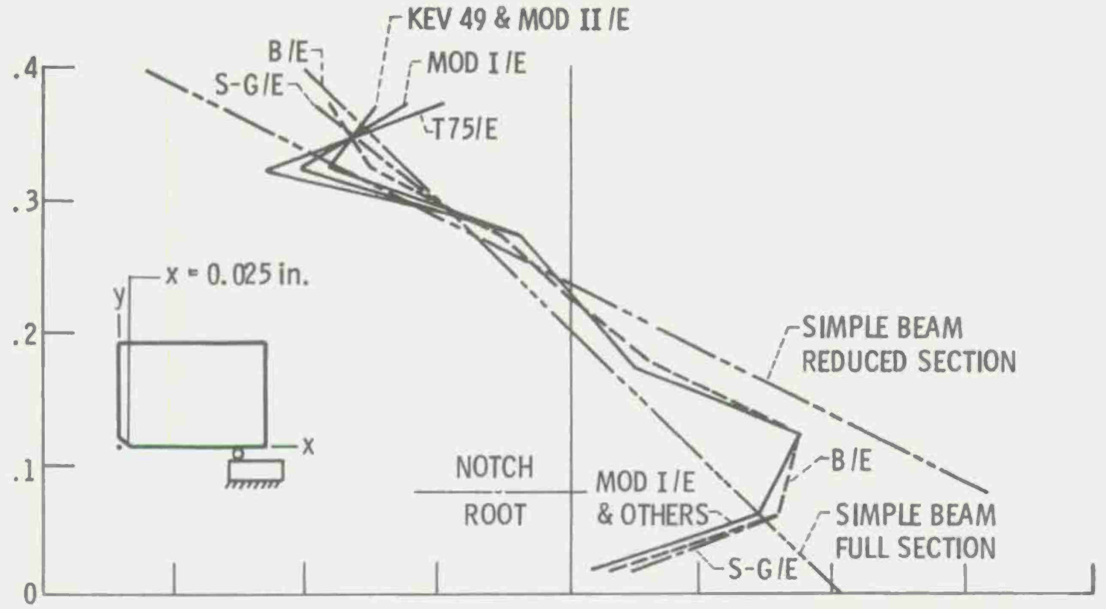

(a) LONGITUDINAL STRESS AT SECTION x = 0.025 in.

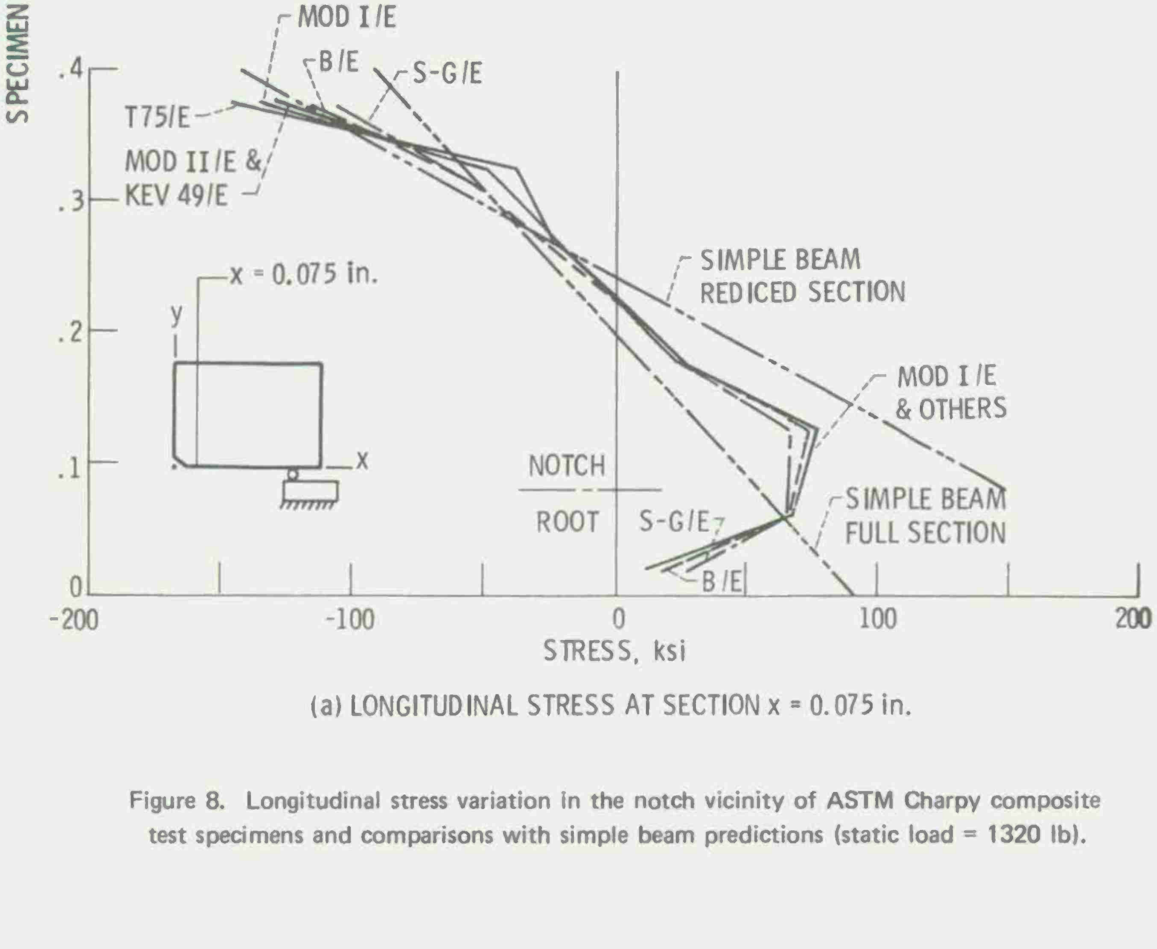

(a) LONGITUDINAL STRESS AT SECTION x = 0.075 in.

Figure 8. Longitudinal stress variation in the notch vicinity of ASTM Charpy composite test specimens and comparisons with simple beam predictions (static load = 1320 lb).

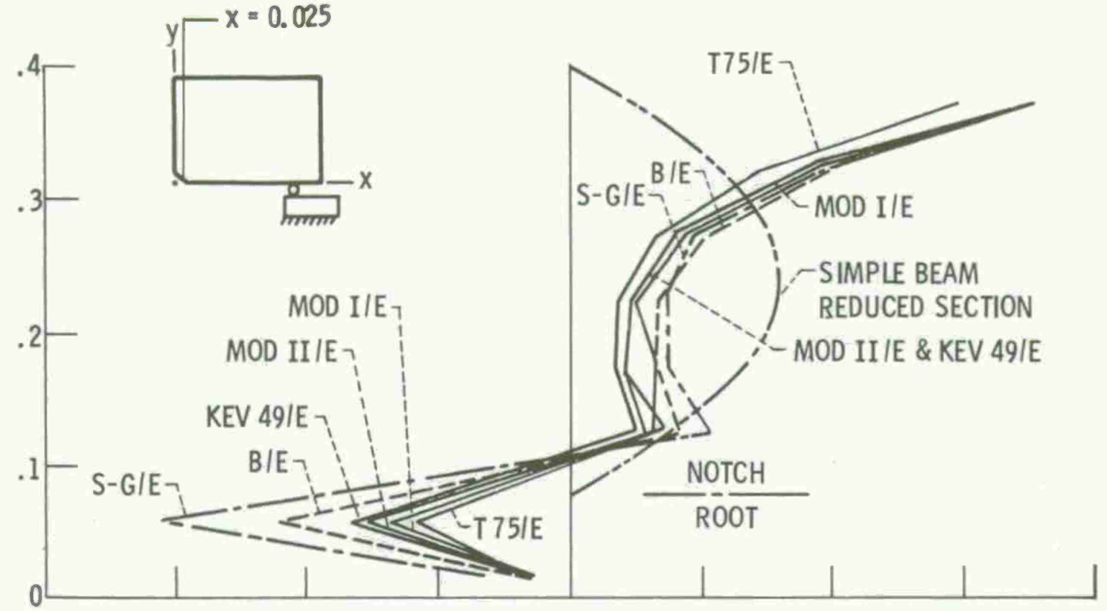

(b) INTERLAMINAR SHEAR STRESS AT SECTION x = 0.025 in.

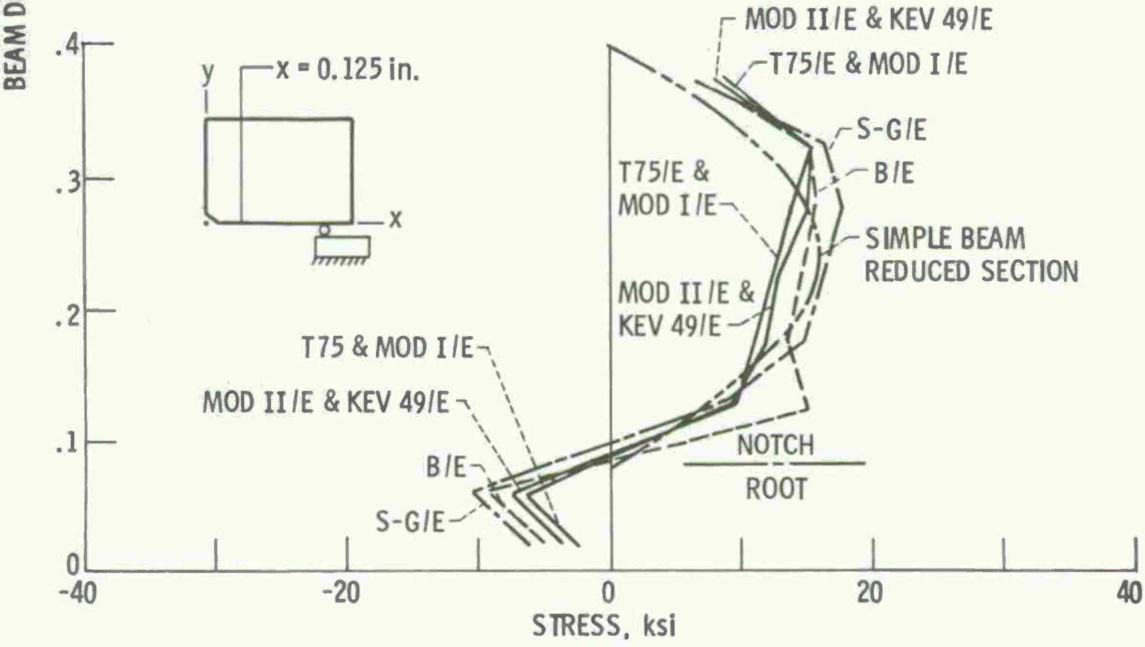

(b) INTERLAMINAR SHEAR STRESS AT SECTION x = 0.125 in.

Figure 9. Interlaminar shear stress variation in the notch vicinity of ASTM Charpy composite test specimens and comparisons with simple beam predictions (static load = 1320 lb).

proportional to the ratio G_{11}/G_{22} table III, also $E_{\ell 11}/E_{\ell 22}$ as may be deduced from equations (1) and (3).

2. The simple beam theory does not predict the interlaminar shear stress variation near the notch at sections closer than the notch depth.

3. The interlaminar shear stress variation appears to be insensitive to composite system at sections which are beyond 1.5 times the notch depth (fig. 9(b)).

4. The simple beam theory predicts interlaminar shear stress variations above the notch root which are comparable to those predicted by the finite element analysis at sections which are beyond 1.5 times the notch depth (fig. 9(b)).

The conclusion from the above observations is that simple beam theory with reduced section can be used to predict the interlaminar shear stress variation at sections which are 1.5 times the notch depth beyond the notch.

Comparison results for the transverse, or through-the-thickness normal stress (y-direction, fig. 2) variations for the various composites are presented in figure 10 for one vertical section (x = 0.025 in.). As can be seen in this figure, this normal stress near the notch root depends on the composite system. The magnitude of this normal stress appears to be inversely proportional to the orthotropy ($E_{\ell 11}/E_{\ell 22}$) ratio as was the case for the interlaminar shear stress. No comparisons with simple beam theory are shown because the simple beam theory does not predict this stress. The following observations are worthy of note from figure 10:

1. The transverse, or through-the-thickess normal stress (y-direction, fig. 2) is insensitive to composite system above the neutral plane (above specimen depth 0.24 in.).

2. The transverse, or through-the-thickness normal stress (y-direction, fig. 2) approaches large compressive magnitudes near the load application point and probably starts inducing local failures at relatively low load values.

Bearing Stresses Near Support

Typical bearing stress variations through the depth near the support are shown in figure 11 for Charpy composite test specimens. The bearing stress variations are shown in figure 11(a) for the three sections noted in the schematic in figure 11(b).

It can be seen in figure 11(a) that the bearing stress is very high near the support and decays rapidly through the depth and away from the support. The bearing stress near the support is of sufficient magnitude to produce local damage in some composites. This is readily established by comparing the transverse compression fracture stress from table II with curve A (fig. 11(a)). The local damage near the end support will most likely be a local indentation which will contribute to the lateral displacement

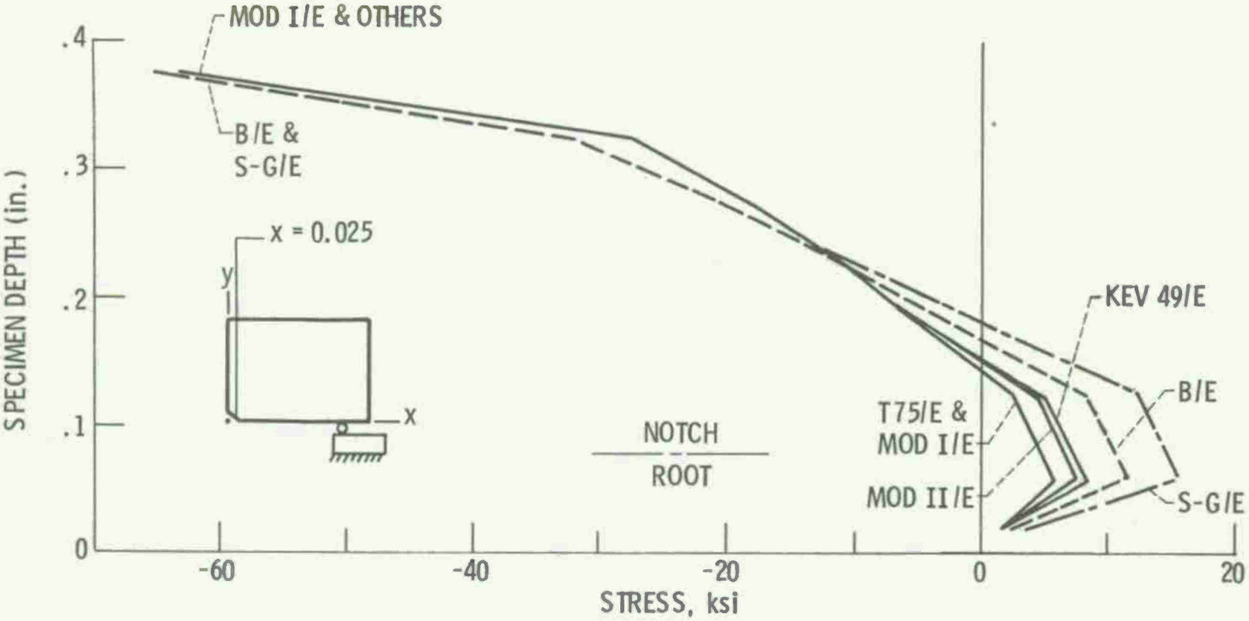

Figure 10. Through-the-thickness normal stress variation in the notch vicinity of ASTM Charpy composite test specimens at section x = 0.025 in. (static load = 1320).

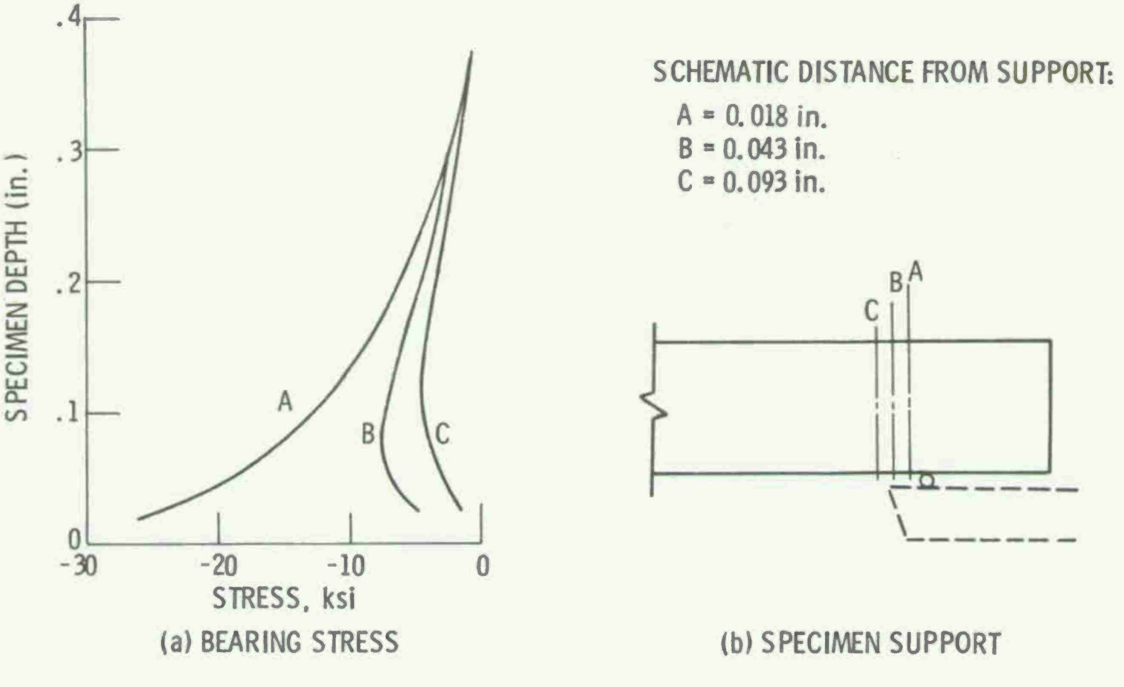

(a) BEARING STRESS

(b) SPECIMEN SUPPORT

Figure 11. Typical bearing stress variation in the vicinity of the support of ASTM Charpy composite test specimens (static load = 1320 lb).

(y-direction, fig. 2) at the beam midlength. It is important to note that simple beam theory does not predict either the local damage near the support or its contribution to the lateral displacement.

The important conclusion from the previous discussion is that the bearing stresses near the support are of sufficient magnitude to produce local damage in Charpy composite test specimens.

FRACTURE MODES

The previous discussion dealing with the stress variations near the notch of Charpy composite test specimens leads to the following hypotheses for fracture modes, fracture initiation, and fracture process in nonmetallic fiber composites.

Fracture Modes

The hypotheses for predominant fracture modes are:

1. Interlaminar shear below the notch root
2. Transverse tension combined with interlaminar shear at the notch root and followed by possible fiber fractures
3. Transverse compression combined with interlaminar shear and longitudinal compression near the load application point
4. Interlaminar shear near the specimen center

Fracture Initiation

The hypothesis for fracture initiation in Charpy composite test specimens is as follows:

1. Near the notch root, fracture initiates when a combination of transverse tensile and interlaminar shear exceed their corresponding fracture stresses (critical values).

2. Near the load application point, fracture initiates when a combination of transverse compression, interlaminar shear, and longitudinal compression exceeds the corresponding fracture stresses.

3. Near the specimen center, fracture initiates when the interlaminar shear stress exceeds the corresponding fracture stress.

It is important to note that fracture may initiate sequentially or simultaneously in the three locations described above. A nonlinear analysis is required to determine the sequence of fracture initiation at these three locations.

Fracture Process

The hypothesis for the fracture process in the Charpy composite test specimen is as follows:

1. The high interlaminar shear stresses cause delamination and thus free surfaces near the notch root and near the load application point.

2. The delaminated surfaces reduce the specimen section to progressively thinner sections. Each delaminated thin section acts as an independent thin beam and continues to carry load in flexure.

3. The process continues, probably simultaneously, from both top and bottom towards the center until the specimen fractures completely either by delamination or fiber fractures or possible combinations of both.

It is noted at this juncture that direct proof of the above three hypotheses would require nonlinear and detailed fractographic analyses both of which are not part of this investigation's objectives.

A logical conclusion from the discussion of the above hypotheses and the results of the detailed stress analysis is that the notched Charpy test method is not suitable to assess the impact resistance of nonmetallic fiber composites directly. Its most serious drawback is that the predominant initial failure modes are combinations of transverse tensile or compression with interlaminar shear. Neither of these modes stresses the composite to its maximum efficienty which is only achieved when fiber fracture occurs.

SUMMARY OF RESULTS AND CONCLUSIONS

The major results of the NASTRAN linear stress analysis of ASTM notched Charpy unidirectional composite test specimens are as follows:

1. The critical stresses near the notch root are transverse tension and interlaminar shear.

2. The critical stresses near the load application point are transverse compression and interlaminar shear.

3. The simple beam theory is not adequate to predict longitudinal and interlaminar shear stresses near the notch. However, this theory may be used to predict the interlaminar shear stress at sections beyond 1.5 times the notch depth.

4. Both the interlaminar shear stress and the transverse tensile stress variations near the notch root depend on the composite system. Their magnitudes appear to be inversely proportional to the orthotropy ratios ($E_{\ell 11}/E_{\ell 22}$) for the same load.

5. The bearing stresses have high magnitudes near the support point and may cause local damage possibly in the form of indentation. These stresses decay rapidly away from the support and appear to be independent of the composite system.

6. The hypotheses formulated for fracture modes, fracture initiation, and fracture process are as follows: The dominant fracture modes are transverse tension, transverse compression, and interlaminar shear. Fracture initiates when combinations of these stresses reach critical values. The interlaminar shear stress causes free surfaces via delaminations which tend to reduce the specimen to thinner flexural type specimens. The process continues until the specimen fractures completely either by delamination, or fiber fracture, or possible combination of both.

7. The notched Charpy test method is not suitable for assessing the impact resistance of nonmetallic fiber composites directly.

REFERENCE

1. Friedrich, L. A. and Preston, J. L., Jr., "Impact Resistance of Fiber Composite Blades Used in Aircraft Turbine Engines," PWA-4727, May 1973; also NASA CR-134502.

FATIGUE DAMAGE IN NOTCHED COMPOSITE LAMINATES[1]

R. Byron Pipes
Associate Professor
Department of Mechanical and Aerospace Engineering
University of Delaware
Newark, DE 19711

S.V. Kulkarni
Senior Engineer

P.V. McLaughlin
Senior Engineer
Materials Sciences Corporation
Blue Bell Office Campus
Merion Towle Bldg.
Blue Bell, PA 19422

ABSTRACT

This paper describes the results of an experimental investigation of the fatigue characteristics of a $[0_2/\pm45]_S$ boron-epoxy laminate containing an unloaded, circular hole. The study focuses upon characterization of the fatigue damage incurred and its influence upon axial tensile residual strength. Two apparent anomolies in the fatigue behavior for this laminate were observed. First, the fatigue damage was observed to propagate tangent to the edge of the notch (parallel to the direction of the load) in contrast to propagation in contemporary metallic materials which is perpendicular to the load direction. Second, the residual strength characteristics for the laminate have revealed a significant increase in residual strength subsequent to a fatigue loading of 500,000 cycles at R=0.1 and S=0.8 and 0.67 (S=maximum stress/static ultimate). Failure Analyses of the fatigue damage are conducted utilizing ultrasonic "C" scan technicues.

INTRODUCTION

The static strength of notched composite laminates containing either circular holes or slit notches has received considerable attention in the recent literature. Waddoups et al. [1] and Whitney [2] showed that the static strength of notched laminates which exhibit collinear (transverse to the direction of the

---

[1] Supported by National Aeronautics and Space Administration, Langley Research Center, under contract no. NAS1 - 13931 to Materials Sciences Corporation.

load, Mode I) crack propagation can be predicted with a two parameter model. The first parameter is an intrinsic laminate strength property while the second accounts for geometric effects. Both models successfully predict the dependence of laminate strength upon hole size.

Another failure model for notched composite laminates has been developed (See Refs. 3, 4 and 5) which treats axial (in in direction of the load, Mode II) as well as, collinear crack propagation and considers the non-linearity (if present) of the in-plane shear stress-strain behavior by approximating the response as elastic-perfectly plastic. Damage of this form was first observed by Durchlab and Freeman [6]. Thus, in addition to the above two parameters, two more parameters (in-plane shear strength and ultimate strain) are needed in order to predict Mode II crack growth.

Based on the static failure model of Reference [5] and the mechanistic wearout concept, a fatigue failure model was constructed in Reference [7] for notched composite laminates. The experimental verification of this model and an analytical/experimental correlation study were the principal aims of the current effort (Ref. [8]) Salient features of the analysis and its correlation with experimental results have been presented in [9]. The present paper examines the experimental aspects of the program. Specifically, the phenomenon of axial damage propagation during fatigue loading and the resulting increase in residual notched strength is investigated.

EXPERIMENTAL PROCEDURE

Test specimens were fabricated from boron-epoxy laminates manufactured by Composite Materials Corporation utilizing 4.0 mil. boron fiber and 3M Company SP296 resin system. Scotchply® tabs were bonded to each end of the laminate and test specimens were cut from the plate with a precision diamond waffering saw. Circular holes were machined in the test specimens employing the diamond core drill apparatus. Specimen dimensions are 12.0 inches in length, 1.5 inches in width, and approximately 0.04 inches in thickness.

For fatigue loading the test specimens were mounted in the Model 1321 Instron Servo-hydraulic test system. The test system allows for control of specimen load, displacement or strain over a load range of 0-±5000 Kg and a frequency range of 0-50 hertz. In addition, the mini computer facilitates computer-controlled testing.

In order to avoid penetrating the test specimens in the regions of the grips, special friction grips were designed and manufactured. Graph paper attached to the specimen allowed axial laminate damage to be monitored during the test. The fatigue test conditions for test program were: sinusoidal loading function, ratio of minimum load to maximum load R=0.1, frequency of 30 hertz, temperature 75°F, and approximately 50% relative humidity. Specimens were instrumented with electrical resistance strain gages after cycling for measurement of residual properties.

TEST RESULTS

Static properties of the $[0_2/\pm45]_S$ boron-epoxy laminate were measured utilizing the grips described earlier, and Instron model TTC static test machine, and electrical resistance strain gages. Each specimen was instrumented with an axial and transverse gage (1/8 inch) midway between the circular notch and grips. In addition, a 1/16 inch gage was mounted adjacent to the circular hole. Results of the static tests are summarized below in Table I. The failed specimens are shown in Fig. 1.

TABLE I

Specimen	Ultimate Stress	Ultimate Strain	Ultimate Strain at Notch
4BCL1	65,850 psi	3750 in/inx10^{-6}	6700 in/inx10^{-6}
4ACL2	63,800 psi	3755 in/inx10^{-6}	6850 in/inx10^{-6}
4CL2	67,282 psi	3575 in/inx10^{-6}	6100 in/inx10^{-6}
AVG.	65,640 psi	3693 in/inx10^{-6}	6550 in/inx10^{-6}

Effective laminate properties determined from three unnotched laminate tests were found to be as follows: Young's Modulus, $17.78\text{x}10^6$ psi and Poisson's Ratio, 0.69. These results were found to be in good agreement with analytical predictions of laminate properties.

The results presented in Table I reveal a strain concentration factor at the edge of the hole equal to 1.77. However, if the analytic solution by Savin [9] for state of strain in the vicinity of a circular hole in an orthotropic plate is examined, the theoretical strain concentration factor is found to be 3.48. The difference between the theoretical and observed strain concentration factors can be attributed to the large strain gradient in the vicinity of the hole. Figure 2 shows the theoretical strain profile for such an orthotropic laminate. Clearly, a 1/16 inch strain gage will yield an average strain in that region and result in an observed strain concentration considerably less than 3.48. The results presented in Figure 2 show that a 1/16 (.0625) inch gage located in the region $.006<Y-D/2<.0685$ would yield a strain concentration factor of 1.77. Hence, the observed average strain concentration from the test results is consistent with theoretical predictions.

Specimens 4BCL1, 4ACL2, and 4CL2 are shown in Figure 3 after static fracture. It should be noted that the fracture for

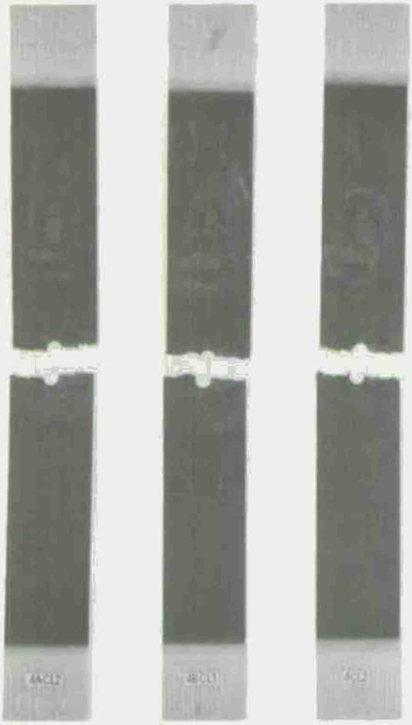

Fig. 1 Static Failure $[0_2/\pm45]$ B/E_p Laminates

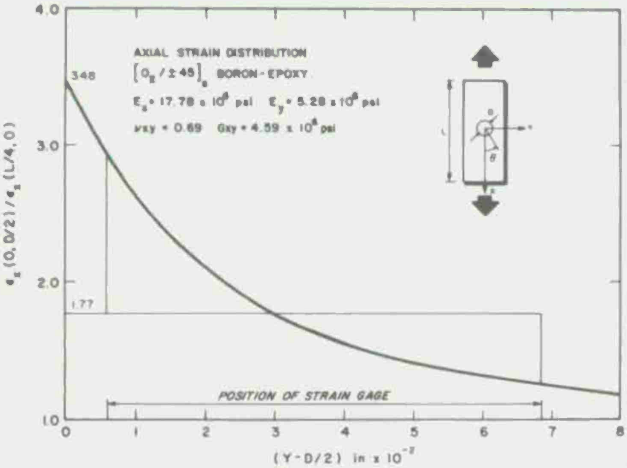

Fig. 2 Axial Strain Distribution

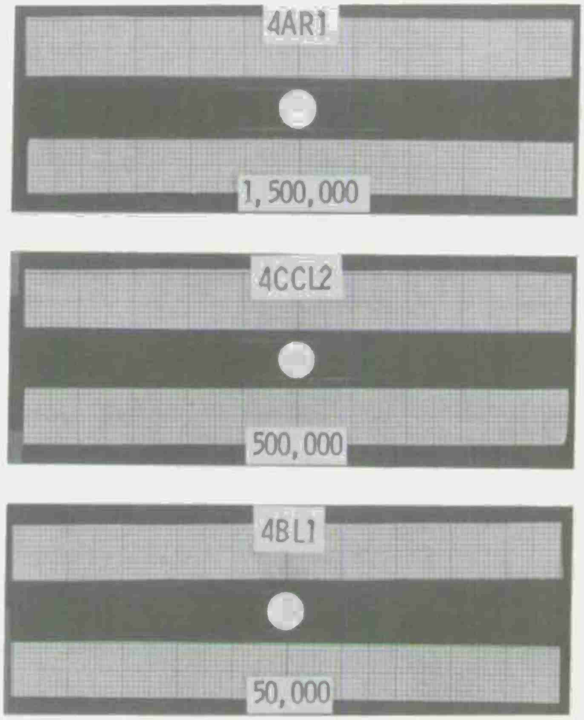

Fig. 3 Axial Fatigue Damage

each of the specimens passes through the point of maximum strain concentration. No branching of the fracture was observed nor did the specimens exhibit damage parallel to the fiber direction in the 0° surface layers.

The fatigue test program is summarized in Table II.

The fatigue program consisted essentially of examining the residual strength of $[0_2/\pm45]_S$ boron-epoxy laminates containing 1/4 inch circular notches after being subjected to fatigue loadings wherein S ranged from 0.67 to 0.80 and the number of cycles, N was varied from 5×10^4 to 10×10^6.

The most apparent fatigue damage observed during the test program was axial cracking emanating from the position (0, D/2) and propagating parallel to the

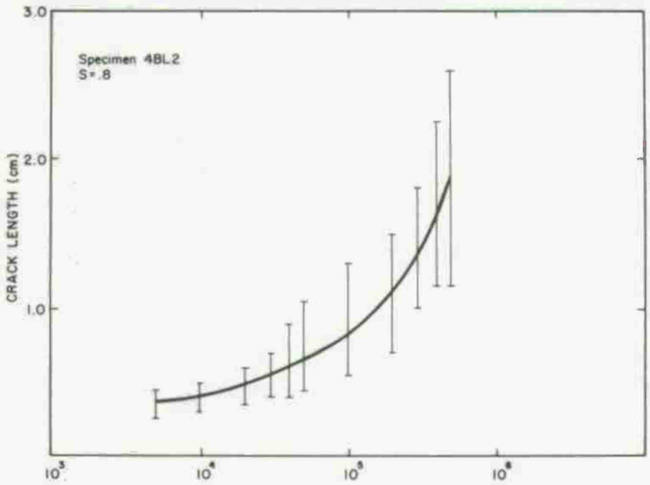

Fig. 4 Axial Crack Growth (S=0.8)

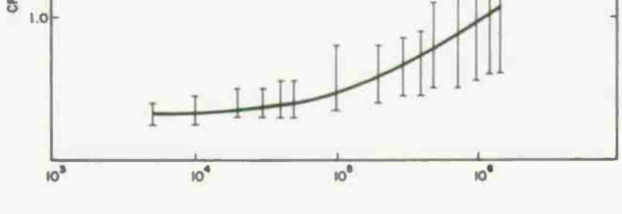

Fig. 5 Axial Crack Growth (S=0.67)

load direction. The length of the axial cracks was observed to increase with increased cycles. This phenomenon is observed in Figure 3 where three specimens have been photographed after $5x10^4$, $5x10^5$, and $1.5x10^6$ cycles. Graphical scales attached to each specimen allow the length of the axial crack to be monitored continuously during the test. It should be noted that no damage in the region of the hole and perpendicular to the load direction is observed in Figure 3. Axial crack length was measured from X=0 in each of the four quadrants and on both sides of the specimens. These data are presented in Figure 4 for S=0.8. It is interesting to note that both the mean crack length and scatter in crack lengths increase with increasing number of cycles. Figure 5 shows axial crack growth data for an S level of 0.67. The growth rate at S=0.67 is seen to be considerably less than that of S=0.80. For example, after $5x10^5$ cycles the mean crack lengths for S=0.67 and 0.80 were found to be 0.7 and 1.86 cm, respectively.

After each test specimen had been subjected to its given fatigue load conditions, it was instrumented with electrical resistance strain gages and tested for residual strength properties. Figure 6 shows a photograph of specimen 4BL2 (S=0.8, $N=5x10^5$) after residual strength test. The photograph reveals that unlike the failure of the specimens subjected to no prior fatigue loading (Figure 1), the fracture for specimen 4BL2 does not pass through the hole. In addition, it would appear that

TABLE II

$[0_2/\pm 45]_S$ B/Ep Fatigue Test Results

Specimen	Failure Site x, in	Max/Ult. Stress	Cycles	Ult. Stress (ksi)	Ult. Strain (μ in/in)	Ult. Strain @ Notch (μ in/in)
4ACL1	0.05	0.80	$5x10^4$	67.9	4150	6800
4ACR2	0.10	0.80	$5x10^4$	76.5	4220	7070
4BL1	0.05	0.80	$5x10^4$	71.5	4175	6950
4BL2	0.50	0.80	$5x10^5$	79.0	4700	6700
4CCL2	0.25/0.10	0.80	$5x10^5$	81.2	4550	7350
4DR3	0.12	0.80	$5x10^5$	66.4	4550	7500
4CR2	0.30	0.80	$1.5x10^6$	82.7	4900	8540
4AR1	0.15	0.80	$1.5x10^6$	71.0	4500	6900
4DR2	0.10	0.67	$5x10^5$	63.5	4550	6550
4AL2	0.05	0.67	$5x10^5$	72.3	4360	7100
4BCR2	0.10	0.67	$5x10^5$	72.7	4400	7000
4DL1	0.12	0.67	$1.5x10^6$	67.4	4550	7150
4BC2	0.00	0.67	$1.5x10^6$	71.4	4400	7550
4BCR1	0.12	0.67	$1.5x10^6$	77.3	4600	7250
4AR2	0.20	0.67	$10x10^6$	77.5	4450	6900
4DL2	0.20	0.67	$10x10^6$	80.9	5470	8850
4AL1	0.10	0.67	$10x10^6$	77.7	4975	7200

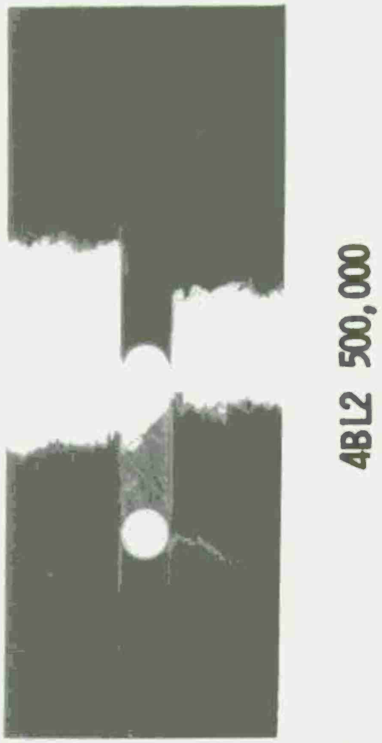

Fig. 6 Residual Strength, 5x10^5 Cycles, S=0.8

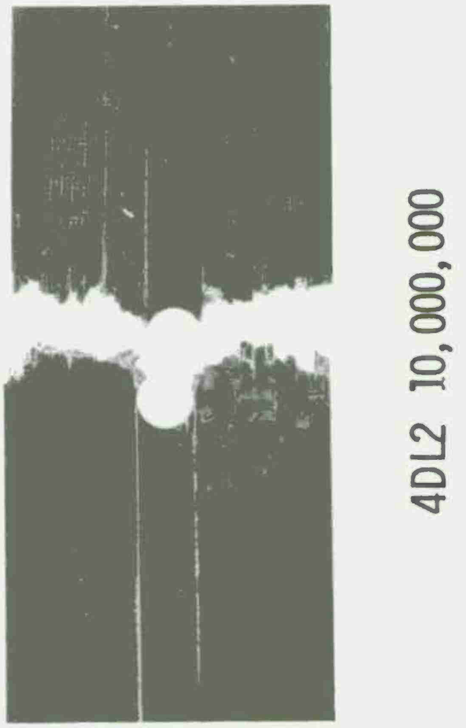

Fig. 7 Residual Strength Fracture 10^7 Cycles, S=0.67

the region of the 0° surface layers between the axial fatigue cracks delaminated either during the fatigue loading or during the residual strength test. The random perpendicular crack in the surface layers near the hole is thought to be the result of the dynamics of laminate fracture and not to have played an important role in failure initiation. The fracture of specimen 4DL2 ($S=0.67$, $N=10^7$) shown in Figure 7 is also quite different from the static test fractures shown in Figure 1. Although the fracture passes through the edge of the hole, it does not pass through the point of maximum stress concentration as might have been expected. Hence, like specimen 4BL2 the fracture site of specimen 4DL2 has moved away from point (0, D/2), the point of initial static failure.

In order to determine the extent of fatigue induced delamination in the vicinity of the circular notch, ultrasonic "C" scans were made of test specimens prior to residual strength tests. Figure 8 shows scans of two typical specimens. The photograph shows that delamination occurs only in a region equal in width to the diameter of the hole and located between the axial fatigue cracks. The axial dimension of delamination was found to vary from specimen to specimen as shown in Figure 8. For example, test specimen 4CL1 was found to delaminate virtually the entire length of the specimen prior to failure. The fracture of specimen 4CL1 ($S=0.8$, $N=1.5\text{x}10^6$) is shown in Figure 9. It is significant to note that the frac-

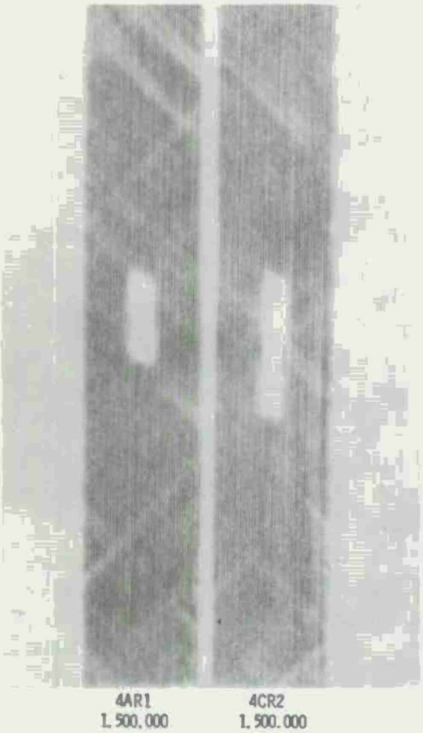

Fig. 8 Typical Ultrasonic "C" Scans

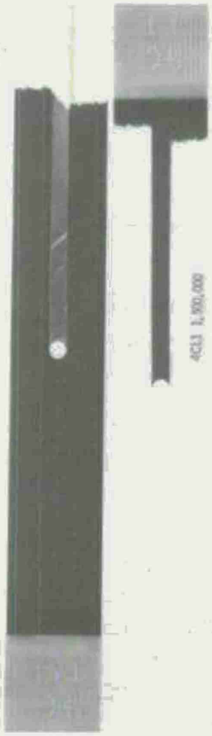

Fig. 9 Delamination Damage, 1.5x10^6 Cycles, S=0.8

ture of this specimen could be considered to be virtually unaffected by the presence of circular hole in the laminate due to the large distance between the hole of the fracture site. The only effect of the hole is due to the delamination which initiates at the hole boundary.

Having instrumented each of the test specimens to monitor strain at the edge of the hole and at a far field position, it is possible to examine changes in strain distribution and ultimate strain which result from fatigue loading. Figure 10 shows both the strain concentration factor at failure and the ratio of ultimate strain to far field strain as a function of number of cycles. Several phenomena are observed in Figure 10. First, the influence of S level (max stress/ultimate stress) upon these results appears to be of second order. Second, the apparent strain concentration diminishes with increased number of cycles. This result implies a change in strain distribution due to damage propagation or local changes in material properties. Finally, the ultimate average strain at the edge of the hole increases with increasing number of cycles. This could only be the result of a local reduction in laminate stiffness accompanied by a reduced stress concentration. Hence, the fatigue loading is found to change the properties in vicinity of the notch to the extent that laminate residual strength increases with increasing number of cycles. In certain cases, the residual laminate strength can approach net section strength with increasing number of cycles. However, eventually material "wearout" will begin to dominate laminate behavior and the residual strength can be expected to diminish with increased fatigue cycles.

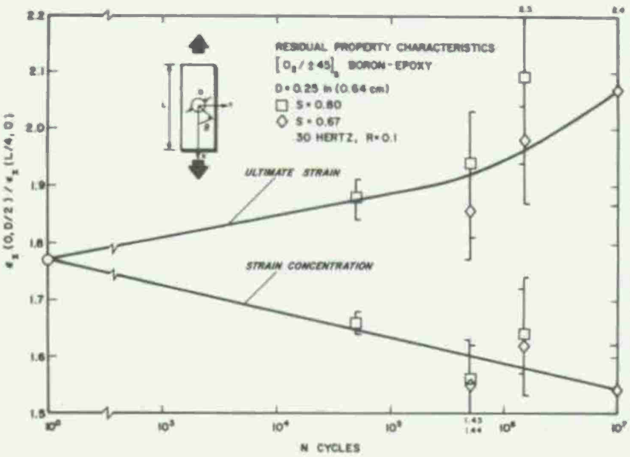

Fig. 10 Residual Property Characteristics

The analytical predictions of the residual strength of notched composite laminates from Reference [8] are compared with the experimental results for S=0.8 and 0.67 in Figure 11. These results indicate that the model predicts the observed axial crack initiation followed by an increase in residual strength approaching net section strength followed by a gradual strength decay due to wearout. Since the model relies upon lamina fatigue data as input for prediction of laminate fatigue response, it is not surprising that the predictions exhibit excellent qualitative form but suffer in the quatitative predictions of life. Improved lamina fatigue data should enhance the predictive ability of the model.

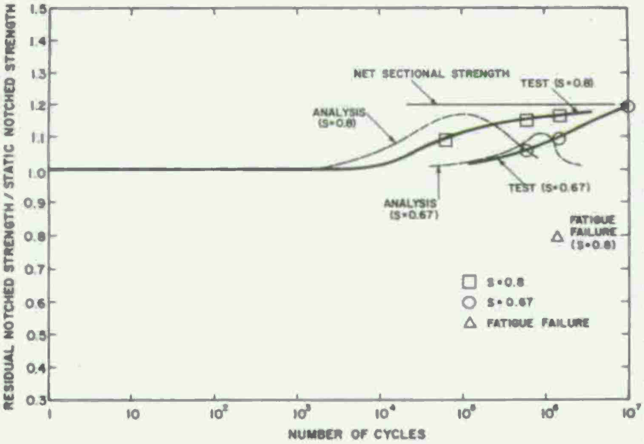

Fig. 11 MSC Model Correlation

CONCLUSIONS

An experimental investigation of the residual strength characteristics of the $[0_2/\pm 45]_S$ boron-epoxy laminate containing a 0.25 inch diameter circular hole and subjected to a sinusoidal loading R=0.1 and frequency of 30 hertz has been undertaken. Evidence has been presented which shows that the residual strength of such a specimen approaches net section strength followed by the onset of wearout. Increases in residual strength are due to changes in "local" material properties near the hole or to fatigue damage in the form of axial cracks in the surface layers parallel to the load direction and delamination of the surface layers. The reduction in local material properties results in an observed reduction in strain concentration factor accompanied by an increase in ultimate strain.

Experimental evidence indicates that math models for prediction of notched laminate residual strength must consider local changes in material properties, as well as, multiple modes of damage propagation. Correlation of experimental data with one such recently developed model shows promising agreement both in residual strength and life.

LIST OF REFERENCES

1. Waddoups, M.E., Eisenmann, J.R., and Kaminski, B.E., Journal of Composite Materials, Vol. 5, October 1971, pp. 446-454.

2. Whitney, J.M. and Nuismer, R.J., Journal of Composite Materials, Vol. 8, July 1974, pp. 253-265.

3. Rosen, B.W., and Zweben, C.H., Tensile Failure Criteria for Fiber Composite Materials, Materials Sciences Corporation Technical Report, 1971, also NASA CR-2057.

4. Zweben, C.H., Fracture Mechanics and Composite Materials: A Critical Analysis, ASTM STP 521, 1973; also Materials Sciences Corporation Technical Report, 1972.

5. Kulkarni, S.V., and Rosen, B.W., Design Data for Composite Structure Safelife Prediction: Analysis Evaluation, TFR/2221, Materials Sciences Corporation, August 1973; also included in Reference 6.

6. Durchlaub, E.C. and Freeman, R.B., Design Data for Composite Structure Safelife Prediction, AFML-TR-73-225, March 1974.

7. McLaughlin, P.V., Jr., Kulkarni, S.V., Huang, S.N., and Rosen, B.W., Fatigue of Notched Fiber Composite Laminates, Part I: Analytical Model, NASA CR-132747, March, 1975.

8. Kulkarni, S.V., McLaughlin, P.V., Jr., Pipes, R.B., "Fatigue of Notched Fiber Composite Laminates", Part II: Analytical and Experimental Evaluation", Final Report, NASA Contract No. NAS1-13931, Materials Sciences Corporation, April 1976.

9. Kulkarni, S.V., McLaughlin, P.V., Jr., Pipes, R.B., and Rosen, B.W., Fatigue of Notched Fiber Composite Laminates: Analytical and Experimental Evaluation; presented at the Fourth ASTM Conference on Composite Materials, Valley Forge, May 1976.

10. Savin, G.N., *Stress Concentrations at Openings*, Gostekhizdal Moscow-Liningrad, 1951 (U.S. Government translation).

FRACTURE BEHAVIOR OF CROSS-PLY COMPOSITE MATERIALS

JOHN M. SLEPETZ
Civil Engineer
Army Materials and Mechanics Research Center
Watertown, Massachusetts 02172

ABSTRACT

Fracture experiments were carried out on cross-ply laminates of S-glass/epoxy and graphite/epoxy. Compact tension specimens were tested in which quantitative as well as qualitative observations were made on the damage zone developed at the specimen crack tip. Test results generally showed that a zone of significant size developed and influenced subsequent fracture behavior. In graphite/epoxy specimens the presence of the zone resulted in higher apparent compliance and fracture toughness values. In glass/epoxy specimens the damage zone dominated behavior to the extent that crack extension did not occur, but instead the damage zone continued to grow with increased load. Failure of glass/epoxy laminates appeared to be too complex to be predicted by the usual fracture mechanics approach.

INTRODUCTION

Failure of notched, fiber-reinforced laminates under tension loading usually occurs by one of two dominant failure modes: either by delamination, characterized by relative sliding of adjacent plies, or by propagation of a sharp crack or crack system throughout the laminate after build-up of a characteristic damage zone. The nature of failure usually depends on the fiber properties. laminate configuration, and orientation of the tension load with respect to the laminate material axes. This study is concerned with tension-dominant failure in composite laminates. Fracture experiments were conducted with one objective being to determine the effect of damage zone build-up at the notch or crack tip on the nature of failure behavior and the magnitude of applicable failure parameters (critical load, fracture toughness, etc.). A second objective was to consider ways in which a conventional fracture mechanics approach could be modified to characterize tension failure in notched, cross-ply laminates. Previous attempts to apply fracture mechanics to composites [1-5] have either ignored the effect of damage zone build-up prior to fracture, or have accounted for it indirectly through a crack length correction or characteristic size effect factor. In the present study, the extent and nature of crack tip damage in compact tension (CT) specimens was observed for two distinctly different cross-ply materials in order to evaluate the suitability of such an approach.

EXPERIMENTAL PROCEDURES

Materials and Specimens

Cross-ply laminate panels were manufactured by standard tape lay-up and autoclave cure procedures. The materials employed were 1002S Scotchply* S-glass/epoxy, Modulite† 5208 and 5206 high-strength graphite/epoxy (MOD II), and MOD II graphite fibers in a BP907 resin matrix. Panels of the latter two material systems were fabricated in-house, and the other panels were made commercially. The 5208 and 5206 MOD II panels were eight plies thick in a $[90, 0]_{2S}$ laminate sequence. The MOD II/BP907 panels were seven plies thick with alternating zero and ninety-degree plies. The 1002S panels were 12 plies thick and were fabricated in a $[90_2, 0]_{2S}$ configuration.

---

* Trade name, 3M Company

† Trade name, Whittaker Division of NARMCO

The elastic properties of the four laminates used in the fracture experiments are given in Table I along with the laminate type designation which will be used hereafter in this paper.

TABLE I. LAMINATE PROPERTIES

Laminate Type	Material	E_1	E_2	G_{12}	μ_{12}
		lb./in.^{2} x 10^6			
A	1002S Scotchply $[90_2, O]_{2S}$	3.55	5.20	1.02	.110
B	MOD II/5208 graphite/epoxy $[90, O]_{2S}$	12.1	12.1	0.95	.035
C	MOD II/5206 graphite/epoxy $[90, O]_{2S}$	10.5	10.5	0.88	.035
D	MOD II/BP907 graphite/epoxy [90, O, 90, O, 90, O, 90]	9.86	12.8	–	.180

The tension properties; E_1, E_2, and μ_{12}, were determined on 0.75 x 9 in. coupons. The in-plane shear modulus, G_{12}, was determined using 1.5 x 6 in. specimens loaded in four-point asymmetrical bending.

The CT specimen configuration used in the fracture experiments was the same as reported in Reference 6. The nominal dimensions were 4 x 3 in. with an initial notch length of 0.75 in. All specimens were machined with the outer plies oriented at 90° to the loading direction. To prevent out-of-plane buckling during fracture tests the specimens were clamped between lubricated steel plates, 0.125 in. thick. Eight specimens of each laminate type were tested in this manner except in the case of the type D laminate, of which four specimens were tested. Compliance and fracture toughness data for an additional eight type B specimens reported in Reference 6 was also used in the results of this study.

Fracture Test Procedure

The CT specimens were loaded quasi-statically in a fixed grip mode at a cross-head speed of 0.01 in./min. The usual compliance calibration procedure was generally followed. Load versus load point displacement was recorded, and crack length was measured by means of a traveling microscope. The compliance relationship with crack length was found by a least-squares fit to the equation

$$C = A_1 (a/W) + A_2 (a/W)^2 + A_3 \frac{1 + a/W + (a/W)^2}{(1 - a/W)^3} \qquad (1)$$

in which C is compliance, a is crack length, W is specimen width measured from the load line. A_1, A_2, and A_3 are the constants determined from the least-squares fit. Eq. (1) can be differentiated to give dC/da from which the strain energy release rate, $\mathcal{G}$, can be determined.

That is,

$$\mathcal{G} = (F^2/2t)\,(dC/da) \tag{2}$$

where F is the applied load and t is the specimen thickness. The strain energy release rate of an elastic, orthotropic material is related to the stress intensity factor, K, in the crack opening mode [7] by

$$\mathcal{G} = K^2 (A_{11}A_{22}/2)^{1/2} \quad [(A_{22}/A_{11})^{1/2} + (2A_{12} + A_{66})/A_{11}]^{1/2} \tag{3}$$

where A_{11}, A_{12}, etc., are the elastic constants associated with the principal material directions, and the crack is aligned in the 1 - direction. By letting

$$E' = \left\{(A_{11}A_{22}/2) \; [(A_{22}/A_{11})^{1/2} + (2A_{12} + A_{66})/A_{66}]\right\}^{-1/2} \tag{4}$$

where E' can be regarded as an effective elastic modulus, the stress intensity factor is found by

$$K = \sqrt{\mathcal{G} E^*} \tag{5}$$

or

$$K = F\sqrt{(E^*/2t)\,(dC/da)} \tag{5a}$$

in terms of the experimentally determined quantities F, C, and a. The maximum load at a given crack length prior to unstable crack growth defines the critical stress intensity factor K_Q in Eq. (5a). Equivalently, the critical strain energy release rate, g_c, is defined in Eq. (2) for $F = F_c$. If K_Q or $\mathcal{G}_c$ is a material constant, either can be used to characterize fracture toughness.

Finite Element Compliance Calibration

In addition to the experimental compliance calibration procedure described, a finite element analytical calibration of the CT specimen was undertaken. Plane stress orthotropic elements having the elastic properties given in Table I for each of the respective materials studied were used in the element mesh arrangement shown in Fig. 1. Compliance as a function of crack length was computed and then used to determine K through Eq. (5a).

Damage Zone Measurements

Several methods were employed in order to obtain quantitative information about the crack tip damage zone and to determine the nature of the damage present. A dye penetrant was used in tests on the S-glass/epoxy laminate. The dye was applied after the appearance of damage while the specimen was under load and quickly spread throughout the surface cracks and delamination region just ahead of the notch tip. When the specimen was back-lighted, the damage zone was clearly visible. Because the graphite/epoxy laminates were opaque, this technique was only effective in tests on glass/epoxy specimens. Several specimens each of both S-glass/epoxy and graphite/epoxy were subjected to C-scan ultrasonic inspection after testing was completed. This method proved to be successful in determining the size of the damage region for all except the type B laminate. The surface roughness and thickness of the type B laminate was apparently unsuitable for this technique to be effective. Finally, several specimens of type A and B laminates were mounted with moiré gratings. The moiré fringe pattern obtained under load conditions was an analog of the notch tip displacement field [8] and provided additional information concerning the size and nature of the damage zone* in the surface plies of the CT specimens.

EXPERIMENTAL RESULTS

Graphite/Epoxy Laminates

The experimental compliance versus crack length curves for all four laminates tested are shown in Figs. 2 and 3. In Fig. 3 the finite element compliance calibration curve for the type B laminate is also shown for comparison. The general behavior of graphite/epoxy specimens during fracture tests was essentially that of a linear elastic, brittle material. This can be seen from the typical load-displacement history of a type D specimen shown in Fig. 4 along with the curves for the other laminates tested. The linear behavior continued even after damage zone build-up and subsequent crack extension for this specimen type as well as for type B specimens. However, in the case of the type C specimens, load-displacement behavior became somewhat nonlinear at a given crack length as damage grew progressively with increasing load before incremental crack growth occurred. The behavior of type C specimens was similar to that of S-glass/epoxy specimens in this respect; and it is significant that the apparent fracture toughness K_Q was the highest observed of any of the graphite/epoxy laminates tested.

Because of the loss of structural integrity of material in the notch tip damage zone, one effect on behavior which would be expected is an increase in overall specimen compliance. This would lead, in turn, to higher observed values of K_Q through use of Eq. (5a). The fact that compliance is higher due to the presence of the damage zone is seen in Fig. 3 which compares experimental and finite element compliance calibrations. The large discrepancy between observed and computed compliance values was thought at first to be due to inaccuracies in modeling the CT specimen in the finite element analysis. However, a subsequent experimental verification of the analysis using aluminum CT specimens indicated that the model was adequate and probably was not responsible for the discrepancy noted in the graphite/epoxy specimens. It is reasonable to assume then that the presence of the damage zone is responsible. Another point to note in Fig. 3 is that the experimental data include specimens with "machined" cracks as well as with natural cracks and that the difference between machined crack data and natural crack data is generally less than the overall data scatter. The development of the damage zone apparently does not require the presence of a very sharp crack in the laminate and may occur regardless of the shape of a geometric discontinuity.

The effect of the damage zone on compliance can be accounted for analytically by assuming an effective crack length, $a + a_o$, as indicated in the sketch of Fig. 3; a_o is the length of the damage zone along the crack plane. The analytical compliance curves (dashed lines) are replotted here for several assumed values of a_o. Rather close agreement with experiment is obtained over a wide range of crack lengths for the case of $a_o = 0.2$. At low values of crack length ($a/W < 0.25$)

---

* More information concerning this technique will be presented in a paper to be published later by F. P. Chiang and the author.

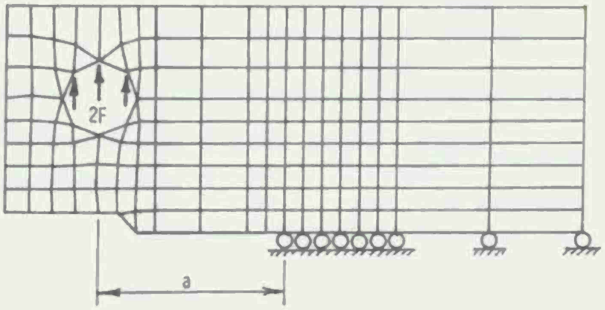

Figure 1. Finite element mesh for compact tension specimens.

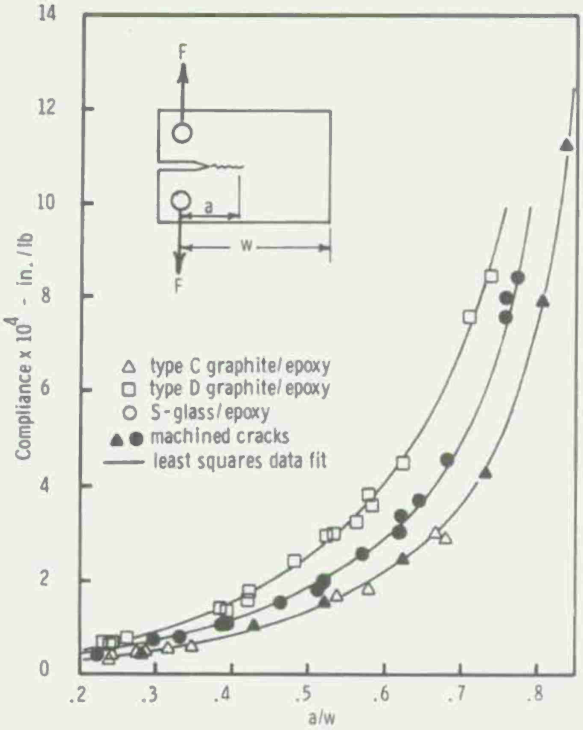

Figure 2. Compliance curves for graphite and glass/epoxy specimens.

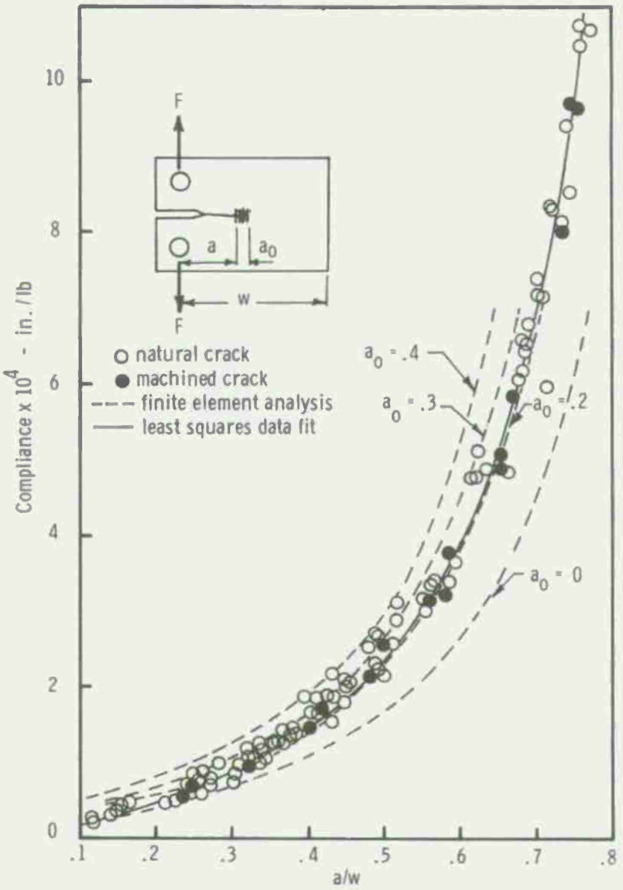

Figure 3. Experimental and analytical compliance curves for type B graphite/epoxy.

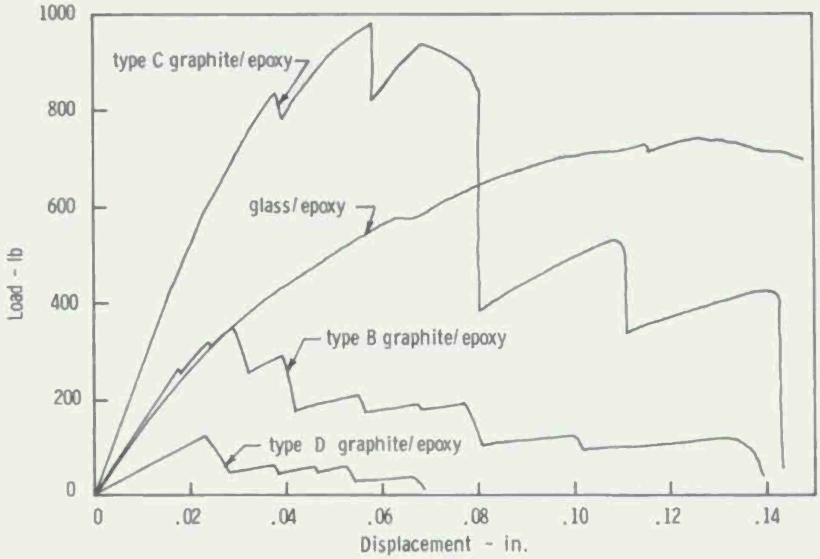

Figure 4. Load-displacement history of typical compact tension specimens.

better agreement is obtained without a damage zone correction length ($a_o = 0$). This may indicate that the damage zone size is dependent on crack length and/or stress intensity in the CT specimens. A comparison of experimental and analytical stress intensity calibration of type B specimens is given in Fig. 5. It is apparent that the analytical curve predicts values of K which are considerably lower than those obtained by experimental calibration. Using a crack length correction factor in the analytical calibration would eliminate the discrepancy in K values. However, the use of CT specimens to characterize fracture of laminates in terms of K_Q becomes questionable for geometries other than the CT specimen unless it can be shown that the damage zone development is independent of geometry.

Fig. 6 shows the C-scan ultrasonic test printout for three types of specimen: (a) type C, (b) type D, and (c) type A (glass/epoxy). In Fig. 6(a) four separate damage zones are indicated, the first at the initial notch and three at successive crack tip locations following incremental growth. The length of the various damage zones ranged from 0.2 to 0.4 in. in the crack plane and the area in the specimen plane varied from 0.07 to 0.55 sq. in. among all the type C specimens examined. While the larger values of K_Q observed roughly corresponded to larger damage zone areas, there did not appear to be a particular relationship linking the two quantities. Table II shows the damage zone length, a_o; area, A_d; and corresponding K_Q values obtained for several type C specimens.

TABLE II. DAMAGE ZONE SIZE IN TYPE C GRAPHITE/EPOXY LAMINATE

Specimen	a in.	a_o in.	A_d in.^{2}	K_Q ksi$\sqrt{\text{in.}}$
C-1	0.8	0.3	.22	35.7
	1.65	0.3	.46	42.6
C-3	0.9	0.2	.16	35.5
	1.65	0.2	.07	46.3
	2.0	0.3	.32	58.1
C-5	0.7	0.2	.07	37.7
	1.6	0.2	.05	47.8
	2.15	0.4	.55	50.0

In Fig. 6(b) it is seen that, unlike the case with type C specimens, crack propagation occurred without development of a large damage zone in type D specimens. Significantly, the fracture toughness K_Q obtained for this laminate was the lowest observed of the three graphite systems tested. By contrast, the notch tip damage zone in a glass/epoxy specimen, Fig. 6(c), is seen to be several times larger than any of those in the type C graphite/epoxy laminate. Typically, a through crack did not propagate from the initial notch of glass/epoxy specimens. Instead, the damage zone itself continued to grow with increasing load.

The variation of K_Q with crack length is shown in Fig. 7 for all three graphite/epoxy laminates tested. While there is considerable data scatter among the type B and type C values, K_Q does appear generally to be independent of crack length. The large scatter range might be expected because of the largely random nature of damage zone build-up, which apparently governs crack extension in cross-ply graphite/epoxy laminates. The least data scatter occurred in the type C specimens

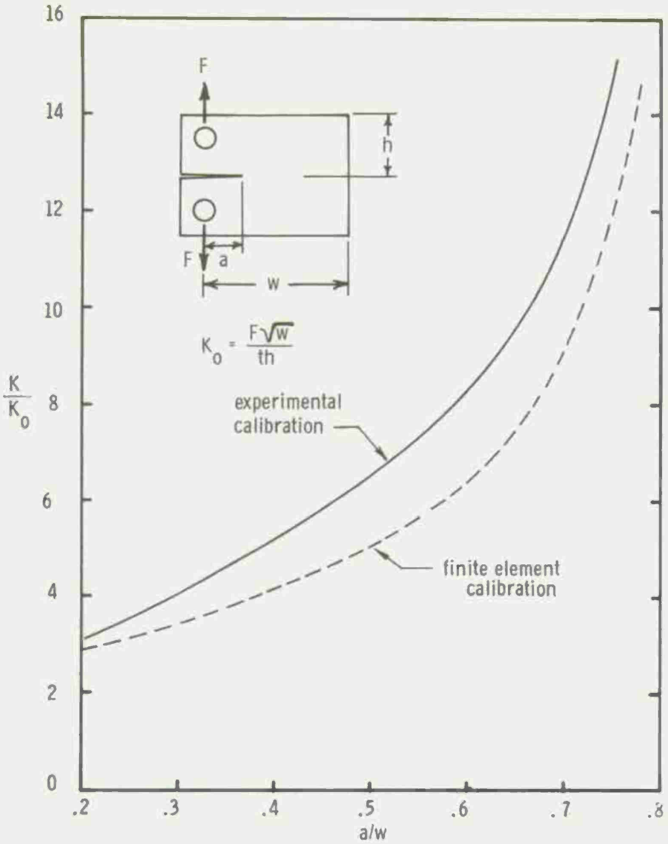

Figure 5. Stress intensity - crack length calibration for type B graphite/epoxy specimens.

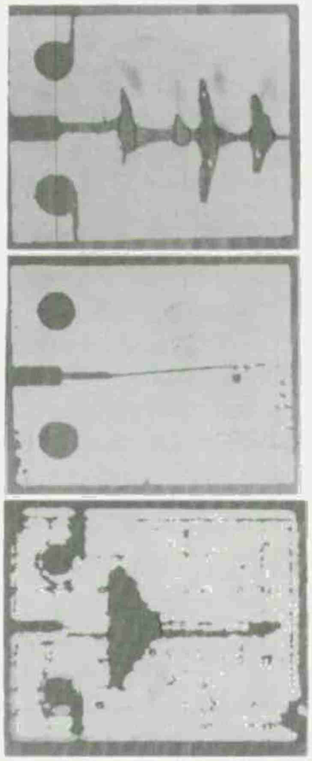

FIGURE 6. DAMAGE ZONE BUILD-UP IN (a) TYPE C GRAPHITE/EPOXY, (b) TYPE D GRAPHITE / EPOXY, AND (c) S-GLASS/EPOXY COMPACT TENSION SPECIMENS.

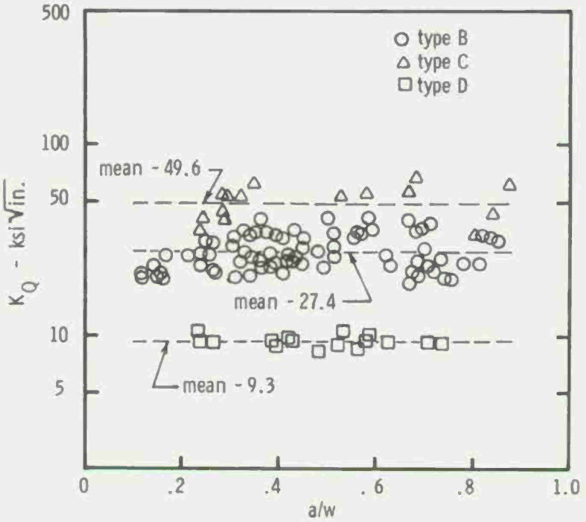

Figure 7. Variation of fracture toughness, K_Q, with crack length in graphite/epoxy laminates.

which exhibited virtually no damage zone build-up detectable by the C-scan analysis. The K_Q values in Fig. 7 are based on the experimental compliance calibration. Mean values for all specimens of the three graphite/epoxy laminates tested are compared with values obtained by finite element compliance calibration and designated as K_Q' in Table III.

TABLE III. MEAN FRACTURE TOUGHNESS VALUES

Laminate Type	$\bar{K}_Q$ ksi$\sqrt{\text{in.}}$	$\bar{K}_Q'$ ksi$\sqrt{\text{in.}}$
B	27.4	22.8
C	49.6	43.9
D	9.3	8.8

Glass/Epoxy Laminates

As already noted, the behavior of glass/epoxy CT specimens was quite different from that of graphite/epoxy specimens. No major crack or crack system propagated from the notch. Instead the damage zone which developed contained a system of subcritical cracks parallel to the fibers in each ply. In addition, the dye penetration and C-scan ultrasonic inspection techniques indicated that debonding between plies occurred to a greater extent than in the graphite/epoxy specimens. The length of the damage zone ranged as high as 0.75 in.; and the area of the zone, unlike the case of graphite/epoxy, continued to grow with increasing load. The difference in damage zone characteristics is demonstrated in Fig. 8 which shows the moiré fringe pattern at the crack or notch tip in a graphite/epoxy specimen, Fig. 8(a), and a glass/epoxy specimen, Fig. 8(b). Since the fringe pattern represents the displacement field of the specimen, points where the fringes are bifurcated indicate a local discontinuity in displacement, as at the tip of a crack [8]. In Fig. 8(b) the eight fringes above and below the notch plane are bifurcated indicating a system of horizontal cracks in the outer ply. By contrast, the fringe pattern of graphite/epoxy specimen in Fig. 8(a), which has the outer plies oriented in the same direction as the specimen in Fig. 8(b), does not exhibit the parallel crack system. However, both glass and graphite specimens did exhibit regularly spaced vertical cracks in the plies parallel to the load.

As was shown in Fig. 4, the load-displacement behavior of glass/epoxy specimens was very nonlinear after the onset of damage at relatively low loads. As damage progressed with increasing load, the behavior became similar to that of a low yield strength, highly ductile metal. The compliance curve for glass/epoxy in Fig. 2 was obtained for the linear region of the load-displacement curve. The stress intensity factor K_{QL} at the onset of damage was determined from this compliance calibration together with the maximum load, arbitrarily taken at a ten percent increase in specimen compliance, representing the upper limit of the undamaged condition. K_{QL} is shown as a function of notch length in Fig. 9. As with graphite/epoxy, there is considerable scatter in the data; but K_{QL} appears to be independent of notch length and has a mean value of 13.4 ksi$\sqrt{\text{in.}}$ The notch length independence might have been expected since the stress field is dominated by the elastic stress intensity factor until the onset of damage. However, the damage zone which subsequently develops is considerably larger than the plastic zone size at the crack tip of a metal specimen; and it is very doubtful that an elastic crack stress analysis would be valid at this and later stages of loading.

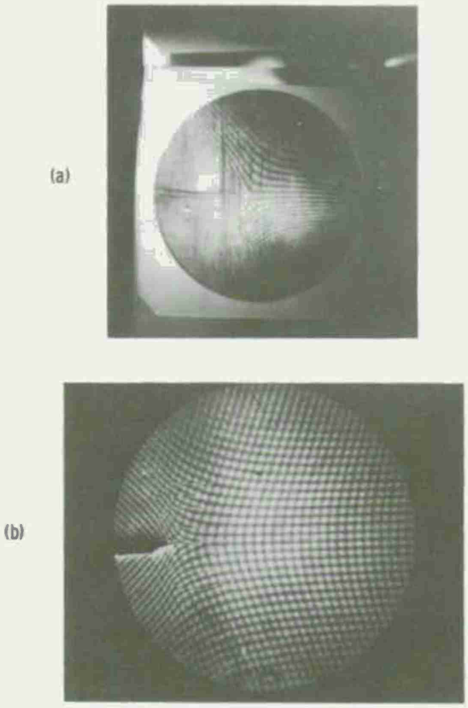

FIGURE 8. CRACK TIP MOIRE FRINGE PATTERN IN (a) S-GLASS/EPOXY AND (b) TYPE B GRAPHITE / EPOXY COMPACT TENSION SPECIMENS.

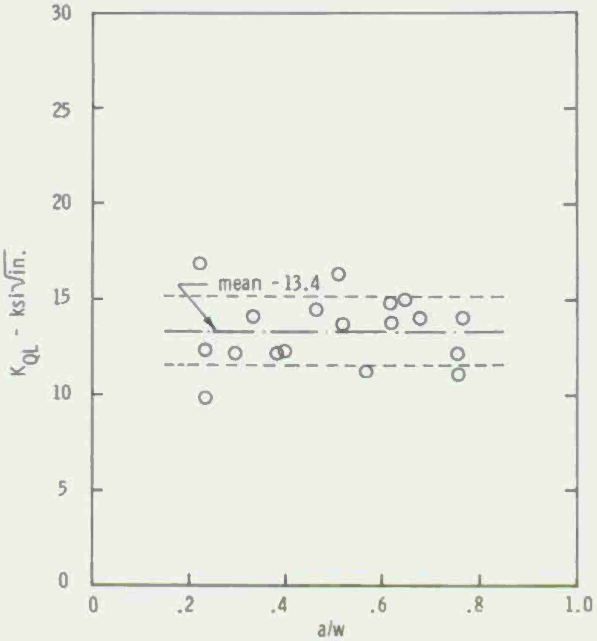

Figure 9. Stress intensity at onset of damage in S-glass/epoxy compact tension specimens.

The damage zone area at a given notch length in glass/epoxy CT specimens appears to depend on load, and it might be reasonable to use this quantity to characterize failure instead of a fracture mechanics indicator such as critical flaw size. Typically, load and damage size increased together in fracture tests until some maximum value of the former was reached. Thereafter, the load leveled off and began to decrease under fixed grip load conditions; whereas the damage zone size continued to increase in a stable manner. The fracture test was generally terminated at this stage; but it was apparent that loading could have continued, at least until the damage zone reached the boundaries of the specimen. The maximum load attained at a given notch length usually ranged from 40 to 80 percent greater than the load at which damage was initiated.

CONCLUSIONS

1. The damage zone developed in notched, cross-ply laminates under tension loading significantly affects subsequent failure behavior.

2. The size of the damage zone varies with the type of composite. In graphite/epoxy it reaches a characteristic size prior to crack propagation. In S-glass/epoxy the zone continues to grow in a benign fashion without the occurrence of critical crack growth.

3. The type of damage which develops in the notch tip vicinity is ply delamination accompanied by parallel ply cracking. Propagation of a major crack can then occur, presumably after the redistributed stresses in the damage zone reach the strength level of the plies parallel to the load. The characteristic damage size would then appear to depend on the ply interlaminar strength to tensile strength ratio. Where this is low, as in S-glass/epoxy, the characteristic zone size would be large; and where it is relatively large, as in MOD II/BP907 graphite/epoxy, the zone size is correspondingly small.

4. The existence of the notch tip damage zone and its role in failure behavior lends some physical basis to the characteristic size effect concept in failure of notched composite laminates.

5. Graphite/epoxy cross-ply laminates generally behave in a manner predicted by fracture mechanics and exhibit a characteristic material failure parameter K_Q. Analytical calibration of the stress intensity factor K can be made to agree with experimental calibration through use of a crack length correction factor based on the damage zone size.

6. It may be possible to use the damage zone itself as a failure parameter in lieu of a critical flaw size in glass/epoxy laminates. More work is required to establish the stability conditions of the damage zone and the significant material and geometric parameters affecting failure.

ACKNOWLEDGMENTS

This work was carried out with funding on Project 1T162105AH84. The assistance of J. L. Smith in performing the c-scan ultrasonic inspection of fracture specimens is gratefully acknowledged.

REFERENCES

1. J. F. Mandell, et al, "Stress Intensity Factors for Anisotropic Fracture Test Specimens of Several Geometries," Massachusetts Institute of Technology Research Report R74-4, 1973.

2. J. F. Mandell, et al, "Fracture of Graphite Fiber Reinforced Composites," Air Force Materials Laboratory, AFML-TR-73-142, 1973.

3. T. A. Cruse, "Tensile Strength of Notched Composites," J. Composite Materials, Vol. 7, April 1973, p. 218.

4. T. A. Cruse and J. R. Osias, "Exploratory Development on Fracture Mechanics of Composite Materials," Air Force Materials Laboratory, AFML-TR-74-111, 1974.

5. J. M. Whitney and R. J. Nuismer, "Stress Fracture Criteria for Laminated Composites Containing Stress Concentrations," J. Composite Materials, Vol. 8, July 1974, p. 253.

6. J. M. Slepetz and L. Carlson, "Fracture of Composite Compact Tension Specimens, "ASTM STP 593, Fracture Mechanics of Composites, 1975, p. 143.

7. P. C. Paris and G. C. Sih, "Stress Analysis of Cracks," ASTM STP 381, 1970, p. 60.

8. F. P. Chiang and J. M. Slepetz, "Crack Measurements in Composite Materials," J. Composite Materials, Vol. 7, January 1973, p. 134.

SESSION VIb: FAILURE MODES

Chairman: G. D'ANDREA
Chief, Organic Materials Laboratory
Watervliet Arsenal

FINITE ELEMENT ANALYSIS OF MECHANICAL AND THERMAL EDGE EFFECTS IN COMPOSITE LAMINATES
C. T. Herakovich, G. D. Renieri and H. F. Brinson, Virginia Polytechnic Institute and State University 237

RELAXATION OF RESIDUAL STRESSES IN ANGLE-PLY COMPOSITE LAMINATES
I. M. Daniel and T. Liber, IIT Research Institute 249

ON THE THREE-DIMENSIONALITY OF FAILURE MODES IN ANGLE-PLY STRIPS UNDER TENSION
D. W. Oplinger, B. S. Parker and A. F. Grenis, Army Materials and Mechanics Research Center 263

FINITE ELEMENT ANALYSIS OF MECHANICAL AND THERMAL EDGE EFFECTS IN COMPOSITE LAMINATES[1]

CARL T. HERAKOVICH, GARY D. RENIERI & HALBERT F. BRINSON
Department of Engineering Science and Mechanics
Virginia Polytechnic Institute and State University
Blacksburg, Virginia 24061

ABSTRACT

This paper considers the problem of combined mechanical and thermal edge effects in finite width advanced composite laminates which are subjected to uniform axial strain loading and uniform temperature loading. Stress distributions near the free edge are determined for linear and nonlinear material behavior. The nonlinear analysis includes the variation of material properties with temperature. Results are presented for boron/epoxy, graphite/epoxy and borsic/aluminum. It is shown that the inclusion of thermal edge effects can alter the stress distribution significantly.

INTRODUCTION

Most failure theories for advanced filamentary composite materials are expressed in terms of the components of stress and strength parameters which are determined from tests on unidirectional laminates [1]. The accuracy of such stress dependent failure criteria depends upon how well the criteria account for all factors affecting failure and also on how accurately the state of stress is known. This paper addresses the question of stress distribution.

Since composite materials are fabricated at elevated temperatures and then cooled to room temperature, residual thermal (curing) stresses are inherently present in these materials when used at any temperature other than the stress-free curing temperature (the temperature at which bonding occurs). These thermal stresses are present on the micromechanics level because of the thermal mismatch between fiber and matrix and on the laminate level because of the thermal mismatch between laminae. As will be shown in this paper, the residual thermal stresses at room temperature can be significant when compared with the stresses due to mechanical loading only.

The failure of a composite material will generally initiate in a region of stress concentration such as at the edge of a hole or cutout, or along the free edge of a laminate. Stress concentrations in such regions have been studied by a number of investigators [2,3,4]. However, except for reference [5], these analyses have been limited to stresses due to mechanical loading only. Reference [5] considered thermal stresses at the free edge of sandwich laminates consisting of a sheet of metal sandwiched between symmetric laminae of unidirectional boron/epoxy.

This paper considers the problem of combined mechanical and thermal edge

---

[1] Supported by NASA Grant NGR 47-004-090

effects in finite width advanced composite laminates which are subjected to uniform axial strain loading and uniform temperature loading. The finite element method is used to obtain results for the room temperature stress distribution near the free edge of bi-directional and angle-ply laminates. Both linear and nonlinear material behavior are considered as well as temperature dependent material properties. Results are presented for boron/epoxy, graphite/epoxy and borsic/aluminum.

PROBLEM FORMULATION

Consider a balanced, symmetric, finite width laminate of homogeneous, orthotropic layers with the principal material directions making angles θ_i with the x-axis (Figure 1). The laminate is subjected to a uniform axial strain ξ_x and a uniform temperature change ΔT from the stress free curing temperature. For such uniform loading, the stresses and strains are independent of the axial coordinate x and the analysis can be restricted to a typical quarter section of the cross-section as shown in Figure 1b.

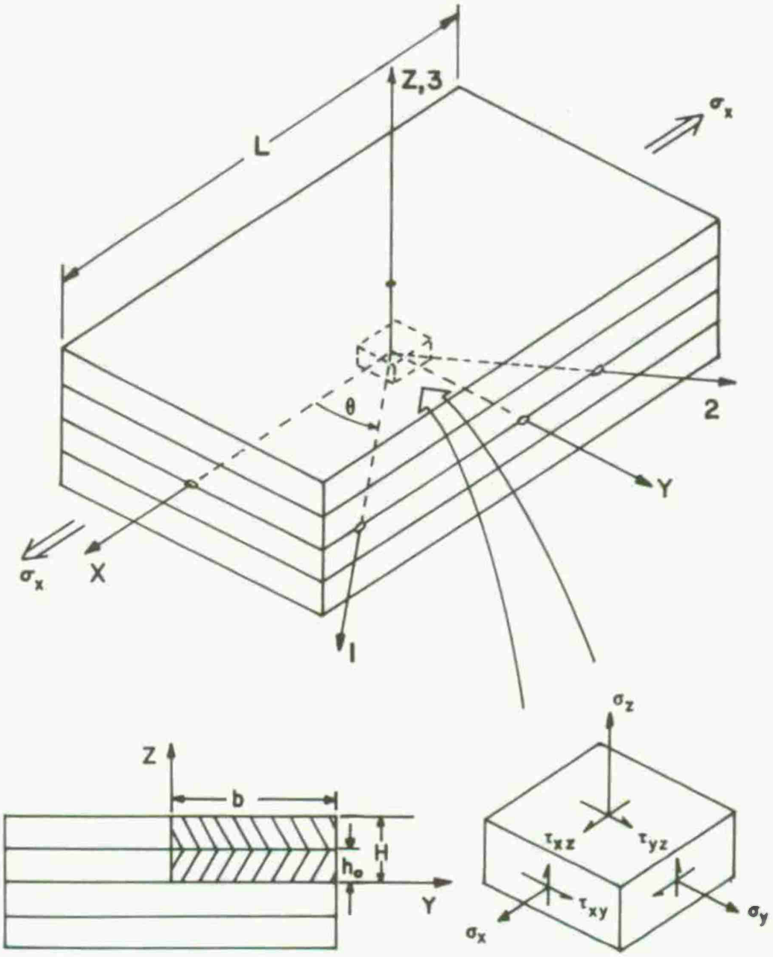

Figure 1 Typical Laminate Geometry

LINEAR ANALYSIS

The layer wise thermo-elastic constitutive equations may be written with respect to the xyz axis as

$$\begin{Bmatrix} \sigma_x \\ \sigma_y \\ \sigma_z \\ \tau_{yz} \\ \tau_{zx} \\ \tau_{xy} \end{Bmatrix}^k = \begin{bmatrix} \bar{C}_{11} & \bar{C}_{12} & \bar{C}_{13} & 0 & 0 & \bar{C}_{16} \\ \bar{C}_{12} & \bar{C}_{22} & \bar{C}_{23} & 0 & 0 & \bar{C}_{26} \\ \bar{C}_{13} & \bar{C}_{23} & \bar{C}_{33} & 0 & 0 & \bar{C}_{36} \\ 0 & 0 & 0 & \bar{C}_{44} & \bar{C}_{45} & 0 \\ 0 & 0 & 0 & \bar{C}_{45} & \bar{C}_{55} & 0 \\ \bar{C}_{16} & \bar{C}_{26} & \bar{C}_{36} & 0 & 0 & \bar{C}_{66} \end{bmatrix}^k \begin{Bmatrix} \varepsilon_x - \alpha_x \Delta T \\ \varepsilon_y - \alpha_y \Delta T \\ \varepsilon_z - \alpha_z \Delta T \\ \gamma_{yz} \\ \gamma_{zx} \\ \gamma_{xy} - \alpha_{xy} \Delta T \end{Bmatrix}^k \tag{1}$$

where $[\bar{C}]^k$ is the stiffness matrix of the kth layer in a coordinate system rotated through an angle θ_k from the principal material direction ΔT is the uniform temperature change, and α's are coefficients of thermal expansion after rotation through the proper angle.

Integration of the strain-displacements relations for a continuum (independent of x) and invoking appropriate symmetry conditions [6] leads to the displacement fields

$$\begin{aligned} u &= \xi_x x + U(y,z) \\ v &= V(y,z) \\ w &= W(y,z) \end{aligned} \tag{2}$$

where U, V and W are unknown functions of y and z only. The appropriate traction free boundary conditions are

$$\sigma_y(\pm b,z) = \tau_{xy}(\pm b,z) = \tau_{yz}(\pm b,z) = 0 \tag{3}$$

along the free edge y = b, and

$$\sigma_z(y,\pm H) = \tau_{xz}(y,\pm H) = \tau_{yz}(y,\pm H) = 0 \tag{4}$$

on the top and bottom surfaces of the laminate. The layerwise displacement-equilibrium equations can be written in terms of the unknown displacement functions and the layer stiffness coefficeints as

$$\begin{gathered} C_{66}U,_{yy} + C_{55},U,_{zz} + C_{26}V,_{yy} + C_{45}V,_{zz} + (C_{36} + C_{45})W,_{yz} = 0 \\ C_{26}U,_{yy} + C_{45}U,_{zz} + C_{22}V,_{yy} + C_{44}V,_{zz} + (C_{23} + C_{44})W,_{yz} = 0 \\ (C_{45} + C_{36})U,_{yz} + (C_{44} + C_{23})V,_{yz} + C_{44}W,_{yy} + C_{33}W,_{zz} = 0 \end{gathered} \tag{5}$$

A finite element computer program was written to solve the problem depicted in Figure 1 and defined by equations 1-5. The program uses triangular finite elements with linear displacement functions (constant strain elements) to minimize the potential energy Φ which can be expresssed as the summation over all M finite elements

$$\Phi = \sum_{\ell=1}^{M} \left[\frac{1}{2} A_\ell \{\varepsilon\}_\ell^T [\bar{C}]_\ell \{\varepsilon\}_\ell - (\{t\}^T \{\delta\})_\ell \right] \tag{6}$$

where $\{t\}$ are the surface tractions, $\{\delta\}$ are node point displacements, A_ℓ is the area of the ℓth element and superscripts T indicate the transpose of the matrix. The strains in (6) are the elastic strains. That is, if $\{\varepsilon^o\}$ are the total strains and $\{\varepsilon^T\}$ are thermal strains, then the elastic strains are

$$\{\varepsilon\} = \{\varepsilon^o\} - \{\varepsilon^T\} \tag{7}$$

The unknown nodal displacements are determined from the set of simultaneous equations obtained by minimizing the potential energy with respect to these unknowns. Back substitution in the stress displacement equations then gives the stresses over each finite element. Since interlaminar stresses were of prime importance in this study, it was necessary to approximate the stress at the "exact" interface in terms of the adjacent finite elements. The results for interlaminar stresses presented in this paper are the average of the stresses on the four elements that have at least one node on a particular segment of the interface. Since interlaminar stresses must be continuous across the interface, such an averaging process should not introduce any substantial error in the results.

NONLINEAR ANALYSIS

An incremental loading procedure was developed in order to take into account the nonlinear behavior and temperature dependent properties of advanced composites. At each stage of the incremental procedure, the mechanical properties of each finite element can be altered depending on the temperature and/or strain level. (Lamina properties in the principal material directions were taken from published experimental results). Initially, the laminates were subjected to an incremental uniform temperature change loading from the elevated stress-free temperature to room temperature.

The laminates were then subjected to an incremental uniaxial strain loading.

Nonlinear lamina principal stress-strain curves were represented by Ramberg-Osgood [7] approximation of published experimental results. A total of five such approximations were used for each material. They were: tension and compression in the fiber direction; tension and compression perpendicular to the fiber; in-plane shear. Shear behavior was assumed to be the same in all three principal planes. The variations with temperature of mechanical properties and coefficients of thermal expansion were modeled through percent retention curves. These curves give the value of the quantity at any temperature as a percent of the room temperature value. Details of the nonlinear and temperature dependent behavior of the materials considered can be found in reference [6].

THE FINITE ELEMENT PROGRAM

The computer program can accept either axial strain or axial load as the applied loading condition. If the axial strain ξ_x is specified, the total stiffness matrix is 3N x 3N with the three displacements at each of the N node points being the 3N unknowns. If the axial load is specified, ξ_x is an additional unknown and the total stiffness matrix is (3N+1) x (3N+1). The additional simultaneous equation is the requirement that the average axial stress is equivalent to the applied load. For thermal loading only, ξ_x is determined by setting the applied axial force equal to zero.

The computer program is a FORTRAN program which has automatic mesh generation capability. The final mesh can also be plotted with all nodes and elements properly numbered. This feature greatly enhances the application of the program when large numbers of finite elements are required. The program was written for an IBM 370/158 and employs double precision variables for the determination of nodal displacements. Tapes are used to reduce the core requirements. Running time is of course problem dependent. (The program is available upon request from the authors.)

RESULTS AND DISCUSSION

Typical results obtained using the finite element program described in the previous sections are presented in Figures 2-9. The results presented in Figures 2 and 3 show the influence of fiber orientation on the maximum value of σ_z and τ_{xz} on the interface of a $[\pm\theta]$ laminate for both mechanical and thermal loading. (As will be shown, the maximum value for both stresses occurs at the free edge.) Stress magnitudes have been normalized with respect to the absolute maximum value for all angles. The mechanical loading results are for an applied strain of 0.7% and the thermal loading results are for an equivalent temperature change from the curing temperature to room temperature as indicated in the figure. An equivalent temperature change was used in this linear analysis to compensate for the variation of properties with temperature. Such a simplification does not affect the influence of fiber orientation.

As indicated in Figure 2, the maximum normal stress occurs at an angle of approximately 30° for mechanical loading of epoxy matrix materials, but for metal matrix materials the maximum stress is at approximately 37°. This shift is attributed to the difference in mechanical properties of the matrix materials. The thermal results in Figure 2 indicate that the maximum thermal stress for both epoxy matrix and metal matrix systems occurs at approximately 50°. This figure also shows that the sign of the interlaminar normal stress is negative for thermal loading, but positive for mechanical loading. Figure 3 shows the influence of fiber orientation on the interlaminar shear stress τ_{xz}. For mechanical loading of epoxy matrix systems the maximum stress occurs at approximately 20°, and for metal matrix systems at approximately 30°. Thermal maximums all occur at approximately 45°. Again, the stresses due to mechanical and thermal loading are of opposite sign.

Figure 4 shows a comparison between linear thermoelastic and nonlinear thermal results for the distribution of σ_z along the interface of a graphite/epoxy bi-directional laminate. As expected, the general shape of the distribution is not affected, but the nonlinear analysis predicts significantly

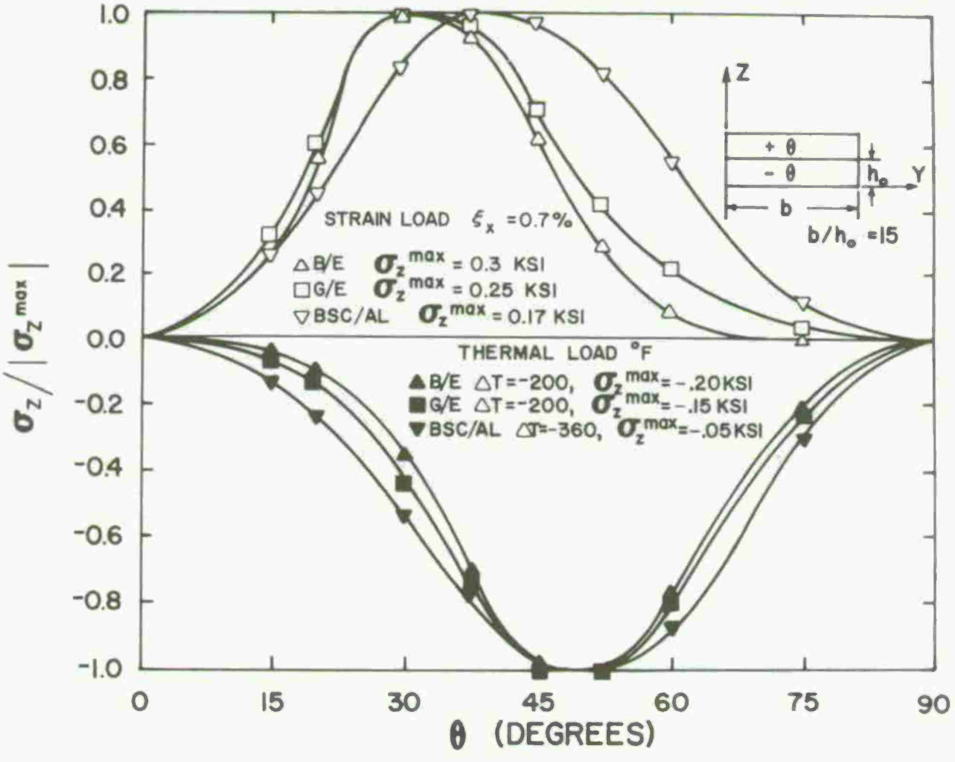

Figure 2 σ_z As a Function of Fiber Orientation

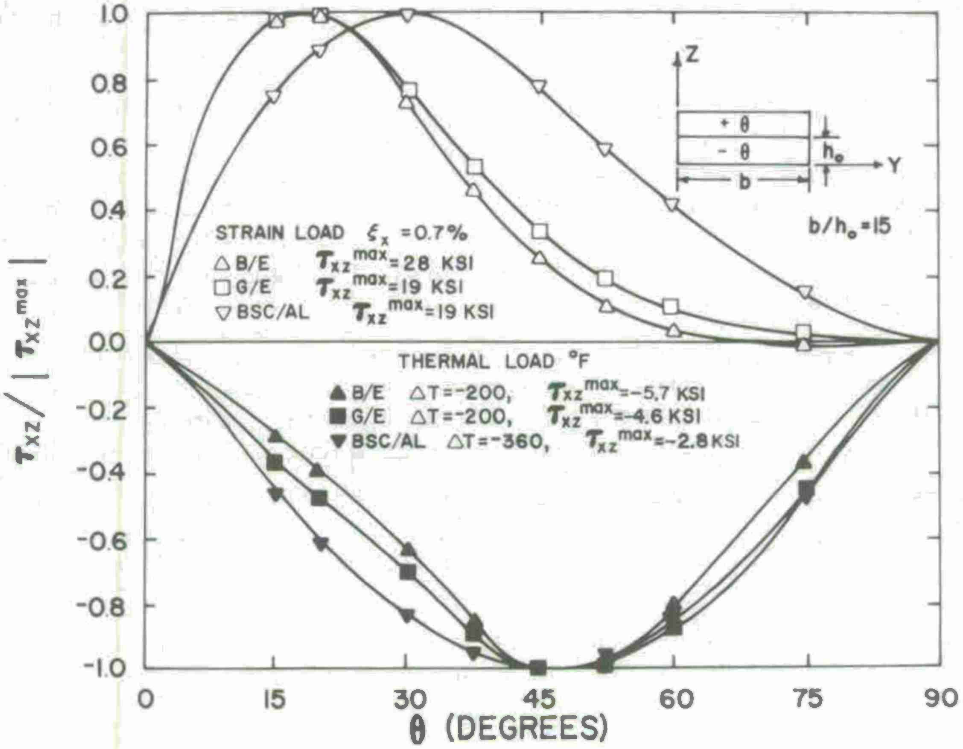

Figure 3 τ_{xz} As a Function of Fiber Orientation

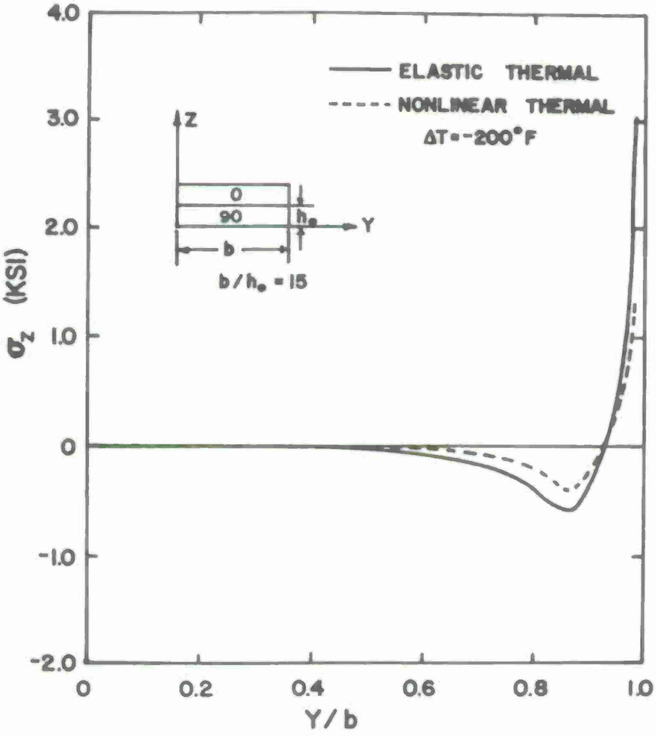

Figure 4 Comparison of Linear & Nonlinear Thermal Stresses

lower maximum values. The results indicate the presence of a thermal stress concentration near the free edge.

The remaining figures present results for the distribution of interlaminar stresses in [0/90] and [±45] graphite/epoxy laminates. Each figure shows a comparison between results for linear elastic material behavior under mechanical loading, nonlinear material behavior under thermal loading and nonlinear material behavior under mechanical and thermal loading. As indicated in Figure 5, the combined nonlinear thermal and mechanical analysis indicates a maximum σ_z at the free edge which is almost three times greater than that predicted by a linear elastic analysis. Mechanical and thermal stresses are of the same sign. Thus, ignoring thermal stresses may cause over-estimation of the strength. The results in Figure 6 for the distribution of τ_{yz} in this same laminate are of a similar nature. The maximum value for the combined nonlinear mechanical and thermal loading is approximately three times the linear elastic result. This figure also shows a deficiency of a finite element solution with a limited number of elements. The boundary condition requires that τ_{yz} be zero at the exact free edge. While not shown in this figure, results obtained using smaller elements near the free edge did show that this component of stress was decreasing near the free edge as it should [6].

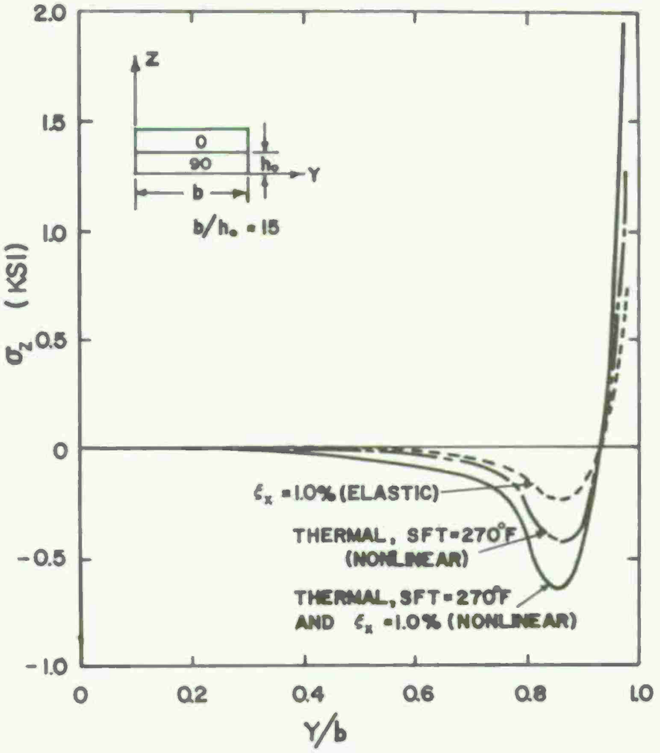

Figure 5 σ_z Distributions for Bi-directional Laminate

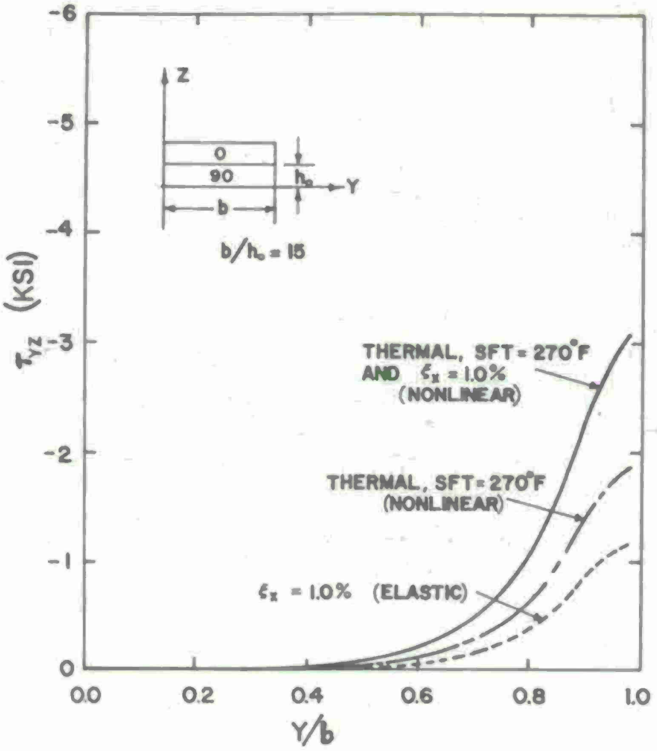

Figure 6 τ_{yz} Distributions for Bi-directional Laminate

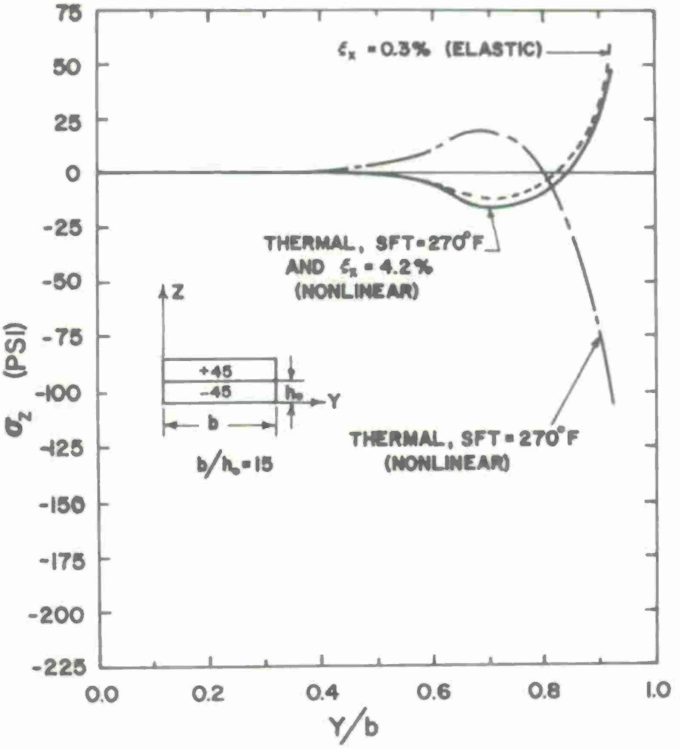

Figure 7 σ_z Distributions for [±45] Laminate

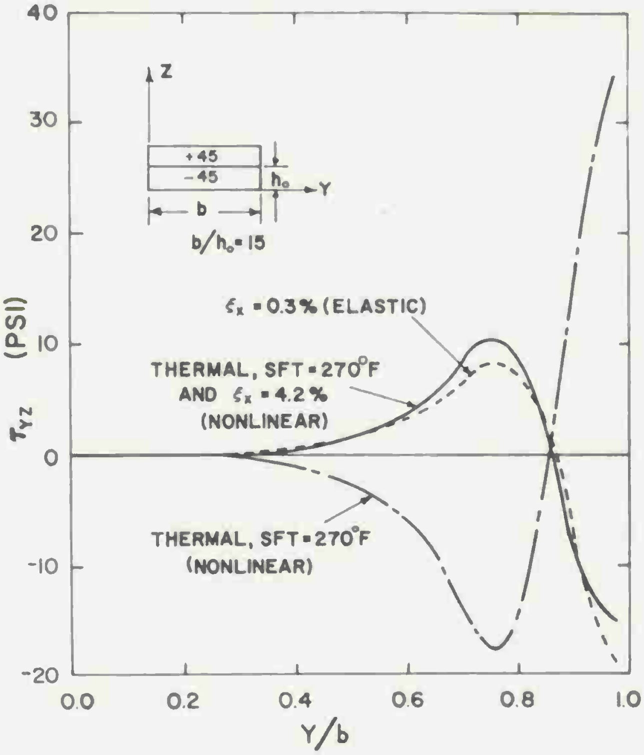

Figure 8 τ_{yz} Distributions for [±45] Laminate

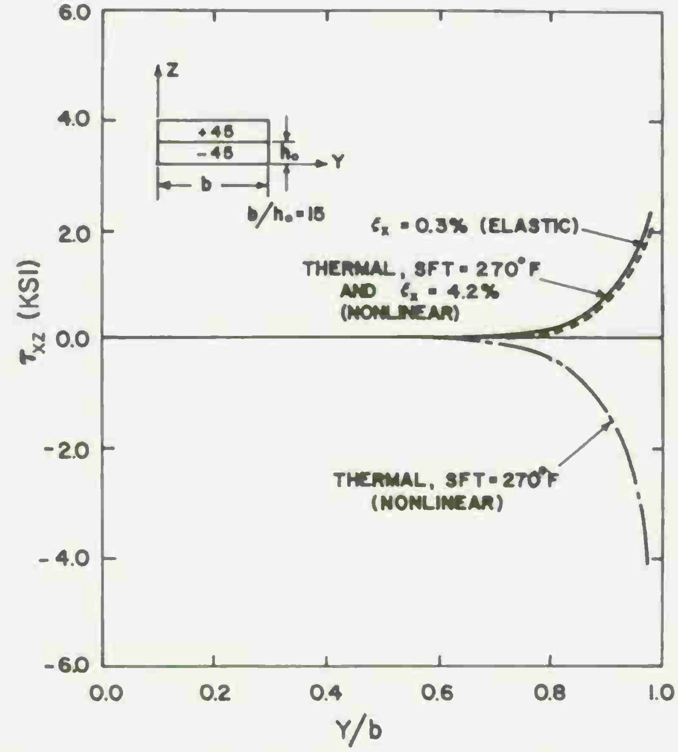

Figure 9 τ_{xz} Distributions for [±45] Laminate

The results for the [±45] angle-ply laminate in Figures 7-9 show a different behavior from the bidirectional laminate. The thermal stress is of opposite sign to that for mechanical loading. Thus, neglecting the thermal stresses in the analysis of such a laminate results in a conservative estimate of the maximum stress. As indicated in the figures, the nonlinear combined mechanical and thermal loading for an applied strain of 4.2% is approximately equivalent to a linear elastic analysis for an applied strain of only 0.3%. For the angle-ply laminate, the critical component of interlaminar stress appears to be the τ_{xz} component which attains a maximum value at the free edge.

CONCLUSIONS

The results of a nonlinear finite element investigation of the combined mechanical and thermal loading of advanced composite laminates has shown that the thermal effects may be significant. For bi-directional laminates, the mechanical and thermal effects are additive and, hence, neglect of thermal effects results in a significantly lower prediction for the maximum stresses. For [±45] angle-ply laminates, the stresses due to mechanical and thermal loading are of opposite sign and, hence, neglect of thermal effects results in a conservative estimate of the maximum stresses.

It has been shown that nonlinear thermal effects are important for the prediction of failure in composites.

ACKNOWLEDGEMENT

This work was supported by NASA Grant NGR 47-004-090. Dr. John G. Davis, Jr. of the Composites Section at NASA's Langley Research Center was the technial monitor and his helpful assistance is appreciated.

REFERENCES

1. Herakovich, C. T. (editor) Inelastic Behavior of Composite Materials ASME, AMD, vol. 13, 1975.

2. Pipes, R. B., Pagano, N. J., "Interlaminar Stresses in Composite Laminates Under Uniform Axial Extension," J. Comp. Mat'ls., vol 4, 1970, 538.

3. Hsu, P. W. and Herakovich, C. T., "Interlaminar Stresses in Composites Laminates - A Perturbation Analysis," VPI-E-76-1, Virginia Polytechnic Institute and State University, Blacksburg, Va., Jan., 1976.

4. Grimes, G. C. and Greimann, L. F., "Analysis of Discontinuities, Edge Effects, and Joints," in Composite Materials, vol. 8, Structural Design and Analysis, Part II, (C. C. Chamis, editor) Academic Press, 1975.

5. Herakovich, C. T., "On Thermal Edge Effects in Composite Laminates," Int. J. Mech. Sciences (in press).

6. Renieri, Gary D. "Nonlinear Analysis of Laminated Fibrous Composites," Ph.D. Thesis, Virginia Polytechnic Institute and State University, Blacksburg, Va., June, 1976.

7. Ramberg, W. and Osgood, W. R., "Description of Stress-Strain Curves by Three Parameters," Tech. Note No. 902, National Advisory Committee for Aeronautics, Washington, July, 1943.

RELAXATION OF RESIDUAL STRESSES IN ANGLE-PLY COMPOSITE LAMINATES

I.M. DANIEL
Science Advisor

T. LIBER
Senior Research Engineer
IIT Research Institute
Chicago, Illinois

ABSTRACT

Lamination residual stresses in composite laminates are produced during curing as a result of the anisotropic thermal deformations of the various plies. The extent of relaxation of these stresses was investigated in $[0_2/\pm45]_s$ laminates of six composite systems. Several means of evaluation of stress relaxation were used. Direct measurement of strain variation with time in angle-ply laminates proved to be very insensitive. An upper limit to the actual amount of residual stress relaxation was obtained by measuring stress relaxation in 90-degree unidirectional laminates. An indirect evaluation was made by determining the elastic and strength properties of angle-ply laminates as a function of time after curing. Results tend to indicate that residual stresses do not relax appreciably with time.

INTRODUCTION

Lamination residual stresses are induced in angle-ply composite laminates during curing as a result of the anisotropic thermal expansions of the various plies. The analysis of these stresses has been the subject of many recent analytical and experimental investigations [1-6]. Residual stresses are a function of many parameters, such as ply orientation, fiber volume ratio, curing temperature and other variables [1, 2]. They can reach values comparable to the transverse strength of the ply and thus induce cracking of that ply within the laminate. Residual stresses in each ply are equilibrated with interlaminar shear stresses transmitted from adjacent plies and thus can cause delamination. These stresses must be taken into account when designing composite structures and must be superimposed onto those produced by external loading.

The various plies of the laminate are cured under conditions restraining their stress-free thermal deformation. The induced restraint is directly related to the residual stresses. The restraint strains remain relatively fixed, allowing only for the possibility of relaxation of the residual stresses. Stress relaxation in composites, being primarily a matrix-controlled property, is most pronounced in the transverse-to-the-fiber direction. The objective of this investigation was to evaluate the extent of relaxation of these residual stresses.

Several means of evaluation of stress relaxation were attempted: (1) Direct measurement of strain changes with time in $[0_2/\pm45]_s$ laminates, (2) Stress relaxation determination in 90-degree unidirectional laminates, and (3) Elastic and strength properties in $[0_2/\pm45]_s$ laminates as a function of time after curing. Six material systems were investigated: Boron/epoxy, boron/polyimide, graphite/low modulus epoxy, graphite/high modulus epoxy, graphite/polyimide and S-glass/epoxy.

RESULTS AND DISCUSSION

Strain Variation in Angle-Ply Laminates

Three 2.54 cm x 22.9 cm (1 in. x 9 in.) $[0_2/\pm45]_s$ S-glass epoxy specimens were prepared with embedded strain gages. This layup is typically used in structural applications such as fan blades subjected to axial tension and torsion. Embedded three-gage rosettes in these specimens were monitored, starting immediately after curing, over periods up to five months. To maintain gage stability, the excitation voltage on the gage was maintained constant throughout the period of monitoring.

The average longitudinal and transverse strain variation for the three specimens is shown in Fig. 1. The variations are very small as expected. Stress relaxation in a given ply in the transverse-to-the-fiber direction is not accompanied by an appreciable strain change, since such a deformation is restrained by the other plies of the laminate. The small strain variations that might accompany stress relaxation are a second order effect and not a sensitive measure of this relaxation.

Stress Relaxation in 90-Degree Unidirectional Laminates

Stress relaxation in composites is a matrix controlled property and as such it is most pronounced in the transverse-to-the-fiber direction. An upper limit to the amount of residual stress relaxation occurring in a given ply of a laminate can be obtained by evaluating the relaxation characteristics of a 90-degree unidirectional laminate under tension. The specimens

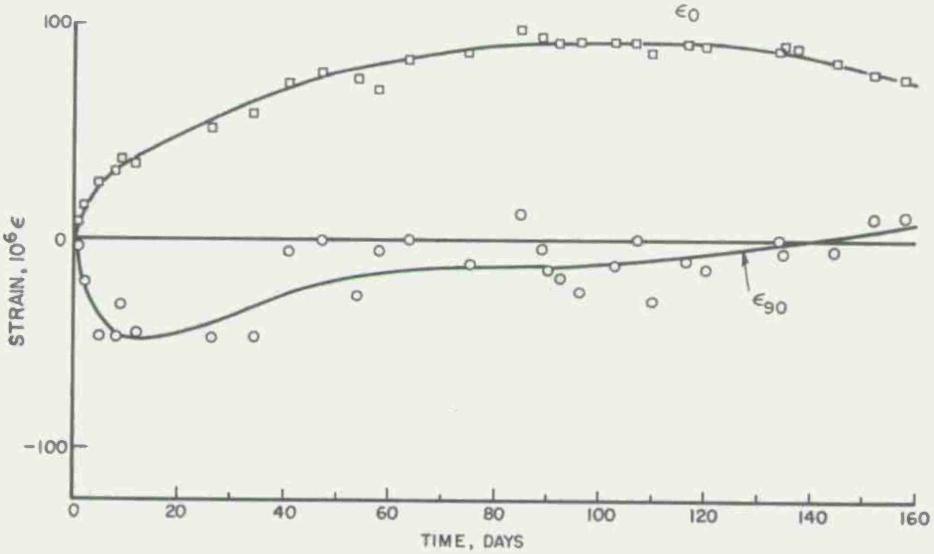

Fig. 1 Strain Variation in $[0_2/\pm 45]_s$ S-Glass/Epoxy Specimens as a Function of Time After Curing (Strain Gages Embedded Between Fourth and Fifth Ply)

were 2.54 cm x 22.9 cm (1 in. x 9 in.) $[90_8]$ coupons. They were loaded in the fixture of Fig. 2 by applying a certain fixed elongation in a short time. The applied strain corresponded to approximately 70 percent of the static strength of the specimen. The change in load (stress) with time was monitored with a semiconductor load cell and also with an aluminum link in series instrumented with strain gages. The strain in the specimen, which is supposed to remain constant throughout the test, was checked before every load reading. Two axial strain gages bonded on the two sides of the specimen at the center were used for the purpose. Small changes in the specimen strain were noticed due to the changing load and the finite compliance of the load cells. These small strain deviations were taken into account in computing the amount of stress relaxation.

The boron/epoxy specimen was loaded with a strain of 2,260 x 10^{-6} corresponding to a stress of 33.8 MPa (4,900 psi). The load variation with time is plotted on a semilogarithmic scale in Fig. 3. Most of the relaxation takes place in the first 24 hours and the load (stress) levels off after that time. The maximum amount of relaxation observed was approximately 20 percent.

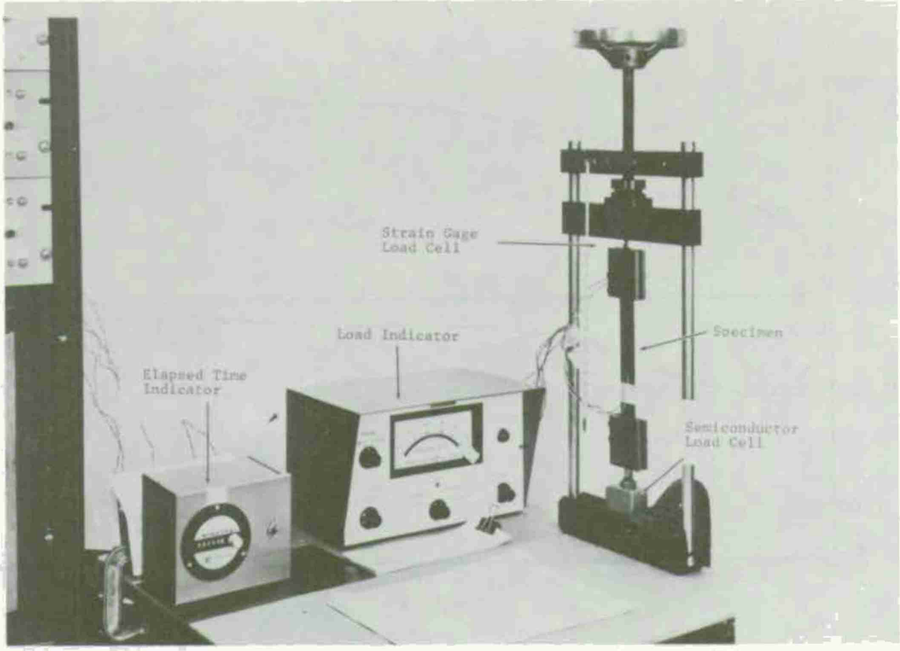
Strain Gage Load Cell
Load Indicator
Elapsed Time Indicator
Specimen
Semiconductor Load Cell

Fig. 2 Experimental Setup for Measuring Stress Relaxation in Composite Specimens

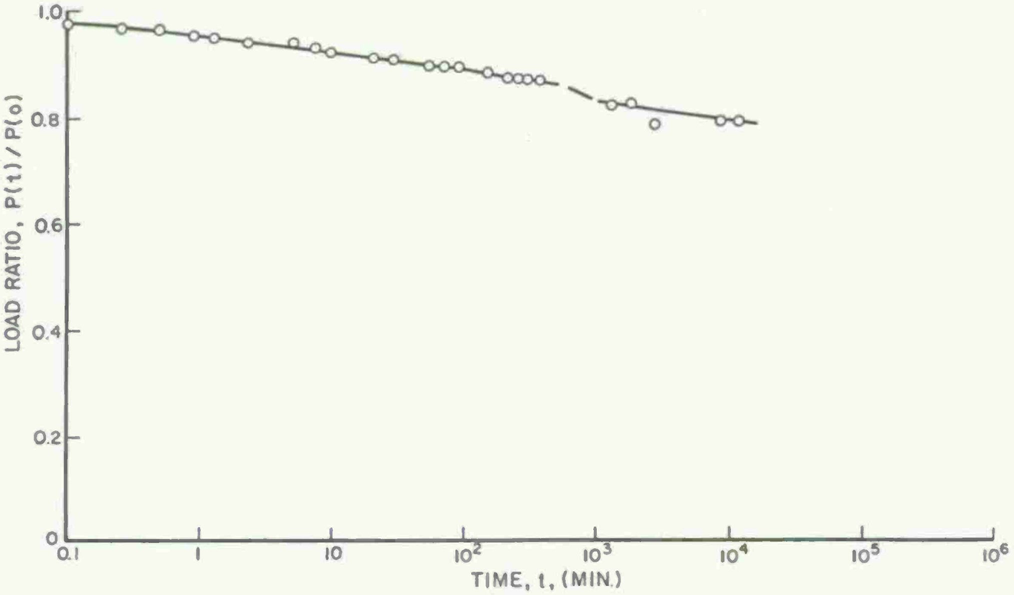

Fig. 3 Stress Relaxation in 90-Degree Unidirectional Boron/Epoxy Specimen

The boron/polyimide specimen was loaded with a strain of 800×10^{-6} producing a near instantaneous stress of 6.9 MPa (1000 psi). The load variation with time is plotted on a semilogarithmic scale in Fig. 4. Two mechanisms of load relaxation are evident. One, predominant up to approximately 500 minutes, must correspond to stress relaxation in the matrix. The other mechanism related to a sharp decrease in load comes into effect after 1000 minutes and is probably related to some failure or degradation taking place in the specimen under load.

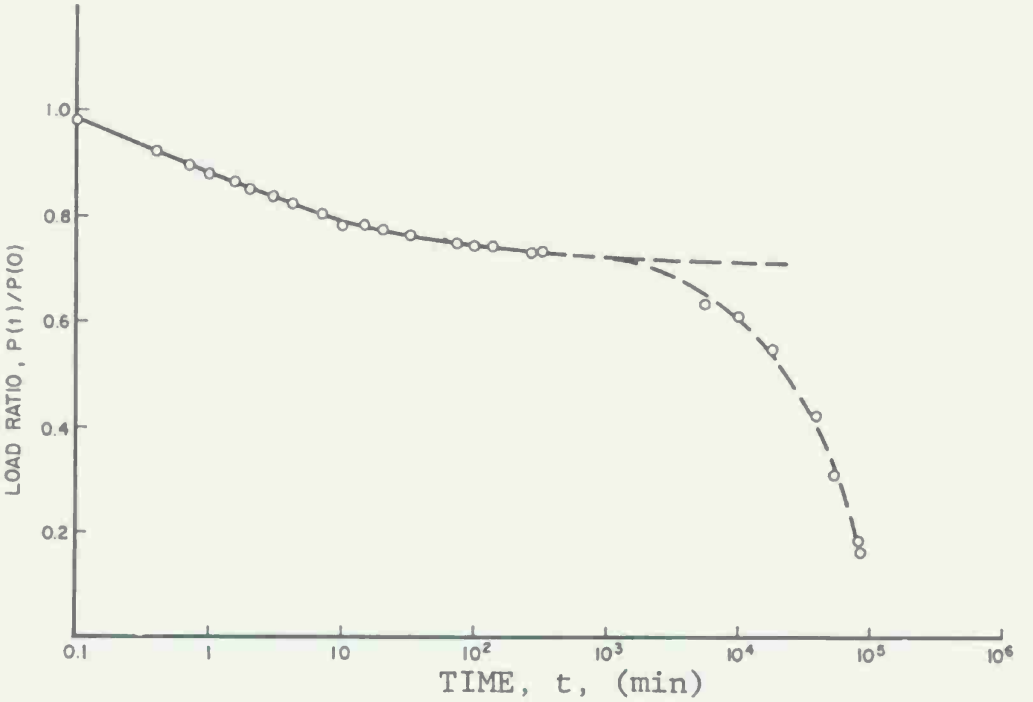

Fig. 4 Stress Relaxation in 90-Degree Unidirectional Boron/Polyimide Specimen

The relaxation test for graphite/low modulus epoxy was not successful because of the high fragility of the 90-degree material.

The graphite/high modulus epoxy specimen was loaded with a strain of $4,476 \times 10^{-6}$ producing a near instantaneous stress of 31.4 MPa (4,545 psi). The load variation with time is plotted in Fig. 5. Stress relaxation was continuing after 25 days of loading.

The graphite/polyimide specimen was loaded with a strain of $2,080 \times 10^{-6}$ producing a near instantaneous stress of 10.5 MPa (1,520 psi), approximately 71 percent of the ultimate stress. The load variation with time is plotted in Fig. 6. The load

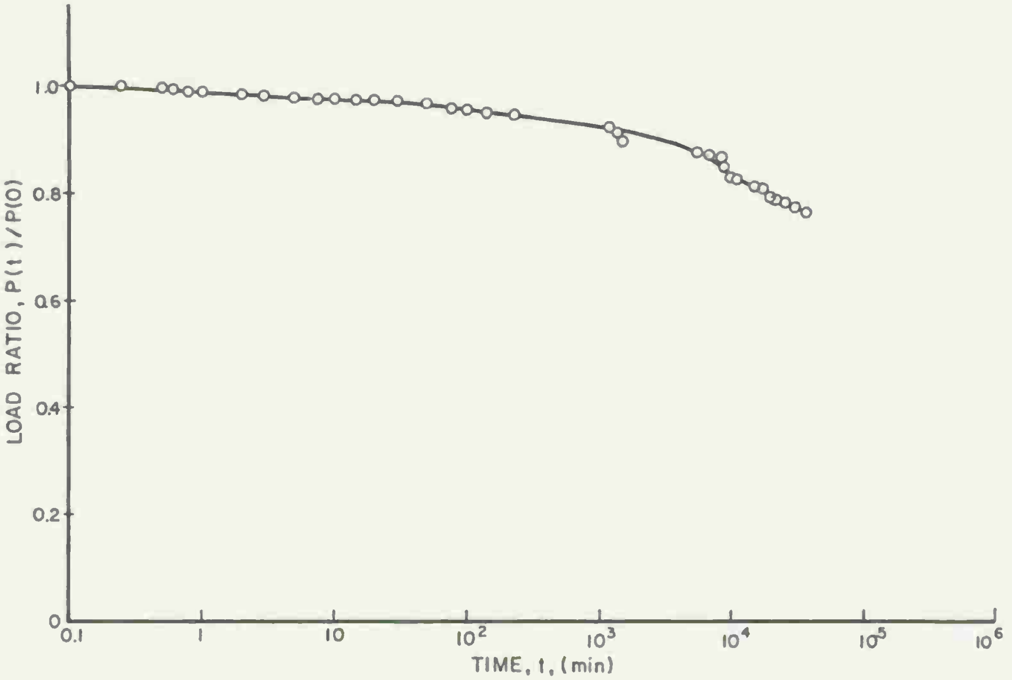

Fig. 5 Stress Relaxation in 90-Degree Unidirectional Graphite/High Modulus Epoxy Specimen

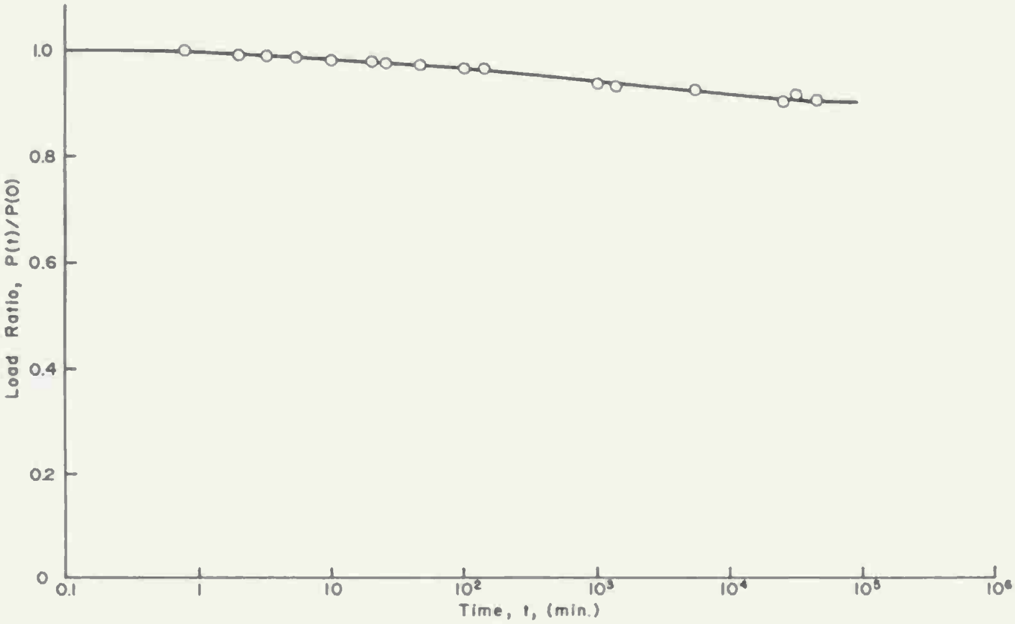

Fig. 6 Stress Relaxation in 90-Degree Unidirectional Graphite/Polyimide Specimen

seems to stabilize at 90 percent of its initial value after approximately 35 days.

The S-glass/epoxy specimen was loaded with a strain of 1,560 x 10^{-6} producing a near instantaneous stress of 39.7 MPa (5750 psi). The load variation with time is plotted in Fig. 7. The load (stress) seems to level off at 86 percent of its initial value after 25 days.

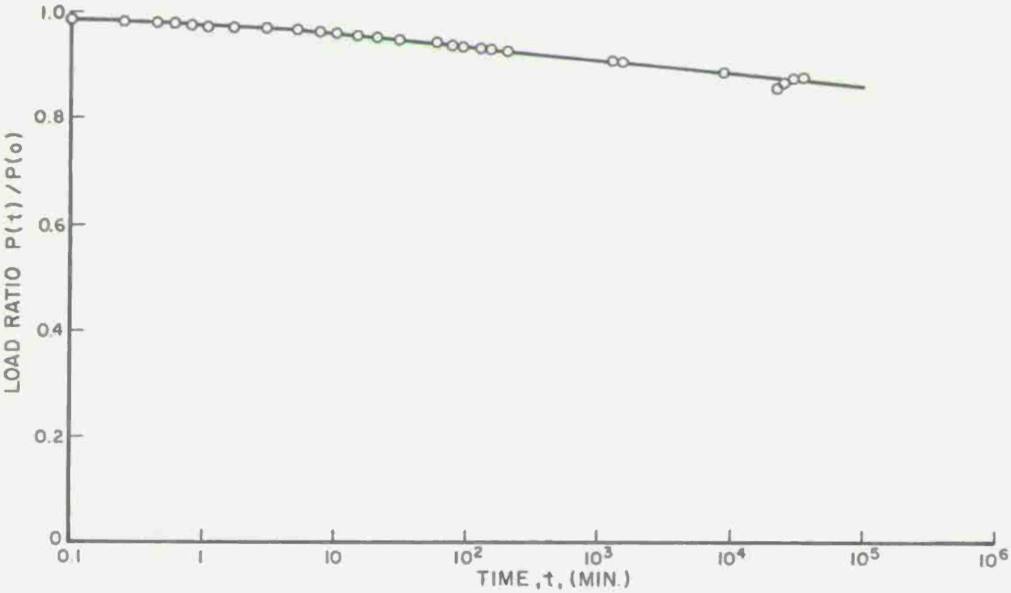

Fig. 7 Stress Relaxation in 90-Degree Unidirectional S-Glass/Epoxy Specimen

The following Table 1 summarizes the results of the relaxation tests described above.

Table 1

Tensile Stress Relaxation in 90-Degree Unidirectional Specimens

Material	Applied Stress, σ_{22} MPa (psi)	Percent Relaxation In 30 Days
Boron/Epoxy	33.8 (4,900)	22.5
Boron/Polyimide	6.9 (1,000)	62.0
Graphite/High Modulus Epoxy	31.4 (4,545)	24.5
Graphite/Polyimide	10.5 (1,520)	9.5
S-Glass/Epoxy	39.7 (5,750)	13.0

The graphite/polyimide displays the lowest stress relaxation, and the boron/polyimide the highest, although both have the same matrix. It is conjectured, however, that the apparent relaxation in the latter is related to microfailure rather than to purely viscoelastic properties of the matrix. Further testing at different stress levels would explain the phenomenon. Of the epoxy matrix composites, the S-glass/epoxy displayed the lowest amount of relaxation. This is probably due to the much higher fiber volume ratio of this material (FVR = 0.72).

The results above serve only as indications of an upper limit of residual stress relaxation that may occur in an angle-ply laminate. The actual conditions in the laminate are more complicated as each ply is subjected to an in-plane biaxial state of stress including shear stresses transmitted from adjacent plies.

Static Properties of $[0_2/\pm 45]_s$ Laminates as a Function of Time After Curing

An indirect evaluation of residual-stress relaxation was made by measuring the stiffness and strength properties of $[0_2/\pm 45]_s$ angle-ply laminates at various times after curing. The underlying reasoning was that residual stresses have an influence on the strength of the laminate and that appreciable relaxation of these stresses would affect the laminate strength noticeably. Two specimens of each material system were tested statically to failure at various times after curing over periods up to 22 months. Stress-strain curves were obtained for each test and the axial modulus, Poisson's ratio and strength were computed.

Figures 8 and 9 show typical stress-strain curves for boron/epoxy specimens tested one and twelve and one-half months after curing, respectively. Figures 10 and 11 show typical stress-strain curves for graphite/polyimide specimens tested one and seventeen months after curing. Similar curves for S-glass/epoxy specimens corresponding to three and twenty-two months after curing are shown in Figures 12 and 13. Figure 12 shows acoustic emission data in addition to strain.

Results of the tests above are summarized in Table 2 where the modulus, Poisson's ratio, strength and age of the specimens are given. In most cases where two or more specimens of any given age were tested the average values are shown. The modulus values do not show any significant variations with time. The fluctuations in strength with time for boron/epoxy, boron/polyimide and graphite/high modulus epoxy are small and certainly not significant. In the case of graphite/low modulus epoxy and graphite/polyimide the apparent reduction in strength after three

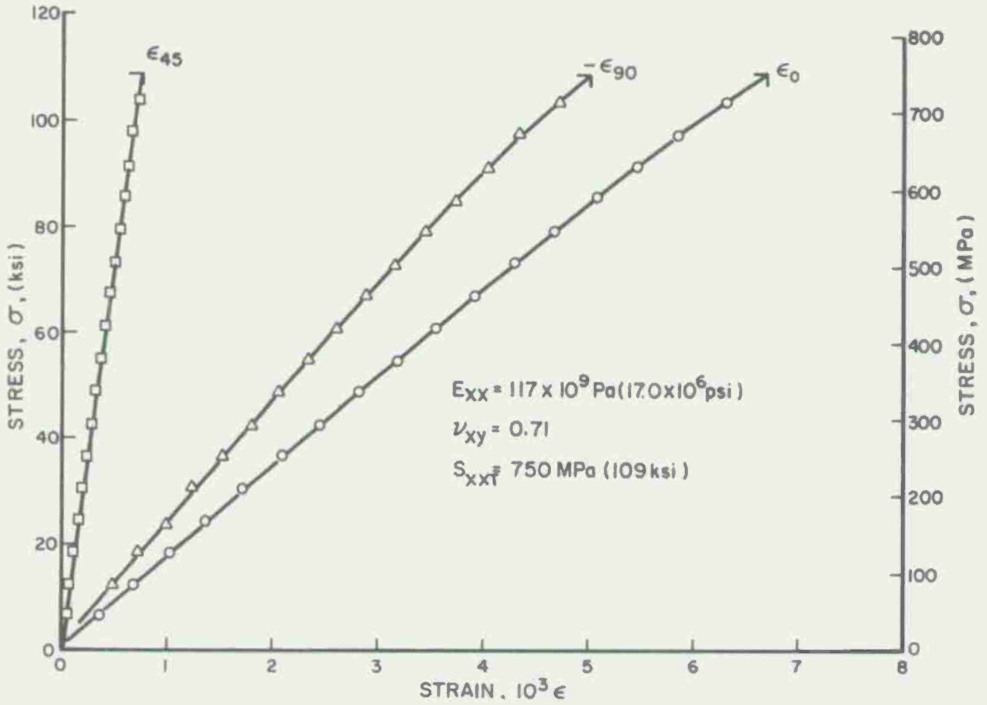

Fig. 8 Strains in $[0_2/\pm45]_s$ Boron/Epoxy Specimen Under Uniaxial Tensile Loading One Month After Curing

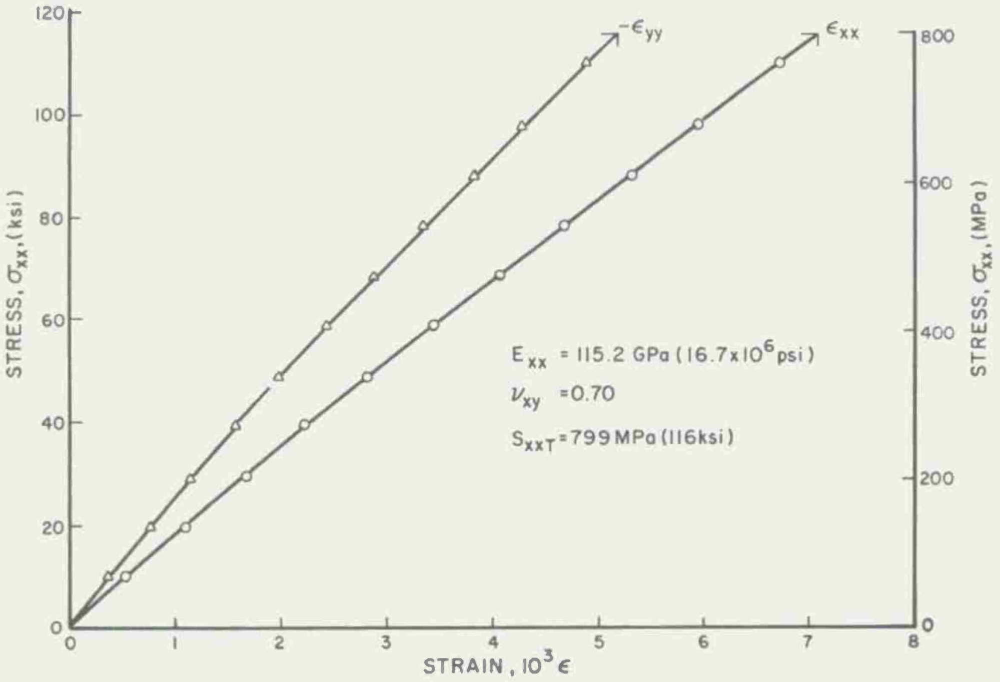

Fig. 9 Strains in $[0_2/\pm45]_s$ Boron/Epoxy Specimen Under Uniaxial Tensile Loading Twelve and One-Half Months After Curing

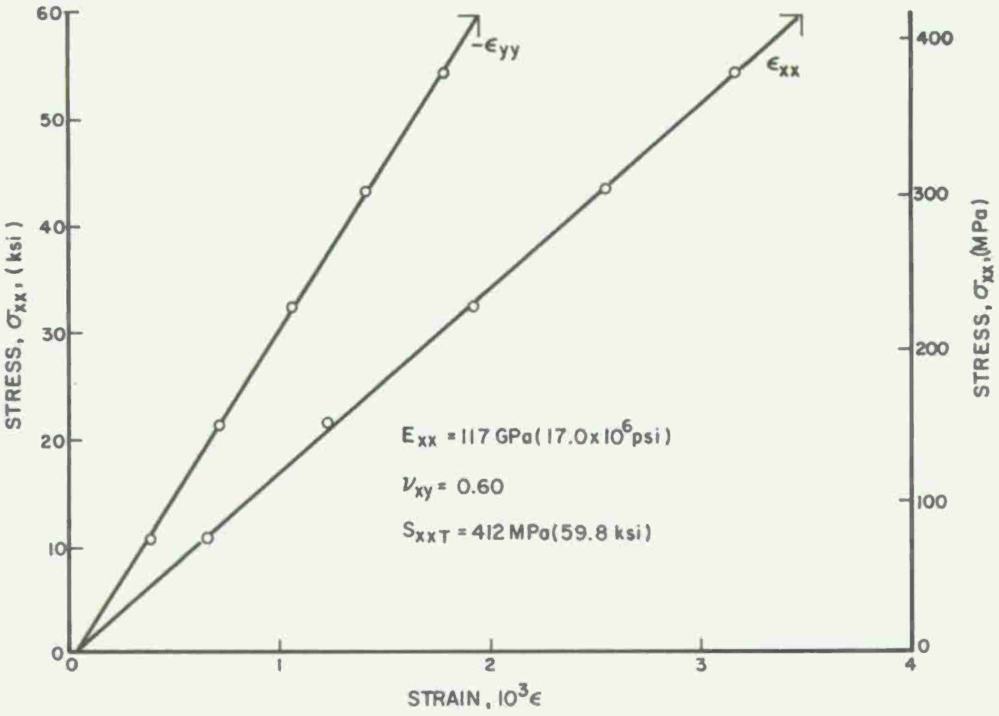

Fig. 10 Strains in $[0_2/\pm45]_s$ Graphite/Polyimide Specimen Under Uniaxial Tensile Loading One Month After Curing

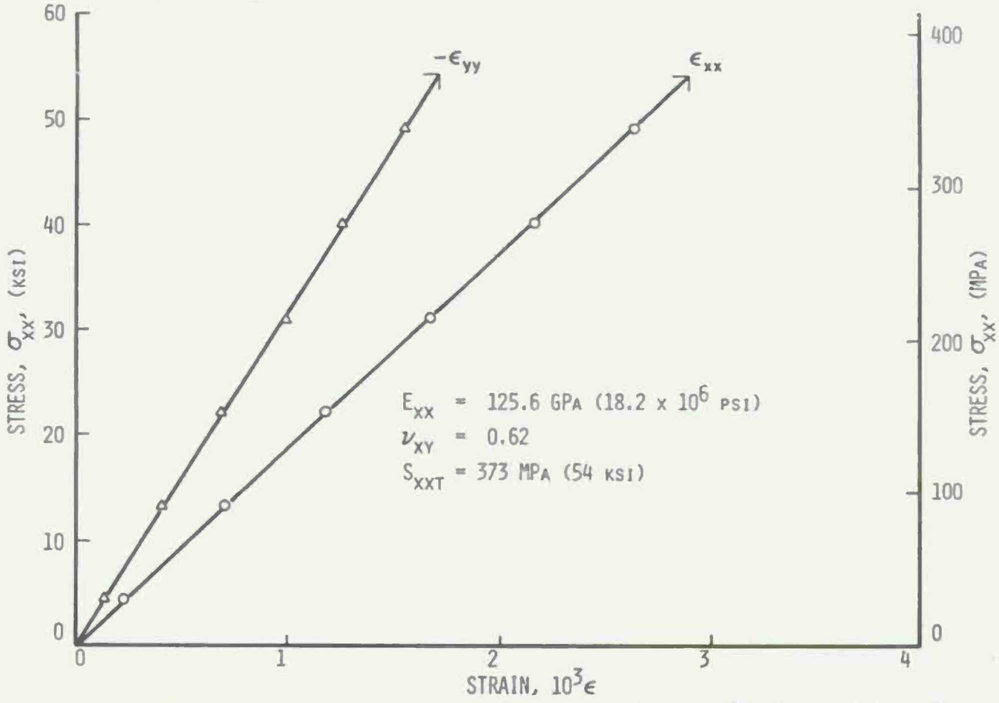

Fig. 11 Strains in $[0_2/\pm45]_s$ Graphite/Polyimide Specimen Under Uniaxial Tensile Loading Seventeen Months After Curing

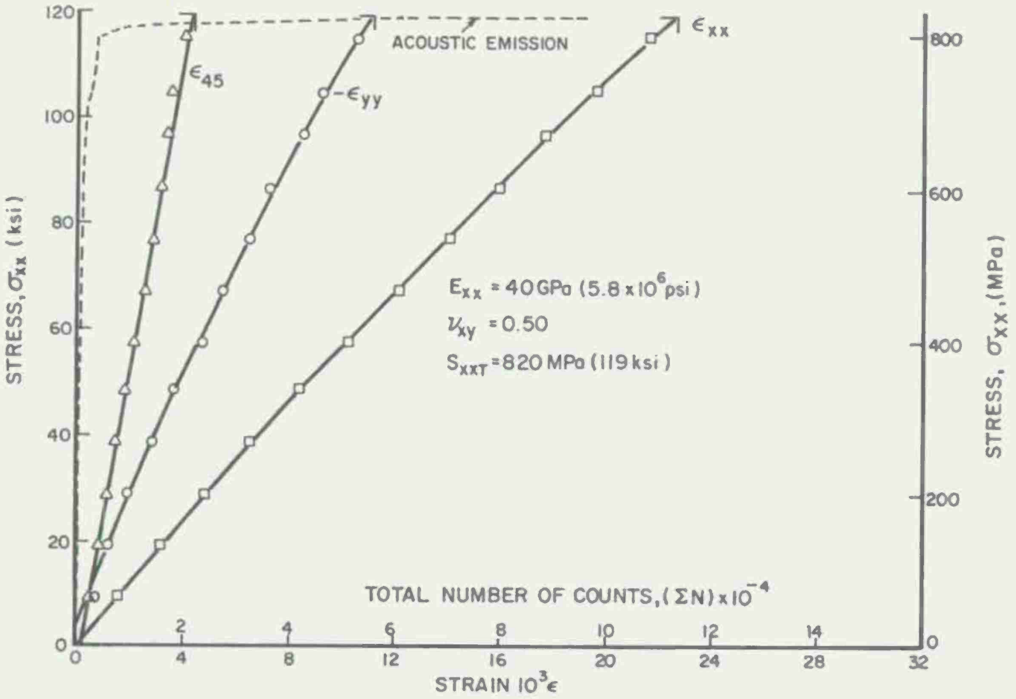

Fig. 12 Strains and Acoustic Emission in $[0_2/\pm45]_s$ S-Glass/Epoxy Specimen Loaded Uniaxially Three Months After Curing

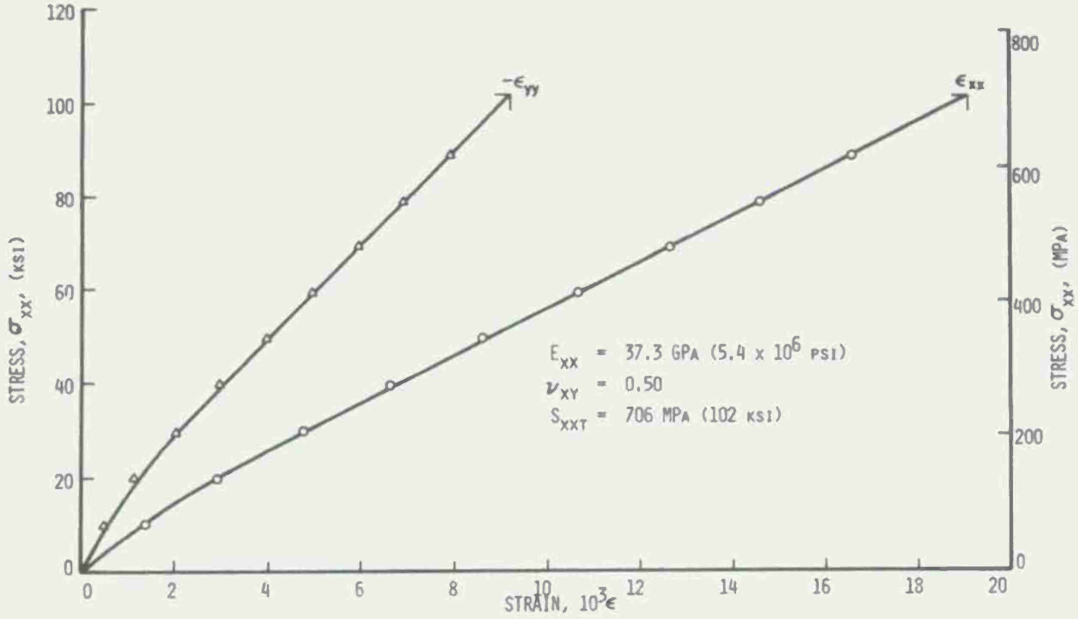

Fig. 13 Strains in $[0_2/\pm45]_s$ S-Glass/Epoxy Specimen Under Uniaxial Tensile Loading Twenty-Two Months After Curing

Table 2

Static Properties of $[0_2/\pm45]_s$ Laminates At Various Times After Curing

Material	Modulus, E_{xx} GPa (10^6 psi)	Poisson's Ratio, ν_{xy}	Strength S_{xxT} MPa (ksi)	Age (Months)
Boron/Epoxy	115 (16.7)	0.70	725 (105)	1-3
	115 (16.7)	0.60	754 (109)	9
	116 (16.8)	0.71	725 (105)	12.5
Boron/Polyimide	117 (17.0)	0.72	562 (82)	1
	114 (16.5)	0.76	522 (76)	4.5
	112 (16.3)	0.77	519 (75)	8
	126 (18.2)	0.69	578 (84)	17
Graphite/Low Modulus Epoxy	111 (16.1)	0.72	562 (82)	1
	110 (15.9)	0.71	350 (51)	3
	105 (15.3)	0.52	350 (51)	6.5
	115 (16.7)	0.80	350 (51)	16
Graphite/High Modulus Epoxy	99 (14.3)	0.72	485 (70)	1-2
	94 (13.6)	0.74	515 (75)	6
	107 (15.6)	0.69	510 (74)	9.5
	112 (16.2)	0.72	497 (72)	19
Graphite/ Polyimide	114 (16.5)	0.71	345 (50)	1
	121 (17.6)	0.67	314 (46)	4
	107 (15.6)	0.72	290 (42)	8
	115 (16.7)	0.65	317 (46)	17
S-Glass/Epoxy	37 (5.3)	0.52	742 (108)	1
	40 (5.8)	0.50	820 (119)	3
	44 (6.4)	0.43	789 (114)	6
	37 (5.3)	0.55	618 (90)	9
	36 (5.2)	0.53	649 (94)	12.5
	37 (5.3)	0.52	696 (101)	22

or four months may be related to the fact that initial values for the strength were obtained from 2.54 cm (1 in.) wide specimens, whereas all subsequent tests were performed with 1.27 cm (0.5 in.) wide specimens. In the case of S-glass/epoxy the apparent variations in strength are due to the fact that two batches of material are represented. The individually prepared 2.54 cm (1 in.) wide coupons with embedded strain gages showed consistently high strength values, 807 MPa (117 ksi), 820 MPa(119 ksi), and 789 MPa (114 ksi) initially, three months and six months after curing, respectively. The strength values at nine, twelve and one-half and twenty-two months obtained from specimens cut from a plate are in closer agreement with the initial value of 675 MPa (98 ksi) obtained from a similar specimen.

SUMMARY AND CONCLUSIONS

Three approaches were investigated for evaluation of residual stress relaxation in angle-ply laminates: (1) Direct measurement of strain changes with time, (2) Stress relaxation determination in 90-degree unidirectional specimens, and (3) Elastic and strength properties of $[0_2/\pm 45]_s$ laminates as a function of time after curing.

Measurement of strain variation is a very insensitive means. Strain variations are very small, sometimes of the order of experimental variability, as they represent a second order effect of stress relaxation.

An upper limit to the amount of residual stress relaxation was obtained by means of direct relaxation tests of 90-degree unidirectional laminates. The amount of relaxation in thirty days in most cases ranged between 9.5 and 24.5 percent, except for the boron/polyimide where a fracture mechanism was possibly operating. This amount of relaxation represents an upper bound to the actual stress relaxation taking place in an angle-ply laminate.

Residual stress relaxation was evaluated indirectly by monitoring the elastic modulus and strength of $[0_2/\pm 45]_s$ specimens over periods up to twenty-two months. No significant variations with time were observed. It can be concluded from the above that the amount of residual stress relaxation in angle-ply laminates is small. In cases when residual stresses are critical means for reducing them must be introduced during the curing process. One such method would be pretensioning all the plies in the fiber direction by an amount equal to the transverse thermal contraction during curing.

ACKNOWLEDGEMENTS

The work described here was sponsored by the NASA-Lewis Research Center, Cleveland, Ohio under Contract No. NAS3-16766. The authors are grateful to Dr. C.C. Chamis of NASA-Lewis for his encouragement and cooperation and to Messrs. M. Iyengar and T. Niiro of the IIT Research Institute for their assistance.

REFERENCES

1. Chamis, C.C., "Design and Analysis of Fiber Composite Structural Components," NASA Report SP227, 1970, pp. 217-228.

2. Chamis, C.C., "Lamination Residual Stresses in Cross-Plied Fiber Composites," Proc. of 26th Annual Conference of SPI, Reinforced Plastics/Composites Division, Paper No. 17-D, Feb. 1971.

3. Daniel, I.M., Liber, T. and Chamis, C.C., "Measurement of Residual Strains in Boron/Epoxy and Glass/Epoxy Laminates," Composite Reliability, ASTM STP 580, American Society for Testing and Materials, 1975, pp. 340-351.

4. Chamis, C.C., and Sullivan, T.L., "A Computational Procedure to Analyze Metal Matrix Laminates with Nonlinear Lamination Residual Strains," Composite Reliability ASTM STP 580, American Society for Testing and Materials, 1975, pp. 327-339.

5. Daniel, I.M., and Liber, T., "Lamination Residual Stresses in Fiber Composites," IITRI Report D6073-I, for NASA-Lewis Research Center, NASA CR-134826, March 1975.

6. Hahn, H.T., and Pagano, N.J., "Curing Stresses in Composite Laminates," J. Composite Materials, Vol. 9, 1975, pp. 91-106.

ON THE THREE-DIMENSIONALITY OF FAILURE MODES IN ANGLE-PLY STRIPS UNDER TENSION

D. W. OPLINGER
Physicist

B. S. PARKER
Mechanical Engineer

A. GRENIS
Physicist

Army Materials and Mechanics Research Center
Watertown, Massachusetts

ABSTRACT

This paper discusses experimental studies of the failure of angle ply laminates consisting of "C" (clustered) $[(+\theta)_4/-\theta)_4]_s$ and "A" (alternating) $(+\theta/-\theta)_4$ configurations, in boron epoxy and graphite epoxy, with θ ranging from 0° to 45°. Comparison of ultimate tensile strength values for the two types of laminates demonstrated the effectiveness of the A configuration in reducing interlaminar shear stresses and thereby enhancing the tensile strength of the laminate. In addition, a number of techniques were used to obtain information on the condition for onset of delamination and the subsequent progression of damage to failure. These included acoustic emission, dye penetrant and high speed cinematography which was enhanced by the presence of a moiré grid to allow the rapid growth of surface cracks to be observed. Results confirmed that the earliest mode of damage is a combination of delamination and fiber separation within plies. The high speed photographs suggested that fiber separation modes progress in distinct steps which are semi-stable for short periods of time. Finally, a mechanism is hypothesized to explain the conditions leading to onset of fiber breakage, a characteristic damage mode in the later stages of failure at orientations of 30° or less. Subsequent experimental and analytical studies which are appropriate for investigating various aspects of the proposed failure process will be described.

INTRODUCTION

The role of non-planar stress states near free edges of fiber-reinforced laminates in the initiation and propagation of failure has been the subject of attention for a number of years as it has become more and more clear that such stresses play a vital role in controlling the strength of composites. The effect of stacking sequence and material parameters have been studied analytically by a number of authors [1–4]. Experimental efforts by Pipes and Daniel [5] and by Oplinger, et al [6] based on the application of moiré techniques confirmed the essential features of the strain field near free edges in $(+\theta/-\theta)$ angle ply laminates; in particular these results demonstrated that for orientation angles, θ, from about 10° to 45°, interlaminar shear strains occur which may be of sufficient magnitude to cause delamination prior to any other mode of damage. The analysis of failure data by Oplinger et al [6] tended to confirm the expected results that ultimate failure of the laminate is determined by the stress state at the free edge where interlaminar shear stresses are present rather than in the interior where the interlaminar shear stress disappears and in-plane shear stresses come into play.

The objective of the present study was to examine in detail the processes which occur in the course of failure associated with $(+\theta/-\theta)$ laminates for ranges of orientations for which interlaminar shear stresses are likely to cause failure initiation. Earlier work of this type was conducted by Lauraitis [7] who used dye penetrants to examine delamination in glass-epoxy angle-ply laminates subjected to sub-ultimate loads. Other studies which concentrated on details of the failure process included that of Pagano and Pipes [8] who investigated $(\pm 25/90_n)$ laminate configurations tending to produce delamination by interlaminar normal rather than shear stressing, and that of Whitney and Browning [9] who investigated the fatigue performance of such laminates. Most recently, Reifsnider et al [10] discussed delamination processes in quasi-isotropic graphite epoxy laminates.

In the present case we are interested in laminates of the type investigated by Lauraitis [7]. The latter interpreted the failure data in terms of a model which visualized an effective crack in the vicinity of the free edge prior to the onset of failure. Evidence in hand suggests that the initial part of the failure process should be interpreted in terms of high but finite interlaminar shear stresses rather than the infinite stresses that the effective crack model of [7] would imply, and we do not intend to pursue the latter approach. It is true that analytical results discussed in [3] have strongly suggested the rise of a nearly singular shear stress at the free edge at the interface between $+\theta$ and $-\theta$ layers in materials such as glass and graphite epoxy containing finely dispersed fibers. However, the success of the stress averaging approach of Nuismer and Whitney [11] in accounting for failure of laminates containing center notches of small tip radius suggests the presence of significant stress-redistributing ability in typical composite materials and leads one to look for a strength criterion for delamination initiation rather than a criterion based on infinite stresses such as the stress intensity approach of linear elastic fracture mechanics.

The effort to be discussed centered around two types of stacking sequence, consisting of eight-layer $(+\theta/-\theta)_4$ configurations (referred to as A or alternating) in which the most complete mixing possible of the $+\theta$ and $-\theta$ layers was incorporated; together with sixteen-layer $[(+\theta)_4/(-\theta)_4]_s$ configurations (referred to as C or clustered) in which $+\theta$ and $-\theta$ plies were grouped together as much as possible consistent with balancing the laminate. The tendency of the A configuration to disperse interlaminar shear stresses as compared with the tendency of the C configuration to aggravate them was discussed in [3]. Early results of the study reported partly in [6] centered on a comparison of laminate strengths obtained with the two configurations and demonstrated the anticipated strength superiority of the A configuration under tensile loading. Further data of this type will be discussed.

The remainder of the study was devoted to examination of the onset and growth of delamination in the C configuration and the relation of delamination to an alternate mode of failure involving fiber breakage. This part of the effort involved the use of acoustic emission instrumentation to detect the onset of delamination so as to permit load removal prior to ultimate failure. Subsequently, dye penetrants were used to visualize delamination cracks; emphasis was given here on ascertaining whether the initial damage took the form of fiber separation within plies or ply separation, both of which are candidate modes for failure initiation. Finally, results were obtained on one configuration using high-speed cinematography (5000 fps) in conjunction with moiré surface strain measurements to trace the progression of fiber separation cracks.

EXPERIMENTAL STUDIES

DESCRIPTION OF LAMINATES

Table 1 gives a description of the materials which were investigated. In addition to AVCO boron epoxy, two types of graphite epoxy, MOD II/5206 (Whittaker) and Thornel 300/E797 (U.S. Polymer), were incorporated. In addition to the unidirectional configuration, MOD II/5206 specimens were fabricated in the A and C configurations with $\theta = 10^\circ, 30^\circ$, and 45°, while the

TABLE I. LAMINATE CONFIGURATIONS FOR EXPERIMENTAL STUDIES

A Configuration		C Configuration	
$+\theta$	8 Plies	$[+\theta]_4$	16 Plies
$-\theta$		$[-\theta]_8$	
$+\theta$		$[+\theta]_4$	
$-\theta$			

	MODMOR II/5206			THORNEL 300/ E797		BORON/5505		
	Unidirectional (8 layers)	A	C	A	C	Unidirectional (8 layers)	A	C
0°	X	–	–	–	–	X	–	–
±10°	–	X	X	–	–	–	X	X
±20°	–	–	–	–	–	–	X	X
±30°	–	X	X	X	X	–	–	–
±45°	–	X	X	X	X	–	X	X

boron/5505 was fabricated with $\theta = 10°, 20°$, and $45°$. The T300/E797 laminates were fabricated with $\theta = 30°$ and $45°$. Experimental studies were conducted on the specimen configuration shown in Figure 1 which depicts standard 1" wide tensile bars with bonded glass epoxy tabs.

FAILURE TESTS

a. Angle Ply Laminate Stress Conditions

The behavior of angle ply laminates under uniaxial tensile loading is characterized by: (1) development of interlaminar shear stresses near free edges, tending to introduce delamination modes of initial damage; (2) the rise of in-plane shear stresses in the interior of the specimen which are required to provide for strain compatibility between adjacent plies. The failure of the laminate can be expected to be influenced by these effects in addition to that of the applied tensile stresses.

Figure 2 depicts the stress state in the interior of the laminate (away from free edges) in a given ply. For balanced laminates all stresses other than σ_x, τ_{xy} and the interlaminar shear stress τ_{xz} are close to zero and may be ignored. Analytical results [1–4] have shown that away from loaded ends, while the axial strain ϵ_x is uniform with respect to all three coordinates, the axial stress σ_x as well as the in-plane shear stress τ_{xy} varies across the width of the specimen. Note that while τ_{xy} is present in the interior it must be zero at the lateral edges to satisfy traction-free boundary conditions. In general, the following constitutive equations involving σ_x and τ_{xy} are satisfied:

$$\begin{aligned} \epsilon_x &= a_{11}\,\sigma_x + a_{16}\,\tau_{xy} \\ \gamma_{xy} &= a_{16}\,\sigma_x + a_{66}\,\tau_{xy} \end{aligned} \tag{1}$$

where the a_{ij}'s are compliance coefficients for the individual plies, and by the usual transformation rules are expressed in terms of the elastic constants of unidirectional plies as follows:

$$\begin{aligned} a_{11} &= \frac{1}{E_L}\,[c^4 + (\rho_G - 2\nu_{LT})\,c^2 s^2 + \rho_E s^4] \\ a_{16} &= \frac{1}{E_L}\,[2(\rho_E\, s^2 - c^2) + (\rho_G - 2\nu_{LT})\,(c^2 - s^2)]\ cs \\ a_{66} &= \frac{1}{E_L}\,[4(1 + \rho_E + 2\nu_{LT} - \rho_G)\,c^2 s^2 + \rho_G] \end{aligned} \tag{2}$$

where

$$\rho_E = \frac{E_L}{E_T};\ \rho_G = \frac{E_L}{G_{LT}}\ ;\ \nu_{LT} = \text{Poisson's ratio};$$

$$c = \cos\theta;\ \ s = \sin\theta$$

Note that the following conditions on the stresses and strains appearing in Equations (1) hold:

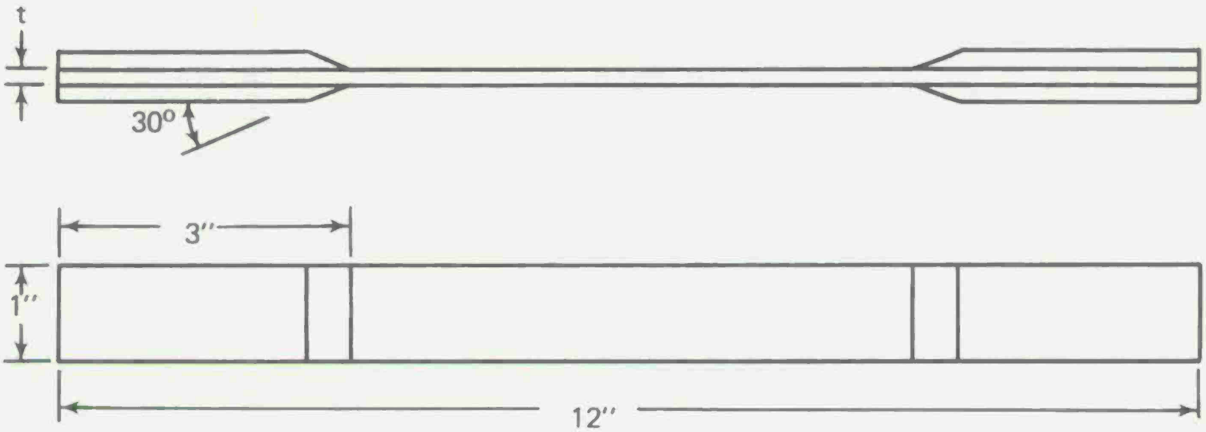

Material	Configuration	Dimension "t"
Boron/5505	UNI, A	0.040-0.043
	C	0.080-0.081
MOD II/5206	UNI, A	0.055-0.059
	C	0.105-0.108
T300/E797	A	0.048-0.050
	C	0.089-0.094

Figure 1. Test Specimen Details

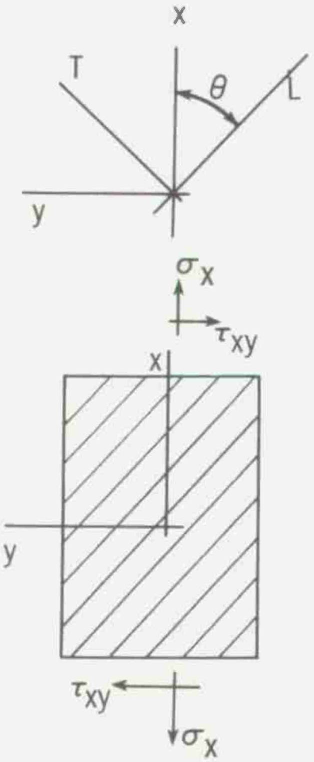
x
T
θ
L
y
σ_x
τ_{xy}
x
y
τ_{xy}
σ_x

Figure 2. Stress State in Interior of Angle Ply Laminate

$$\underline{\text{Free Edge}}\ (y = \pm b) \quad \tau_{xy} = 0; \tag{3.1}$$

$$\epsilon_x = a_{11}\sigma_x \tag{3.2}$$

$$\underline{\text{Interior Region}} \quad \gamma_{xy} = 0; \tag{4.1}$$

$$\tau_{xy} = -\frac{a_{16}}{a_{66}}\sigma_x \tag{4.2}$$

$$\epsilon_x = a_{11}\left(1 - \frac{a_{16}^2}{a_{11}a_{66}}\right)\sigma_x \tag{4.3}$$

By comparing Equations (3.2) and (4.3) and noting the assertion given earlier that ϵ_x is uniform throughout the region of interest the following relations show the comparison of axial stress at the free edge and in the interior:

$$\bar{\sigma}_x \equiv \sigma_x\,(\text{interior}) = \frac{\epsilon_x}{a_{11}} / \left(1 - \frac{a_{16}^2}{a_{11}a_{66}}\right) \tag{5}$$

$$\sigma_x\,(\text{free edge}) = \bar{\sigma}_x\left(1 - \frac{a_{16}^2}{a_{11}a_{66}}\right)$$

In addition the shear stress is related to $\bar{\sigma}_x \equiv \sigma_x$ (interior) by (Equation (4.2))

$$\left.\tau_{xy}\right)_{int} = -\frac{a_{16}}{a_{66}}\bar{\sigma}_x \tag{6}$$

while

$$\tau_{xy}\,(\text{free edge}) \equiv \left.\tau_{xy}\right)_{fe} = 0$$

Ignoring for the moment the effect of interlaminar shear stress, the effect of τ_{xy} and σ_x on failure is best seen by resolving them in the L–T coordinate system shown in Figure 2. By the usual transformation laws we have, from Equations (5) and (6):

$$F_L \equiv \frac{\sigma_L}{\bar{\sigma}_x} = (1 - k\rho_{16})\ c^2 + 2\,cs\ \mu_{16}\ (1-k)$$

$$F_T \equiv \frac{\sigma_T}{\bar{\sigma}_x} = (1 - k\rho_{16})\ s^2 - 2\,cs\,\mu_{16}\ (1-k) \qquad (7)$$

$$F_{LT} \equiv \frac{\tau_{LT}}{\bar{\sigma}_x} = (1 - k\rho_{16})\ cs\ - (c^2 - s^2)\,\mu_{16}\ (1-k)$$

in which

$$\rho_{16} = \frac{a_{16}{}^2}{a_{11}a_{66}};\quad \mu_{16} = \frac{a_{16}}{a_{66}}$$

$$\begin{aligned} k &= 1\ \text{(free edge)} \\ &= 0\ \text{(interior)} \end{aligned} \qquad (8)$$

Inserting the expressions for σ_L, and σ_T and τ_{LT} given in Equations (7) into an appropriate failure rule gives a means of predicting the value of $\bar{\sigma}_x$ at which failure due to in-plane stresses alone will take place, as opposed to delamination failure at the free edge. For the present study we have used the modified quadratic expression due to Hoffman [12]:

$$\frac{\sigma_L^2\ (1 - \ell\frac{\sigma_T}{\sigma_L}) + (S_{Lc} - S_{Lt})\ \sigma_L}{S_{Lc}S_{Lt}} + \frac{\sigma_T^2 + (S_{Tc} - S_{Tt})\ \sigma_T}{S_{Tc}\,S_{Tt}} + \frac{\tau_{LT}^2}{T_{LT}^2} = 1 \qquad (9)$$

which has a potential advantage over quadratic expressions not containing linear terms, in allowing for a possible strengthening effect against shear failure when σ_T is compressive. The parameter ℓ in the interaction term $\sigma_L^2\ (1 - \ell\ \frac{\sigma_T}{\sigma_L})$ in the first term of Equation (9) is set to 1. More generally, Tsai and Wu [13] have recommended letting it be determined experimentally in accordance with their tensor failure rule but for convenience a value of unity has been retained here.

The parameters S_{Lt}, S_{Lc}, S_{Tt}, S_{Tc} and T_{LT} are measured ultimate strengths for simple loading of unidirectional plies in longitudinal tension (S_{Lt}), compression (S_{Lc}), transverse tension (S_{Tt}), compression (S_{Tc}), and in-plane shear (T_{LT}). Introducing Equations (7) into Equation (9) and letting

$$\sigma = \frac{\bar{\sigma}_x}{S_{Lt}}$$

Equation (9) becomes a quadratic in σ:

$$(C_{2L}\ F_L^2 + C_{2T}\,F_T^2 + C_{2LT}F_{LT}^2)\,\sigma^2 + (C_{1L}F_L + C_{1T}F_T)\sigma - 1 = 0 \qquad (10)$$

which is solved for σ by standard formula. In Equation (10) we have

$$C_{2L} = \frac{S_{LT}}{S_{Lc}}; \; C_{2T} = \frac{S_{Lt}^2}{S_{Tc}S_{Tt}} \quad ; \; C_{2LT} = \frac{S_{Lt}^2}{T_{Lt}^2} \tag{11}$$

$$C_{1L} = \frac{(S_{Lc}-S_{Lt})}{S_{Lc}} \quad ; \; C_{1T} = \frac{(S_{Tc} - S_{Tt})\, S_{Lt}}{S_{Tc}\; S_{Tt}}$$

When differences in F_L, F_T and F_{LT} indicated in Equation (7) when k is changed from its free edge value of unity to its value in the interior (zero) are allowed for, sizeable changes in the value of $\sigma = \overline{\sigma}_x/S_{Lt}$ predicted by Equation (10) are encountered. The curves in Figure 3 illustrate this. The predictions are made using the elastic constants and strength parameters listed in Tables II and III for MOD II/5206. The greater strength of the laminate against failure in the interior is found to be due to the terms containing μ_{16} in the second and third of Equations (7) when k is set to zero. These tend to reduce F_T and F_{LT} in absolute value sufficiently to cause the marked increase in strength seen in Figure 3 for θ less than 50°.

It may be hypothesized that the behavior of the laminate is not strictly determined by the low strength at the free edge which is indicated by the predictions shown in Figure 3. The transition from the stress state near the free edge to that at the interior takes place in a narrow boundary layer corresponding to the region in the curves shown in Figure 4 obtained from moiré measurements [6] where the axial displacement is varying. As shown in the analytical results given in Figure 5 [3], the boundary layer in the A configuration is only ¼ the thickness of that in the C configuration, and it is anticipated that in such cases for which the boundary layer is extremely small, failure will be controlled by the interior stress state rather than by the stresses at the free edges. This concept is somewhat analogous to the Nuismer-Whitney treatment of crack-like notches in composites [11] by the approach of stress averaging over a particular length. Such a stress averaging approach in the case of free edges would tend to show the free edge stress state to be less important than the interior stress state for laminates with small boundary layer thickness.

In addition to the effect of boundary layer thickness the analytical results of [3] have indicated that for a given applied stress $\overline{\sigma}_x$ the interlaminar shear stress is greater in the boron epoxy C configuration by a factor of about 2 over that of the A configuration. In the case of graphite epoxy the C configuration again experiences higher interlaminar shear stresses than the A configuration although the ratio is less because of effects related to the yarn-type structure of the reinforcement.

Because of the combination of smaller boundary layer thickness and lower interlaminar shear stress, it was anticipated that A configuration laminates would tend to exhibit the higher strengths which could be expected to be characteristic of the interior region of the laminate. The failure tests to be discussed next were conducted to determine the extent to which the expected strength enhancement associated with the A configuration is realized in practice.

b. Test Results

Table II gives the strength values which were obtained from unidirectional A-configuration and C-configuration laminates. The elastic constants of the unidirectional plies are given in Table III. As noted in that table, the shear moduli were determined by a fit of measured axial moduli of A and

TABLE II. TENSILE STRENGTH MEASUREMENTS OF ANGLE PLY LAMINATES

Values in 10^3 psi (K bars; 1 bar = 100 KN/m^2 = 14.505 psi)

UNIDIRECTIONAL STRENGTHS (8 PLY LAMINATES)

	Ave.	Coef. Var.	No. of Specimens
Boron/5505	240.2(1655)	4.1%	4
MODII/5206	175.3(1208)	10.9%	5

ORIENTATION, deg.	A CONFIGURATION			C CONFIGURATION		
BORON/5505	Ave.	Coef. Var.	No. of Specimens	Ave.	Coef. Var.	No. of Specimens
±10°	172.6 (11.89)	9.7%	8	129.7 (8.94)	4.5%	3
±20°	121.8 (8.39)	6.4%	8	72.56 (5.00)	3.4%	3
±45°	21.0 (1.48)	2.8%	8	16.85 (1.16)	9.4%	7
MOD II/5206						
±10°	106.8 (7.36)	18.4%	8	79.6 (5.48)	4.0%	3
±30°	57.2 (3.94)	9.4%	7	27.4 (1.88)	10.4%	6
±45°	20.7 (1.43)	2.9%	3	11.7 (0.80)	2.5%	5
T300/E797						
±30°	71.6 (4.93)	5.0%	6	40.5 (2.79)	9.4%	5
±45°	25.2 (1.73)	2.0%	6	13.8 (0.95)	10.1%	4

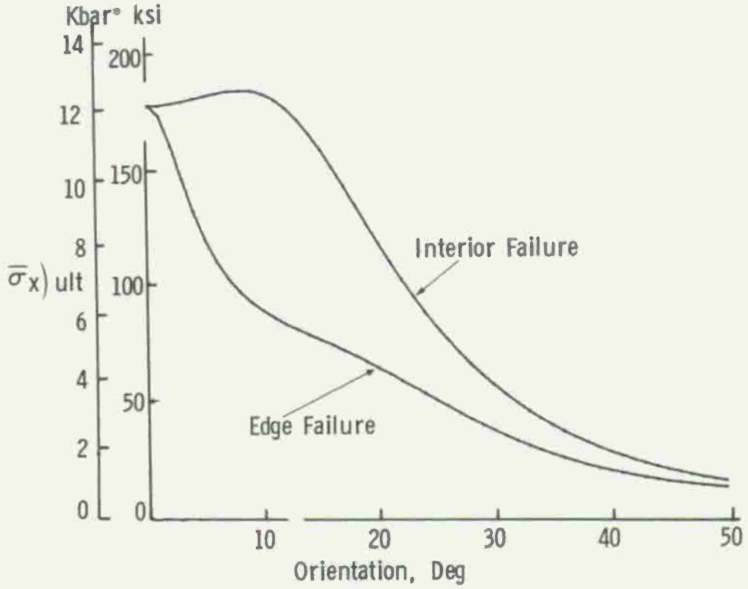

*1 Bar = 0.1 MN/m^2 = 10^6 Dyne/cm^2

Figure 3. Predicted Failure in Graphite Epoxy Angle Ply Laminates

TABLE III. ELASTIC CONSTANTS OF UNIDIRECTIONAL LAMINATES

Moduli Given in 10^6 psi (M bars; 1 bar = 100 KN/m^2 14.505 psi.)

MATERIAL	E_L		E_T		G_{LT}*	ν_{LT}	
	Ave.	Coef. Var.	Ave.	Coef. Var.		Ave.	Coef. Var.
BORON/5505	29.9 (2.06)	1.4%	2.98 (.205)	†	0.8 (0.055)	0.212	2.3%
MOD II/5206	19.9 (1.37)	2.6%	1.25 (.086)	†	0.8 (.055)	0.34	2.9%

---

* G_{LT} determined from fit of E_x vs fiber orientation in $\pm\theta$ laminates. Other constants from stress-strain curves of unidirectional materials.

† One determination only.

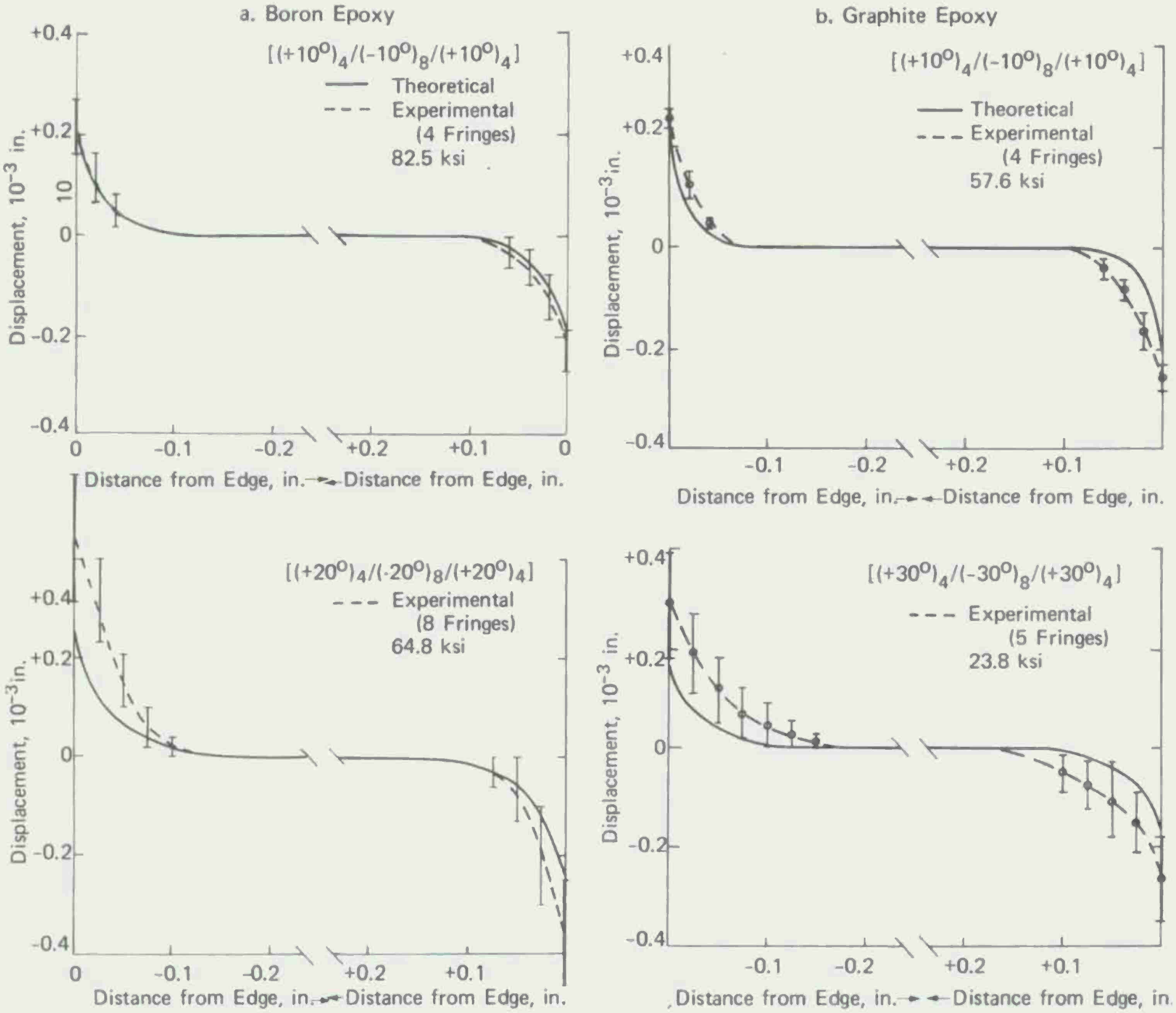

Figure 4. Comparison of Experimental and Theoretical Shear Displacements - Face Views. Ref. 6

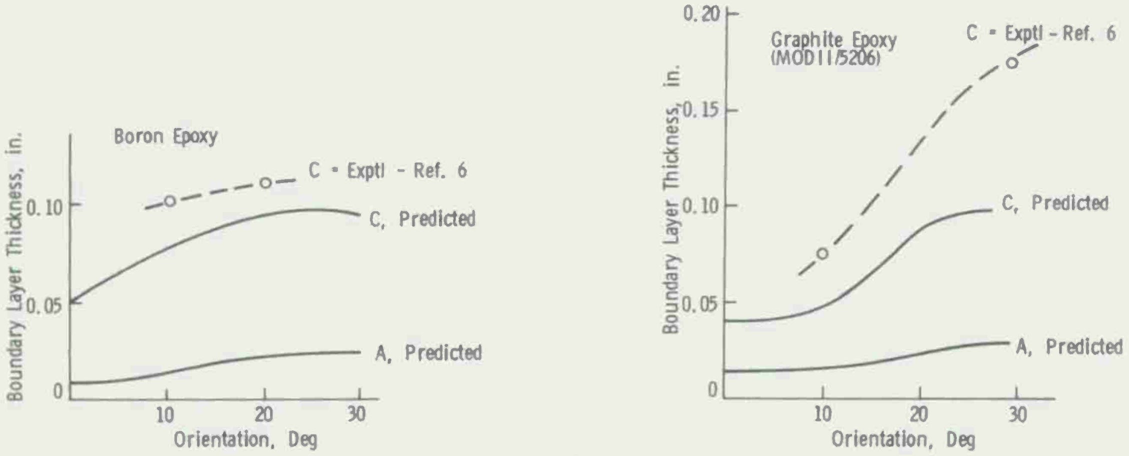

Figure 5. Boundary Layer Thickness Versus Orientation

C configuration laminates as a function of orientation. With a_{11} given by the first of Equations (2) and ρ_{16} given in Equation (8), the measured axial modulus E_x for ± θ laminates not dominated by stresses at the free edge is given by

$$E_x = \frac{1}{(1-\rho_{16})a_{11}} \tag{12}$$

Figure 6 shows a plot of measured values of a_{11}/a_L versus θ, where $a_L = 1/E_L$, together with predicted values obtained from the constants given in Table III. The closeness of the fit is a measure of the accuracy of the G_{LT} values of Table III, the other constants having been obtained from the tests on the unidirectional materials as previously discussed.

In Figures 7 to 9 the tensile test results are compared with predicted stresses for interior and edge failure. The tendency of the C configuration laminates to fail near the stresses predicted for edge failure is clearly demonstrated. The A configuration laminates fail considerably above the edge failure curve over the range of interest, achieving the values predicted for interior failure in the case of ± 30° A and ± 45° A MOD II/5206, as well as for ± 45° A boron/5505. The comparison in Figure 9 of T300/E797 with T300/5208 data taken from [14] is of additional interest. Although the latter is for $(\pm\theta)_{2S}$ laminates as opposed to the A configuration laminates treated here, the differences between the laminates is trivial with respect to the stress field which may be expected to occur under tensile load. The close proximity of the strength values which were obtained is consistent with this expectation.

"C" CONFIGURATION FRACTURE MORPHOLOGY

a. General Characteristics of Failure

Figure 10 shows two distinct types of failure which were obtained with the C configuration laminates. At the higher orientations, 30° to 45°, the failures tended to appear as in Figure 10(A) while at lower orientations the type of failure shown in Figure 10(B) was common. Three types of failure processes can generally be distinguished in these results, fiber separation (FS) within plies, delamination (DEL), and fiber breakage (FB). The sketches shown in Figure 11 depict these features more clearly. In the failure shown in Figure 10(A) no fiber breakage is present and the result can be called a DEL–FS mode. The failure of Figure 10(B), on the other hand, can be called a "partial FB" mode since it initiates as DEL–FS and converts at a certain point to FB. The sketch shown in Figure 11(C) shows the details of the situation where the FB mode seems to begin. Note that in the initial DEL–FS phase two fiber separation surfaces are created, one along the $+\theta$ fibers and one along the $-\theta$ fibers. The two FS surfaces run along fiber directions and subsequently converge at the intersection point labeled I in Figure 11(C), Plan View. The perpendicular distance from the edge to the intersection point I is governed by the length ℓ_p, shown in Figure 11(C) as the distance along the edge between the points where FS initiates in the $+\theta$ and $-\theta$ plies, and is given by $\ell_p = \ell_c \tan\theta$. It is possible that the tendency for FB to initiate at point I is related to the ratio of the distance ℓ_p to the specimen width. As discussed later the fracture surface, which becomes a "through crack" at point I, may be equivalent to a sharp edge notch of length ℓ_p, and because of unloading of much of the material around this notch, it is possible that interlaminar shear and normal stresses are drastically reduced, relieving the tendency for delamination to progress further. Without such an effective edge notch the resolved tensile stresses along the fibers tend to be much below the value at which fiber breakage can possibly take place for θ values above 10°.

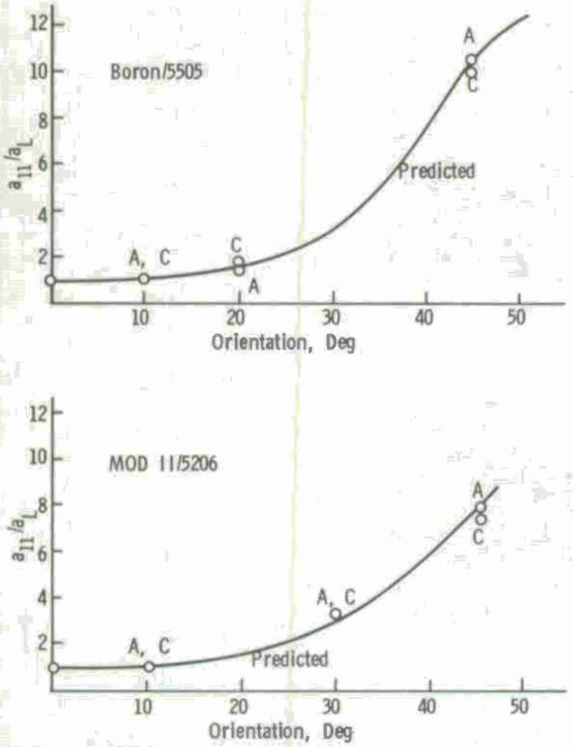

Figure 6. Predicted Versus Observed Axial Compliance in A and C Configuration Angle Ply Laminates. $a_{11} = 1/E_x(\theta)$. $a_L = 1/E_L$

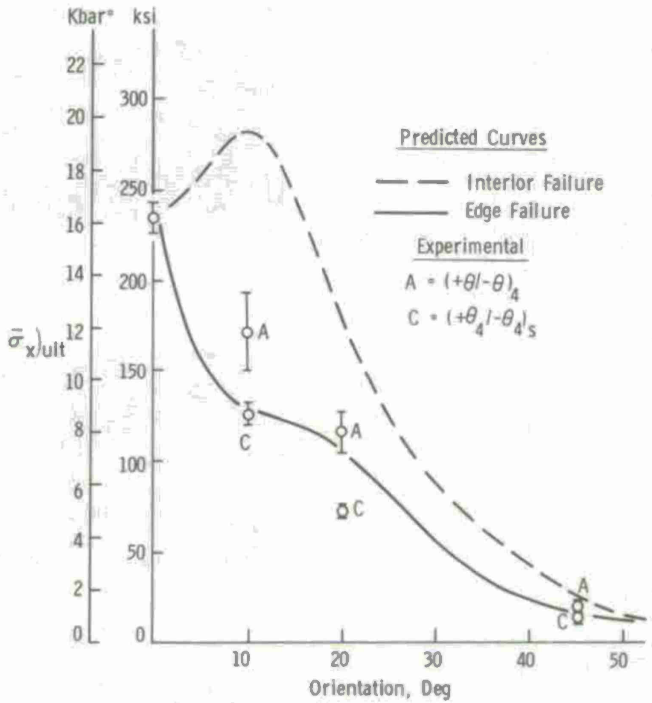

*1 Bar = 0.1 MN/m^2 = 10^6 Dyne/cm^2 = 14.505 psi

Figure 7. Tensile Test Results, Boron/5505

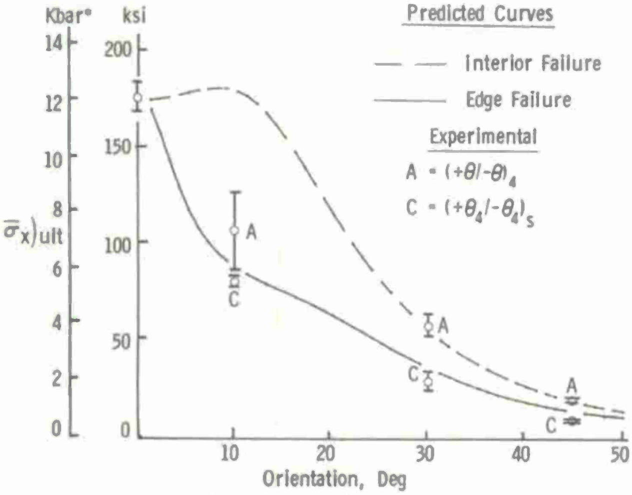

*1 Bar = 0.1 MN/m^2 = 10^6 Dyne/cm^2 = 14.505 psi

Figure 8. Tensile Test Results, MOD II/5206

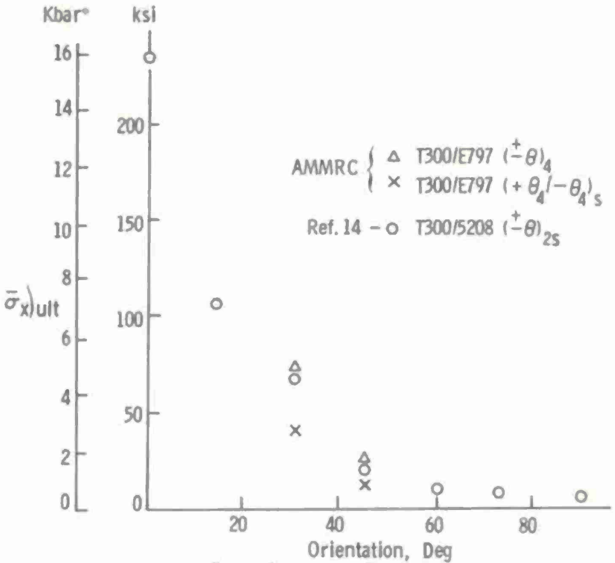

*1 Bar = 0.1 MN/m^2 = 10^6 Dyne (cm^2 = 14.505 psi)

Figure 9. Tension Test Results, T300/E797. Comparison with Results for T300/5208. Ref. 14

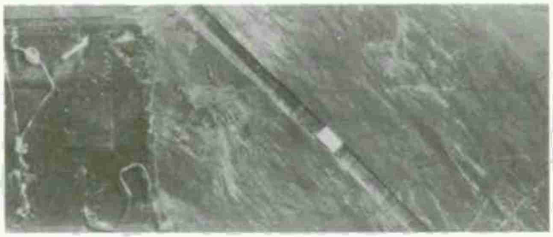

MOD II/5206 $(+45_4/-45_4)_s$

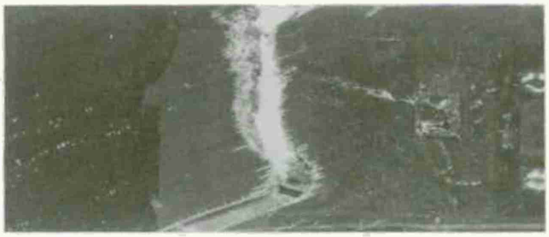

Boron/5505 $(+20_4/-20_4)_s$

Figure 10. Typical Angle Ply Failures

19-066-1029/AMC-76

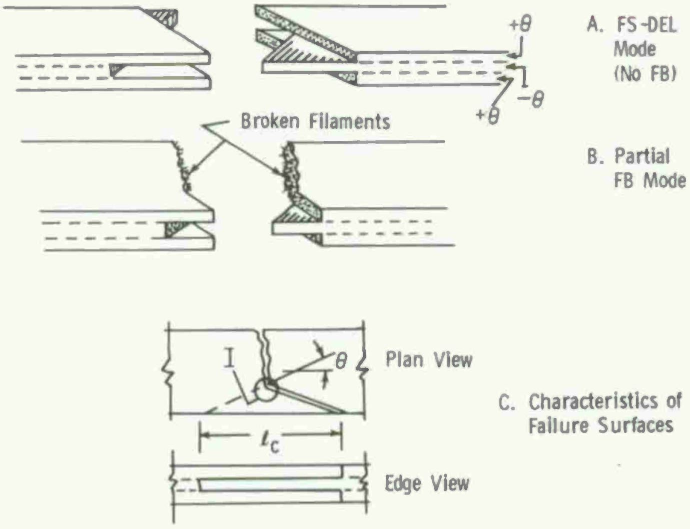
+θ
A. FS-DEL Mode (No FB)
−θ
+θ
Broken Filaments
B. Partial FB Mode
I
θ
Plan View
C. Characteristics of Failure Surfaces
ℓ_c
Edge View

Figure 11. Characteristic Features of Failures in Angle Ply Laminates

b. Acoustic Emission–Dye Penetrant Studies

In order to gain further information on the early stages of failure, a method for loading the specimen to a point of initial damage but adequately below the ultimate load to avoid catastrophic failure was desired. Acoustic emission techniques proved to offer an ideal approach to obtaining such a result. By use of acoustic emission it was found that the load level could be readily adjusted to a point which insured that DEL–FS had initiated but which avoided the risk of more complete stages of failure.

The experimental setup for providing acoustic emission monitoring capability is shown in Figure 12. The acoustic emission unit consisted of: (1) a preamplifier and amplifier having a gain selectable up to 100 dB and a bandwidth ranging from 100 kHz to 2000 kHz; (2) a totalizer having selectable pass bands; (3) an audio monitor having a speaker and amplifier with volume control; and (4) a transducer for detecting acoustic emission at a peak response of 115 kHz ± 5%. The system had the capability of recording both total acoustic emission count (events) and acoustic emission rate on x-y-y′ recorders together with the stress-strain relationship of the pertinent specimen when subjected to stress. (An emission event is defined as a rapid physical change in a material, such as the breaking of a fiber in a composite, that releases energy which appears as acoustic emission [15].)

Exploratory investigations were conducted to determine whether features in the acoustic emission record might be found during the loading of C configuration laminates which could be used as an indicator of early damage. Figure 13 shows a typical record obtained from a C configuration laminate during loading to failure. The traces appear to be free of acoustic activity up to a point at about 64% of ultimate load. At that point the acoustic output starts to take place and thereafter monotonically increases in intensity up to the point of failure. The generous separation between the point of acoustic emission onset and ultimate failure provides more than enough latitude in adjustment of the load level to insure that early phases of failure can be captured.

This type of trend having been established, selected specimens were loaded to the point of the initially rising signal and then removed for dye penetrant inspection. With graphite epoxy composites it was helpful to precoat the specimen with white spray paint prior to applying the dye penetrant in order to obtain sufficient optical contrast to insure visibility of cracks. Figures 14 and 15 show two specimens subjected to such treatment. The T300/E797 specimen seen in Figure 14 shows clear-cut evidence of the initial DEL–FS failures described in Figure 11(C), (Edge View). Figure 15 shows results obtained on a film-reinforced angle ply laminate consisting of ± 30° C MOD II/5206 to which are added Kapton film layers containing vapor-deposited boron. (The film-reinforced composites were produced by the Cabot Corporation. Properties of film-reinforced composites as well as the boron-on-Kapton film were discussed by Padawer [16].) The film layers tend to provide in-plane shear rigidity to the composite which helps to reduce the magnitude of interlaminar shear stresses as well as the boundary layer thickness.

The fracture surface seen in Figure 14 clearly shows the development of both DEL and FS-type failures. That in Figure 15 suggests that delamination is the first damage mode to occur as the FS mode is less clearly developed here than in Figure 14. This is to be expected since the film provides a large degree of enhancement of the transverse strength in the plies making up the laminate.

In general the results shown in Figures 14 and 15 tend to confirm the assumption that failure in the C configuration laminates initiates in the vicinity of the free edge in the form of combined DEL–FS fracture. It is of some interest to determine whether the DEL or FS mode is the earliest form of damage since this would affect the way failure predictions should be applied to the stress

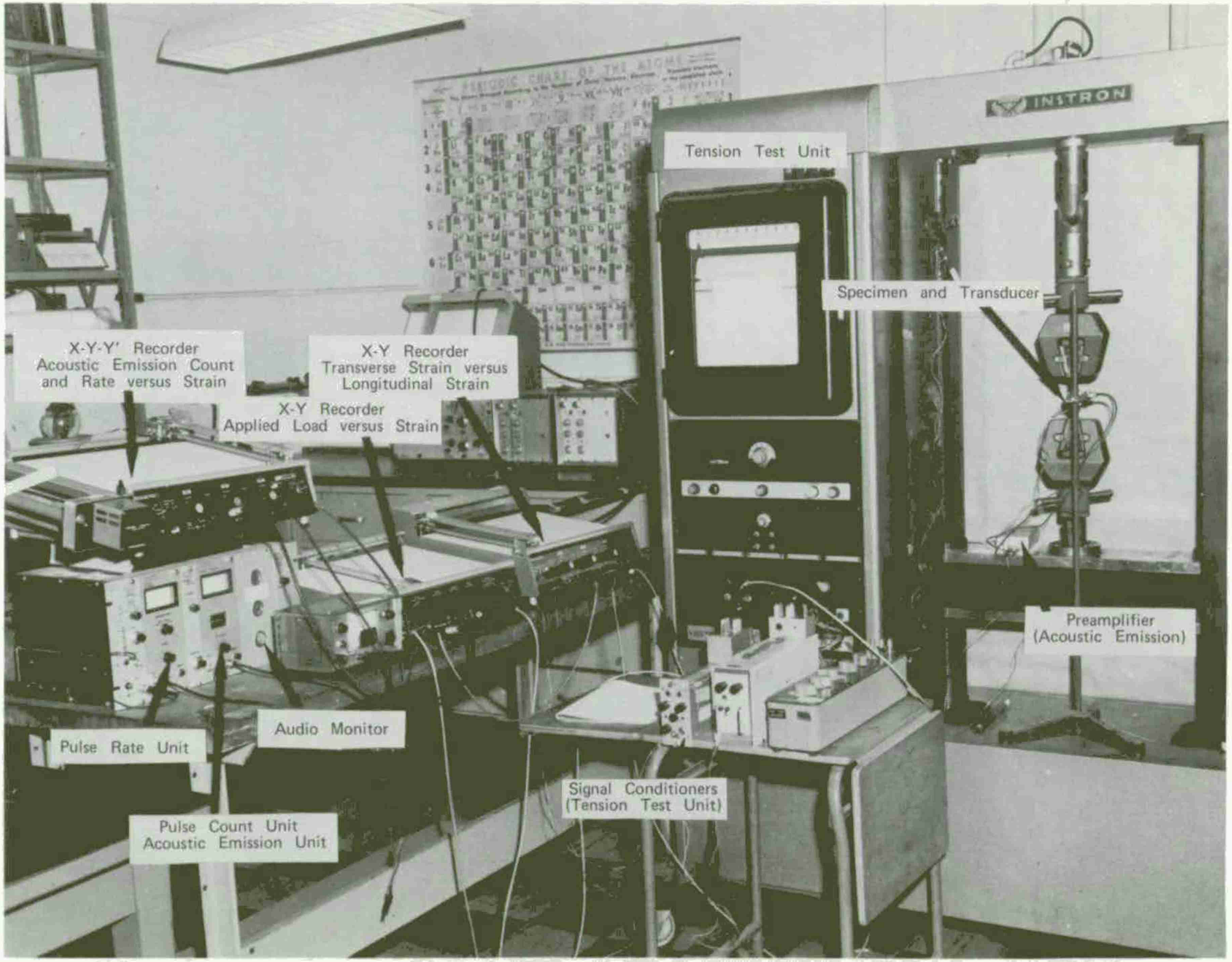
Tension Test Unit
INSTRON
Specimen and Transducer
X-Y-Y' Recorder Acoustic Emission Count and Rate versus Strain
X-Y Recorder Transverse Strain versus Longitudinal Strain
X-Y Recorder Applied Load versus Strain
Preamplifier (Acoustic Emission)
Audio Monitor
Pulse Rate Unit
Signal Conditioners (Tension Test Unit)
Pulse Count Unit Acoustic Emission Unit

Figure 12. Acoustic Emission and Tension Test Apparatus

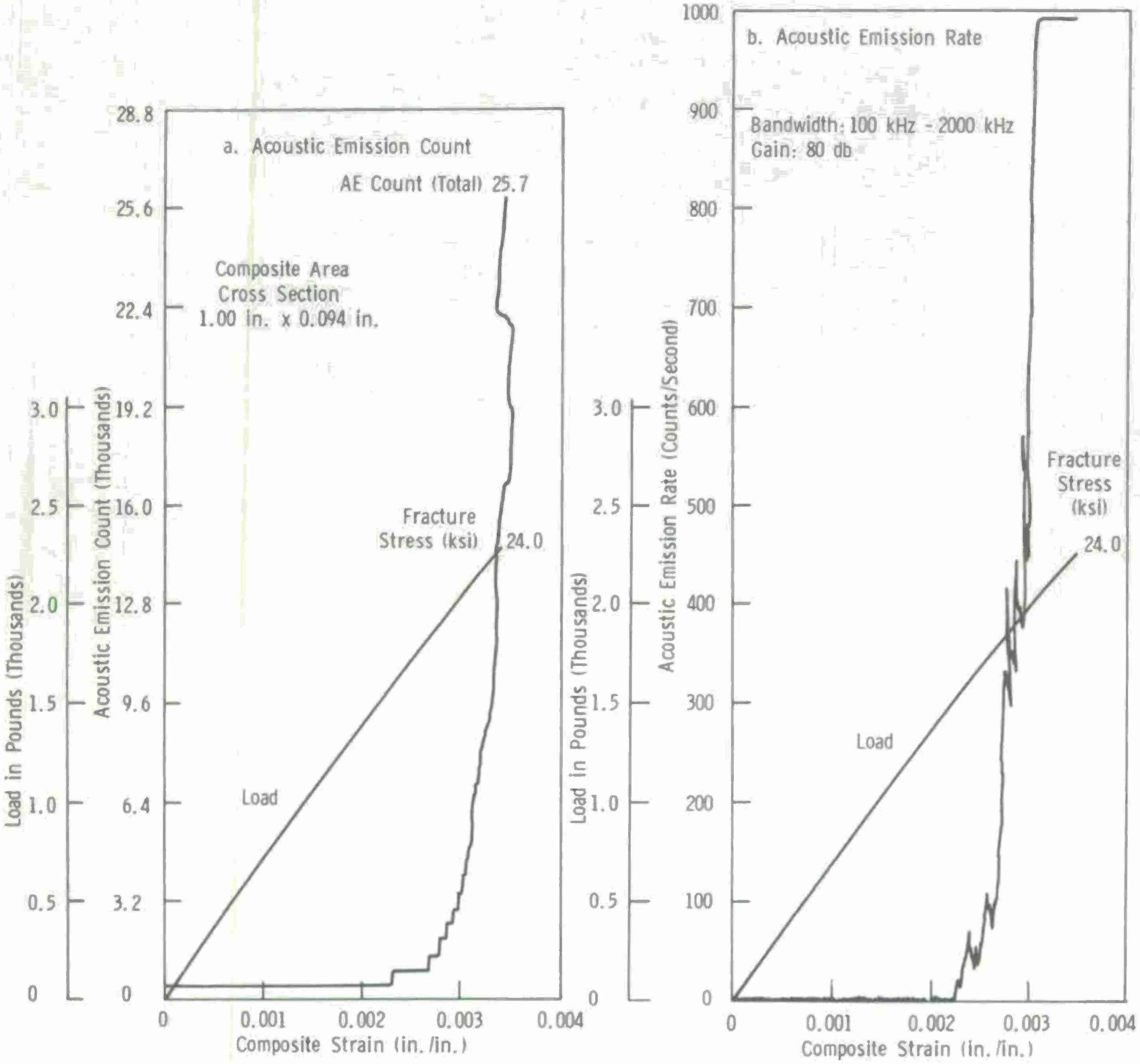

Figure 13. Acoustic Emission Count and Rate Plus Composite Load as a Function of Composite Strain for MOD II/5206, ±30°C Configuration

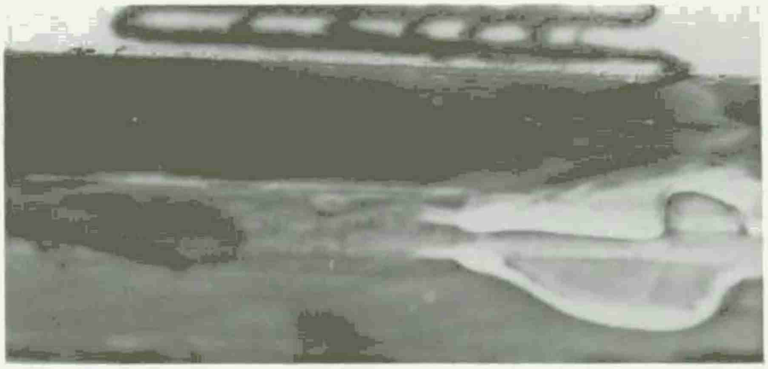

Figure 14. Initial Damage in $(+30_4/-30_4)_S$ T300/E797

19-066-1028/AMC-76

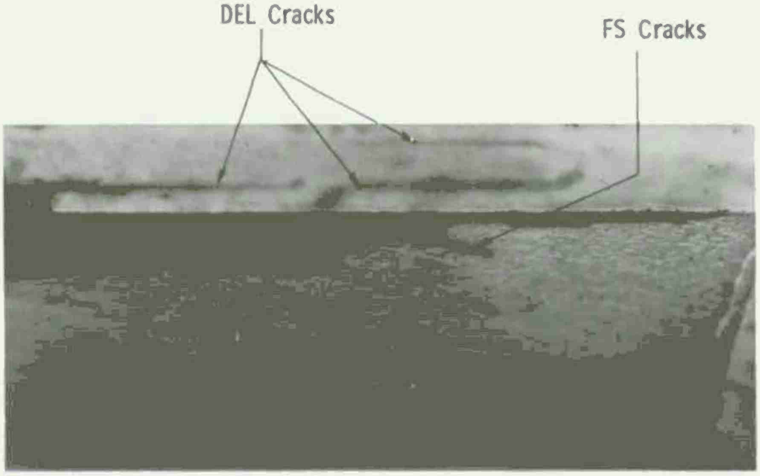

Laminate Construction: $\{[+30^0\ \text{GR-E}/I_3]_4/[-30^0\ \text{GR-E}/I_3]_4\}_S$

I = PVD Boron/Kapton Substrate. Ref. 16

GR-E = MOD II/5206

Figure 15. Initial Damage in Film-Reinforced ±30°C, MOD II/5206

19-066-1027/AMC-76

state at the free edge. The results to date do not resolve the exact sequence of events but it is felt that the techniques which have been discussed have the power to do so provided more complete observations are made at the early part of the failure process.

A further result of the dye penetrant studies is the indication that the initial DEL–FS failure is semi-stabilized in the early stages of loading. If this were not true, it would not be possible to effect load removal before the initial failure propagated across the whole width of the specimen. This stabilization of the initial damage is further confirmed by the observations made using high speed cinematography to be discussed next.

c. High Speed Cinematography

One 30°C specimen (MOD II/5206) was loaded at a deflection rate of 2 in./min. corresponding to a nominal strain rate of 0.55%/sec, considering the gage length to be the 6″ distance between tab ends indicated in Figure 1. A Hycam* 16-mm model 41-0004 high speed camera was used to photograph the specimen at 5411 frames/sec during the loading period. The specimen was provided with a 1000 line/in. moiré grating using the technique described in [6], so that the visual record illustrated by the results shown in Figure 16 consisted of a time history of the axial displacement field as seen looking normal to the 1″ face of the specimen. The filmed record which was retained included the last 460 frames prior to failure, corresponding to a time increment of 0.085 sec or a strain increment of about 0.04675%; this increment amounts to about 10% of the ultimate strain capability of the specimen.

Moiré fringes of the type seen in Figure 16 were discussed in Ref. [6]. These were used to obtain the displacement profiles shown in Figure 4. The main feature of the results shown in Figure 16 is the development of an FS crack at the upper edge near the right side of the picture, starting at frame 149. The distortion of the bright fringes into an arch-shaped formation indicates that different-order fringes have come into contact, a situation signalling the presence of a crack-like dislocation across which a displacement discontinuity can take place. Since successive fringes represent increases in displacement of 0.001″ corresponding to the 1000 line/in. grating density, an arch formation developed by the joining of fringes separated by n orders represents a displacement discontinuity of n X 0.001″ which gives an estimate of the crack opening displacement at the point where the crack intersects the arch. Figure 17 shows the crack advance history (i.e., distance of advance normal to specimen edge) which can be deduced from the results shown in Figure 16. Note that a period occurs during the last 0.02 second of loading during which no advance takes place. This is consistent with the conclusion obtained from the dye penetrant examinations that the DEL–FS failure tends to become temporarily stabilized. At present it is felt that the stabilization point may be related to the intersection point I designated in Figure 11(C).

PROPOSED MODEL FOR THE FAILURE OF ANGLE PLY LAMINATES

Understanding of the progression of failure in composite materials is made difficult by the possibility that the interaction of adjacent layers may have a large effect on the nature of the failure after it has initiated. The initial form of damage can be predicted in most situations by existing computational tools. Once a crack has formed in a given layer, however, it is generally bridged by fibers of some other layer and unless the first damage involves fiber breakage, its progression may be strongly inhibited by the bridging fibers so that subsequent damage may be forced to take a form different from that of the initial damage mode.

---

*Manufactured by Red Lake Corporation, Santa Clara, California.

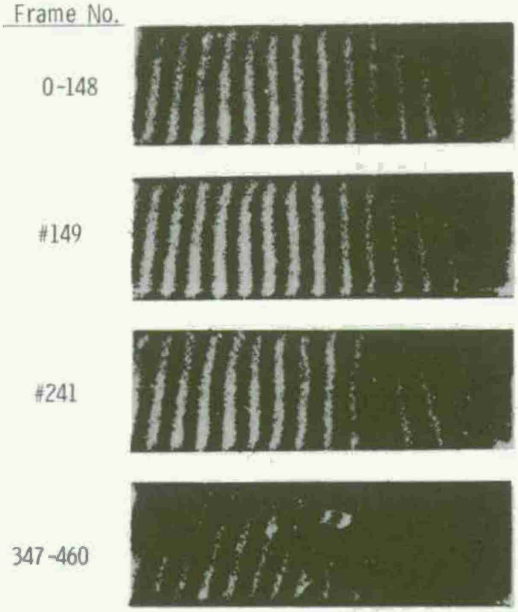

Figure 16. Selected Frames from High Speed Film Strip (5411 Frames per Second). $(+30_4/-30_4)_S$ MOD II/5206. Applied Strain 0.5% to 0.55%. Moire Grating 1000 Lines per Inch.

19-066-1026/AMC-76

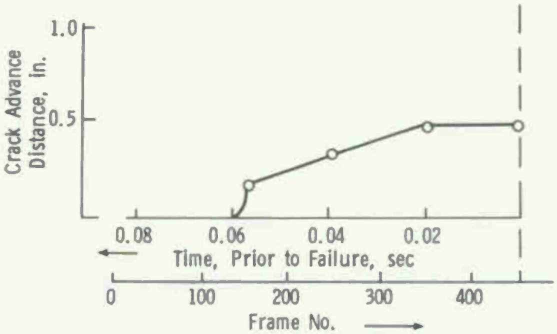

Figure 17. Progression of FS Crack Determined from High Speed Motion Picture

Figure 18 shows a possible scheme describing the progression of events in DEL–FS failure, beginning with an initial FS crack in the outer ($+\theta$) layer which is stopped at the $-\theta$ plies which bridge it. Subsequently, the shear stress at the root of the FS crack gives rise to delamination failure as the next stage in the process, this being the only available failure mode at that point. It is likely that as a portion of the upper $+\theta$ layer is unloaded by the Stage II delamination, increases take place in the in-plane stresses in the central ($-\theta$) layer, corresponding to increases in σ_T and τ_{LT} in that layer. At some point after the delamination begins, a second FS crack therefore develops. Again the FS crack is bridged by the fibers of the neighboring $+\theta$ layers and it can progress only through the thickness of the $-\theta$ layer, being followed by a second delamination shown as Stage III in Figure 18. Eventually these combined events lead to the converging FS and DEL surfaces sketched in Figure 11(C).

An alternative scheme may be proposed in which the first damage is the DEL mode but which. again, causes aggravation of stresses σ_T and τ_{LT} resulting in FS crack formation at the tip of the DEL crack. Existing analysis [1–4] which can be used to compare the relative levels of in-plane stresses and interlaminar shear stresses can be used to resolve which mode is likely to be the first, and can identify the load level at which the earliest damage can be expected.

Once the FS surfaces have converged to their intersection point, it is of interest to determine the conditions under which the FB mode develops as opposed to further propagation of the DEL–FS failure. Figure 19 describes the details of a concept for pinpointing the features which control the transition situation. As shown in Figures 19(A) and (B), the FS cracks form the boundaries of a triangular region containing essentially unloaded material, with the result that the V notch shown in Figure 19(C) has effectively formed at the edge of the strip. In-plane stresses in the fiber directions would rise considerably around the tip of such a notch due to the associated stress concentration, and for low orientations would tend to become high enough to break fibers at relatively low loads. (Indeed for an ideal sharp tipped notch the stresses would be infinite, similar to the situation at a crack tip.) At the same time the delamination and fiber separation cracks tend to unload the laminate in a direction causing lowering of interlaminar shear stresses so that the tendency for FS and DEL to propagate further is reduced. Some light on this aspect of the problem is given by the results of [17] which dealt with three-dimensional analysis of stresses around edge cracks in graphite epoxy angle ply laminates. Near the crack flanks where the material is unloaded to a large extent the interlaminar shear stresses appeared to be much below the values observed near free edges in unnotched laminates [1–4, 17]. The situation in the case of V notches would vary somewhat from that of the edge crack but similar tendencies should be observed in regions of unloaded material near the notch flanks. While the studies conducted here do not provide sufficient information to determine which mode will be obtained after the FS intersection point has been reached, they do point out what further steps can be taken to clarify the situation.

Two types of study are of immediate interest in this regard: (1) an experimental study of V-notched angle ply laminates to confirm that their failure load and type of failure is similar to that ultimately obtained in unnotched angle ply laminates; (2) an analytical study involving 3D stress analysis of V-notched laminates to determine the relative level of interlaminar shear stresses, thereby confirming that these are sizably reduced when the effective V notch has formed.

The main result of the present study has thus been to identify the distinct phases of the failure process in angle ply laminates and to single out the above points for further clarification which will provide improved understanding of the failure of composite laminates in general.

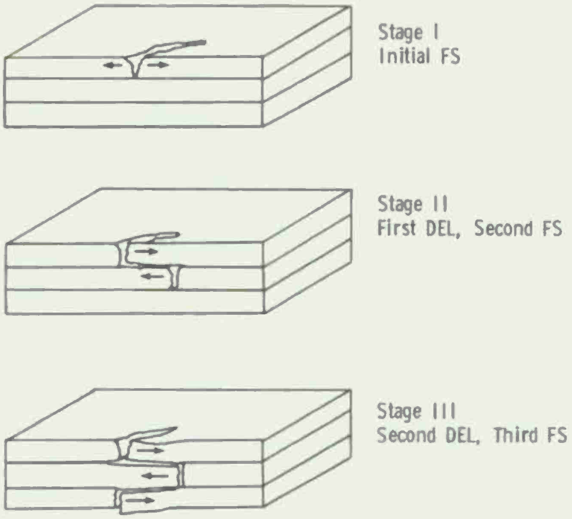
Stage I
Initial FS
Stage II
First DEL, Second FS
Stage III
Second DEL, Third FS

Figure 18. Proposed Model for Development of FS - DEL Damage Zone

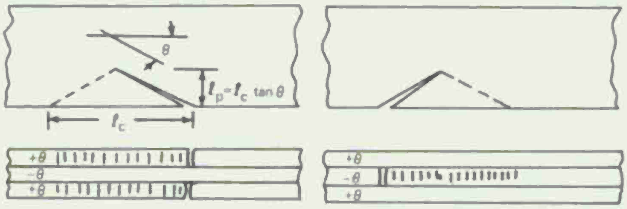
θ
$l_p = l_c \tan\theta$
l_c
+θ
-θ
+θ
+θ
-θ
+θ

A. FS Crack in Outer Layers B. FS Crack in Inner Layer

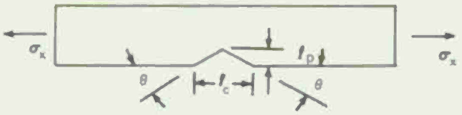
σ_x
σ_x
l_p
θ
l_c
θ

C. Effective Edge Notch

Figure 19. Details of FS-DEL Failure Zone and Effective Edge Notch Model

CONCLUSIONS

The results of the failure tests on A and C configuration laminates provides clear evidence that the mixing of orientations as in the A configuration is effective in eliminating the degrading effects of the stress field in the vicinity of free edges. Failures in C configuration laminates tend to take place at the low loads predicted for failure at the free edge where in-plane shear stresses which tend to strengthen the laminate in the interior regions are lacking. Failure stresses in A configuration laminates are significantly higher than in the C configuration and in some cases reach the predicted values for the interior region which take the in-plane shear stresses fully into account. Lower interlaminar shear stresses and smaller boundary layer thicknesses which are believed to occur in A configuration laminates are the main factors involved in achievement of higher tensile strength values.

At high orientation angles failures tend to take place purely through DEL–FS, with no fiber breakage. At low orientations the FB mode becomes important and appears to initiate at the intersection point of the FS surfaces in the $+\theta$ and $-\theta$ layers.

The triangular zone of material bounded by the FS surfaces being unloaded, the initial FS–DEL forms an effective V notch at the edge of the composite. Whether the FB mode comes into being or subsequent failure involves further DEL–FS is a function of the in-plane stress concentration at the V-notch tip, the resolved tensile stresses in the fiber direction and the degree to which interlaminar stresses are lowered in forming the effective notch.

Acoustic emission appears to be a valuable tool for identifying first damage modes. Further study involving the use of acoustic emission to signal the point of earliest damage together with dye penetrant inspection to identify the nature of the damage, especially to determine whether DEL or FS takes place first, is desirable.

RECOMMENDATIONS

Further studies should be carried out to establish the validity of the "effective V notch" concept for understanding failure progression beyond the FS intersection point. These would include: (1) experimental studies of edge-notched angle ply laminates to establish the similarity of failures to those in unnotched laminates; (2) 3D stress analyses to determine the degree to which interlaminar shear stresses are reduced when the effective V notch has formed.

Additional studies using acoustic emission together with dye penetrant or other appropriate methods for damage characterization should be carried out.

ACKNOWLEDGMENTS

Professor F. P. Chiang of the State University of New York at Stoney Brook provided valuable help in obtaining and evaluating the high speed motion picture results. The camera was operated by Mr. J. Rainey of AMMRC.

REFERENCES

1. Pupo, A. H., and Evansen, H. A., J. Composite Materials, v. 4, 1970, 204.

2. Pipes, R. B., and Pagano, N. J., J. Composite Materials, v. 4, 1970, 538.

3. Oplinger, D. W., AMMRC Technical Report AMMRC TR 71–62, 1971.

4. Rybicki, E. F., J. Composite Materials, v. 5, 1971, 354.

5. Pipes, R. B., and Daniel, I., J. Composite Materials, v. 5, 1971, 225.

6. Oplinger, D. W., Parker, B. S., and Chiang, F. P., Experimental Mechanics, v. 14, 1974, 347.

7. Lauraitis, K., Univ. of Illinois, Th. and App. Mech. Report UILU-ENG-71-6009, 1971.

8. Pagano, N. J., and Pipes, R. B., Int. J. Mechanical Sciences, v. 15, 1973, 679.

9. Whitney, J. M., and Browning, C. E., J. Composite Materials, v. 6, 1972, 300.

10. Reifsnider, K. L., Stinchcomb, W. W., and Henneke, E. G., "Delamination in Quasi Isotropic Graphite Epoxy laminates", 4th ASTM Conference on composites, Valley Forge, Pa. (May, 1976) to be published in the Proceedings.

11. Nuismer, R. J., and Whitney, J. M., ASTM STP 593, Fracture Mechanics of Composites, American Society for Testing of Materials, 1975, 117.

12. Hoffman, O., J. Composite Materials, 1969, v. 1, 200.

13. Tsai, S., and Wu, E., J. Composite Materials, v. 5, 1971, 58.

14. Sendeckyj, G., Air Force Flight Dynamics Laboratory Report AFFDL-TM-74-89-FBC, 1974.

15. Acoustic Emission, ASTM Special Technical Publication 505, Philadelphia, Pa., American Society for Testing and Materials, 1972, 355-357.

16. Padawer, G. E., "The Notch Sensitivity of Film Reinforced Multi-Fastened Mechanical Joints in Fibrous Composites", Final Technical Report, Contract N00019-71-C-0435, Naval Air Systems Command, 1972.

17. Mandell, J. T., Wang, S. S., and McGarry, F. J. "Fracture of Graphite Fiber Reinforced Composites", Air Force Materials Laboratory Report AFML-TR-73-142, July 1974.

AUTHOR INDEX

Avery, J. G.	Boeing Aerospace Company	Seattle, WA	138
Brinson, H. F.	Virginia Polytechnic Institute and State University	Blacksburg, VA	237
Chamis, C. C.	NASA-Lewis Research Center	Cleveland, OH	193
Chick, LTC, E. E.	Army Materials and Mechanics Research Center	Watertown, MA	3
Daniel, I. M.	IIT Research Institute	Chicago, IL	249
Demuts, E.	Air Force Flight Dynamics Laboratory	Wright-Patterson AFB, OH	123
Doble, G. S.	Materials Technology - TRW, Inc.	Cleveland, OH	45
Evangelides, J. S.	The Aerospace Corporation	Los Angeles, CA	98
Gehring, R. W.	Rockwell International Corp., Columbus Aircraft Div.	Columbus, OH	45
Grenis, A. F.	Army Materials and Mechanics Research Center	Watertown, MA	263
Halpin, B. M.	Army Materials and Mechanics Research Center	Watertown, MA	26
Herakovich, C. T.	Virginia Polytechnic Institute and State University	Blacksburg, VA	237
Jemian, W. A.	Auburn University	Auburn, AL	5
Jortner, J.	McDonnell Douglas Astronautics Company	Huntington Beach, CA	81
Klouman, F. L.	Norwegian Defence Research Establishment	Norway	62
Kulkarni, S. V.	Materials Sciences Corporation	Blue Bell, PA	212
Lamothe, R. M.	Army Materials and Mechanics Research Center	Watertown, MA	26
Lenoe, E. M.	Army Materials and Mechanics Research Center	Watertown, MA	26,171
Liber, T.	IIT Research Institute	Chicago, IL	249
Malvern, L. E.	University of Florida	Gainsville, FL	9
Mayerjak, R. J.	Kaman Aerospace Corporation	Bloomfield, CT	153
McLaughlin, P. V.	Materials Sciences Corporation	Blue Bell, PA	212
Neal, D. M.	Army Materials and Mechanics Research Center	Watertown, MA	171
Oplinger, D. W.	Army Materials and Mechanics Research Center	Watertown, MA	263
Parker, B. S.	Army Materials and Mechanics Research Center	Watertown, MA	263
Pipes, R. B.	University of Delaware	Newark, DE	212
Porter, T. R.	Boeing Aerospace Company	Seattle, WA	138
Renieri, G. D.	Virginia Polytechnic Institute and State University	Blacksburg, VA	237
Ross, C. A.	Air Force Armament Laboratory	Eglin AFB, FL	9
Sierakowski, R. L.	University of Florida	Gainsville, FL	9
Singley, III, G. T.	Army Air Mobility R&D Laboratory, Eustis Directorate	Eustis, VA	153

AUTHOR INDEX (Continued)

Slepetz, J. M.	Army Materials and Mechanics Research Center	Watertown, MA	223
Spier, E. E.	General Dynamics, Convair Division	San Diego, CA	62
Strickland, W. S.	Air Force Armament Laboratory	Eglin AFB, FL	9
Verette, R. M.	Northrop Corporation	Hawthorne, CA	123
Wright, E. S.	Army Materials and Mechanics Research Center	Watertown, MA	1

AMMRC MS 76-2

PROCEEDINGS OF THE ARMY SYMPOSIUM ON SOLID MECHANICS, 1976 - COMPOSITE MATERIALS: THE INFLUENCE OF MECHANICS OF FAILURE ON DESIGN

September
1976

DEPARTMENT OF THE ARMY
ARMY MATERIALS AND MECHANICS RESEARCH CENTER
Watertown, Massachusetts 02172

OFFICIAL BUSINESS

POSTAGE AND FEES PAID
DEPARTMENT OF THE ARMY
DOD 314

THIRD CLASS MAIL